Spatial presentation of tissue specific extracellular matrix components and growth factors on porous electrospun fibre scaffolds for bone-ligament interface tissue engineering

A thesis submitted to Trinity College Dublin, the University of Dublin, in partial fulfilment of the requirements for the degree of Doctor in Philosophy.

Dublin, Ireland; 2018

Dinorath Pamela Olvera Ramos

Supervisor: Professor Daniel J. Kelly

Internal examiner: Professor David Taylor

External examiner: Catherine K. Kuo

Declaration

I declare that this thesis has not been submitted as an exercise for a degree at this or any other university and it is entirely my own work. I agree to deposit this thesis in the University's open access institutional repository or allow the library to do so on my behalf, subject to Irish Copyright Legislation and Trinity College Library conditions of use and acknowledgement.

Dinorath Pamela Olvera Ramos

Dublin, 2018

Summary

In many clinical situations ligament or tendon replacements are required, such as for the surgical replacement of a torn anterior cruciate ligament (ACL). The current 'gold standard' treatment is resection of the torn ligament and replacement by an autologous tendon graft harvested from the patient's hamstring or patellar tendon. Limitations of this approach include donor site morbidity and a limited availability in the quantity of tissue available for harvest. Furthermore, the interface between the tendon graft and the bone heals as a loose fibrovascular tissue instead of a resilient fibrocartilage enthesis, which leads to long term mechanical instability of the replacement graft. This has motivated the search for alternative strategies to regenerate damaged ligaments. The field of tissue engineering aims to regenerate or replace damaged tissues through a combination of three-dimensional scaffolds, cells and signalling molecules. Currently, ligament tissue engineering strategies that consider the bone-ligament interface have generally focused on the direct osteogenic priming of mesenchymal stem cells (MSCs), or on maintaining an osteoblastic phenotype in the osseous region of a multi-layered scaffold. However, realising the importance of re-establishing a cartilaginous transition tissue between ligament and bone have led to increased interest in the tissue engineering of a cartilaginous interface between the ligament and bone regions of tissue engineered constructs.

This thesis aims to develop a mechanically functional scaffold that provides spatially defined regulatory cues for ligament tissue engineering, with the specific goal of regenerating the stratified interface between ligament and bone. This thesis began by investigating how fibre alignment and growth factor stimulation interact to regulate the chondrogenic and ligamentous differentiation of MSCs. To this end aligned and randomly-aligned electrospun microfibrillar scaffolds were seeded with bone marrow derived MSCs and stimulated with transforming growth factor β3 (TGFβ3) or connective tissue growth factor (CTGF), either

individually or sequentially. Aligned microfibres were found to facilitate either a ligamentous or a chondrogenic phenotype depending on the specifics of the growth factor stimulation regimen. It was shown that, for the engineering of ligamentous grafts, aligned electrospun microfibres in synergy with CTGF can be used to enhance ligamentous matrix production, while aligned microfibres combined with TGF-β3 can be used to promote cartilaginous matrix production.

A methodology to engineer human scale ligament scaffolds using aligned electrospun PCL fibres was then developed. By high speed collection, electrospun fibres with a higher fraction of unwelded fibres were produced. Increasing the fraction of unwelded fibres during electrospinning reduced the flexural rigidity of the resultant electrospun-sheets, which in turn allowed the bundling of fibres into 3D scaffolds with dimensions comparable to the human ACL. These unwelded fibres allowed for higher interfibrillar spacing, which in turn facilitated the rapid migration of MSCs into the body of the scaffold. The high-speed collection induced higher molecular chain orientation in the PCL fibres, which in turn resulted in the development of scaffolds with a Young's modulus approaching that of the native human ACL.

Next, the tissue-specific bioactivity of cartilage and ligament extracellular matrix (ECM) to direct MSC fate was examined after immobilization onto electrospun scaffolds. It was shown that functionalising electrospun scaffolds with the solubilized ligament ECM promotes homologous bioactivity over and above that observed with commercially available type 1 collagen. It was also found that the immobilisation method (physical adsorption or covalent conjugation) played a key role in the bioactivity of the solubilized ECM. Functionalising electrospun scaffolds with the solubilised cartilage ECM provided a substrate to support the development of a more cartilaginous tissue characteristic of the enthesis.

The next stage of the thesis explored controlling the spatial presentation of ECM and growth factors to create contiguous ligament, cartilage and endochondral/osseous regions

within an electrospun scaffold. This required developing a strategy to generate a mineralized phase to support an endochondral phenotype within the osseous region of the scaffold. To that end, simulated body fluid was used to deposit hydroxyapatite (HA) onto the fibre scaffolds. The scaffolds functionalised with cartilage ECM and a HA coating were found to support an endochondral phenotype, thereby enabling the production of scaffolds which support spatially defined differentiation of MSCs. Combining growth factors with ECM cues did not further enhance MSC differentiation over that observed with ECM stimulation alone.

To conclude, this thesis describes a novel methodology to develop a human sized, mechanically functional scaffold for ligament tissue engineering with spatially defined regions with the potential to regenerate the stratified interface between ligament and bone. This work provides insights into the appropriate combinations of biophysical and biochemical factors that can be used to engineer the interface between ligament/tendon and bone, the application of which will be significant as tissue engineering strategies move towards enthesis regeneration.

Acknowledgements

I would like to thank my supervisor, Professor Daniel J. Kelly for believing in me and encouraging me to apply for the Irish Research Council scholarship to undertake this project. Thank you for your exceptional guidance and support during my PhD, and for the great research environment in the Trinity Centre for Bioengineering.

I would like to thank the Irish Research Council for funding my research. I also want to thank all the past and present members of the Kelly, Hoey, Lally, and Ahearne Labs. Thank you all for your helpful discussions and for the fun times. Thank you to all the post-docs for facilitating my work, specially to Dr. Binulal Sathy for his mentoring and to Dr. Gráinne Cunniffe and Dr. Dave Browe for all their help. I would like to acknowledge my friends Paola Aprile, Rossana Schipani, Léa Dejob and Olwyn Mahon who contributed in some way to the research covered in this thesis. Thank you to Pattie Mathieu for her help with statistics and to Elena Stravenschi for her help with qRT-PCR. Thank you to Dr. Gavin McManus for his help with confocal microscopy. Thank you to Michael Reilly for his fantastic support in the workshop. Thank you to Peter O'Reilly for his help with the Zwicks. Thank you to Dr. Romina Charifou for her help with DSC scanning, and to Dr. Cian Cummings for his help with XPS.

I would like to thank my family and friends in Aguascalientes, and my friends in the lab, specially to Jennifer Gansau, Susan Critchley, Michele Corrigan, Julia Fernandez, Tomás González and Pedro Díaz Payno, for their support, help and good times.

Thank you to my parents, Leonardo and Rebeca, and to my sister Giselle for their unconditional support, example and love. Thank you to James, my love, for his patience and to his family for adopting me in Dublin.

Contents

List of Tables 1

Nomenclature 2

Publications 3

Chapter 1 Introduction 5

1.1 Anterior cruciate ligament and repair 5

1.2 Interface tissue engineering 9

1.3 Objectives 11

Chapter 2 Literature Review 13

2.1 Structure and function of the bone-ligament interface 13

2.2 Developmental process of the ligament to bone insertion 26

2.3 Electrospinning 32

2.4 Electrospinning for tissue engineering 35

2.5 Strategies to engineer the bone-ligament interface 38

2.6 Extracellular matrix to enhance biomimetic scaffolds 45

2.7 Mesenchymal stem cells 46

2.8 Summary and future perspectives 49

Chapter 3 Modulating microfibrillar alignment and growth factor stimulation to regulate mesenchymal stem cell differentiation 51

3.1 Introduction 51

3.2 Materials and methods 53

3.2.1 Electrospinning of polycaprolactone (PCL) microfibre scaffolds 53

3.2.2 Characterization of scaffolds 54

3.2.3 Isolation and expansion of bone marrow-derived MSCs 54

3.2.4 Scaffold cell-seeding and culture conditions 55

3.2.5 Cell viability and fluorescent imaging of cell morphology 56

3.2.6 RNA isolation and Quantitative Real-Time PCR 57
3.2.7 Biochemical analysis 58
3.2.8 Histological and immunohistochemical analysis 59
3.2.9 Dual chamber culture 60
3.2.10 Statistics 60
3.3 Results 61
3.3.1 Fabrication of microfibrillar scaffolds with defined architectures 61
3.3.2 MSCs adopt distinct morphologies in response to CTGF and TGF-β3 stimulation depending on the alignment of the underlying substrate 64
3.3.3 MSCs display distinct gene expression profiles in response to CTGF and TGF-β3 stimulation that depend on the underlying substrate alignment 66
3.3.4 Sequential supplementation with CTGF and TGFβ3 supports fibrocartilaginous differentiation on microfibrillar scaffolds 69
3.3.5 Growth factor stimulation regulates tissue development with MSC-seeded electrospun scaffolds 72
3.3.6 Culturing a scaffold with spatially defined presentation of CTGF and TGFβ3 ... 77
3.4 Discussion 78
3.5 Conclusions 85
Chapter 4 Electrospinning of human scale microfibrillar scaffolds for ligament tissue engineering 87
4.1 Introduction 87
4.2 Materials and Methods 89
4.2.1 Electrospinning 89
4.2.2 Alignment and diameter of microfibers 91
4.2.3 Indirect measurements of fibre welding in electrospun-sheets 92
4.2.4 Isolation and expansion of bone marrow derived MSCs 92

4.2.5 Cell viability and visualization of cell morphology 92
4.2.6 Mechanical testing 93
4.2.7 Differential scanning calorimetry (DSC) analysis 94
4.2.8 Microcomputed tomography (µCT) scans for 3D geometry 95
4.2.9 Density of the fibre bundles, porosity and pore size 96
4.2.10 Validating cell infiltration potential 97
4.2.11 Culture conditions for MSC differentiation 97
4.2.12 Gene expression 98
4.2.13 Statistical analysis 99
4.3 Results 100
4.3.1 Fabricating bundles of aligned PCL fibres using high speed electrospinning .. 100
4.3.2 The mechanical properties of electrospun fibre bundles are strongly dependent on the rotational velocity of the collector 105
4.3.3 MSCs rapidly migrate into the highly porous bundles generated by high speed electrospinning 112
4.3.4 Evaluating the instructive potential of 3D fibre-bundles towards chondrogenesis and ligamentogenesis 116
4.4 Discussion 117
4.5 Conclusions 123
Chapter 5 Assessing the bioactivity of ligament and cartilage derived extracellular matrices (ECM) for interface tissue engineering 125
5.1 Introduction 125
5.2 Materials and Methods 127
5.2.1 Electrospinning 127
5.2.2 Solubilization of cartilage and ligament ECM 127
5.2.3 SDS-PAGE 128

5.2.4 Protein immobilization and characterization of functionalized scaffolds.....129
5.2.5 Changes in surface composition and ECM distribution.....130
5.2.6 SEM.....131
5.2.7 Quantification of immobilized solubilized ECM.....131
5.2.8 Immobilization of solubilized ECM and collagen type I onto the PCL fibres by physical adsorption for cell culture studies (sections 5.3.2 – 5.3.4) 132
5.2.9 Immobilization of solubilized ECM and collagen type I onto the PCL fibres by covalent conjugation for cell culture studies (sections 5.3.2 – 5.3.4) 132
5.2.10 Isolation and expansion of mesenchymal stem cells (MSCs).....132
5.2.11 Seeding of MSCs on scaffolds and culture conditions 133
5.2.12 Cell viability, visualization of cell morphology, and counting of pre-adipocytes135
5.2.13 Gene expression 136
5.2.14 Histology 137
5.2.15 Statistical analysis 137
5.3 Results.....138
5.3.1 Characterization of the ECM-functionalized scaffolds 138
5.3.2 The bioactivity of solubilized ligament and cartilage ECM.....145
5.3.3 Effect of solubilized ligament and cartilage ECM on MSC differentiation in the presence of CTGF.....150
5.3.4 Effect of solubilized ligament and cartilage ECM on MSC differentiation in the presence of TGF-β3 154
5.4 Discussion 158
5.5 Conclusions 161
Chapter 6 : Spatial presentation of growth factors and extracellular matrix components for bone-ligament tissue engineering.....163

6.1 Introduction 163
6.2 Materials and Methods 165
6.2.1 Electrospinning 165
6.2.2 Isolation and expansion of mesenchymal stem cells (MSCs) 165
6.2.3 Solubilization of cartilage and ligament ECM 166
6.2.4 SEM 166
6.2.5 Cell viability 167
6.2.6 Gene expression 167
6.2.7 DNA quantification 168
6.2.8 Study 1. Finding the appropriate composition of culture media 168
6.2.9 Study 2. Coating of electrospun PCL scaffolds with hydroxyapatite 170
6.2.10 Study 3. Controlling the spatial presentation of ECM components and growth factors 172
6.2.11 Statistical analysis 174
6.3 Results 175
6.3.1 Finding the appropriate culture media composition 175
6.3.2 Hydroxyapatite coating 178
6.3.3 Spatial functionalization of scaffolds with ECM and growth factors 181
6.4 Discussion 185
6.5 Conclusions 188
Chapter 7 Discussion and conclusions 189
7.1 Limitations 193
7.2 Conclusions 196
7.3 Future work 197
Bibliography 199

List of Figures

Figure 1.1 Gross observation and histology images of the ACL 7

Figure 1.2 Schematics of ACL reconstruction using a patella tendon-bone graft. 8

Figure 1.3 Electrospun fibre scaffold spatially functionalized with extracellular matrix (ECM) and/or growth factors within appropriate regions of the construct for (1) mineralized, (2) cartilage, (3) ligament regions.....12

Figure 2.1 Types of ligament/tendon-bone insertions 14

Figure 2.2 Histology sections of tendons. 16

Figure 2.3 Mineralized and unmineralized fibrocartilage in the enthesis.....17

Figure 2.4 Structural hierarchy of ligaments and tendons 19

Figure 2.5 The structure of tendon and ligament fibres changes before attaching to bone...21

Figure 2.6 ACL stretch longitudinally. 22

Figure 2.7 Mineral distribution at the enthesis. 24

Figure 2.8 Contribution of the *Scx*$^{+}$/*Sox9*$^{+}$ cell lineage to the formation of ligaments and the entheseal side of tendons 28

Figure 2.9 Establishment of the junction between cartilage and tendon/ligament along the *Scx/Sox9* axis.. 29

Figure 2.10 A fibrocartilaginous transition zone did not develop between the supraspinatus tendon and the humeral head until postnatal time points (Toluidine blue stain). 31

Figure 2.11 Electrospinning process. 34

Figure 2.12 Twisted fibres into 3D scaffolds for ACL reconstruction. 39

Figure 2.13 Fibre-based scaffolds incorporating bony regions. 40

Figure 2.14 Formation of brushite cement anchor/tissue interface.. 41

Figure 2.15 Graded scaffolds.....43

Figure 2.16 Electrospun fibrous scaffolds. 44

Figure 2.17 Collagen-GAG scaffolds fabricated by freeze-drying suspensions of collagen and GAG incorporating a mineralized matrix. 45
Figure 3.1 Microfibrillar scaffolds with specific fibre diameter and alignment..... 62
Figure 3.2 Live-dead staining at day 20. 63
Figure 3.3 Fibre alignment and growth factor stimuli influence MSC morphology. 64
Figure 3.4 Number of clusters and cluster's area in TGF-β3-stimulated cells on aligned and randomly-aligned scaffolds at 5% O_2..... 66
Figure 3.5 Gene expression at day 10 67
Figure 3.6 qRT-PCR gene expression at day 10 in lower cell-seeding density groups..... 68
Figure 3.7 Gene expression at day 20. 71
Figure 3.8 Evaluation of DNA, collagen and sGAG content. 73
Figure 3.9 Immunohistochemistry of collagen type I.. 74
Figure 3.10 Immunohistochemistry of collagen type III. 75
Figure 3.11 Immunohistochemistry of collagen type II.. 76
Figure 3.12 Aligned scaffolds seeded with MSCs and cultured in both CTGF and TGFβ3 using a dual-chamber 78
Figure 3.13 Graphical summary of the findings. 83
Figure 4.1 Bundling of fibres sheets collected at low and high speeds. 91
Figure 4.2 Characterization of the microfibers and MSC-microfibers interaction 102
Figure 4.3 MSC viability and cell morphology. 103
Figure 4.4 Load-strain curves of fibre-sheets when loaded perpendicular to the fibre axis. 104
Figure 4.5 Mechanical properties increase as collection velocity increases 106
Figure 4.6 Stress-strain curves of 500, 1500, 2500 and 3500 RPMs 107
Figure 4.7 Material properties using the cross-sectional area (CSA) of compressed bundles and the theoretical CSA. 108
Figure 4.8 Unwelded fibres confer higher Young's modulus compared to welded fibres.... 113

Figure 4.10 MSCs infiltrate through the thickness of the scaffolds.....115

Figure 4.11 Cell morphology and gene expression of MCS on fibre-bundles. 117

Figure 5.1 Basal media composition was favorable for MSCs with the addition of CTGF 135

Figure 5.2 Characterization of the ECM and of the ECM-functionalized scaffolds. 139

Figure 5.3 Hydrolysis of polycaprolactone with NaOH to expose carboxylic groups. 141

Figure 5.4 Atomic composition of the PCL scaffolds before and after alkaline hydrolysis.. ..142

Figure 5.5 ECM components were covalently conjugated onto the hydrolysed PCL surface by a condensation reaction between the carboxylic acid groups on the hydrolysed PCL surface and the primary amines (-NH2) of ECM components using carbodiimide chemistry 143

Figure 5.6 XPS spectrum of bare PCL and scaffolds that underwent collagen immobilization. 144

Figure 5.7 Live/dead staining (green: 'live', red: 'dead') of MSCs 24 h after seeding.....146

Figure 5.8 Cell nuclei (blue) and F-actin (green) staining of MSCs on bare and functionalized scaffolds in the absence of growth factors 147

Figure 5.9 Circularity, aspect ratio and area of MSCs in the absence of growth factors. 148

Figure 5.10 Gene expression of cartilage and ligament genes of MSCs in the absence of growth factors. 149

Figure 5.11 Cell nuclei (blue) and F-actin (green) staining of MSCs on bare and functionalized scaffolds in the presence of CTGF. 151

Figure 5.12 Circularity, aspect ratio and area of MSCs stimulated with CTGF. 152

Figure 5.13 Gene expression of cartilage and ligament genes in MSCs stimulated with CTGF 153

Figure 5.14 Cell nuclei (blue) and F-actin (green) staining of MSCs on bare and functionalized scaffolds in the presence of TGFβ3. 155

Figure 5.15 Circularity, aspect ratio and area of MSCs in the presence of TGFβ3. 156

Figure 5.16 Gene expression of cartilage and ligament genes in MSCs stimulated with TGF-β3. 157

Figure 5.17 Histology images of Picrosirius red and Alcian blue for the TGF-β3..... 158

Figure 6.1 Schematic representation of the regions in the scaffolds. 172

Figure 6.2 Immobilization of growth factors on ECM-PCL scaffolds..... 174

Figure 6.3 Viability of MSCs seeded on to the scaffolds after 10 days in culture. 176

Figure 6.4 DNA quantification and gene expression of MSCs at day 10..... 177

Figure 6.5 The effect of hydroxyapatite (HA) coating on cell viability and gene expression of MSCs after 10 days in culture.. 180

Figure 6.6 Viability and morphological differences of MSCs within each one of the regions.. 182

Figure 6.7 Gene expression at day 10. 184

List of Tables

Table 2.1 Human ACL mechanical properties 26

Table 2.2 Expression of matrix and growth factor genes during tendon-to-bone insertion development, localized to the four insertion zones. 30

Table 3.1 Primer sequences used for qPCR..... 58

Table 4.1 Primer sequences used for qPCR..... 99

Table 4.2 Airflow generated at each RPM..... 103

Table 4.3 Material properties of the bundles calculated using the apparent cross-sectional area. 107

Table 4.4 Material properties calculated using the compressed CSA (true material CSA)109

Table 4.5 Material properties calculated using the theoretical CSA 109

Table 4.6 Thermal properties of bulk and electrospun PCL fibres..... 110

Table 5.1 Primer sequences used for qPCR..... 137

Table 5.2 Chemical composition of PCL scaffolds after physical or chemical immobilization 144

Table 6.1 Primer sequences used for qPCR..... 168

Table 6.2 Supplements for each media composition for CTGF-mediated fibrogenesis... 169

Table 6.3 Supplements for each media composition for TGFβ3-mediated chondrogenesis.170

Table 6.4 Reagents for preparing 1X SBF (pH 7.4, 1L) 171

Table 6.5 Reagents for preparing 10X SBF (pH 4.3, 1L) 171

Table 6.6 Groups with spatial immobilization of growth factors, ECM or both. 172

Nomenclature

3D	Three dimensional
ACAN	Aggrecan
ACL	Anterior cruciate ligament
ALP	Alkaline phosphatase
ANOVA	Analysis of variance
BMP	Bone morphogenetic protein
BSA	Bovine serum albumin
CDM	Chemically defined medium
C-ECM	Decellularized cartilage extracellular matrix
COMP	Cartilage oligomeric matrix protein
CSA	Cross-sectional area
CTGF	Connective tissue growth factor
DAB	3,3’ Diaminobenzidine
DiI	1,1'-Dioctadecyl-3,3,3',3'-Tetramethylindocarbocyanine Perchlorate
DSC	Differential scanning calorimetry
ECM	Extracellular matrix
EDC	1-Ethyl-3-(3-dimethylaminopropyl)carbodiimide
EDTA	Ethylenediaminetetraacetic Acid
FBS	Fetal bovine serum
FGF	Fibroblastic growth factor
GAG	Glycosaminoglycan
GAPDH	Glyceraldehyde-3-phosphate dehydrogenase
HA	Hydroxyapatite
H&E	Haematoxylin and Eosin
L-ECM	Decellularized ligament extracellular matrix
MFC	Mineralized fibrocartilage

MMP	Matrix metalloproteinase
MSC	Mesenchymal stem cell
NFC	Non-mineralized fibrocartilage
NHS	*N*-Hydroxysuccinimide
PBS	Phosphate buffered saline
PCL	Polycaprolactone
sGAG	Sulphated glycosaminoglycan
SEM	Scanning electron microscopy
TE	Tissue engineering
TGFβ3	Transforming growth factor β3
μCT	Micro-computed tomography
XPS	X-ray photoelectron spectroscopy

Publications

Journal publications

Olvera, D., Sathy, B. N., Kelly, D. J. 2017. Modulating microfibrillar alignment and growth factor stimulation to regulate mesenchymal stem cell differentiation. Acta Biomaterialia 64, 148-160.

Conference abstracts

Olvera, D., Sathy, B. N., Kelly, D. J. Developing a platform that coaxes adult stem cells to recapitulate the bone-ligament interface. Proceedings of the 22nd Annual Conference of the Section of Bioengineering of the Royal Academy of Medicine in Ireland, January 2016, Galway, Ireland.

Olvera, D., Sathy, B. N., Kelly, D. J. 2017. Integrating biochemical and topographical cues to direct stem cell fate. Tissue Engineering and Regenerative Medicine International Society (TERMIS), European Chapter, June 2016, Uppsala, Sweden.

Olvera, D., Sathy, B. N., Kelly, D. J. 2017. Microfibrillar scaffolds incorporating spatially defined extracellular matrix components for bone-ligament junction regeneration. Proceedings of the 23rd Annual Conference of the Section of Bioengineering of the Royal Academy of Medicine in Ireland, January 2017, Belfast, United Kingdom.

Olvera, D., Sathy, B. N., Kelly, D. J. 2017. Modulating microfibrillar topography, collagen presentation and growth factor stimulation to regulate MSC differentiation for interface tissue engineering. Orthopaedic Research Society (ORS), March 2017, San Diego, United States of America.

Olvera, D., Sathy, B. N., Kelly, D. J. 2018. Towards engineering the bone-ligament interface using human scale microfibrillar scaffolds spatially functionalised with decellularized extracellular matrix. 8th World Congress of Biomechanics (WCB), July 2018, Dublin, Ireland.

Chapter 1 Introduction

1.1 Anterior cruciate ligament and repair

Knee soft tissues such as the anterior and posterior cruciate ligaments (ACL and PCL respectively), the medial collateral ligament, articular cartilage, and menisci are critical to joint function and stabilization. They also protect the bones by absorbing impact and play a key role in the transition of mechanical load (Schünke *et al.*, 2006). Ligaments (and tendons) attach to bone through a specialized fibrocartilaginous interface tissue called the enthesis (Benjamin *et al.*, 2006) (Figure 1.1). The complex architecture of the enthesis modulates load transfer between the bone and ligament (and tendons), reducing the stresses at the interface of a stiff bone and a compliant soft ligament (Zantop, Petersen and Fu, 2005). This thesis focuses on the ACL because of its clinical relevance; the rupture of the ACL is one of the most common ligament injuries (Spindler and Wright, 2008). Immense stresses (e.g. landing in downhill skiing results in a peak ACL force of 2017 N (Heinrich, van den Bogert and Nachbauer, 2014) can be placed across the ACL during pivoting and jumping. Planting the foot and suddenly changing direction, landing with a straight knee, neuromuscular fatigue during vigorous activity, hyperextending (e.g. uncontrolled landing) or hyperflexing the leg, can expose the ACL to injury (Di Brezzo and Oliver, 2000). Typically, the ACL ruptures occur at the femoral insertion or at the midsubstance of the ligament, demonstrating the resilience of the fibrocartilaginous enthesis (Benjamin and Ralphs, 1998). When the ACL tears, it shows extremely low and inefficient natural healing due to its hypocellularity and hypovascularity relative to other soft tissues (Pedowitz, O'Connor and Akeson, 2003). Moreover, the intra-articular environment presents harsh conditions that hinder ACL self-healing (Vunjak-Novakovic *et al.*, 2004). The disruption of the synovial sheath dissipates blood, preventing local hematoma formation, crucial for the onset of the inflammatory response that would stimulate primary healing (Leong, Petrigliano and McAllister, 2014). As a result, greater than 85% of ACL disruptions require surgical reconstruction (Prodromos *et al.*, 2007).

While certain ligaments can be repaired by suturing the injured tissue back together, repairing ligaments that do not heal (commonly the ACL and PCL) requires the use of autografts or allografts (Woo *et al.*, 2006). In current ACL reconstructions, the torn ligament is resected along with the fibrocartilaginous interface and bone from the drilled tunnel and the entire ligament unit is replaced by a homogenous autologous or allogeneic tendon graft (Figure 1.2). Both replacements have inherent limitations. The harvest of autologous tendon grafts such as the middle third of the patellar, hamstring or quadriceps tendon is the preferred option for ACL reconstruction; however, it results in a second surgical site with potential complications such as rupture of donor tendon, chronic pain, and decreased muscle strength at the donor site (Aune *et al.*, 2001; Kartus, Movin and Karlsson, 2001; Spindler *et al.*, 2004). The use of an allogeneic tendon from deceased donors avoids damaging healthy tissue, but risks pathogen transmission and are in limited supply (Pedowitz, O'Connor and Akeson, 2003). Synthetic grafts have been developed to address these limitations, but so far have displayed limited success (Legnani *et al.*, 2010). Synthetic ACL grafts include the Ligament Augmentation and Reconstruction System (LARSTM, polyethylene terephthalate) (Smith *et al.*, 2014), Leeds-Keio ligaments such as Poly-Tapes (polyethylene terephthalate) (Murray and Macnicol, 2004), the Gore-Tex augmentation device (polytetrafluoroethylene), and the Artelon ligament (Shaerf *et al.*, 2014). Limitations are due to plastic deformation, weakened mechanical strength compared to the pre-operative implant, and fragmentation of the replacement material due to wear and chafing at the edges of the bone tunnels (Lu and Jiang, 2006).

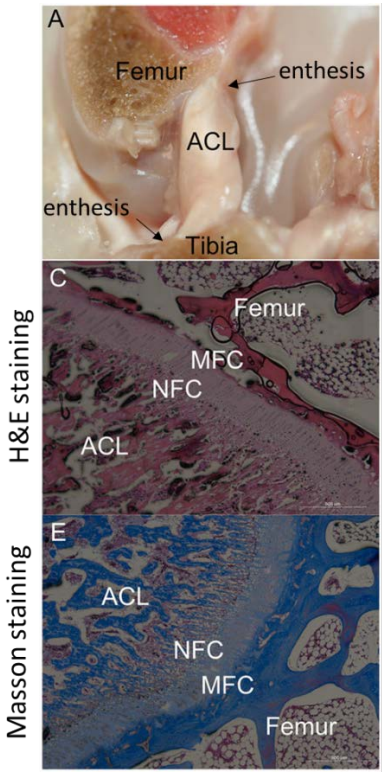

Figure 1.1 Gross observation and histology images of the ACL (A), H&E staining (C), and Masson straining (E); ACL: anterior cruciate ligament; NFC: non-mineralized fibrocartilage; MFC: mineralized fibrocartilage. Magnification 50 X (Wu *et al.*, 2017).

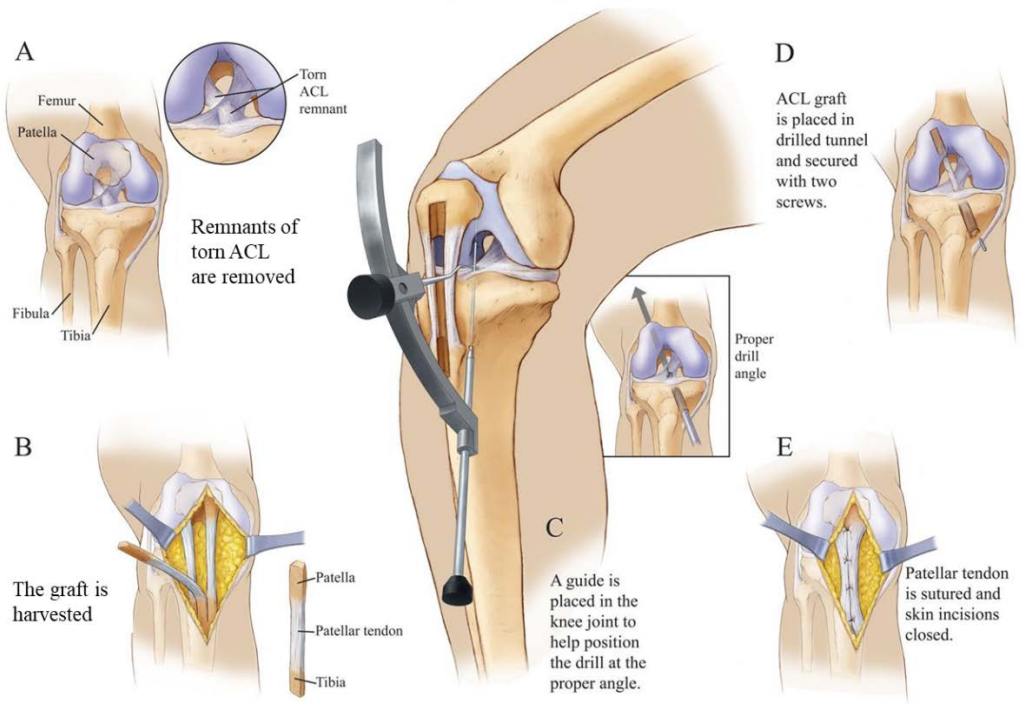

Figure 1.2 Schematics of ACL reconstruction using a patella tendon-bone graft. **A**, Remnants of the torn ACL are cleared. **B**, The graft is harvested; typically an autologous or allogenic tendon graft; in this case a patella tendon with bone plugs at distal ends. **C**, A guide is placed in the knee joint to help position the drill at the proper angle. **D**, The ACL graft is placed in the drilled tunnel and secured with two screws. **E**, The patellar tendon is sutured and the skin incisions closed (Image from compelvisuals.com).

Post-implantation of such grafts, it is expected that they will be vascularized and that the graft acts as a scaffold for host cell migration. The graft generally osteointegrates within the host bone tunnel forming a fixation that holds it *in situ*. In some cases, the patellar tendon grafts are harvested with bone plugs at distal ends to encourage fixation (Brand *et al.*, 2000). The tendon-bone interface is thought to osteointegrate over time. For example, in animal models of ligament reconstruction, specimens failed during tensile loading by pull-out from the tunnel in the first 8 weeks after surgery. From week 12 and thereafter failure occurred at the tendon-clamp junction (i.e. interface) or by rupture of the tendon midsubstance (Rodeo *et al.*, 1993; D. Lee *et al.*, 2014). Patients that re-join high levels of physical activity post-surgery place extensive demands on ACL grafts, especially on the fixation strength. Concurrently, the

number of revision surgeries has increased significantly (Lu and Jiang, 2006), providing evidence that inadequate tissue integration, poor graft remodelling and a failure to re-establish a normal enthesis severely limits the initial mechanical properties of the ligament substitutes used in the clinical setting (Rodeo *et al.*, 1999). Revision rates are as high as 28% in adolescents (Deneweth *et al.*, 2010; Ellis *et al.*, 2012; Engelman *et al.*, 2014; Faunø, Rahr-Wagner and Lind, 2014b).

The long-term functional outcome of the ACL after reconstruction largely depends on the integration of the graft with the host bone and the re-establishment of the enthesis. However, the torn ligament is replaced by a tendon graft that fails to regenerate the enthesis. The interface formed is a loose fibrovascular scar tissue with inferior mechanical properties (Rodeo *et al.*, 1993; Chen, 2009; D. Lee *et al.*, 2014). This predisposes the tissue at the bone insertion site to high stress concentrations which is believed to contribute to the high re-failure rates.

1.2 Interface tissue engineering

The enthesis integrates different musculoskeletal components into a single functional unit. To achieve this integration, the ligament-to-bone enthesis transitions through a specialized graded fibrocartilage tissue which plays a pivotal role in load transfer (Benjamin *et al.*, 2006). Failing to restore the enthesis may cause instability of the knee joint, predisposing such surgically repaired knees to high re-failure rates (Deneweth *et al.*, 2010; Ellis *et al.*, 2012; Engelman *et al.*, 2014; Faunø, Rahr-Wagner and Lind, 2014a) and the development of degenerative joint diseases (Schwartz *et al.*, 2012). This has motived the development of tissue engineering (TE) strategies for ligament regeneration.

TE approaches aim to overcome the shortcomings associated with existing ACL reconstruction techniques. It is believed that by developing a bioactive construct capable of osteointegration with the host subchondral bone, and by regenerating the transition zones of the enthesis, it is possible to develop a functional ACL repair (Phillips *et al.*, 2008; Caliari *et al.*, 2015). While several studies have successfully reproduced the ligament and the bone regions of such a unit, recapitulation of the fibrocartilaginous interface region remains a challenge. Notable examples have developed stratified scaffolds using multiple cell types (namely fibroblasts, chondrocytes, and osteoblasts) to recapitulate the heterogeneity of cells at the interface (Spalazzi *et al.*, 2008; Li *et al.*, 2016). These scaffolds supported multilineage cellular interactions and tissue infiltration, and induced zone-specific matrix production *in vivo* (Spalazzi *et al.*, 2008). Other studies have designed biomaterials to mimic the architecture and/or composition of different regions of the bone-ligament interface to provide biophysical and biochemical cues to resident cells (Spalazzi *et al.*, 2006; Phillips *et al.*, 2008; Xie *et al.*, 2010; Samavedi *et al.*, 2012; Caliari *et al.*, 2015; Criscenti *et al.*, 2016; Li *et al.*, 2016). These studies stress the need for distinct zones to guide and maintain distinct cellular regions and phase-specific extracellular matrix deposition. Examples of such strategies include the design of scaffolds with spatial variation in biochemical cues such as the incorporation of calcium-phosphate, while achieving associated mechanical gradients (Phillips *et al.*, 2008; Li *et al.*, 2009; Xie *et al.*, 2012). The calcified region in the scaffold is thought to enhance osteointegration with the host bone and a graded overlapping matrix between the main body of the ligament and the calcified tissue is thought to mimic aspects of the enthesis.

Despite these advancements, a solution to regenerate the bone–calcified cartilage–fibrocartilage–ligament interface has yet to be established. Successful clinical translation of tissue engineered constructs will depend on the development of strategies that form the enthesis, achieve osteointegration and possess the necessary mechanical properties to withstand the *in vivo* environment while regeneration progresses.

1.3 Objectives

The objective of this thesis is to develop a mechanically functional, spatially defined scaffold for ligament tissue engineering with the potential to regenerate the stratified interface between ligament and bone. It is hypothesized that an electrospun fibre scaffold spatially functionalized with extracellular matrix (ECM) and/or growth factors can direct the differentiation of mesenchymal stem cells (MSCs) down the ligament, cartilage, and endochondral/bone pathways within appropriate regions of the construct (see Figure 1.3). This hypothesis has been motivated by observations reported in literature of how these factors in isolation regulate stem cell differentiation (Cardwell, Dahlgren and Goldstein, 2014; Yin *et al.*, 2015; Rothrauff, Yang and Tuan, 2017). This hypothesis will be tested using electrospun polycaprolactone (PCL) microfibers as a scaffolding biomaterial. The first part of this thesis (Chapter 3) will explore the role of the electrospun fiber alignment and the presentation of growth factors on MSC differentiation towards an endochondral, chondrogenic, fibrochondrogenic and ligamentogenic phenotype. The second part of this thesis (Chapter 4) aims to produce an electrospun scaffold with human scale dimensions for ligament TE. The mechanical properties of this scaffold will be compared with those of the human ACL (Noyes and Grood, 1976). The third phase of the thesis (Chapter 5) will assess the tissue-specific bioactivity of cartilage and ligament decellularized extracellular matrix (ECM) to direct MSC fate after immobilisation onto electrospun scaffolds. Cartilage and tendon ECM have been proposed as tissue-specific biomaterials due to the preservation of biophysical and biochemical motives found in their native counterparts (Rothrauff, Yang and Tuan, 2017). The final phase of this thesis (Chapter 6) will test the hypothesis that the controlled spatial presentation of decellularized ECM and growth factors along the length of an electrospun scaffold could act as a template for ligament regeneration that promotes the development of an appropriate interface between the mineralising tissue and new ligament tissue.

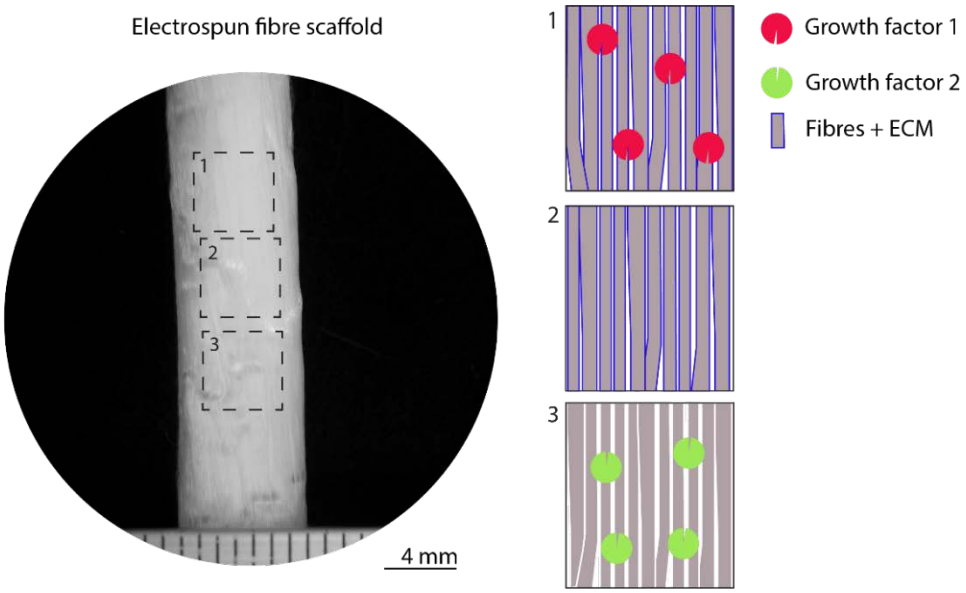

Figure 1.3 Electrospun fibre scaffold spatially functionalized with extracellular matrix (ECM) and/or growth factors within appropriate regions of the construct for (1) mineralized, (2) cartilage, (3) ligament regions. Scale bar, 4 mm.

Chapter 2 Literature Review

2.1 Structure and function of the bone-ligament interface

The basic function of any enthesis it to attach the ligament or tendon to the skeleton; this function is central to force transmission. Two different types of enthesis can be distinguished: fibrous and fibrocartilaginous (Benjamin and Ralphs, 1998). In a fibrous enthesis, Sharpey's collagen fibres connect the ligament and bone forming acute angles, for example in the interface between the periodontal ligament and the alveolar bone (Figure 2.1 a). These collagen fibres are inserted into bone via the periosteum, which gives a firmer hold to short ligaments and tendons. The fibrocartilaginous entheses found in ligaments such as the anterior cruciate ligament (ACL), which connects the femur and tibia, are more common (Lu and Thomopoulos, 2013); they transition in composition and structure from one tissue to another and generally approach the bone at large angles (up to 90°). This transition displays a heterogeneous distribution of cell types within matrices of distinct biochemical and biophysical components, resulting in different tissue mechanical properties and biomolecular environments (Benjamin, Evans and Copp, 1986; Moffat *et al.*, 2008). Traditionally, in the fibrocartilaginous enthesis the fibre orientation of collagen is described as becoming more disorganized as the collagen fibres from the ligament/tendon reach the bone (Figure 2.1 b), however, recently it has been found that the collagen fibres from the ligament/tendon unravel into thinner fibres that insert into bone (Figure 2.1 c).

a

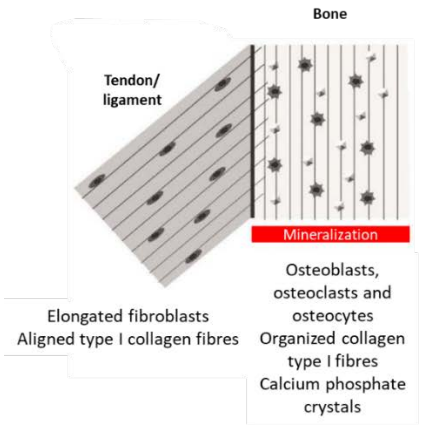

b

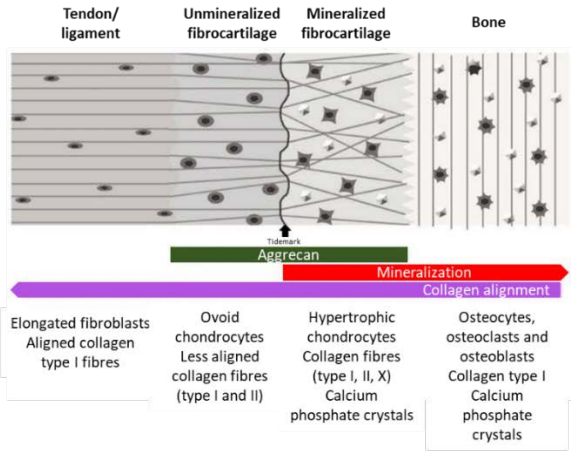

c

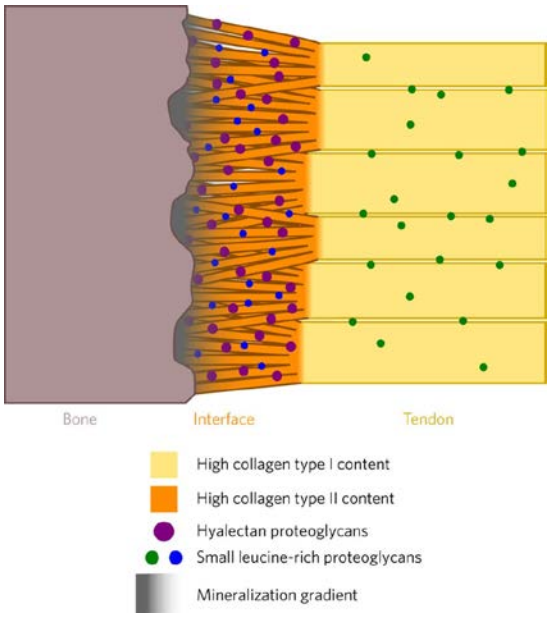

Figure 2.1 Types of ligament/tendon-bone insertions. **a**, Sharpey's fibres connect directly to the periosteum layer of the bone forming acute angles in a fibrous enthesis. **b**, Gradual transition in fibrocartilaginous enthesis. Collagen fibers become more disorganized and mineral content increases as the soft tissue reaches the bone. These illustrations shows orthogonal views of the tissues so that the vertical lines in the bone represent the lamellae (Paxton, Barr and Grover, 2012). **c**, Collagen type I-rich ligament/tendon fibres run towards the bone and unravel into thinner interface fibres before inserting into bone (Rossetti *et al.*, 2017).

The ACL originates at the femoral condyle and runs distal to the insertion at the tibial eminence. Due to its orientation within the knee joint, it restrains the anterior tibial translation and the internal rotation of the knee (Dienst, Burks and Greis, 2002). The ACL-to-bone interface is relatively small, in the order of 100 µm – 1mm, depending of the species and age (Wang *et al.*, 2006). The ACL-to-bone is avascular at insertion sites and within fibrocartilage zone, only the ligament portion is vascularized from the middle genicular artery and vessels of the infrapatellar fat pad and adjacent synovium (Toy *et al.*, 1995). Both, the femoral and the tibial junctions are composed of four distinct tissues along the entheses: (1) ligament, composed of a relatively small fraction of parenchymal fibroblasts (with a cell density 810 ± 81 /mm^2) characterized by low mitotic activity (Doroski, Brink and Temenoff, 2007) and low collagen-production (Van Eijk *et al.*, 2004). Parenchymal fibroblastic tissues display poor healing capacity. Ligamentocytes and tenocytes share many common characteristics, they typically arrange in elongated rows separated by bundles of collagen fibres. Longitudinally, ligamentocytes and tenocytes are elongated and have spindle-shaped nuclei; transversely, the nuclei are commonly stellate (see Figure 2.2 for tenocytes). The row arrangement of cells precedes fibrillogenesis, as it is the arrangement of the cells that determines the organization of collagen bundles, and not vice versa (Benjamin and Ralphs, 1998). As development proceeds, the rows of ligamentocytes become pushed apart by their newly synthesized collagen fibrils. Thus, ligamentocytes extend flat sheet-like processes laterally toward other processes belonging to adjacent cells to establish continuous cell contact. This arrangement creates tunnels through which collagen bundles run longitudinally. Collagen in the ligamentous region is aligned, dense and rich in collagens I and III (in a ratio of 7:1 (Amiel *et al.*, 1983)). Type III collagen fibrils separate the type I collagen bundles. This region is also composed of small amounts of proteoglycans byglican, aggrecan, elastin, fibronectin, decorin, tenascin-C and small amounts of other proteins (Wang *et al.*, 2006). Elastin, in particular, plays

a mechanical role in bundle reorganization following ligament deformation (Smith *et al.*, 2011). Adjacent to the ligament is the (2) fibrocartilage.

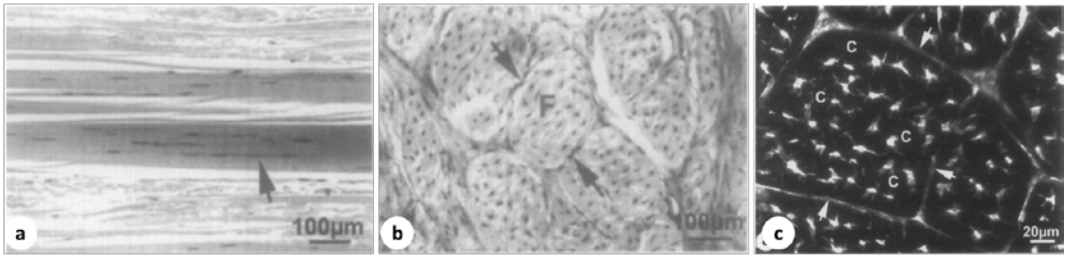

Figure 2.2 Histology sections of tendons. **a**, Longitudinal section of a portion of a typical tendon showing elongated fibroblasts arranged in longitudinal rows (arrow) between parallel arrays of collagen fibers. All that is visible of the cells are the elongated and darkly stained nuclei. **b**, Transverse section of a multifascicular tendon. The arrows highlignt the thin films of loose connective tissue endotenon around a fascicle (F). Within each fascicle and in the endotenon, the dark dots are the nuceli of fibroblasts. Sections are stained with H&E. **c**, Confocal laser scanning microscopy images of rat digital flexor tendons cut in transverse section. 3D projection of a fascicle stained with Dil to highlight the cells. The fascicle is bounded by endotenon (arrows), and the collagen fibers within it are unstained but would fill the dark areas (Benjamin and Ralphs, 2000).

Fibrocartilage cells (fibrochondrocytes) usually adopt a round or oval shape and lie in lacunae like articular chondrocytes (see Figure 2.3 for fibrochondrocytes in a tendon-bone enthesis). The fibrocartilage region divides into non-mineralized and mineralized fibrocartilage. The first is composed of fibrochondrocytes in a matrix predominantly of collagen I, and collagen II in the pericellular matrix of the chondrocyte-like cells. There are small amounts of aggrecan and decorin. The mineralized fibrocartilage contains fibrochondrocytes that appear more circular and hypertrophic. They lie within a matrix of collagens II, X and aggrecan (Visconti *et al.*, 1996). Collagen type X, a specific marker for chondrocytes undergoing hypertrophy and subsequent mineralization, is found exclusively within the mineralized fibrocartilage (Niyibizi *et al.*, 1996). A tidemark delineates the limit of calcification and thus traces a boundary between mineralized and non-mineralized fibrocartilage. In contrast to the articular cartilage tidemark, it is not thought to contain tidemark-specific molecules, simply it represents the point at which calcification ceased and

at which material has accumulated (Benjamin, Evans and Copp, 1986). In the case of the ACL, which enthesis is immediately adjacent to articular cartilage, then the tidemark is continuous across both (Benjamin, Evans and Copp, 1986). The mineralized fibrocartilage interfaces directly with the (3) subchondral bone, composed predominantly of hydroxyapatite and type I collagen populated by osteoblasts, osteocytes and osteoclasts (Moffat *et al.*, 2008). Apart from their mineralization potential, ACL enthesis fibrochondrocytes behave more similar to articular chondrocytes than to meniscal fibrochondrocytes or ligament fibroblasts in terms of growth rate and biosynthesis (Sun, Moffat and Lu, 2007).

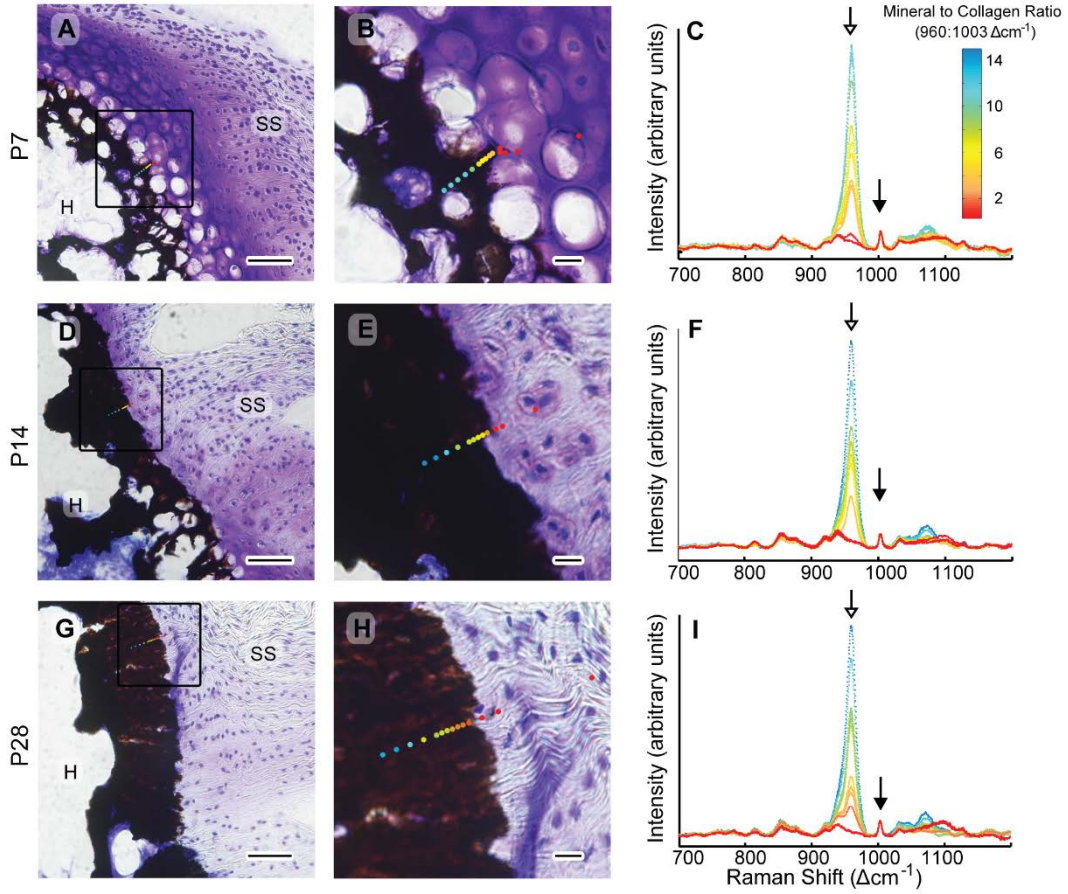

Figure 2.3 Mineralized and unmineralized fibrocartilage in the enthesis. Raman microprobe analysis of developing supraspinatus tendon (SS) insertion. Top row (**A-C**) shows a P7 insertion, middle row (**D-F**) a P14 insertion, and bottom row (**G-I**) a P28 insertion. The insertion is populated by fibrochondrocytes (note the pericellular region). Left column, **A, D, G**: 20 µm-thick sections stained with toluidine blue and according to von Kossa's method (scale bar= 50 µm). Note that despite the sharp front of mineralization in these figures suggested by the von Kossa staining, a graded mineralization front is evident from the Raman scans. Middle column **B, E, H**: magnified view of square region of interest shown in images in the left column (scale bar= 10 µm). The relative mineral concentration determined by the ratio of the

heights of 960 Δcm^{-1} to 1003 Δcm^{-1} Raman peaks (corresponding to the v1 P-O stretching band of hydroxyapatite and the aromatic ring stretching band of phenylalanine in collagen, respectively) is indicated by the colour gradient of the overlaid points. SS: supraspinatus tendon and H: humeral head. Right column **C, F, I**: baseline-corrected Raman spectra corresponding to points along a traverse from tendon (no mineral - dark blue) to bone (high mineral - red). The mineral peak (960 Δcm^{-1}) is indicated with a hollow arrow and the collagen peak (1003 Δcm^{-1}) is indicated with a black-filled arrow (Schwartz *et al.*, 2012).

Even though the entheses of the ACL are composed of the same structure compartments, there are differences in anatomy between the femoral and tibial entheses. The femoral enthesis exhibits a more acute ligament attachment angle than the tibial enthesis and greater calcified and uncalcified fibrocartilage area and depth. This might explain why the femoral origin is more vulnerable to failure (Beaulieu *et al.*, 2015).

The bone-ligament construct behaves as a multiphasic fibre-reinforced, nonlinear viscoelastic, anisotropic material that exhibits high tensile strength and stiffness, allowing it to withstand millions of cycles of load over a lifetime. These complex mechanical properties arise from its heterogeneous extracellular matrix (ECM) content, decreasing fibre orientation and increasing mineral concentration, explaining site-specific stiffness over the length of the construct.

The ECM of the ligamentous phase consists predominantly of water (65-80%) and a solid phase composed primarily of collagen type I and proteoglycans (Rumian, Wallace and Birch, 2007). Collagen type I in the ACL strongly determines its load-bearing mechanical properties. Collagen provides high tensile strength and stiffness, which relates to the structure of the molecule (a superhelix formed by three smaller rigid and inelastic helices) and the diameter of the fibres formed (Silver, Freeman and Seehra, 2003). The ligamentous phase behaves anisotropically due to the hierarchical organization of collagen (several collagen fibrils form a collagen fibre, and several fibres form a fibre) parallel to the direction of the force bundle (Silver, Freeman and Seehra, 2003) (Figure 2.4).

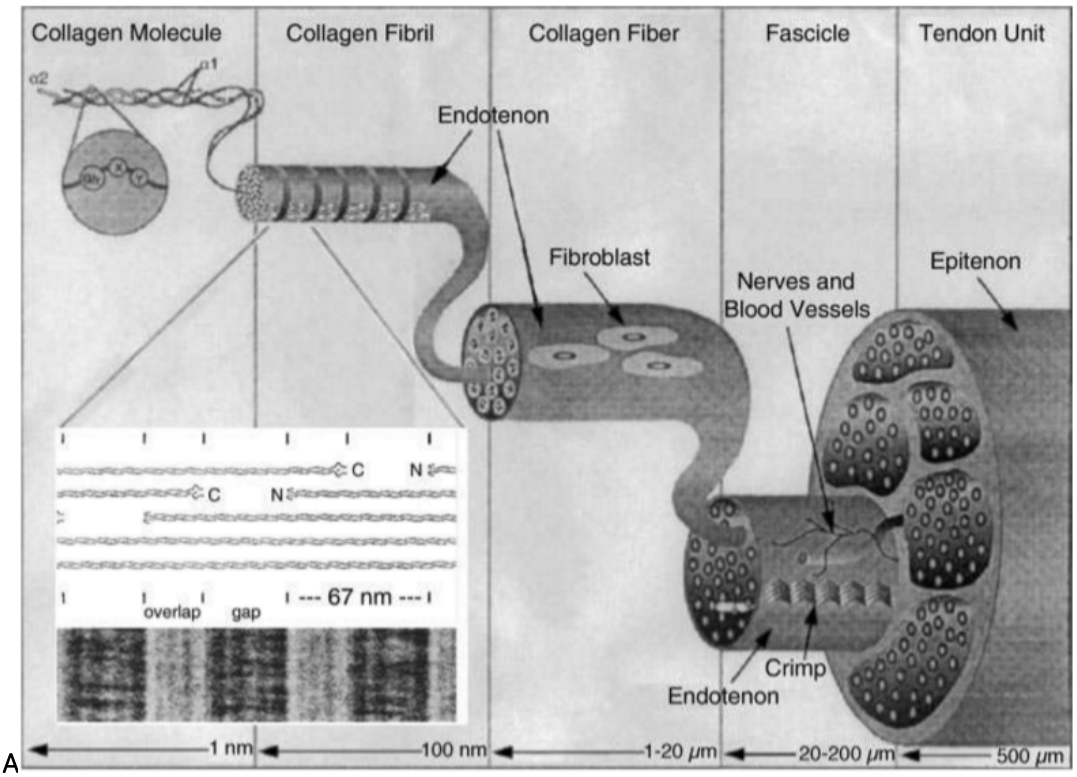

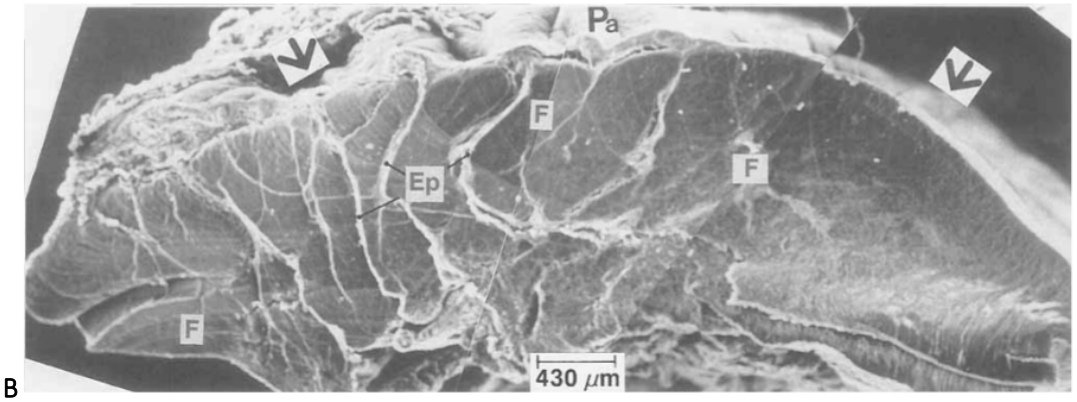

Figure 2.4 Structural hierarchy of ligaments and tendons. A, Collagen molecules form a collagen fibril. Each collagen fibril is covered by a thin layer of endotenon. Fibrils are grouped to form collagen fibres which are populated by fibroblasts. A group of collagen fibres organize to form fascicles. A ligament or tendon unit is composed of many fascicles (Silver, Freeman and Seehra, 2003). B, SEM micrograph of tibial cross-section of a canine ACL showing individual fascicles delineated by epitenon (Ep) on the left and a single fascicle (F) on the right. The sheath seen on the anterior side of the ligament (arrow) is the paratenon (Pa) embedded in a loose connective tissue (Yahia and Drouin, 1989).

Histologically, in ligament and tendons collagen crimps in unloaded conditions. During flexion, the fibres remain isometric in length to equally distribute the load among the fibre

bundles (Silver, Freeman and Seehra, 2003). As the ligament or tendon enters the interface, the collagen fibres unravel into thinner interface fibres before attaching to bone (Rossetti *et al.*, 2017). (Figure 2.5). Glycoproteins and glycosaminoglycans enable the ligament to distribute stresses uniformly. Proteoglycans add lubrication and viscoelasticity to the matrix acting as a hydraulic damper, as well as allowing the fascicles to slide past each other (Pedowitz, O'Connor and Akeson, 2003). Decorin helps the tissue to adapt and compensate for tensile forces and prevents aberrant lateral fusion of collagen fibrils. Aggrecan swells the collagen network promoting a structure that resist compressive loading. The rest of proteoglycans influence the fibril diameter, cellular proliferation and migration, and attract water to hydrate the tissue (Scott-Burden, 1994).

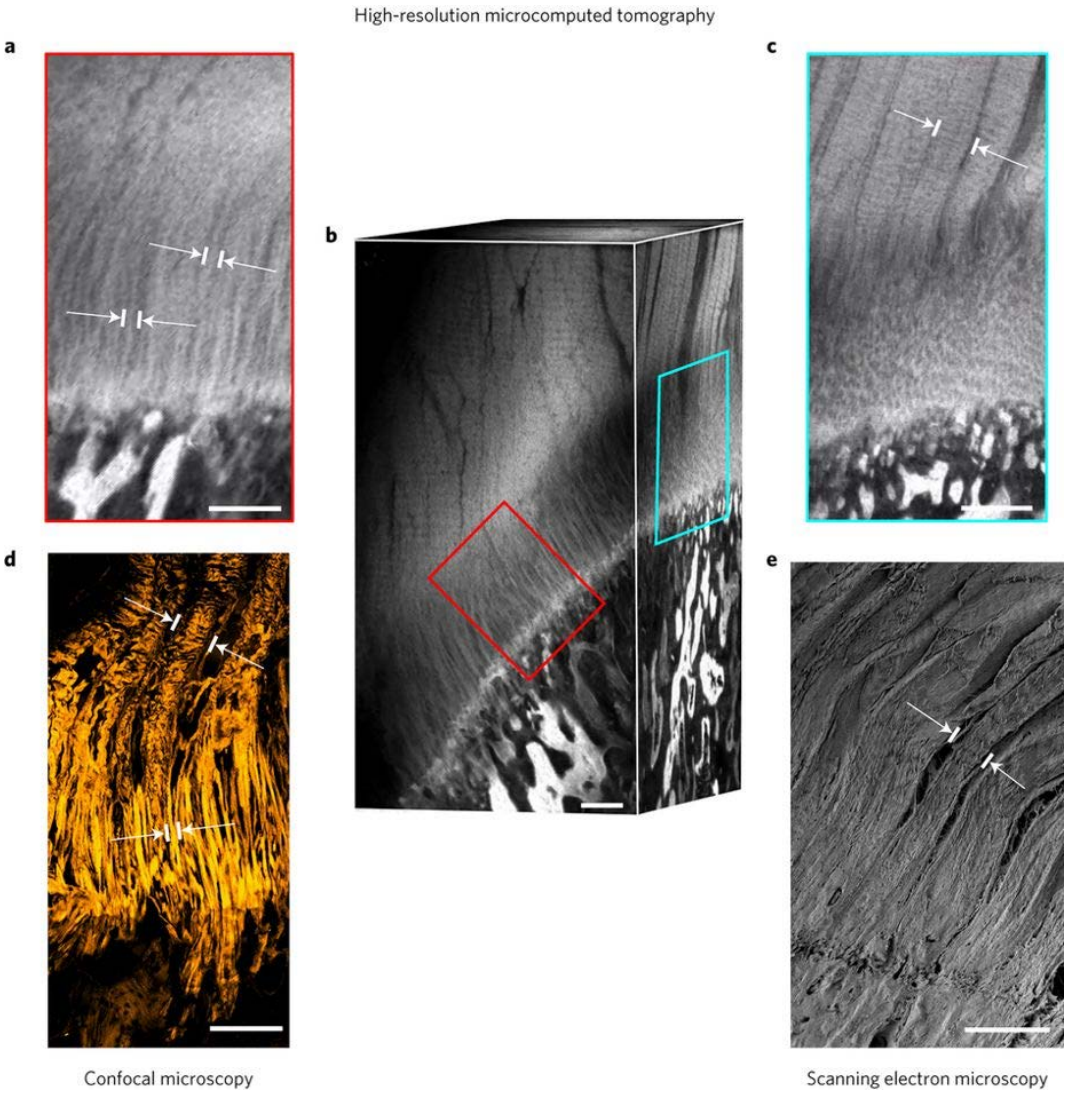

Figure 2.5 The structure of tendon and ligament fibres changes before attaching to bone. Enthesis high-resolution microcomputed tomography (µCT) and confocal reflection imaging as well as scanning electron microscopy show that fibres continue from tendon towards bone. Fibres unravel into thinner interface fibres upon entering the interface region with spans ~500 µm between bone and tendon. **a**, Interface fibres observed with high-resolution µCT. **b**, Rendered volume of µCT acquisition showing both interface fibres as well as tendon fibres. **c**, Tendon fibres in µCT. d, Tendon fibres and interface fibres imaged with confocal reflection microscopy of enthesis cryocut sections. e, Tendon fibres observed with scanning electron microscopy. White arrows mark fibre width. Scale bars, 250 µm (Rossetti *et al.*, 2017).

Ligaments contain a large amount of highly organized collagen to withstand the large tensile stresses it is subjected to, while tissues subjected to compressive loading (e.g. articular cartilage and the nucleus pulposus of the intervertebral disc) contain large amounts of glycosaminoglycans (GAGs). Fibrocartilage tissues are subjected to both tension and

compression and therefore fibrochondrocytes secrete an ECM rich in aggrecan and densely packed collagen type II fibres (Nerurkar *et al.*, 2011). The compressibility of fibrocartilage enables it to dissipate stress at the ligament-bone junction and to absorb shock. Without the fibrocartilagenous zone, the mechanical mismatch at the interface between two different tissues would result in stress concentrations (Benjamin and Ralphs, 1998). From testing bone-ligament-bone constructs in tension, it is known that the construct deforms non-uniformly upon stretch, with the highest deformation occurring near or at the ligament insertion sites to bone (Woo *et al.*, 1983). As the ACL stretches, the fibrochondrocytes in the non-mineralized fibrocartilage zone act like taut springs resisting transverse shortening in response to the stretch (Figure 2.6). The ligament is loaded primarily in tension, the fibrocartilage enthesis is subjected to tensile, shear and compressive components.

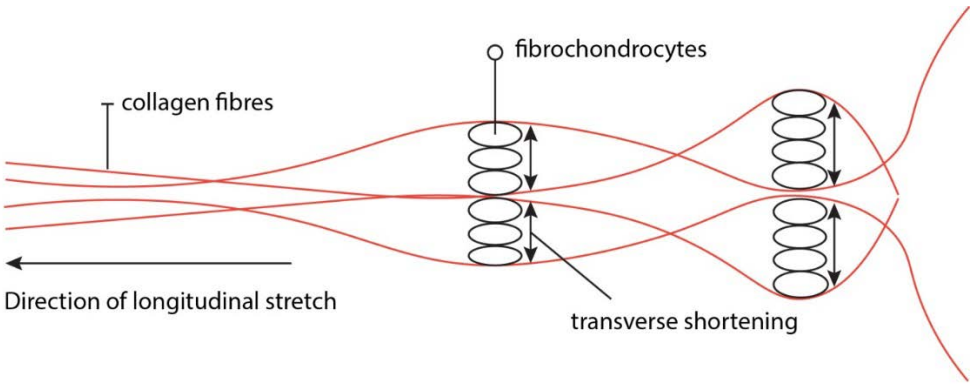

Figure 2.6 ACL stretch longitudinally. As the ACL stretches longitudinally, the fibrochondrocytes in the non-mineralized fibrocartilage zone act like taut springs resisting transverse shortening in response to the stretch (Schünke *et al.*, 2006). Finite-element analysis of a medial collateral ligament (MLC) loaded in tension predicts that the largest principal tensile stresses happen at the ligament midsubstance, and the greatest principal compressive stresses occur near the distal edge of the MCL-to-bone insertion (Matyas *et al.*, 1995).

Calcium and phosphate mineral content increases from ligament to bone (Figures 2.3 and 2.7); concurrently, the ligament-to-bone construct becomes gradually stiffer, as the tensile modulus goes from 200 MPa for ligament (in tension) to 20 GPa for bone (both tension

and compression) (Moffat *et al.*, 2008). This region-dependent stiffness across the interface dissipates stress concentrations, allowing for effective load transfer from ligament to bone. The Young´s modulus of the ACL-to-bone fibrocartilage is similar in magnitude to that of articular cartilage tested under similar conditions (Moffat *et al.*, 2008). Similarity between the insertion fibrocartilage and articular cartilage is not surprising, especially in immature developing time points. The biochemical composition of the immature ACL-to-bone insertion resembled that of the hyaline cartilage at the same age. As the interface matures, collagen fibres mineralize in the mineralized fibrocartilage matrix which alters the mechanical response of the interface regions. Some of the human ACL characteristics and mechanical properties are presented in Table 2.1.

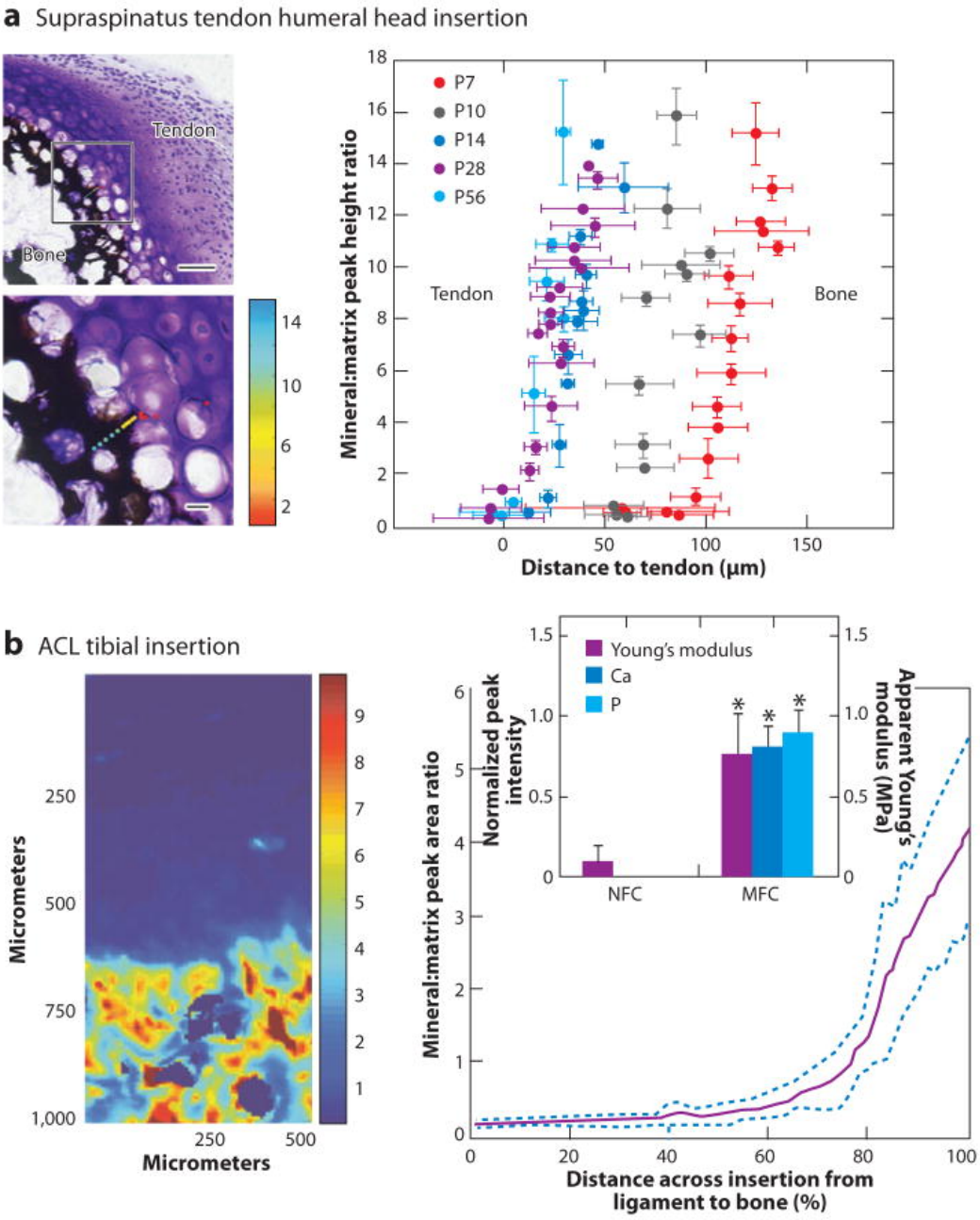

Figure 2.7 Mineral distribution at the enthesis. a, (left) Spatial gradients in mineral form between supraspinatus tendon and bone at the developing enthesis from the onset of endochondral ossification (age P7 in the mouse, determined via Raman spectroscopy, scale bars = 50 μm from upper left image and 10 μm for lower left image). a, (right) the mineral gradient migrates from the centre of the humeral head at P7 to the tendon attachment by P14. b, (left) Mineral distribution at the ACL-to-bone insertion increased exponentially across the calcified fibrocartilage region (neonatal bovine, determined via Fourier transform infrared imaging). b, (right) Ca and P content are significantly higher in the mineralized fibrocartilage (MFC) versus the non-mineralized fibrocartilage (NFC) region, accompanied by a significant increase in Young's modulus (Lu and Thomopoulos, 2013).

Property	Reported values for human ACL	Observations
Length	~ 32 mm (Amis and Dawkins, 1991)	Crimp structure allows for 7-16% of creep prior permanent deformation and ligament damage (Vunjak-Novakovic *et al.*, 2004).
Width	7 – 12 mm (Amis and Dawkins, 1991)	
Cross-sectional area	44 – 58 mm^2 (Noyes and Grood, 1976; Bonnin *et al.*, 2012)	Femoral attachment area in the human ACL is 113 mm^2 and 136 mm^2 at the tibia insertion (Harner *et al.*, 1995).
Tensile forces	67 N (for ascending stairs) – 630 N (jogging) (Chen and Black, 1980)	
Maximum stress	13.3 MPa (> 48 yrs.) – 38 MPa (16-26 yrs) (Noyes and Grood, 1976)	
Strain at maximum stress	30 % (> 48 yrs.) – 45% (16-26 yrs) (Noyes and Grood, 1976)	
Ultimate load Tensile strength	1725 ± 269 N (Canale and Beaty, 2012); in younger specimens (22-35 yrs.) 2160 ± 157 N (Woo *et al.*, 1991)	1,730 N is the established standard for ACL grafts (Vunjak-Novakovic *et al.*, 2004)
Stiffness/ Linear stiffness	182 ± 33 N/mm (Canale and Beaty, 2012); in younger specimens (22-35 yrs.) 242 ± 28 N/mm (Woo *et al.*, 1991)	182 N/mm is the established standard for ACL grafts as reported by (Vunjak-Novakovic *et al.*, 2004)
Yield point	~1200 N (Noyes and Grood, 1976)	
Strain at failure	48 % (> 48 yrs.) – 60 % (16-26 yrs) (Noyes and Grood, 1976)	

Energy absorbed to failure	12.8 ± 2.2 N-m (Canale and Beaty, 2012)	12.8 N-m is the established standard for ACL grafts (Vunjak-Novakovic *et al.*, 2004)
Glycosaminoglycan (GAG) content	7.4 µg/mg (Amiel *et al.*, 1983)	
Total collagen (%) (mg of collagen/ g of dry tissue) for cruciate ligaments	80.3 ± 1 (Amiel *et al.*, 1983)	ACL and PCL combined
Elastic modulus	The Young's modulus of ACL is 111 ± 26 MPa for younger humans (16–26 years) and 65 ± 24 MPa for older humans (48–86 years) (Noyes and Grood, 1976)	

Table 2.1 Human ACL mechanical properties

2.2 Developmental process of the ligament to bone insertion

Progenitors for tendons, ligaments, cartilage and bone originate from the sclerotome, the lateral plate mesoderm and the neural crest (Mori-Akiyama *et al.*, 2003; Christ, Huang and Scaal, 2004; Akiyama *et al.*, 2005). These progenitor populations migrate and settle in the prospective area to give rise to tendon, ligament, and cartilage primordia during early stages of musculoskeletal development (Sugimoto, Takimoto, Akiyama, *et al.*, 2013). Each primordium for the musculoskeletal component initially develops as an individual unit, but later they integrate with each other. To achieve the tendon/ligament-bone integration, progenitors of tendon/ligament and bone establish a coordinated development that involves SYR-box containing gene 9 (*Sox9*) and scleraxis (*Scx*) (Sugimoto, Takimoto, Akiyama, *et al.*, 2013).

SYR-box containing gene 9 (*Sox9*) and Scleraxis (*Scx*) regulate cartilage and tendon/ligament formation, respectively. *Sox9* is required for several steps of the chondrogenic differentiation pathway before and after cartilaginous condensation (Bi *et al.*, 1999; Akiyama *et al.*, 2002). *Scx* encodes a transcription factor persistently expressed throughout tendon and ligament cell lineage differentiation (Schweitzer *et al.*, 2001; Pryce *et al.*, 2007). *Scx* induces tenomodulin (*TNMD*), a transmembrane glycoprotein that aids in the organization of collagen into fibrils and suppresses vascularization of ligaments (Murchison *et al.*, 2007). At early stages of musculoskeletal development, both *Sox9* and *Scx* are detected in the subpopulation of tendon/ligament progenitors and chondroprogenitors around the chondro-tendinous/ligamentous junction (the prospective enthesis) (Akiyama *et al.*, 2005; Brent, Braun and Tabin, 2005; Sugimoto, Takimoto, Hiraki, *et al.*, 2013). A study on *Sox9* lineage tracing in Scx^{+} cells found that during murine development Scx^{+} cell population can be subdivided into two distinct populations: $Scx^{+}/Sox9^{+}$ and $Scx^{+}/Sox9^{-}$ progenitors (Sugimoto, Takimoto, Akiyama, *et al.*, 2013). Tenocytes descend from both $Scx^{+}/Sox9^{+}$ and $Scx^{+}/Sox9^{-}$ progenitors. Ligamentocytes descend from $Scx^{+}/Sox9^{+}$ progenitors. Chondrocytes around the chondro-tendinous/ligamentous junction are also descendants of $Scx^{+}/Sox9^{+}$ (Figure 2.8). The closer the tendon/ligament and cartilage are to the prospective enthesis, the more tenocytes/ligamentocytes and chondrocytes originate from $Scx^{+}/Sox9^{+}$ progenitors (Figure 2.9). As differentiation proceeds *Sox9* expression disappears from tendons and ligaments. Further functional analysis revealed that the $Scx^{+}/Sox9^{+}$ cell population contributes to the establishment of the enthesis. The authors conclude that $Scx^{+}/Sox9^{+}$ progenitors are a unique multipotent cell population that differentiate into chondrocytes and tenocytes/ligamentocytes to form the junction between hyaline cartilage and tendon/ligament. The $Scx^{+}/Sox9^{+}$ progenitor population is predominantly distributed across the prospective enthesis to form the chondro-tendinous/ligamentous junction during development. During postnatal growth, it is likely that cells in this transitional zone give rise

to fibrochondrocytes. The cellular origin of fibrochondrocytes remains uncertain, but it is known that entheseal fibrocartilage develops in response to compressive loads postnatally (Benjamin and Ralphs, 1998).

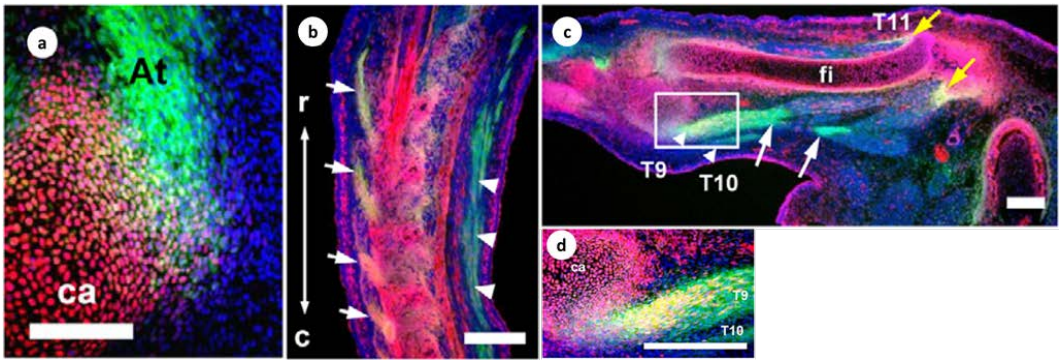

Figure 2.8 Contribution of the *Scx*$^{+}$*/Sox9*$^{+}$ cell lineage to the formation of ligaments and the entheseal side of tendons. **a**, Distribution of *Sox9*$^{+}$ and *Sox9*$^{-}$ cells in *Scx*$^{+}$ region of mouse embryos. In ScxGFP transgenic mouse embryos, *Sox9*$^{+}$ cells (red) and *Scx*$^{+}$ cells expressing GFP (green) were detected by double immunostaining with antibodies specific for *Sox9* and GFP, respectively, and nuclei were stained with DAPI (blue). *Scx*$^{+}$*/Sox9*$^{+}$ chondrogenic cells are found in the entheseal region of the Achilles tendon (At) and the calcaneus (ca) at E14.5 (merged image). Scale bar, 100 µm. **b**, Contribution of *Sox9*$^{+}$ progenitors to axial tendon and ligament formation. Sections were prepared from Sox9$^{Cre/+}$;Ai14;ScxGFP embryos and cells of the *Sox9*$^{+}$ lineage were detected by tdTomato reporter expression and *Scx*$^{+}$ cells were detected with anti-GFP antibody. Shown is a sagittal section of the developing tail, with arrows and arrowheads indicating tendons associated and not associated with the vertebrae, respectively. Rostral and caudal sides are indicated by r and c, respectively. Scale bar, 200 µm. **c**, Distribution of Scx-expressing tendons and ligaments (GFP, green) with a *Sox9* expression history (tdTomato, red) were analysed in a Sox9$^{Cre/+}$;Ai14;ScxGFP mouse embryo at E14.5. Image shows sagittal section of the hindlimb. Arrows and arrowheads indicate tendon and ligaments, respectively. White and yellow arrows in (**c**) indicate the force-transmitting and the anchoring tendons at the lower leg, respectively. The boxed region in (**c**) is shown at a higher magnification in (**d**). This analysis shows that the insertion sites of the tendons into the vertebrae were derived from *Scx*$^{+}$*/Sox9*$^{+}$ progenitors, whereas tendons located further away from vertebrae were almost exclusively *Sox9*$^{-}$ and *Scx*$^{+}$ (Sugimoto, Takimoto, Akiyama, et al., 2013).

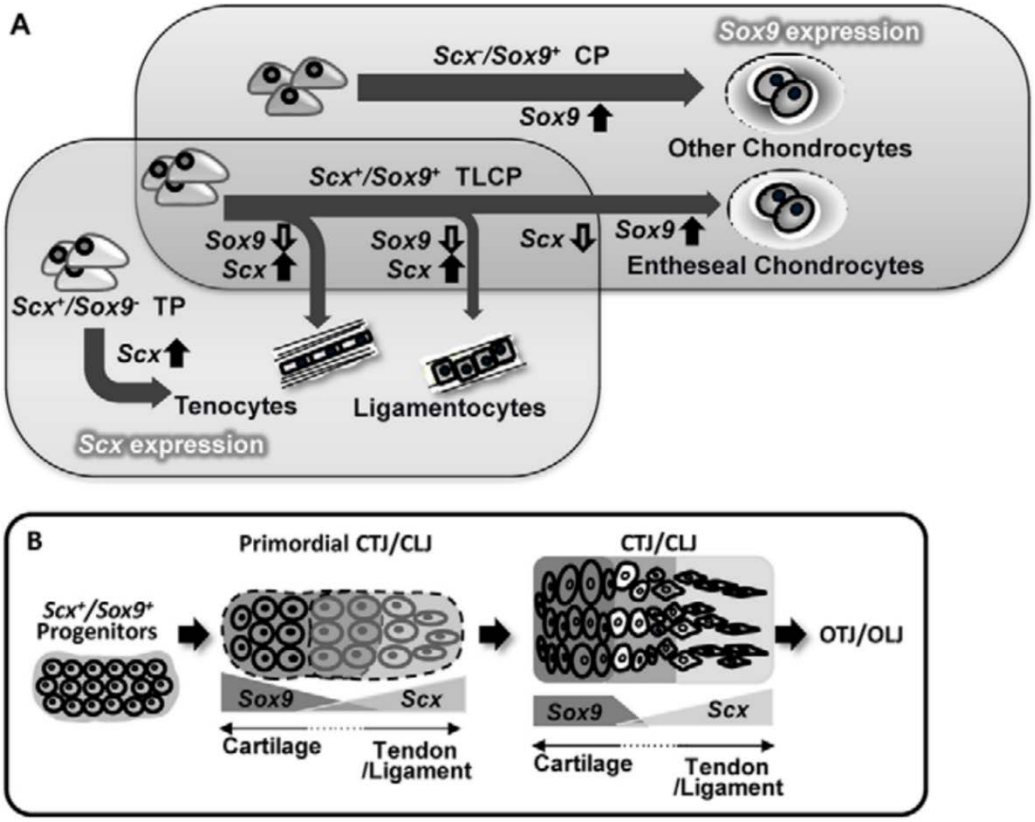

Figure 2.9 Establishment of the junction between cartilage and tendon/ligament along the *Scx/Sox9* axis. A, Differentiation of the tendogenic, ligamentogenic and chondrogenic cell lineages along the *Scx/Sox9* axis. The differentiation pathways of $Scx^{-}/Sox9^{+}$ chondroprogenitors (CP), $Scx^{+}/Sox9^{+}$ teno-/ligamento-/chondroprogenitors (TLCP) and $Scx^{+}/Sox9^{-}$ tenoprogenitors (TP) are shown. B, Establishment of the chondro-tendinous/ligamentous junction (CTJ/CLJ) to form the osteo-tendinous/ligamentous junction (OTJ/OLJ). $Scx^{+}/Sox9^{+}$ progenitors give rise to the primordial CTJ/CLJ. The established CTJ/CLJ further develops to form the OTJ/OLJ during postnatal growth. Expression levels of *Sox9* and *Scx* are represented in dark and light grey, respectively (Sugimoto, Takimoto, Akiyama, et al., 2013).

A study on the development of the supraspinatus tendon-to-bone insertion in a mouse model, showed that the fibrocartilaginous transition zone between the supraspinatus tendon and the humeral head did not develop until postnatal time-points. This study elucidate the temporal and localized expression of some growth factors and ECM gene expression characteristic of tendon/ligament, fibrocartilage, mineralized fibrocartilage and bone during tendon/ligament-bone insertion development in the mouse (Galatz *et al.*, 2007) (Table 2.2). A different study using genetically modified mice with muscular defects demonstrated that

muscle loading was not required for initiation of enthesis formation, but it was necessary for subsequent growth and maturation of the enthesis (Blitz *et al.*, 2009)

Time point	Zone 1: tendon/ ligament	Zone 2: fibrocartilage	Zone 3: mineralized fibrocartilage	Zone 4: bone
13.5 dpc	Col I, TGFβ3	-	-	Col II
15.5 dpc	Col I, TGFβ1, 3	-	-	Col II
18.5 dpc	Col I, TGFβ1	-	-	Col II
Neonatal	Col I	-	-	Col II
3 days	Col I	-	-	Col II
7 days	Col I	Col I, II	Col II	Col II
14 days	Col I	Col I, II	Col II, X	Col II
21 days	Col I	Col I, II	Col II, X	Bone
28 days	Col I	Col I	Col II, X	Bone
56 days	Col I	Col I	Col II, X	Bone

Table 2.2 Expression of matrix and growth factor genes during tendon-to-bone insertion development, localized to the four insertion zones. dpc, days postconception; -, zones not yet distinct (Galatz et al., 2007). The fibrocartilaginous zone of the tendon insertion site develops at approximately 14 days postnatally in murine model.

At 13.5 dpc, chondrocytes expressing type II collagen formed the humeral head. At 15.5 dpc, the supraspinatus tendon appeared as a condensation of cells directly adjacent to the humeral head and expressed collagen type I (Figure 2.10). At 18.5 dpc, neonatal, and 3-day postnatal time-points, cells in the tendon progressively changed its shape to more spindle and became oriented along the axis of the tendon. During these time-points the humeral head expressed collagen type II. Seven days postnatally a transition zone between the supraspinatus tendon and the humeral head was evident; at this interface fibrochondrocytes expressed both type I and II collagen. At 7 days, the chondrocytes in the humeral head were hypertrophic in

morphology and expressed type II collagen. At 14 days, the hypertrophic chondrocytes near the tendon insertion started to express collagen type X. At this time-point, chondrocytes were absent in the bone next to the insertion. At 21 and 28 days, a four-zone transition was apparent between the supraspinatus tendon and the humeral head. Fibroblasts in the tendon (zone 1) expressed type I collagen, fibrochondrocytes in zone 2 expressed collagen types I and II, hypertrophic chondrocytes in zone 3 expressed collagen types II and X, and mature bone was evident in zone 4. At 56 days, the expression patterns for collagen I, II, and X were identical to the previous time-points, the four-zone insertion site was clear between tendon and bone. Notably, hypertrophic chondrocytes were no longer present at the mature insertion, while expression of type X collagen persisted. Similar patterns have been described for rat Achilles tendon insertions and for bovine ACL insertions postnatally (Fujioka *et al.*, 1997; Wang *et al.*, 2006).

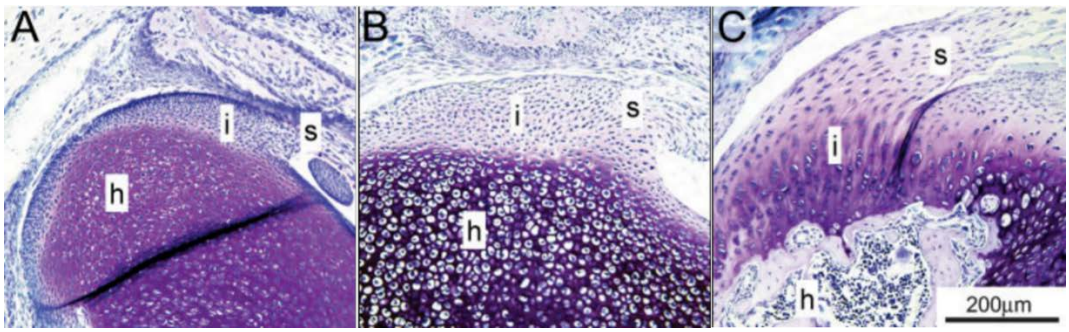

Figure 2.10 A fibrocartilaginous transition zone did not develop between the supraspinatus tendon and the humeral head until postnatal time points (Toluidine blue stain). A, 15.5 dpc; B, neonatal; C, 21 days. s, supraspinatus tendon; h, humeral head; i, interface(Galatz et al., 2007).

The way the hypertrophic chondrocytes express type X collagen to form the mineralization front of the insertion (zone 3) is in a similar pattern to that seen at growth plates (Galatz *et al.*, 2007). The hypertrophic chondrocytes of the growth plate mineralize the matrix between the cells, producing a zone of provisional mineralization. Collagen X is expressed at sites of endochondral ossification and in areas of transition from mineralized to soft tissue. While collagen X production and expression ceases at the onset of calcification of

cartilaginous regions (such as in growth plates and fracture callous), it persists in areas with strict delineation between bone and soft tissue (e.g. tendon/ligament insertion sites). Collagen X may have a key role in maintaining the distinct zones between mineralized and unmineralized soft tissues. It has been demonstrated that instead of co-developing with fibrocartilage, the mineral gradient is constitutive to mineralization fronts associated with endochondral ossification (Schwartz *et al.*, 2012). Mineralization front is evident adjacent to the developing soft tissue by 14 days postnatally.

The factors that modulate growth plate maturation also play a role in enthesis formation. Specifically, the Indian hedgehog (Ihh)/parathyroid hormone–related protein (PTHrP) feedback loop is critical for mineralization at the growth plate (Lu and Thomopoulos, 2013). The Ihh/PTHrP loop regulates chondrocyte differentiation and homeostasis and thus could play a role in enthesis development. PTHrP, for example, prevents proliferating chondrocytes in the growth plate (or other proliferative zones) from becoming hypertrophic chondrocytes (which eventually mineralize). PTHrP maintains a population of proliferative chondrocytes available for growth rather than for hypertrophy and mineralization. Graded expression of Ihh and PTHrP at the enthesis may regulate the formation of a graded transition between mineralized and unmineralized tissue (Lu and Thomopoulos, 2013).

2.3 Electrospinning

Many studies have used biofabrication processes such as electrospinning to create scaffolds for tissue engineering. Electrospinning provides a simple way to fabricate fibrous polymer scaffolds. Developing fibre structures is appealing because a great variety of natural ECM components exist in fibrous form and structure, such as collagen, fibronectin and laminin. Fibres in the ECM are characterized by well-organized hierarchical fibrous structures ranging from nanometre to millimetre scale (Wong, Baji and Leng, 2008). To electrospin a polymer, a

high voltage electric field is applied to a viscous polymer solution, a continuous jet of polymer from the nozzle is deposited onto an oppositely charged grounded collector. The potential difference between the needle tip and the collector draws the polymer as a jet towards the oppositely charged collector. In the absence of the electric field the polymer droplet is held at the capillary tip by surface tension of the liquid; when the electric field is applied, the droplet elongates and forms a 'Taylor cone'. When the strength of the electrical field is sufficient to overcome the surface tension of the liquid, the fine fibre jet is ejected from the tip of the Taylor cone. As the fibres jet travels through the air, the solvent evaporates and charged, solid polymer fibres are deposited on the collector where the charges on the fibres are neutralized (Figure 2.11). These fibres are collected in large quantities to produce 3D fibrous scaffolds. Electrospinning generates fibre scaffolds with high porosities, large surface area-to-volume ratios, and a wide range of fibre diameters by modulating a combination of solution and processing variables in addition to ambient parameters (such as temperature, humidity and air velocity) (Pham, Sharma and Mikos, 2006a). Solution properties include polymer concentration, viscosity, dipole moment, dielectric constant and molecular weight, solvent volatility and conductivity, and surface tension. Processing variables include flow rate, needle size, distance to the collector and applied voltage. An extensive array of polymers can be electrospun, both natural and synthetic, spanning a range of stiffness and fibre diameters (50 nm to 10 μm) (Pham, Sharma and Mikos, 2006b) that capture the biological diversity of fibres in fibrous tissues.

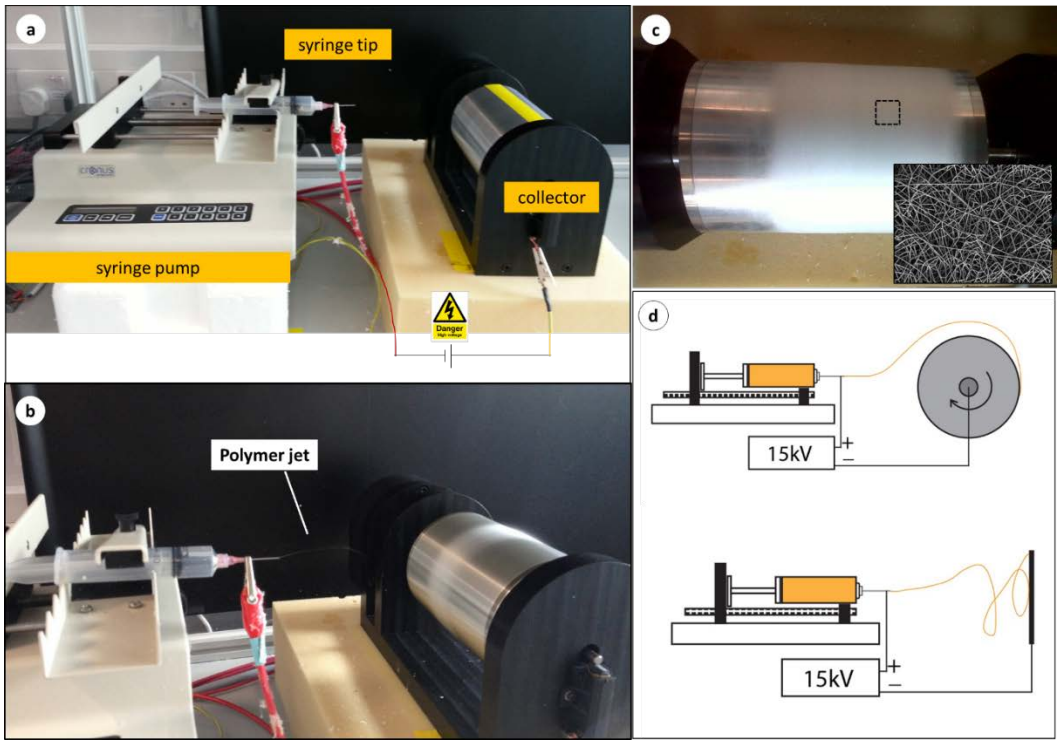

Figure 2.11 Electrospinning process. **a**, The electric field deforms the fluid contained within the needle and forces the formation of a strand. **b**, A continuous jet of polymer from the nozzle is draw to the grounded collector. **c**, As the fibre jet travels through the air, the solvent evaporates and solid polymer fibres are deposited onto collector where they are neutralized. **d**, the collector could be a rotating mandrel (top) or a static plate (bottom).

As general rules, higher viscosities give larger fibre diameters, a small distance between the collector and the ejecting nozzle results in incomplete evaporation of the solvent and thus, welded fibres. The applied voltage is a tricky processing parameter since an increase in the voltage will initially decrease the fibre diameter but with further increase of voltage the fibre diameter will increase. This is related to how the applied voltage modifies the Taylor cone. A characteristic problem when using a suboptimal voltage is the presence of beads (i.e. beaded fibres). Polymer flow rate has an impact on fibre size and shape, generally fibre diameter (and associated pore size) increase with increasing flow rate. With high flow rates fibres are unable to dry completely before depositing. Incomplete fibre drying leads to the formation of flattened fibres as opposed to fibres with circular cross-section. The fibre diameter decreases with increasing distances from the Taylor cone. In terms of the solution

parameters, there are no defined rules as every polymer-solvent relationship is different, however some of the trends observed in this work using polycaprolactone and chloroform are that fibre diameter increases with increasing polymer concentration. Chloroform shows convenient volatility (similar to tetrahydrofuran (THF), much higher than dimethylformamide (DMF)) which can result in smooth or textured fibres.

The electric field during electrospining elongates and stretches the fibres. The fluid instability in the polymer jet causes whip-like motion in the jet, thereby increasing the degree of stretching before reaching the grounded collector. The elongation that the material experiences can be quantified using the draw ratio. It is calculated as the ratio of collector velocity to ejection velocity of the polymer solution from the tip of the nozzle (Wong, Baji and Leng, 2008). The fibres collected experience a huge material elongation rate and related reduction in the cross-sectional area (order of 10) (Wong, Baji and Leng, 2008). The evaporation of the solvent leads to a gradual increase of the relaxation times, thus the elongation and stretching of the jet that forces the polymer chain to align can be locked by the rapid solvent evaporation. It is a competition between the elongation forces (that orient polymer chains along the deformation direction), and the orientation relaxation of the PCL chains (that promote a return to the equilibrium state). We encouraged the residual solvent to evaporate to lock in the oriented fibre structure (out-of-equilibrium) and to discourage further orientation relaxation after electrospinning.

2.4 Electrospinning for tissue engineering

Electrospinning have shown promise in the tissue engineering of cartilage, meniscus, tendon/ligament, bone, fat and muscle. The research interest stems from the technique versatility, electrospinning can produce hollow fibres, textured fibres, etc. with tailored diameter size that can support cell attachment, release drugs or be chemically functionalized.

Besides controlling the fibre diameter, electrospinning allows for fibre alignment. Anisotropy influences directional stiffness as well as to contact guidance where cell phenotype is altered and consequently the structure of the extracellular matrix synthesized. By contact guidance cells respond to structural cues of the substrate to adopt a specific phenotype associated to differentiation into a specific cell lineage. For example. ligamentous differentiation is enhanced in anisotropic scaffolds (Subramony *et al.*, 2013; Yin *et al.*, 2015).

Guiding MSCs towards a specific lineage and maintaining this phenotype involves the appropriate application of mechanical, chemical and structural cues, acting individually or combined. Several studies have demonstrated that the physical properties of the substrate, such as fibre diameter, length, substrate geometry, scale, cross-linking pattern, topography, stiffness etc. affect the cellular adhesion, degree of cytoskeletal tension, morphology, proliferation, migration and differentiation of MSCs (McBeath *et al.*, 2004; Engler *et al.*, 2006; Dalby *et al.*, 2007; Gentleman *et al.*, 2009; Lutolf, Gilbert and Blau, 2009; Oh *et al.*, 2009; Chowdhury *et al.*, 2010; Kilian *et al.*, 2010). Furthermore, unlike chemical stimulation, for which time and concentration dependence is difficult to control, topographical cues can be developed with greater control (Subramony *et al.*, 2013). Topographical cues from the extracellular microenvironment can influence cellular proliferation and differentiation. Electrospun fibres, for example, provide contact guidance for cell orientation and migration.

Electrospun fibres have been braided, woven, rolled, fan-folded and knitted to form scaffolds. These scaffolds showed high mechanical strengths compared to hydrogels or self-assembly of cells, and topographical cues to align cells and direct matrix deposition. But dense 3D arrangement hindered cell invasion and minimize diffusion. Nanofiber sheets of tightly packed 3D configurations (resulting from braiding, weaving, rolling and knitting scaffolds) show limited cell infiltration, nutrient diffusion and waste transport.

Researchers circumvent these limitations by improving the porosity of the scaffold. Strategies include laser cutting holes in the electrospun sheets (Petrigliano *et al.*, 2015), using a slow rotating frame collector to extend the pore size (Zhu *et al.*, 2008), or layered hydrospinning showing a porosity of 99% (Tzezana, Zussman and Levenberg, 2008). An improvement in cellular infiltration while maintaining alignment has been observed. Another way to circumvent limited porosity in densely packed fibrous scaffolds is co-electropinning sacrificial fibres, typically of water-soluble poly(ethylene oxide) (PEO) (Baker *et al.*, 2008; Ifkovits *et al.*, 2010). Composites of two distinct fibre fractions are electrospun: a slow-degrading poly(ε-captrolactone) and sacrificial PEO which can be selectively removed to increase pore size. However, the structural integrity of the scaffold was compromised when PEO was greater than 60% (Baker *et al.*, 2008). Electrospinning of salt particles into scaffolds, which are subsequently leached from the system is based on the same principle (Nam *et al.*, 2007).

Another way to circumvent rolling/braiding etc. was proposed as the 'core-shell' concept. It relies on lyophilized collagen to modulate pore size and density to incorporate spatially graded directional cues and calcium phosphate mineral, which combined with biochemical supplementation, and/or mechanical stimulation have shown to support tendogenic, osteogenic, and chondrogenic cell proliferation and bioactivity (Caliari, Ramirez and Harley, 2011; Caliari and Harley, 2014b, 2014a). Although the accomplished tensile modulus is lower than that of native tissues, their results elucidate on the structural and biochemical composition needed in a platform for interface regeneration. Based on the core-shell concept, other studies (Webb *et al.*, 2013) used the synthetic polymer poly(3-hydroxybutyrae-co-3-hydroxyhexanoate (PHBHHx) for the shell and collagen for the core, which offers superior mechanical performance. Attention is draw to the failure to incorporate directional cues to align cells and matrix.

Although there is a general agreement that aligned fibres are more suitable for ligament differentiation, less of a consensus is reached about fibre diameter. A study aimed to determine the effect of fibre diameter and the degree of fibre alignment on MSCs morphology, proliferation and ligament gene expression, showed that fibroblasts adopted a more spindle-shape morphology on fibres with a diameter of 0.82 – 2.3 µm, but observed a decrease in the expression of col I, tenomodulin (*TNMD*) and decorin (*DCN*) (marker genes of mature ligamentocytes) on these fibres. They concluded that submicron fibres may be preferable for ligament tissue engineering. A recent study from the same group conducted with the same purpose, reported that fibres larger than 2 µm (opposed to <1 µm – <2 µm) induced highest expression of col I, *DCN* and scleraxis (*Scx*); and presumably larger fibres allow larger interfibre spaces for a better diffusion of nutrients and cellular penetration into the electrospun meshes. This is relevant since collagen fibres found in ligament are within the range of 1 – 20 µm (Cardwell, Dahlgren and Goldstein, 2014).

2.5 Strategies to engineer the bone-ligament interface

Tissue engineering strategies have been intensively developed as alternatives to the current standard for ACL reconstruction (e.g. ligament proper) (Altman et al., 2002; Cooper et al., 2005). Early studies in ACL tissue engineering (TE) focused on creating a ligament substitute, overlooking the need for graft integration into bone and for the enthesis development. Generally, the objective of these early studies was to match the mechanical requirements of native ACL. For this purpose, silk fibroin fibres twisted or braided into 3D scaffolds were designed (Altman *et al.*, 2002). This silk fibres matched the mechanical requirements of the native human ACL, including adequate fatigue performance. Silk fibre scaffolds support the differentiation of human bone marrow stem cells (hBMSCs) towards ligament lineage. A limitation of this design was that ingrowth of newly formed tissue was

inhibited by the limited porosity in these twisted/braided scaffolds (Cooper *et al.*, 2007; Freeman, Woods and Laurencin, 2007; Fan *et al.*, 2009). With a similar design, another study braided polylactide-co-glycolide (PLAGA) fibres. The authors emphasized the importance of porosity for tissue ingrowth (Cooper *et al.*, 2005).

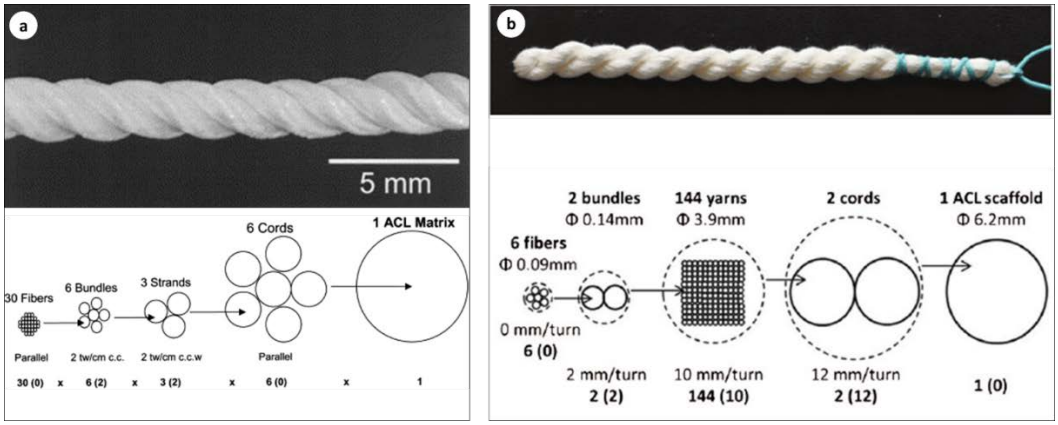

Figure 2.12 Twisted fibres into 3D scaffolds for ACL reconstruction. a, Photograph of a single silk fibroin cord containing a total of 540 individual fibres. Six parallel cords are used to generate the ACL matrix. (bottom) Schematic of an ACL 6-cord matrix hierarchy (Altman et al., 2002). b, Photograph and schematic of silk ACL scaffold with wired architecture.

The second phase of ACL TE considered the need to promote graft integration, yet overlooking the enthesis development. Many groups successfully engineered the intraarticular ligament and the femoral and tibial bony attachments representing clear advancements over homogenous ACL grafts. Motivated by the mechanical properties achieved with braided scaffolds for ligament TE, researchers incorporated two distal regions for bony attachment into the polymer braid. For example, a braided scaffold from polylactide-co-glycolide (PLAGA) fibres comprised three regions: one middle section with higher porosity for ligament ingrowth, and two bony attachment regions with smaller pore size and lower porosity (Figure 2.13 a). Primary rabbit ACL cells and mouse fibroblasts grew on the braided scaffold for 8 days in culture. The authors emphasized that their design could withstand the rigors of surgical fixation within the bone tunnels (Cooper *et al.*, 2005). Another study

suggested to combine knitted silk fibroin and collagen to reconstruct a rabbit ACL. Their aim was to assess its *in vivo* performance compared to an autograft. They observed that compared to the autograft group, the tissue engineered construct osteo-integrated better as there was evidence of trabecular bone growth into the scaffold (Bi *et al.*, 2015) (Figure 2.13).

a b

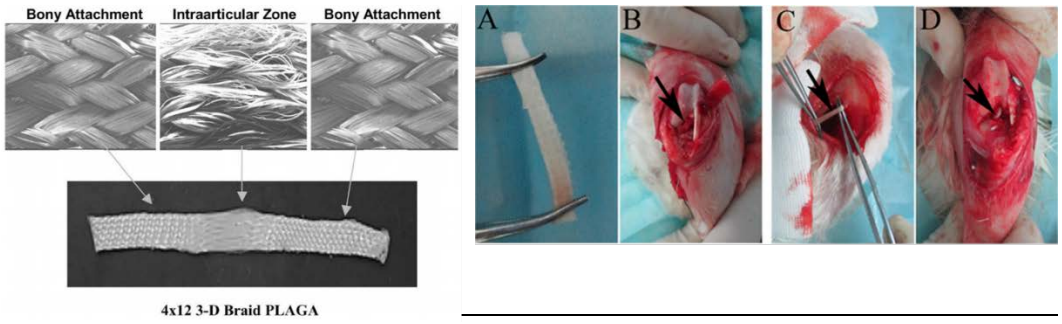

Figure 2.13 Fibre-based scaffolds incorporating bony regions. **a**, bony attachments with smaller pore size and lower porosity compared to the middle section (Cooper et al., 2005). **b**, A rolled-up shaft of silk-collagen scaffold with the two ends clamped by forceps (A). (B) Gross observation of ACL reconstruction (the black arrow points to the silk-collagen graft). (C) The auto-semitendinosus tendon (arrow) was harvested before exposing the knee joint. (D) Gross observation of ACL reconstruction (the black arrow points to the autograft) (Bi et al., 2015).

An alternative approach was proposed, by embedding a poly(l-lactide) (PLL) braid into porous poly(1,8-octanediol-co-citric acid)-hydroxyapatite nanocomposite (POC-HA) to create a tri-component graft (i.e. bone-ligament-bone). These grafts were used to reconstruct the ACL of rabbits allowing weight-bearing capability after 6 weeks of implantation. They showed tissue infiltration throughout the entire scaffold, tissue ingrowth and interlocking within the bone tunnels. The authors highlighted the importance of fixation; they attribute some inflammatory response to debris of the POC-HA from micromotions at the bone tunnels (Chung *et al.*, 2014). A potential way to form the 3D arrangement without braiding is to allow the cells to self-organize into a 3D construct. The first report on primary skeletal muscle cells self-organization was by Strohman et al. (Strohman *et al.*, 1990). They reported a starfish-

shaped muscle structure held in tension by cellular adhesion to stainless-steel pins which eventually developed into connective tissue layers. These newly formed tissue expressed more developmentally mature myosin heavy chains than cells in monolayer culture (Huang *et al.*, 2005). Since then, various groups have largely based their work on this technique for scaffold-free 3D skeletal tissue, especially for muscle tissue (Huang *et al.*, 2005) and then for tendon (Calve *et al.*, 2004) and ligament tissues (Hairfield-stein *et al.*, 2007; Paxton *et al.*, 2010). For example, fibroblasts and brushite ($CaHPO_4 2H_2O$) cement anchors (Paxton *et al.*, 2010) (Figure 2.14). In most of the scaffold-free approaches, ligament-like tissue forms from the self-assembly of fibroblasts or bone marrow stem cells, however they show poor mechanical integrity orders of magnitude lower than those of native ligament, and there is limited control on the size of the formed sinew.

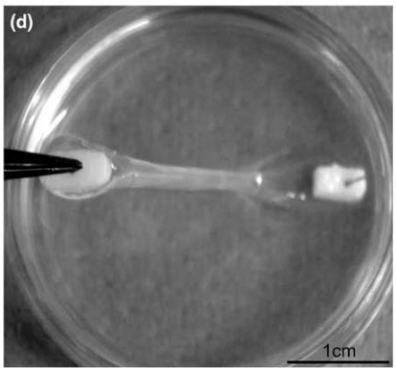

Figure 2.14 Formation of brushite cement anchor/tissue interface**.** TE-ligament formation with cell-seeded fibrin gel and brushite cement anchors at 7 days (Paxton et al., 2010).

Nanofibre scaffolds have been electrospun to exhibit the structural organization of collagen fibres seen in the ligament-to-bone interface. Nanofiber mats of aligned-to-random fibres were conceived to mimic the highly aligned collagen matrix in ligament and the random region to mimic the less organized collagen matrix in bone (Xie *et al.*, 2010). The same group has incorporated a mineral gradient and demonstrated that adipose derived stem cells seeded onto such scaffold exhibited different morphologies at different locations (Xie *et al.*, 2012).

Various growth factors and gene transfer have been used to augment healing/integration after ACL reconstruction.

The next challenge is engineering the enthesis. Some strategies aim to replicate the complex composite unit of bone–calcified fibrocartilage–fibrocartilage–ligament, as it is an attractive approach serving a twofold purpose: the calcified region in the scaffold is thought to enhance osteointegration with the host bone (Phillips *et al.*, 2008; Caliari *et al.*, 2015); and a graded overlapping matrix between the main body of the ligament and the calcified tissue is thought to mimic the enthesis role in knee homeostasis (Li *et al.*, 2016). To achieve the complexity of this strategy, researchers had focus on multiple cell types, bioinspired stratified or gradient scaffold designs aiming to replicate the structural and compositional heterogeneity inherent across the distinct tissues that make up the enthesis (Spalazzi *et al.*, 2006; Phillips *et al.*, 2008; Samavedi *et al.*, 2012; Caliari *et al.*, 2015; Criscenti *et al.*, 2016; Li *et al.*, 2016). The inherent complexity of achieving these strategies places limitations in the current studies. Graded scaffolds incorporating an array of different cell types (fibroblasts, chondrocytes and osteoblasts for the ligament, fibrocartilage and bone phases respectively) have been developed (Spalazzi *et al.*, 2006, 2008; Li *et al.*, 2016) (Figure 2.15). While this approach created zones as seen in the native structure, there are several challenges, including the necessity for multiple cell types. Many studies have attempt to recreate the biochemical composition along the length of the scaffold. Some have demonstrated a gradient of mineral content(Lu and Jiang, 2006; Li *et al.*, 2009), for example, a study combined polylactidecoglycolide (PLAGA) alone for the ligament region and PLAGA with bioactive glass (BG) to engineer a composite scaffold for the bony region (PLAGA-BG). PLAGA-BG is reported to be osteointegrative and so it was hypothesized that an intermediate region will be formed at the interface of ACL fibroblasts and osteoblasts as well as increasing mechanical properties in the zones with BG(Lu and Jiang, 2006). Gradients of genetic material have also been incorporated along the length of the scaffold. In a study, primary dermal fibroblasts were

seeded onto scaffolds containing a gradient of immobilized retrovirus encoding the osteogenic transcription factor Runx2. The authors achieved spatial patterns of transcription factor expression, osteoblastic differentiation and mineralized matrix deposition(Phillips *et al.*, 2008). However, Runx2-expressing cells were visible in the soft tissue zone.

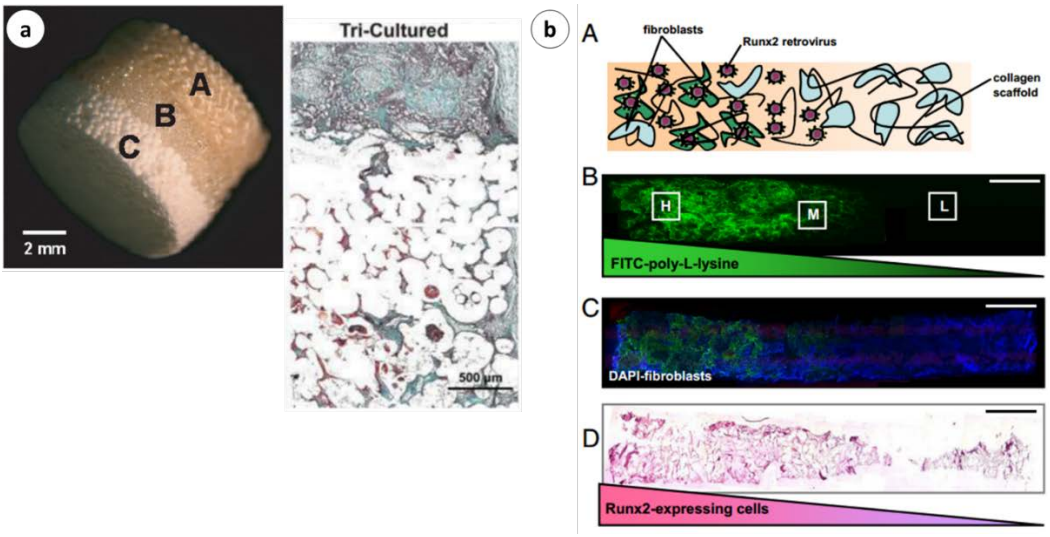

Figure 2.15 Graded scaffolds. **a**, Triphasic scaffold with 3 distinct yet continuous phases for soft tissue, interface and bone formation (A, B, C). Host tissue infiltration into the multiphasic scaffold at week 4. (Modified Goldner's Masson trichrome, collagen production appears in green) (Spalazzi *et al.*, 2008). **b**, Spatially regulated genetic modification of fibroblasts within 3D matrices. Schematic representation of a fibroblast-seeded construct containing spatial patterns of non-covalently immobilized retrovirus (Phillips *et al.*, 2008).

Another group proposed the use of electrospun meshes consisting of an aligned poly-(-ε-caprolactone) (PCL) fibre region, a randomly oriented poly(lactic-co-glycolic acid) (PLGA) fibre region, and a transition region containing both, aligned PCL and random PLGA fibres (Samavedi *et al.*, 2014) (Figure 2.16). Cell culture in 2D meshes showed that MSCs were aligned on aligned PCL regions and polygonal when grown on the random PLGA fibres. The 2D sheets were rolled into 3D cylindrical scaffolds and encapsulated within photo-crosslinkable polyethylene glycol diacrylate (PEGDA). Upon rolling and wetted with PEGDA, PCL fibres packed into an undesirable thinner midsection. Additionally, the tensile modulus of the PCL 2D meshes did not translate into an equivalent or superior tensile modulus in the 3D scaffold.

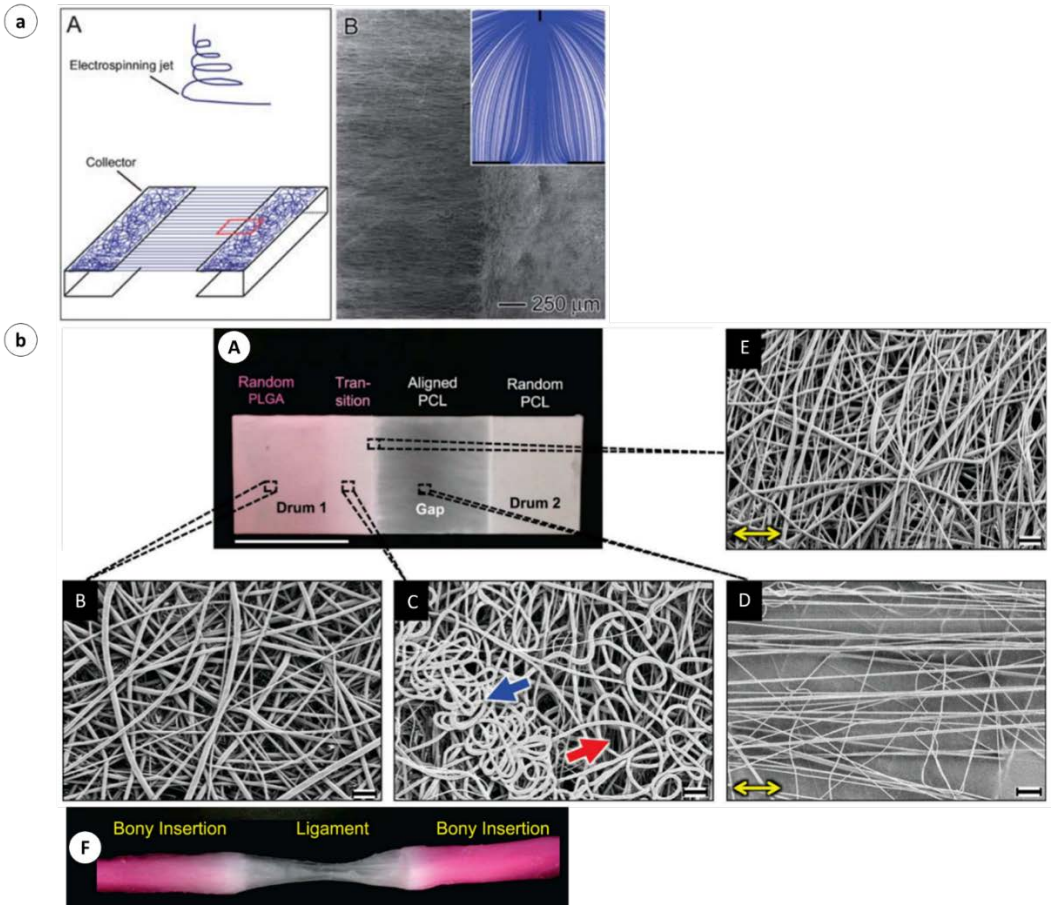

Figure 2.16 Electrospun fibrous scaffolds. **a**, Aligned-to-random gradation of nanofibers for potential interface applications (Xie *et al.*, 2012). **b**, Photograph of electrospun mesh comprising 4 regions: random PLGA (pink), transition (light pink), aligned PCL (white), and random PCL (also white). Scale bar, 2.5 cm (A). SEM micrographs (B-E) of the fibres in each region. Scale bar, 10 µm. Arrows indicate the axis of the collector. (F) Photograph of a 3D cylinder composite scaffold fabricated by rolling the electrospun mesh and encapsulating it within PEGDA (Samavedi *et al.*, 2014).

Others have developed substrates with gradient mechanical properties to mimic the corresponding tissue property gradient from soft tissue to bone at the insertion site (Sharma and Snedeker, 2010). Another approach to create contiguous pro-osteo and pro-soft tissue microenvironments was by incorporating calcium phosphate in collagen-GAG scaffolds (Caliari *et al.*, 2015) (Figure 2.17). Recently, bone marrow-derived mesenchymal stem cells (bMSCs) genetically modified with bone morphogenetic protein 2 (BMP2) and basic fibroblastic growth factor (bFGF) were surgically implanted into the tendon-bone interface after ACL reconstruction. Cartilage-like cells at the insertion, smaller tibial bone tunnel and higher

ultimate load and stiffness was observed. Further, the co-application of these two genes was more powerful and efficient than either single gene (Chen *et al.*, 2016).

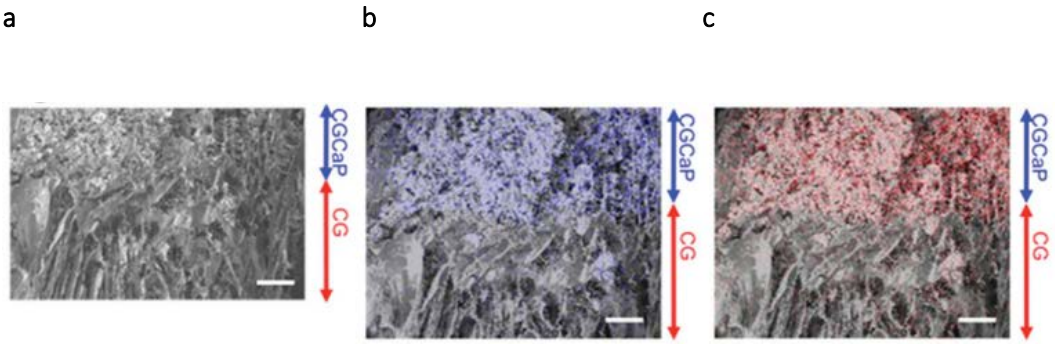

Figure 2.17 Collagen-GAG scaffolds fabricated by freeze-drying suspensions of collagen and GAG incorporating a mineralized matrix. **a**, interface between a region with aligned pores. Mineralized region with (**b**) phosphorus (blue) and (**c**) calcium (red). Scale bars, 200 µm (Caliari *et al.*, 2015).

2.6 Extracellular matrix to enhance biomimetic scaffolds

The extracellular matrix (ECM) is a complex network of molecules assembled into structures specific to each tissue. The ECM provides the cells with structural support and with chemical and mechanical cues that activate cell machinery through cell-matrix interactions that influence cell morphology, movement, function and fate (Lin *et al.*, 2012). The ECM is a dynamic structure that is continuously remodelling to maintain tissue homeostasis and development (Benders *et al.*, 2013). ECM-based tissue engineering approaches have been successfully used clinically for the regeneration of heart valves, trachea, muscle, tendon and abdominal walls by using matrices derived from the bladder and small intestine submucosa (SIS), for example (Ricchetti *et al.*, 2012; Benders *et al.*, 2013). In the repair of the muscle-tendon junction, SIS ECM was seeded with progenitor cells and ultimately replaced by functional contractile muscle-like and tendon-like tissues (Turner *et al.*, 2010). A major advantage of using ECM-based scaffolds is that they can retain the native structure of the original tissue rather than forming a less functional scar tissue (Benders *et al.*, 2013). This,

however, depends on the method of harvesting, decellularization and sterilization of the ECM scaffolds. For example, decellularization should remove all cells while preserving the bioactive cues, such as growth factors, in the ECM. Harsh washing steps may remove GAGs, consequently the tissue may lose water and hence loss of viscoelastic properties. Freeze-thaw cycles may introduce crystals that may disrupt the collagen structure.

Recently, scaffolds incorporating tissue-derived ECM have been shown to promote tissue-specific stem cell differentiation through the preservation of biophysical and biochemical motifs characteristic of the native tissues (Keane *et al.*, 2015; Hussey, Keane and Badylak, 2017; Nyberg *et al.*, 2017). Furthermore, recent studies have pointed to the potential of solubilized ECM derived biomaterials for orthopaedic tissue engineering applications (Rothrauff, Yang and Tuan, 2017). Specifically, solubilized ECMs derived from tendon and cartilage have been proposed as tissue-specific biomaterials (Rothrauff, Yang, and Tuan 2017). When seeded with MSC, tendon derived biomaterials were found to enhance scleraxis expression, while cartilage derived biomaterials were found to upregulate SOX9 expression. Other studies have shown that the inner meniscus ECM in combination with a polyethylene glycol (PEG) hydrogel-based scaffold enhances fibrocartilaginous differentiation of bone marrow MSCs, while the outer meniscus promotes a more fibroblastic phenotype. These results support the feasibility of using region-specific meniscus ECM for meniscus tissue engineering (Shimomura, Rothrauff and Tuan, 2017). The observed bioactivity of decellularized ECM on MSCs is postulated to reflect the abundance and variety of ECM ligands present that play a role in activating MSC integrin signalling pathways (Lin *et al.*, 2012).

2.7 Mesenchymal stem cells

Engineering the bone-ligament interface requires the regeneration of multiple types of tissues on a single material scaffold, therefore a growing approach is to spatially pattern

instructive cues onto these biomaterials to drive site-specific lineage commitment of MSCs. It is recognized that MSCs can generate cells of the stromal lineage with a degree of plasticity (Pittenger *et al.*, 1999). MSCs can give rise to osteogenic, chondrogenic, adipose, fibroblastic, and myoblastic lineages including cells within a range of developmental stages (Pittenger *et al.*, 1999; Crisan *et al.*, 2008). MSCs can be readily isolated from bone marrow and are thought to retain their multipotency over expansion in culture (Caplan, 2007; Chamberlain *et al.*, 2007).

Fibroblasts comprise a small volume of the ligament tissue (less than 5% (Hildebrand, Frank and Hart, 2004)) and show low mitotic activity (Van Eijk *et al.*, 2004). Thus, isolating ACL ligamentocytes yields a low cell number, which is a limiting factor for their use in ligament tissue engineering. Owing to the clinical limitations associated with their isolation, an alternative reliable source of cells is required. Research shows that the rate of proliferation and collagen deposition is higher in MSCs than isolated ACL fibroblasts (Van Eijk *et al.*, 2004; Ge, Goh and Lee, 2005). There is no established differentiation media towards the ligamentous lineage differentiation of MSCs. Both biological and mechanical stimuli have been employed to induce the differentiation of MSCs towards the ligament lineage. Several studies have exposed MSCs with a broad range of growth factors to promote the expression of fibroblastic hallmarks. These factors are epidermal growth factor (EGF), basic fibroblast growth factor (bFGF), insulin-like growth factor-II (IGF-II), transforming growth factor-beta (TGF-β), connective tissue growth factor (CTGF) (Vunjak-Novakovic *et al.*, 2004; Lee *et al.*, 2010; Brown *et al.*, 2015). CTGF stimulation has been shown to induce fibroblastic differentiation of MSCs by increasing the expression of the fibroblastic hallmarks collagen I, III and tenacin-C (Lee *et al.*, 2010). In this study, the delivery of CTGF stimulated postnatal connective tissue to undergo fibrogenesis rather than ectopic mineralization in a rodent *in vivo* model (Lee *et al.*, 2010).

Fibrochondrocytes share characteristics of both chondrocytes and fibroblasts. They have a round morphology, a pericellular coat and produce collagen type II as chondrocytes, yet they produce collagen type I like fibroblasts. Fibrocartilaginous-like tissues have been engineered using isolated chondrocytes (Hoben *et al.*, 2007), fibrochondrocytes (Mueller, 1999), co-cultures of fibrochondrocytes and chondrocytes (Mueller, 1999; Tanaka, Fujii and Kumagae, 1999) and mesenchymal stem cells (Nerurkar *et al.*, 2011; C. H. Lee *et al.*, 2014). A study that explored the capacity of chondrocytes and MSCs therapies for enthesis regeneration in a rat model, showed that MSCs produced a better regeneration of the fibrocartilage tissue than using chondrocytes (Nourissat *et al.*, 2010). Other studies have shown that meniscus fibrochondrocytes are unable to retain their phenotype when expanded in culture, loose the expression of type II collagen, and type I collagen expression is increased and they undergo a morphological change to fibroblast-like cells (Adesida *et al.*, 2006, 2012). Furthermore, MSCs isolated from aged donors do not compromise their fibrocartilaginous potential (Barry *et al.*, 2001) .

Various growth factors including insulin-like growth factor 1 (IGF-I), transforming growth factor- β1 (TGFβ1), transforming growth factor- β3 (TGFβ3), bone morphogenetic protein 2 (BMP2), and bone morphogenetic protein 6 (BMP6) have been used to direct the production of collagens type I and II from bone marrow derived MSCs, evidence of fibrochondrogenic-like cells (Baker and Mauck, 2007; Athanasiou and Sanchez-Adams, 2009; Nerurkar *et al.*, 2009). Recently, it was demonstrated that the sequential application of CTGF followed by TGFβ3 propelled MSCs to differentiate and yield a fibrocartilaginous matrix for knee meniscus regeneration, positive for type I and II collagens (C. H. Lee *et al.*, 2014). MSCs regenerated the knee meniscus fibrocartilage upon implantation of a scaffold that spatiotemporally released CTGF followed by TGFβ3 (C. H. Lee *et al.*, 2014). This combination yielded a higher number of fibrochondrocyte-like cells than the reverse (TGFβ3 → CTGF) or the combination (TGFβ3 + CTGF). CTGF and TGFβ3 alone failed to yield fibrochondrocytes. It

was demonstrated that sequential application was necessary and sufficient to induce MSCs into fibrochondrocytes that synthesized collagen I and II.

2.8 Summary and future perspectives

The current clinical repair to an ACL tear is achieved through mechanical fixation instead of biological re-integration to recapitulate the elegant pattern of biophysical and biochemical features seen in the native ligament-bone interface. The emergent strategies for ligament tissue engineering, therefore aim to recapitulate the ligament-bone interface. To this end, spatially graded biomaterials for the that maintain the different cell types seen along the length of the interface, or that regulate stem cell fate in a spatially-defined manner are designed. The challenges of engineering the ligament-to-bone interface are to promote osteointegration, to recapitulate the enthesis, and to achieve mechanical parity to native tissues. Some of these requirements have been fulfilled in isolation, therefore the next generation of engineered tissues should explore strategies to achieve all requirements. There are attractive tools such as

Chapter 3 Modulating microfibrillar alignment and growth factor stimulation to regulate mesenchymal stem cell differentiation

3.1 Introduction

Soft tissues such as the anterior cruciate ligament (ACL) attach to bone through a fibrocartilage interface which minimizes stress concentrations and mediates load transfer (Benjamin, Evans and Copp, 1986). Successful surgical reconstruction of such tissues depends on the osteointegration of an autograft or allograft and the re-establishment of the fibrocartilage interface (Rodeo *et al.*, 1993; Weiler, Hoffmann, *et al.*, 2002; Chen, 2009), termed the enthesis. However current ACL reconstruction techniques generally fail to regenerate the graded structure of the enthesis, predisposing the tissue at the bone insertion site to high stress concentrations which is believed to contribute to high re-failure rates, with revision rates reported to be as high as 28% in adolescents (Deneweth *et al.*, 2010; Ellis *et al.*, 2012; Engelman *et al.*, 2014; Faunø, Rahr-Wagner and Lind, 2014b). This has motived the development of tissue engineering (TE) strategies for ligament regeneration (Kuo, Marturano and Tuan, 2010; Nau and Teuschl, 2015). A number of studies have attempted to engineer stable fibrocartilaginous tissue or a mineral gradient to interface between the calcified region and the main body of the engineered ligament (Spalazzi *et al.*, 2006; Phillips *et al.*, 2008; Samavedi *et al.*, 2012; Caliari *et al.*, 2015; Li *et al.*, 2016), although the ideal solution has yet to be identified. Electrospinning of polymeric scaffolds is a particularly promising approach for engineering load-bearing musculoskeletal tissues as the mechanical properties of such biomaterials can be tuned to specific applications (Baker and Mauck, 2007; Choi *et al.*, 2008; Nerurkar *et al.*, 2009; Ghasemi-Mobarakeh *et al.*, 2010). Furthermore, electrospinning permits the fabrication of aligned fibres that serve as a template for the deposition of a unidirectional organized extracellular matrix (ECM) by resident cells, thereby generating anisotropy for tissues where direction dependence is essential for function. This makes them an ideal

biomaterial for ligament tissue engineering (Lee *et al.*, 2005; Bashur, Dahlgren and Goldstein, 2006; Criscenti *et al.*, 2016; Pauly *et al.*, 2017). However, directing stem cell differentiation within such scaffolds towards the different tissue types that make up the bone-ligament interface remains a challenge. Controlling the alignment of fibres within electrospun scaffolds, as well as the growth factors presented to cells within such scaffolds, represents a promising strategy to direct MSCs towards the endochondral, chondrogenic, fibrochondrogenic or ligamentous phenotypes that make up a fibrocartilaginous enthesis.

Scaffold topography is a potent structural cue that regulates the fate of stem cells seeded onto such constructs. For example, aligned electrospun fibres that replicate the anisotropy of the collagen fibres in ligaments and tendons have been shown to promote the expression of key ligament/tendon markers (Cardwell, Dahlgren and Goldstein, 2014; Yin *et al.*, 2015). Furthermore, in the absence of aligned structural cues, it has been demonstrated that cells are unable to generate a highly organized ECM architecture, even when mechanically stimulated (Subramony *et al.*, 2013; Yin *et al.*, 2015). Both aligned and randomly-oriented electrospun scaffolds have both been used to generate fibrocartilaginous tissues for meniscus and annulus fibrosus regeneration (Baker and Mauck, 2007; Nerurkar *et al.*, 2011). As well as scaffold fibre alignment, fibre diameter has also been shown to direct cell fate (Cardwell, Dahlgren and Goldstein, 2014; Bean and Tuan, 2015). Scaffolds engineered using electrospun micro fibres, as opposed to nano fibres, have larger pores and a higher porosity for cell infiltration and nutrient diffusion, while inducing higher expression of type I collagen, decorin and scleraxis (Cardwell, Dahlgren and Goldstein, 2014) (marker genes of mature ligamentocytes (Shukunami *et al.*, 2016)). Further, chondrogenic gene expression, and collagen and sGAG synthesis has been reported to be enhanced on microfibers in comparison to nanofibre scaffolds (Bean and Tuan, 2015).

MSCs have shown their potential to differentiate towards the tissue types that make up the bone-ligament interface tissues. Appropriate presentation of growth factors is key to regulating the differentiation of MSCs (Lee *et al.*, 2010; Bian *et al.*, 2011). Numerous studies have reported fibroblastic differentiation of MSCs using CTGF (Lee *et al.*, 2010; Pauly *et al.*, 2017), while TGFβ superfamily members are key mediators of chondrogenesis (Johnstone *et al.*, 1998; Tuli *et al.*, 2003). The hypothesis of this study is that MSCs can differentiate into either ligament or cartilage forming cells within electrospun scaffolds when presented with the appropriate underlying fiber alignment and growth factors. To test this hypothesis, MSCs were cultured on aligned and randomly-aligned microfibers and exposed to either transforming growth factor β3 (TGFβ3) or connective tissue growth factor (CTGF). Changes in cell morphology and cartilage and ligament-specific gene expression were assessed over time. We then investigated how the sequential supplementation of TGFβ3 and CTGF regulated gene expression and matrix synthesis within electrospun microfibrillar scaffolds, demonstrating how the integration of structural and biochemical cues can be used to support either the endochondral, chondrogenic, fibrochondrogenic or ligamentous differentiation of MSCs.

3.2 Materials and methods

3.2.1 Electrospinning of polycaprolactone (PCL) microfibre scaffolds

Polycaprolactone (PCL, MW 70 – 90 kDa, Sigma-Aldrich) was dissolved at 25% w/v in chloroform. Electrospinning of microfibers was performed in a custom-made electrospinning set-up using reported parameters (Binulal et al. 2010) as a reference. The polymer solution was loaded in a 20-ml syringe and extruded using a syringe pump through a 20G blunt-end needle charged to 15 kV. Continuous polymeric fibres were collected on a grounded mandrel (Ø 10 cm) with a flow rate of 4 ml/h. The aligned microfibers were collected with the mandrel rotating at 1500 rpm positioned 15 cm from its centre to the tip of the needle. The randomly-

aligned microfibers were collected with the mandrel rotating at 200 rpm positioned 18 cm from its centre to the tip of the needle. Fibres were collected for 1 h to produce scaffolds with a thickness of ~300 µm. Scaffolds were punched from the electrospun sheets into 8 mm diameter discs using dermal biopsy punches (Hibernia Medical).

3.2.2 Characterization of scaffolds

Samples were sputter coated with a mixture of gold palladium (80:20) to a thickness of ~10 nm (Cressington 108) and imaged by scanning electron microscopy (SEM, Zeiss Ultra FE-SEM) at an accelerating voltage of 5 kV. The average fibre diameters were determined by measuring the fibres from SEM micrographs (n = 3 scaffolds, n≥ 15 images per scaffold) using DiameterJ plugin for ImageJ (National Institutes of Health). A total of 1,500 – 3,000 fibres were analysed for aligned and randomly-aligned scaffolds. Porosity was calculated by gravimetry according to the equation $\varphi = 1 - \frac{\rho_{scaffold}}{\rho_{PCL}}$; the density of the scaffold ($\rho_{scaffold}$) was determined by measuring its mass and volume (Pham, Sharma, and Mikos 2006). The volume of the scaffold was determined using the known diameter (8 mm) and measured thickness using electronic callipers (n ≥ 6 scaffolds). The principal axis of fibre orientation was computed using the Directionality plugin of ImageJ based on Fast Fourier Transform (FFT) analysis (n = 3 scaffolds, n ≥ 10 images per scaffold). This plugin reports 'Direction' (°) of the centre of the Gaussian and the angle of dispersion (standard deviation of the Gaussian).

3.2.3 Isolation and expansion of bone marrow-derived MSCs

Bone marrow derived porcine MSCs were isolated from 3-month old pigs as previously described (Thorpe et al. 2012). To confirm multipotency, colony-forming cells were tested for adipogenic, chondrogenic and osteogenic differentiation potential. One isolate of porcine MSCs was used for all the experiments. MSCs were expanded in expansion media consisting of high-glucose Dulbecco's modified Eagle's medium (DMEM) GlutaMAX supplemented with

10% fetal bovine serum (FBS), penicillin (100 U/mL)-streptomycin (100 µg/mL) (all from Gibco, Biosciences) and 0.25 µg/mL amphotericin B (Sigma-Aldrich) in a humidified atmosphere at 37 °C, 5% CO2 to passage 2.

3.2.4 Scaffold cell-seeding and culture conditions

Electrospun scaffolds were sterilized by ethylene oxide (EtO) (Anprolene, Anderson products). Sterile scaffolds were hydrated and pre-wet by incubating in expansion media overnight before cell seeding. At passage 2, MSCs were trypsinized and seeded onto one side of the electrospun scaffolds at a density of 500,000 cells per scaffold or 125,000 cells per scaffold using custom designed scaffold holders as seen in previously published studies (Sathy et al. 2015). The 500,000 cells per scaffold condition was used to support high levels of ECM deposition, while the 125,000 cells per scaffold condition was used to better visualize cell-matrix interactions. To obtain the percentage of adhered cells in the optimization phase, we seeded the cells onto the scaffolds with one 30 µl aliquot of cells (0.5 million cells/ml). As a control, 30 µl aliquots were put in microtubes and centrifuged to pellet the cells and then measured the total amount of DNA using a Picogreen assay. After 4 h of attachment period, we removed the scaffolds from culture, lysed the cells using CelLytic (Sigma-Aldrich) according to manufacturer's instructions, and vortexed the scaffolds, then we measured the amount of DNA present on the scaffold. The fraction of adhered cells was calculated as the DNA on the scaffolds divided by the DNA measured in the control microtubes. Scaffolds retained 82 – 87% of the seeded cells, with no significant difference between groups (data not shown).

After 4 h of seeding the cells, 1 ml of expansion media was added. The next day, the scaffolds were transferred to fresh 24-well plates and growth media was replaced by 1 ml of chemically defined media. Cell-seeded scaffolds were maintained in expansion medium, ligament induction medium, or chondrogenic medium at 5% CO2 for 20 days. Ligament induction

medium was adapted from previously published studies (Chang H Lee et al. 2010), it consisted of high-glucose DMEM GlutaMAX supplemented with 2% FBS, penicillin (100 U/ml) streptomycin (100 µg/ml), 0.25 µg/ml amphotericin B, 50 µg/ml L-ascorbic acid 2 phosphate and 100 ng/ml recombinant human connective tissue growth factor (CTGF; ProSpec Tany, TechnoGene Ltd.), hereafter referred to as CTGF treatment. Chondrogenic medium consisted of high-glucose DMEM GlutaMAX, penicillin (100 U/ml)-streptomycin (100 µg/ml), 100 µg/ml sodium pyruvate, 40 µg/ml L-proline, 4.7 µg/ml linoleic acid, 50 µg/ml L-ascorbic acid 2-phosphate, 1.5 mg/ml bovine serum albumin (BSA), 1X insulin-transferrin-selenium, 100 nM dexamethasone, 0.25 µg/ml amphotericin B (all from Sigma-Aldrich), and 10 ng/ml recombinant human transforming growth factor-β3 (TGF-β3; ProSpec-Tany, TechnoGene Ltd.), hereafter referred to as TGF-β3 treatment. Medium was changed twice weekly. MSC-seeded scaffolds were cultured on the scaffold holders suspended above the underlying tissue culture surface.

3.2.5 Cell viability and fluorescent imaging of cell morphology

Cell viability was assessed by staining cell-seeded scaffolds with Live/dead assay kit (Invitrogen, Bioscience) using 4 mM calcein-AM and 2 mM ethidium homodimer-1 in phenol red-free DMEM for 1 h at 37 °C. Samples were examined under a scanning confocal microscope (Olympus FV1000). F actin staining was used to evaluate the morphology of MSCs. Glutaraldehyde-fixed specimens were permeabilized in 0.5% Triton-X 100, incubated in 1.5% bovine serum albumin (BSA) to block non-specific labelling and stained with a 1.5% BSA solution containing rhodamine phalloidin (1:40) for 1 h at room temperature (RT). Cell nuclei were stained with 4',6-diamidino-2-phenylindole (DAPI, 1:100) for 10 min at RT (all from Sigma). Samples were imaged using a scanning confocal microscope (Leica SP8) at an excitation/emission of 540/565 nm for rhodamine phalloidin and 358/461 nm for DAPI.

Analysis was performed in Leica Application Suite X (LAS X) software. Cell-formed aggregates were measured and quantified from confocal images (n = 3 scaffolds, n = 4 images per scaffold) using particle analysis in ImageJ.

3.2.6 RNA isolation and Quantitative Real-Time PCR

Cells seeded on the scaffolds were analysed for their gene expression using quantitative real-time PCR at days 10 and 20 of culture. In addition, real-time PCR was undertaken for cells harvested at day 0 that were not seeded on scaffolds. Cells were lysed using RLT lysis buffer (Qiagen) supplemented with 10 µl/ml β-mercaptoethanol (Sigma-Aldrich) and stored at –80°C (n = 5/group/time point). At the time of isolation, lysates were thawed and homogenized using QIAshredder columns (Qiagen). Total RNA was isolated and further purified using RNeasy Mini kits (Qiagen) following the manufacturer's instructions. RNA yield and purity were quantified using a NanoDrop spectrophotometer (Labtech International). 100 ng total RNA per sample was reverse transcribed into cDNA per 20 µl of reaction volumes, 1 µl of cDNA equivalent to 50 – 100 ng cDNA was used for qRT-PCR. High-Capacity cDNA Reverse Transcription Kits (Applied Biosystems) were used as per manufacturer's instructions. Quantitative PCR was performed using SyberGreen select master mix (Applied Biosystems) in an ABI 7500 sequence detection system (Applied Biosystems). Expression of collagen type I (*COL1A1*), II (*COL2A1*), III (*COL3A1*), X (*COL10A1*), tenomodulin (*TNMD*), α-actin (*ACTA2*), lysyl oxidase (*LOX*), aggrecan (*ACAN*), SRY-Box 9 (*SOX9*), bone morphogenetic protein 2 (*BMP2*), runt-related transcription factor 2 (*RUNX2*), alkaline phosphatase (*ALPL*), and glyceraldehyde-3-phosphate dehydrogenase (*GAPDH*) was evaluated. The porcine specific primer sequences (KiCqStart SYBR Green Primers, Sigma) used for amplification are listed in Table 3.1. CT values were analysed using the comparative CT method with GAPDH as the internal control (Schmittgen and Livak 2008). Relative expression of the genes is presented as fold change relative to the

same population of cells harvested at day 0 that were not seeded on scaffolds (except for *COL2A1*). *COL2A1* gene expression was undetected in the cells harvested at day 0, hence *COL2A1* was normalized to the 'Control' group (MSCs on scaffolds cultured in expansion media for either 10 or 20 days).

Gene	Forward	Reverse
GAPDH	TTTAACTCTGGCAAAGTGG	GAACATGTAGACCATGTAGTG
COL1A1	TAGACATGTTCAGCTTTGTG	GTGGGATGTCTTCTTCTTG
COL2A1	CGACGACATAATCTGTGAAG	TCCTTTGGGTCCTACAATATC
COL3A1	TCATCCCACTGTTATTTTGG	CTCTATCCGCATAGGACTG
COL10A1	GTAGGTGTTTGGTATTGCTC	GAGCAATACCAAACACCTAC
ACTA2	CAAAAGAGGAATCCTGACC	CATTGTAGAAAGAGTGGTGC
ACAN	GACCACTTTACTCTTGGTG	TCAGGCTCAGAAACTTCTAC
LOX	TGTGAAATTCGCTACACAG	GGGAGTTGCTTTCTAATACG
TNMD	GCTAATTGTCCTATTTTGGGG	GAAAGTGTGTTCCATGTCG
SOX9	CAGACCTTGAGGAGACTTAG	GTTCGAGTTGCCTTTAGTG
RUNX2	CCAACAGAGGCATTTAAGG	CCAAAAGAAGTTTTGCTGAC
ALPL	TTTCACTCTTCTTAGTGCTG	CGTTACGGAATGAGGAAAC
BMP2	ATGTGGAGGCTCTTTCAATG	CATGGTCGACCTTTAGGAG

Table 3.1 Primer sequences used for qPCR

3.2.7 Biochemical analysis

Biochemical content was analysed from samples at day 0 (24 h after cell seeding) and day 21 (n = 4). Samples were digested with 3.88 U/ml papain enzyme in 100 mM sodium phosphate buffer containing 5 mM ethylenediaminetetra-acetic acid (EDTA) and 10 mM L-cysteine hydrochloride (HCl), pH 6.5 (all Sigma-Aldrich) for 18 h at 60 °C under constant rotation.

Following digestion of the samples, DNA content was quantified using the Hoescht Bisbenzimide 33258 dye assay (Quant-iT ssDNA assay kit, Biosciences). Sulphated glycosaminoglycan (sGAG) content was quantified using the dimethylmethylene blue (DMMB) dye-binding assay (Blyscan, Biocolor Ltd.). Collagen content was determined by quantifying the hydroxyproline content using the dimethylaminobenzaldehyde and chloramine-T assay (Kafienah and Sims 2004). A hydroxyproline-to-collagen ratio of 1:7.69 was used (Ignat'eva et al. 2007).

3.2.8 Histological and immunohistochemical analysis

Samples were embedded in optimal cutting temperature (O.C.T.) compound (VWR Chemicals) and flash frozen with liquid nitrogen. Embedded samples were cryo-sectioned longitudinally to 10 µm thickness perpendicular to the fibre plane. Sections were fixed in 4% paraformaldehyde (PFA) for 5 min at RT and stained with Picrosirius Red or Alcian Blue (Sigma-Aldrich) to assess collagen or sGAG content, respectively. To perform immunohistochemistry, sections were pretreated with chondroitinase ABC for 5 min at 37°C for antigen retrieval, blocked in PBS containing 1% BSA and 10% goat serum (Sigma G-9023) for 30 min at RT. Sections were incubated in primary antibodies, anti-collagen type I antibody (mouse monoclonal, ab90395, 1:400), anti-collagen type II (mouse monoclonal, ab3029, 1:100), and anti-collagen type III (mouse monoclonal, ab23445, 1:400) (all from Abcam) overnight at 4°C. Sections were rinsed in PBS and subjected to endo-peroxidase activity blocking for 20 min at RT. Sections were rinsed in PBS and incubated in secondary antibody anti-mouse IgG biotin produced in goat (B7151, 1.5:200, Sigma). Colour was developed using the Vectastain ABC reagent kit (Vector Laboratories) followed by exposure to peroxidase DAB peroxidase substrate (DAB peroxidase HRP substrate kit; Vector Laboratories). Reaction was stopped

when colour was developed in the positive control. Sections were dehydrated through alcohol gradients and mounted using Vectashield (Vector Laboratories).

3.2.9 Dual chamber culture

By electrospinning at 1500 RPM for 1 h, aligned ~5 µm fibre-sheets were made. Rectangular strips of 3 X 1 cm were cut from the electrospun-sheets and conditioned as described in section 3.2.4. Strips were placed inside custom-made Teflon wells and $1.5X10^6$ cells in a 400 µl aliquot were seeded on top of each scaffold. After 4 h, 400 µl of growth media were added on top of the fibre-strip. The next day the scaffolds were placed in dual-chamber culture wells. Dual-chamber culture wells were used to culture both conditions simultaneously. The chamber consisted of an agarose well (1 mm in thickness) of 5 cm in diameter divided into two chambers separated by a median dividing solid wall of 1 mm in thickness. This dual-chamber design was validated to ensure spatial media presentation (data not shown) and was previously validated by others (Harris et al. 2017). To place the electrospun-fibre strip, a 10-mm long incision was made with a scalpel through the divisor wall. The MSC-seeded strip was slid through so that one half of the strip was in one of the two hemi-chambers with chondrogenic media and the other half in the second hemi-chamber with ligament media. 3 ml of chemically defined chondrogenic or ligamentous media were immediately added into their corresponding side of the chamber.

3.2.10 Statistics

Statistical analyses were performed in GraphPad Prism software (v.6, GraphPad). D'Agostino-Pearson normality test was used to test the normality of data distribution. Statistical differences were determined by analysis of variance (ANOVA) followed by Tukey's multiple comparison test or Student's t-test where appropriate. Statistical significance was accepted at

$p \leq 0.05$. Data are presented as mean ± standard deviation, and mean ± standard error of the mean (SEM) for qPCR. Sample size (n) is indicated within the corresponding figure legends.

3.3 Results

3.3.1 Fabrication of microfibrillar scaffolds with defined architectures

Polycaprolactone (PCL)-fibre scaffolds consisting of aligned or randomly-aligned fibres with a thickness of ~300 µm were fabricated by electrospinning. Anisotropy of the microfiber-scaffolds was confirmed by scanning electron micrographs (SEM) and FFT analysis (Figure 3.1). Aligned fibres were parallel to each other with a small angle of dispersion (4.48 ± 0.9°), while random fibres showed no preferred fibre orientation with nearly equal distributions at all angles (Figure 3.1 a, b). The electrospinning parameters produced aligned and randomly-aligned microfibers with diameter ~5 µm (5.2 ± 0.2 µm and 5.1 ± 0.3 µm respectively; $P = 0.39$). The porosity of aligned and randomly-aligned scaffolds was 0.76 ± 0.004 and 0.79 ± 0.012 ($P = 0.0015$) respectively. MSCs remained viable on microfibrillar scaffolds (Figure 3.1 c shows data for day 0; Figure 3.2 shows data for day 20) with similar numbers of cells adhering to scaffolds 24 hours after seeding (as also demonstrated by the DNA content of scaffolds at day 0; see Figure 3.8 c).

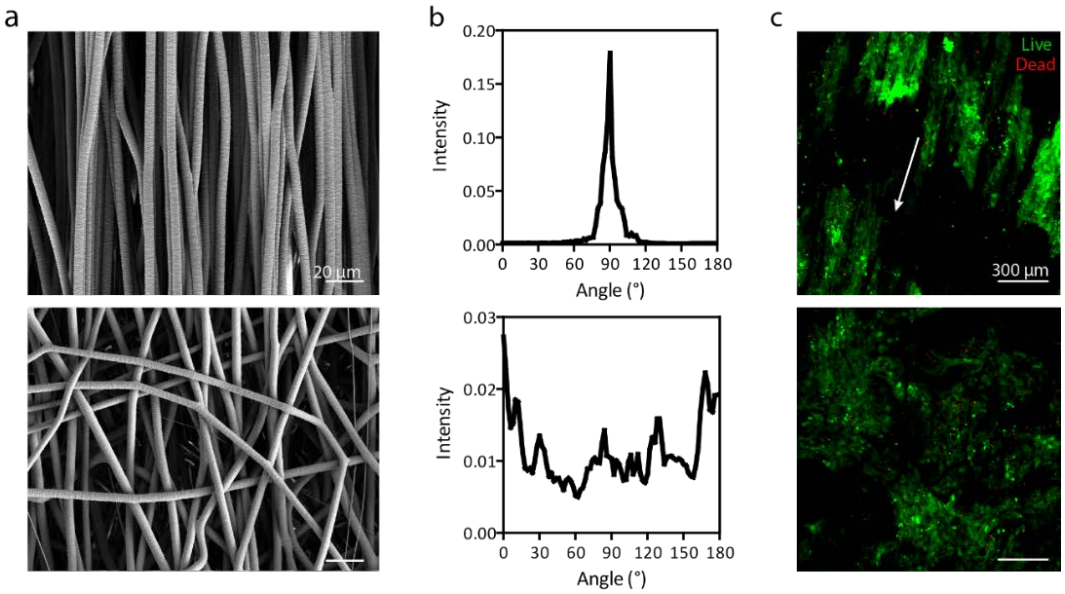

Figure 3.1 Microfibrillar scaffolds with specific fibre diameter and alignment. **a,** Scanning electron micrographs (SEM) of aligned and randomly-aligned microfibers. Scale bars, 20 µm. **b,** Principal axes of fibre orientation of representative images for aligned and randomly-aligned fibres; plot shows alignment angle (x-axis) and frequency (y-axis; arbitrary units). **c,** Cell viability on aligned and randomly-aligned microfibres was demonstrated with live/dead staining (green: 'live', red: 'dead'. Initial cell density, 0.5 X 10^5 cells/scaffold); white arrow indicates fibre orientation on the aligned scaffold. Scale bars, 300 µm.

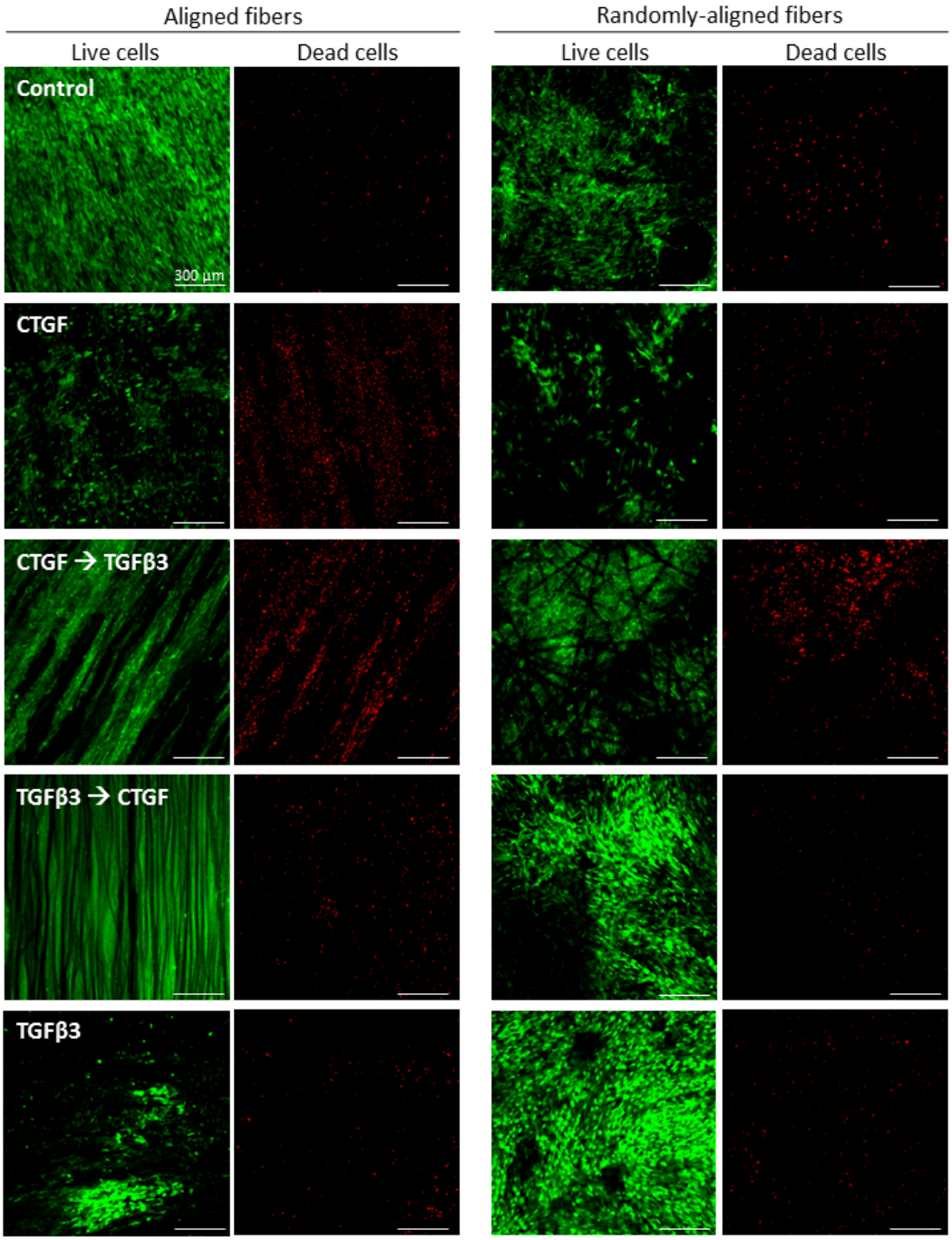

Figure 3.2 Live-dead staining at day 20. Viability of MSCs seeded on aligned (left) and randomly-aligned fibres (right) was demonstrated with live-dead staining (green: 'live', red: 'dead'). Initial cell density 0.5 X 10^5 cells/scaffold. Scale bars, 300 µm.

3.3.2 MSCs adopt distinct morphologies in response to CTGF and TGF-β3 stimulation depending on the alignment of the underlying substrate

To identify the effect of the underlying substrate alignment on MSC morphology, the cytoskeletal organization was examined in MSCs cultured on aligned and randomly-aligned microfiber-scaffolds at two seeding densities (125,000 and 500,000 cells/scaffold). In the absence of growth factor stimulation, cells predominately aligned in the direction of the underlying substrate. Cells on aligned microfibrillar scaffolds elongated and organized parallel to the orientation of the fibres. On randomly-aligned fibres, cells spread and adopted more random orientations (Figure 3.3 a).

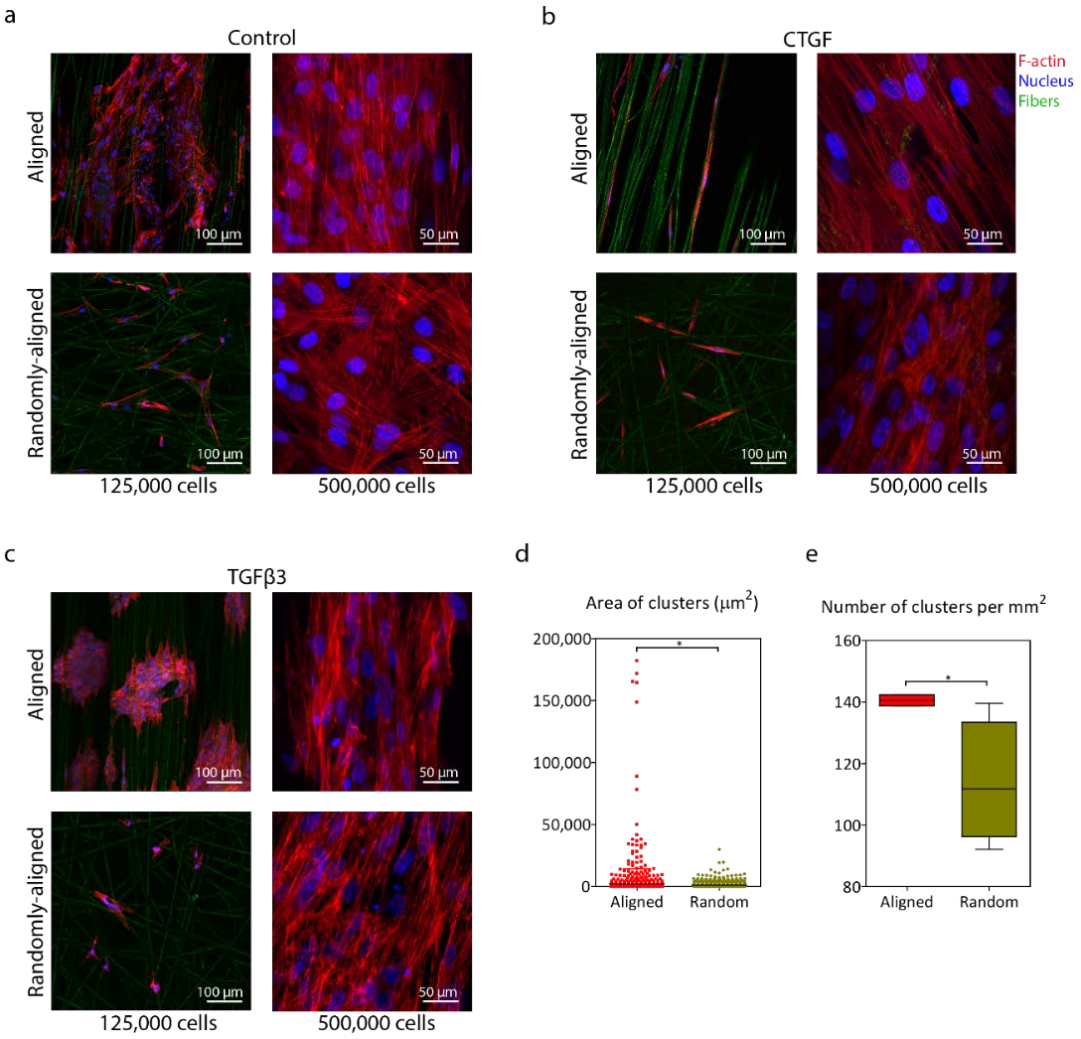

Figure 3.3 Fibre alignment and growth factor stimuli influence MSC morphology. F-actin stained of representative MSCs cultured in expansion media ('Control') (**a**), in the presence of CTGF (**b**) and TGF-

β3 (c). MSCs were stained for F-actin (red) and cell nuclei (blue) at low (1.25 X 10^5 cells, day 10) and high cell seeding densities (5 X 10^5 cells, day 20). Aligned and randomly-aligned fibres are shown in green. **d**, Quantification of cluster area in TGFβ3 group; **P* < 0.05. **e**, Quantification of number of clusters per mm^2 in TGF-β3 group; *n* ≥ 580 regions of interest (ROI), **P* < 0.05.

In the presence of connective tissue growth factor (CTGF), MSCs adopted a more elongated morphology, characteristic of a fibroblastic phenotype, displaying long and thin cell bodies without protrusions on both aligned and non-aligned scaffolds (Figure 3.3 b). On both fibre alignments, MSCs appeared to follow the orientation of the individual microfibers to which they attached. As a result, at higher cell-seeding densities CTGF-stimulated MSCs on aligned fibres formed a highly organized cellular structure, while this organization was lost on random fibres. Thus, the aligned fibres serve as a template for the aligned CTGF-stimulated MSCs to organize unidirectionally.

TGFβ3-stimulated cells adopted distinct morphologies depending on the underlying fibre-alignment. MSCs on aligned fibres clustered into large aggregates (these clusters were easily identifiable in the lower cell-density samples) (Figure 3.3 c, d). In comparison, cells cultured on random fibres spread and formed fewer and smaller clusters (Figure 3.3 c-e). This clustering of MSCs on aligned fibres were observed at different external oxygen tensions (Figure 3.4).

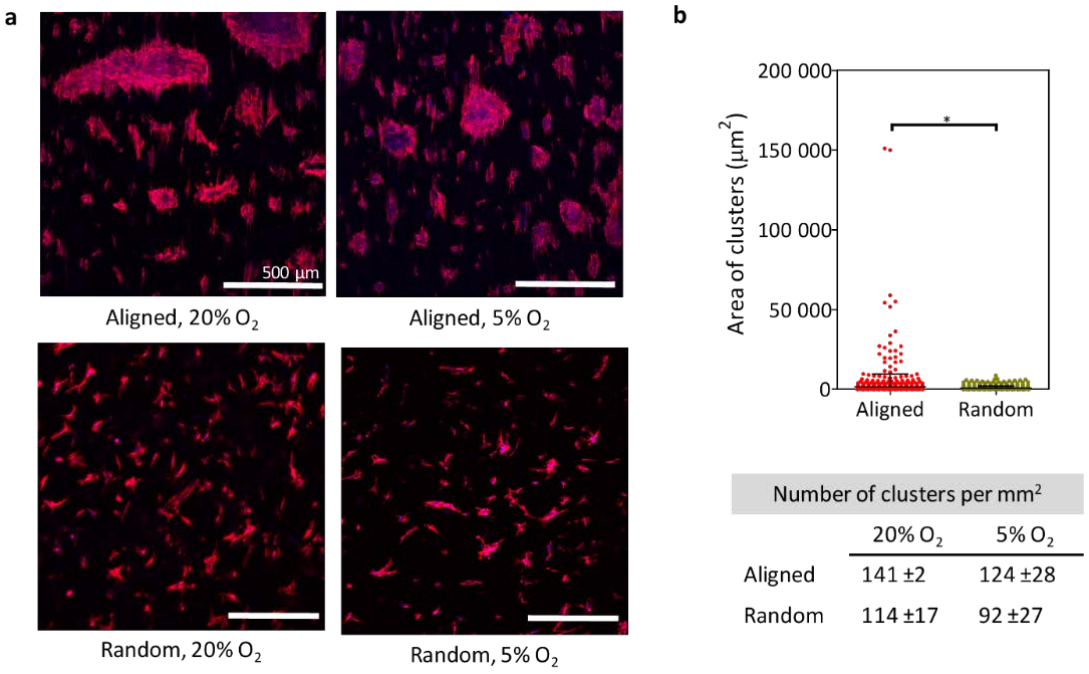

Number of clusters per mm²		
	20% O_2	5% O_2
Aligned	141 ±2	124 ±28
Random	114 ±17	92 ±27

Figure 3.4 Number of clusters and cluster's area in TGF-β3-stimulated cells on aligned and randomly-aligned scaffolds at 5% O_2. **a,** Actin cytoskeletal organization of representative MSCs on aligned and random fibres stained for F-actin (red) and cell nuclei (blue) at ay 10, initial cell seeding density: 1.25 X 10^5 cells/scaffold. **b**, Quantification of clusters area in TGFβ3 groups; *P < 0.05. **c**, Number of clusters per mm^2 in TGFβ3 groups; $n \geq 580$ regions of interest (ROI), *P < 0.05. The area of the clusters was significantly larger in those on aligned fibers compared to those on randomly-aligned fibers. The number of clusters formed in the aligned fibers was higher than on the random fibers.

3.3.3 MSCs display distinct gene expression profiles in response to CTGF and TGF-β3 stimulation that depend on the underlying substrate alignment

Next the gene expression profile of MSCs was assessed in response to the combination of fiber alignment and growth factor stimuli (Figure 3.5 shows data for 500,000 cells/scaffold; Figure 3.6 shows data for 125,000 cells/scaffold). The expression profile of cells that were not subjected to growth factor stimulation (labelled 'control') was also assessed to elucidate the inherent effect of fiber alignment on MSC differentiation. In these control conditions, MSCs on aligned microfibrillar scaffolds expressed higher levels of tenomodulin (*TNMD*) and aggrecan (*ACAN*) compared to cells on randomly-aligned microfibrillar scaffolds. In general, however, the expression of key markers of MSC differentiation did not dramatically change over baseline levels seen at day 0 in the absence of growth factor stimulation.

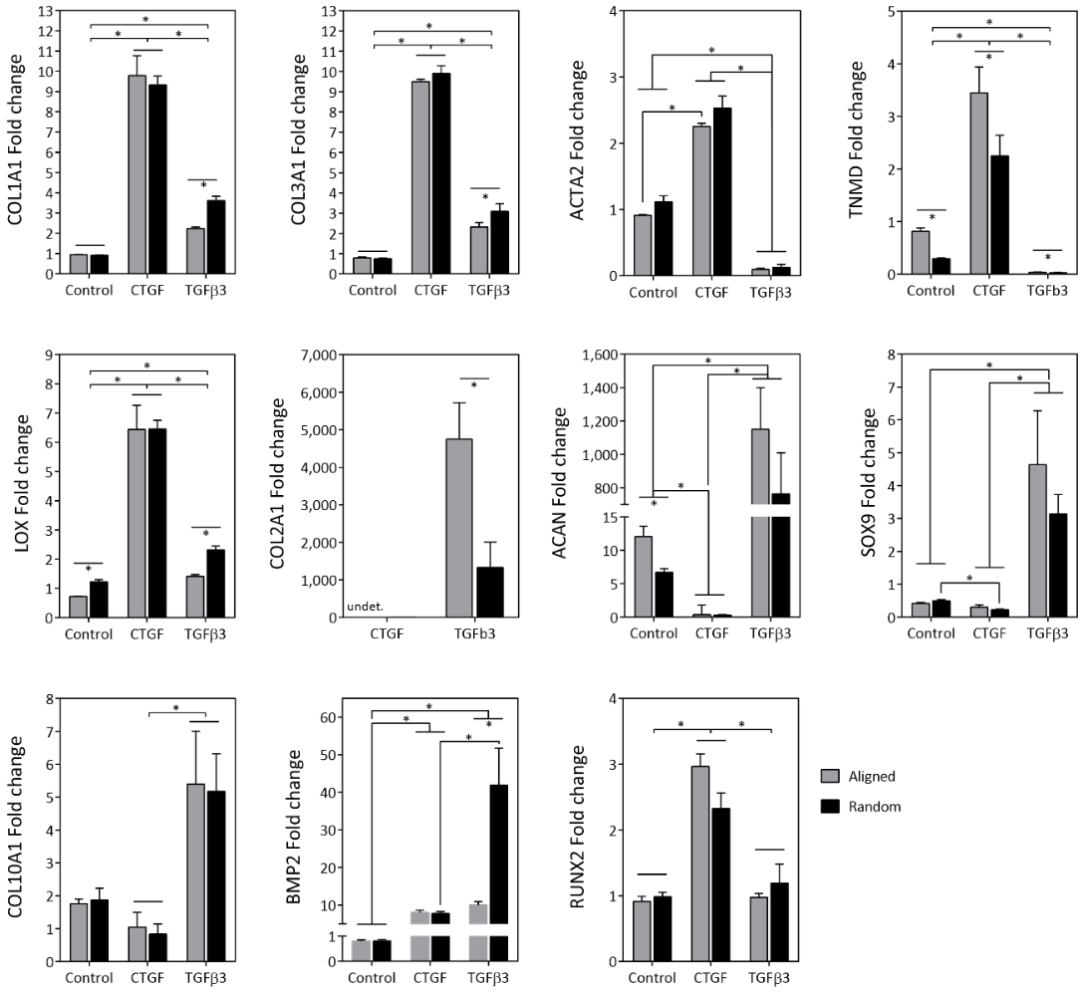

Figure 3.5 Gene expression at day 10. Collagen type I (*COL1A1*), II (*COL2A1*), III (*COL3A1*), X (*COL10A1*), tenomodulin (*TNMD*), α-actin (*ACTA2*), lysyl oxidase (*LOX*), aggrecan (*ACAN*), SRY-Box 9 (*SOX9*), bone morphogenetic protein 2 (*BMP2*), runt-related transcription factor 2 (*RUNX2*). Data is reported as fold-change relative to the same population of cells harvested at day 0 that were not seeded on scaffolds. *COL2A1* was normalized to control group (MSCs on scaffolds cultured in the absence of growth factors) as expression of this gene at day 0 was undetected. The values plotted are means ± SEMs of $n = 5$ scaffolds for each condition, $^*P < 0.05$. Alkaline phosphatase (*ALPL*) expression was undetected in all groups. 'undet.' means the gene expression was undetermined.

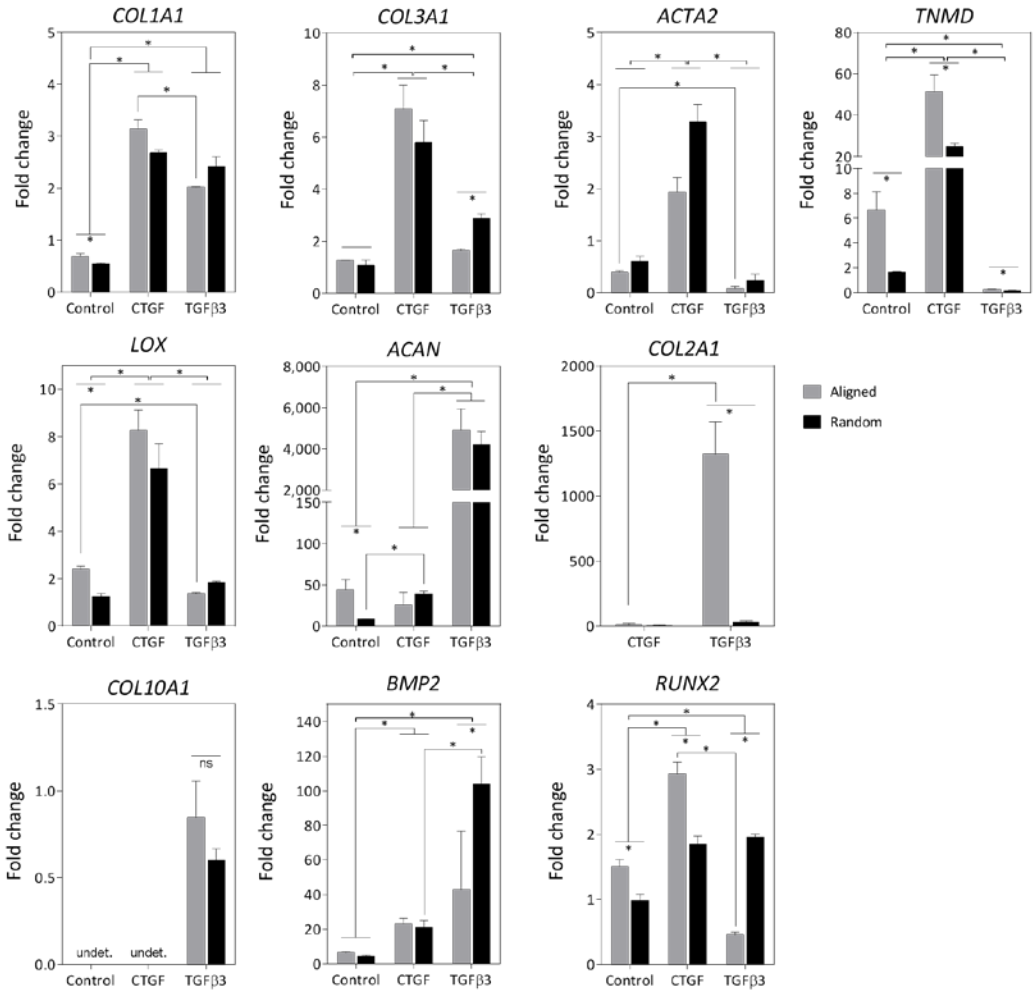

Figure 3.6 qRT-PCR gene expression at day 10 in lower cell-seeding density groups. Data is reported as fold-change relative to the same population of cells harvested at day 0 that were not seeded on scaffolds. *COL2A1* was normalized to control group (MSCs on scaffolds cultured in the absence of growth factors) as expression of this gene at day 0 was undetected. ALPL expression was undetected in all groups. The values plotted are means ± SEMs of N=5 scaffolds for each condition, $*P < 0.05$. Abbreviation: undet., undetermined.

The ligament markers – collagen types I (*COL1A1*) and III (*COL3A1*), α-actin (*ACTA2*) and *TNMD* – were highly upregulated in CTGF-stimulated MSCs compared with controls and with MSCs cultured in the presence of TGF-β3. Consistent with their elongated cell shape on both substrates, the relative expression of these ligamentogenic genes in CTGF-stimulated MSCs was comparable on aligned and randomly-aligned fiber-scaffolds. The exception to this finding was for *TNMD* expression, which was significantly higher on aligned scaffolds

compared to randomly-aligned scaffolds. *TNMD* and *ACTA2* were exclusively upregulated in CTGF-stimulated MSCs. *LOX* expression (which plays a key role in cross-linking collagen) was also ~6-fold higher in CTGF-stimulated groups compared to other conditions.

The chondrogenic markers – collagen types II (*COL2A1*) and X (*COL10A1*), aggrecan (*ACAN*) and SRY-Box 9 (*SOX9*) – were highly upregulated in TGF-β3-stimulated MSCs. As expected, TGF-β3 supplementation was necessary to upregulate SOX9 (a gene essential for cartilage formation (Bi et al. 1999)) and *COL2A1*. Chondrogenic gene expression was higher in TGF-β3-stimulated cells on aligned fibers, especially *COL2A1* expression, which correlates with the formation of larger cell aggregates on this substrate (Figure 3.3 c-e).

Bone morphogenetic protein 2 (*BMP2*) and collagen type I (*COL1A1*) expression was significantly higher in TGF-β3-stimulated cells on randomly-aligned fibers, suggesting that such scaffolds were supporting progression along the endochondral pathway. The relative gene expression profile was maintained with time and in lower cell-seeding densities (Figure 3.6). Furthermore, at lower seeding densities runt-related transcription factor 2 (*RUNX2*), an essential molecular switch for bone formation, was higher in TGFβ3-stimulated cells on randomly-aligned fibers.

3.3.4 Sequential supplementation with CTGF and TGFβ3 supports fibrocartilaginous differentiation on microfibrillar scaffolds

Next it was examined whether the sequential supplementation of CTGF and TGF-β3, coupled with the appropriate substrate alignment, could promote MSC specification towards the fibrocartilaginous lineage (cells that express high levels of both types I and II collagen). This hypothesis was motivated by findings of others that the sequential supplementation of CTGF and TGFβ3 promote fibrochondrogenic differentiation of MSCs (C. H. Lee *et al.*, 2014). To

evaluate the effects of the sequential supplementation, gene expression of MSCs stimulated with CTGF for 10 days followed by TGF-β3 for a further 10 days (CTGF → TGFβ3) or vice versa (TGFβ3 → CTGF) was analysed.

MSCs exposed to the sequential growth factor supplementation expressed higher levels of *COL1A1* and *COL2A1* on both aligned and randomly-aligned substrates compared to control conditions (Figure 3.7). *COL2A1* gene expression was significantly higher on aligned-fibre scaffolds for all groups stimulated with TGFβ3, transient or continuous. Introducing CTGF supplementation to the TGFβ3-stimulated cells (TGFβ3 → CTGF) on aligned fibres, decreased the expression of type II collagen (*COL2A1*) compared to that of cells continuously stimulated with TGFβ3. In the same way, introducing TGFβ3 to cells stimulated with CTGF (CTGF → TGFβ3) decreased the expression of *COL1A1* compared to that of cells exclusively stimulated with CTGF. There was a slight increase in *COL1A1* expression in the sequential supplementation groups compared to TGFβ3 only group, but this effect was not statistically significant. MSCs exposed to TGFβ3 → CTGF maintained a gene expression profile more similar to cells exclusively exposed to TGFβ3, compared to cells exposed to the reverse (CTGF → TGFβ3). MSCs on aligned substrates exposed to CTGF → TGFβ3 expressed higher levels of type 10 collagen (*COL10A1*) compared to those on randomly-aligned scaffolds. In contrast, there was a downregulation of *COL10A1* under TGFβ3 → CTGF supplementation on both aligned and randomly-aligned scaffolds.

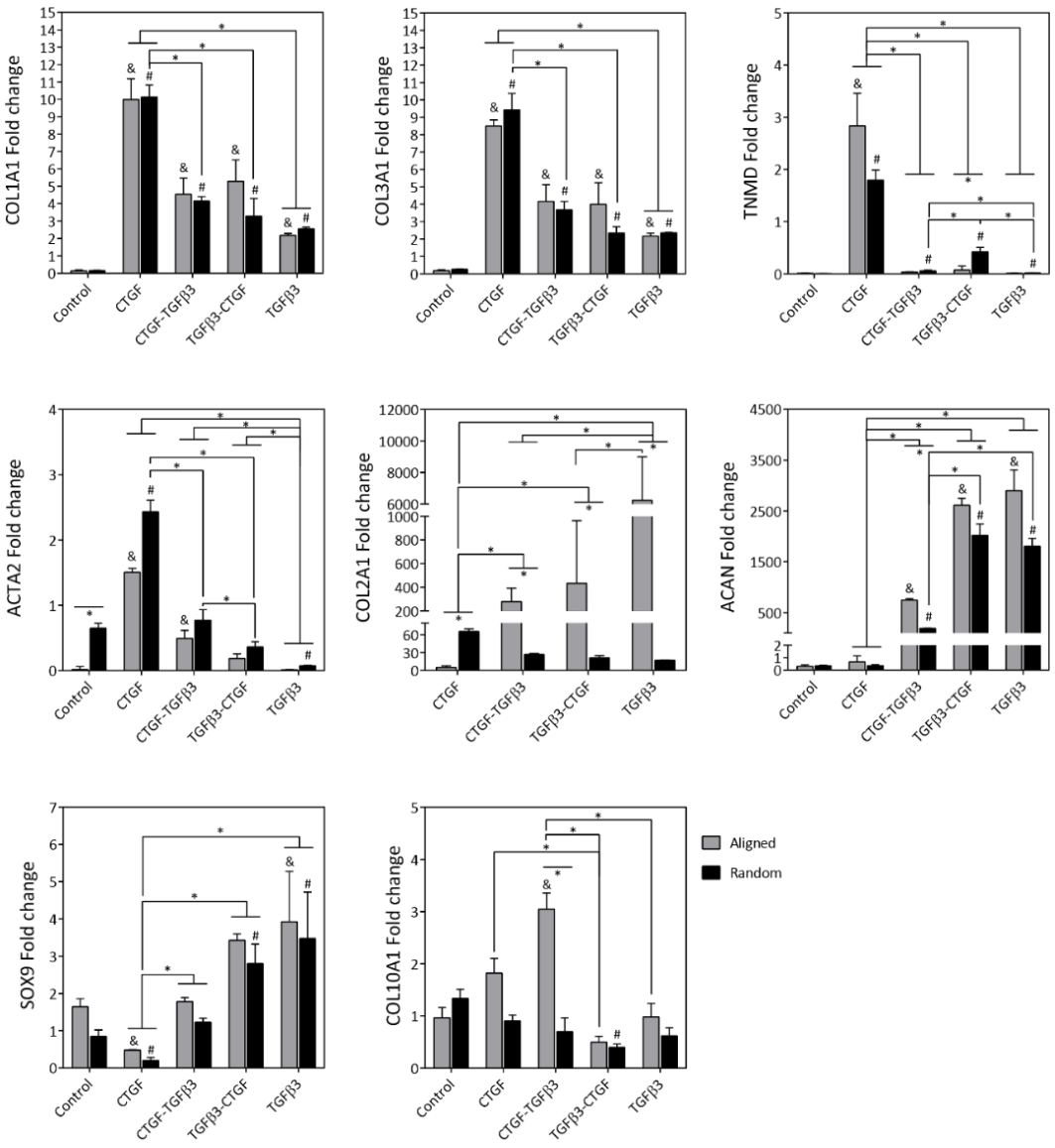

Figure 3.7 Gene expression at day 20. MSCs exposed to CTGF treatment for 10 days followed by TGFβ3 treatment for 10 days (CTGF → TGFβ3) and vice versa (TGFβ3 → CTGF). MSCs exposed to CTGF for 20 days (CTGF) and those exposed solely to TGFβ3 treatment (TGFβ3). COL2A1 was normalized to Control group (MSCs on scaffolds cultured in the absence of growth factors) as expression of this gene at day 0 was undetected. The values plotted are means ± SEMs of n = 5 scaffolds for each condition. &, significantly different from aligned control, $P < 0.05$. #, significantly different from random control, $P < 0.05$. *, $P < 0.05$.

Consistent with the gene expression data at day 10 (Figure 3.5), it was observed that *TNMD* was upregulated exclusively on CTGF-stimulated cells, and *COL2A1* upregulation was highest in the aligned microfibrillar scaffolds. After 20 days in culture, the expression of *COL10A1* was lower in TGFβ3-stimulated cells compared to day 10.

3.3.5 Growth factor stimulation regulates tissue development with MSC-seeded electrospun scaffolds

We next assessed the effects of single growth factor and the sequential growth factor supplementation on collagen and sulphated glycosaminoglycans (sGAGs) synthesis (Figure 3.8 shows data for 500,000 cells/scaffold). MSCs seeded on aligned and randomly-aligned scaffolds penetrated the scaffold, proliferated, and deposited collagen and sGAGs on the surface and through the thickness of the scaffold (Figure 3.8 a, b). Stronger picrosirius red staining for collagen was prevalent at the surface of the aligned fibre-scaffold for CTGF-stimulated cells, with immunohistochemistry confirming the presence of collagen types I and III (Figure 3.9 and Figure 3.10). A significant amount of collagen also accumulated in the CTGF→TGF-β3 and TGF-β3 groups. These groups were positive for collagen type II staining (Figure 3.11). TGFβ3 containing groups stained intensely for Alcian blue, while low levels of sGAGs deposition were observed in CTGF and control groups.

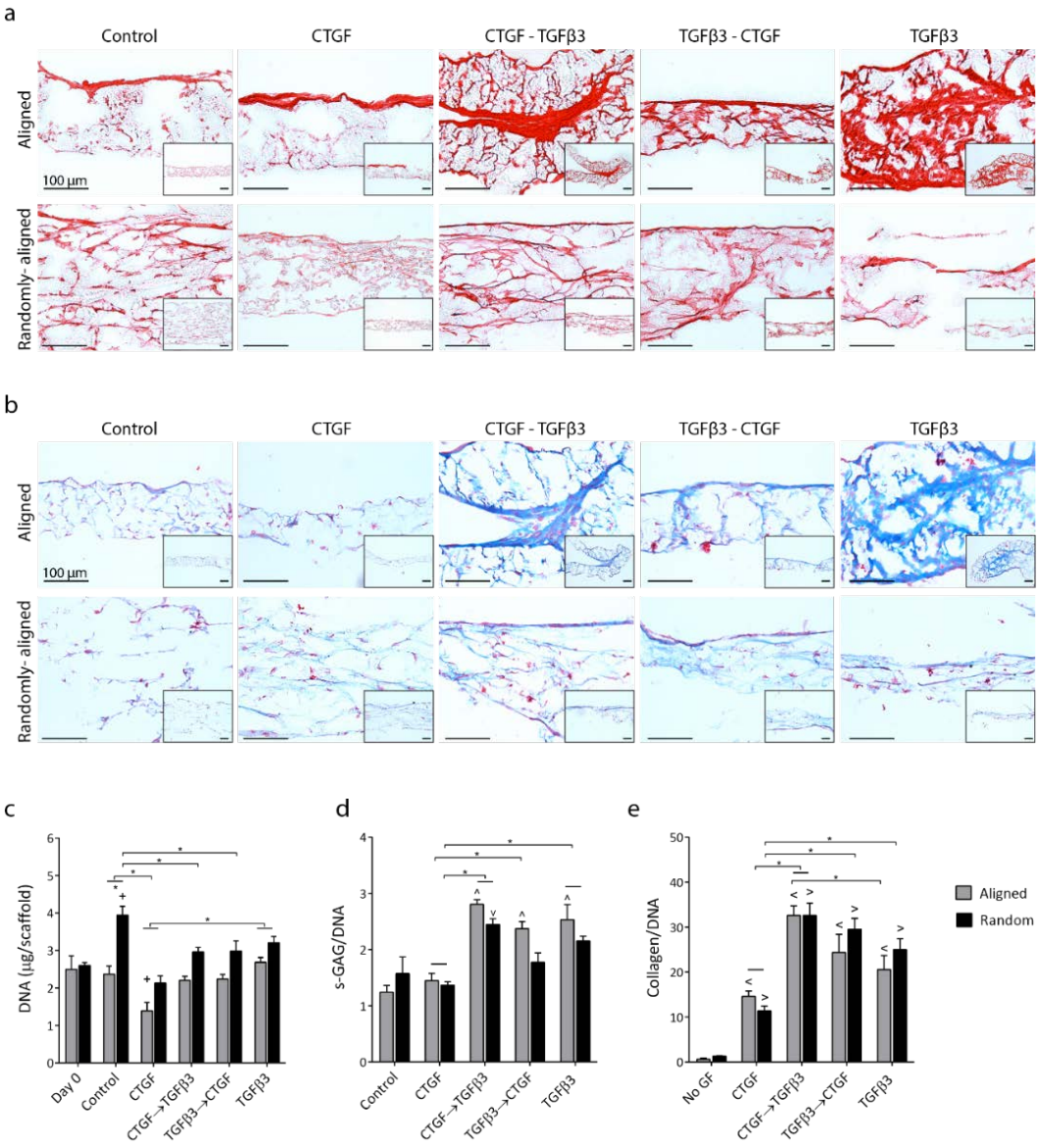

Figure 3.8 Evaluation of DNA, collagen and sGAG content. **a, b**, Cross-sections of aligned and randomly-aligned scaffolds stained using Picrosirius red and Alcian blue stainings for collagen and sGAGs, respectively. Stains reveal collagen and sGAG-rich regions through the thickness of the scaffold. CTGF-TGF-β3 and TGF-β3 aligned fibre-scaffold groups folded by the longitudinal axis. **c**, DNA content; +: $P < 0.05$, significantly different from day 0. **d**, sGAG content; ^,v: $P < 0.05$, significantly different from aligned and randomly-aligned controls. **e**, collagen content; <, >: $P < 0.05$, significantly different from aligned and randomly-aligned controls.

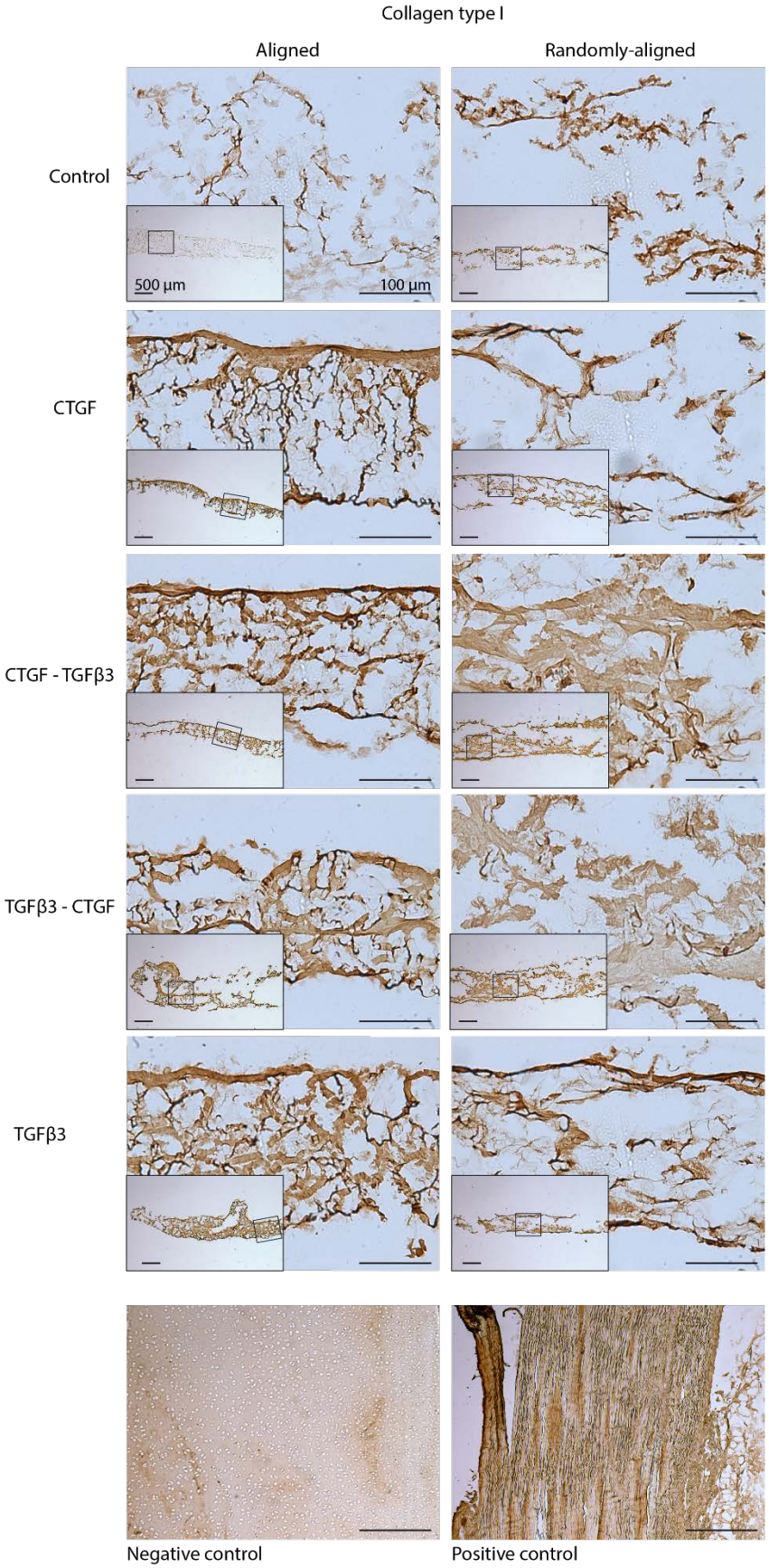

Figure 3.9 Immunohistochemistry of collagen type I. Scale bar, 100 µm. Scale bar in the insert 500 µm. Negative control: cartilage tissue; positive control: ligament tissue.

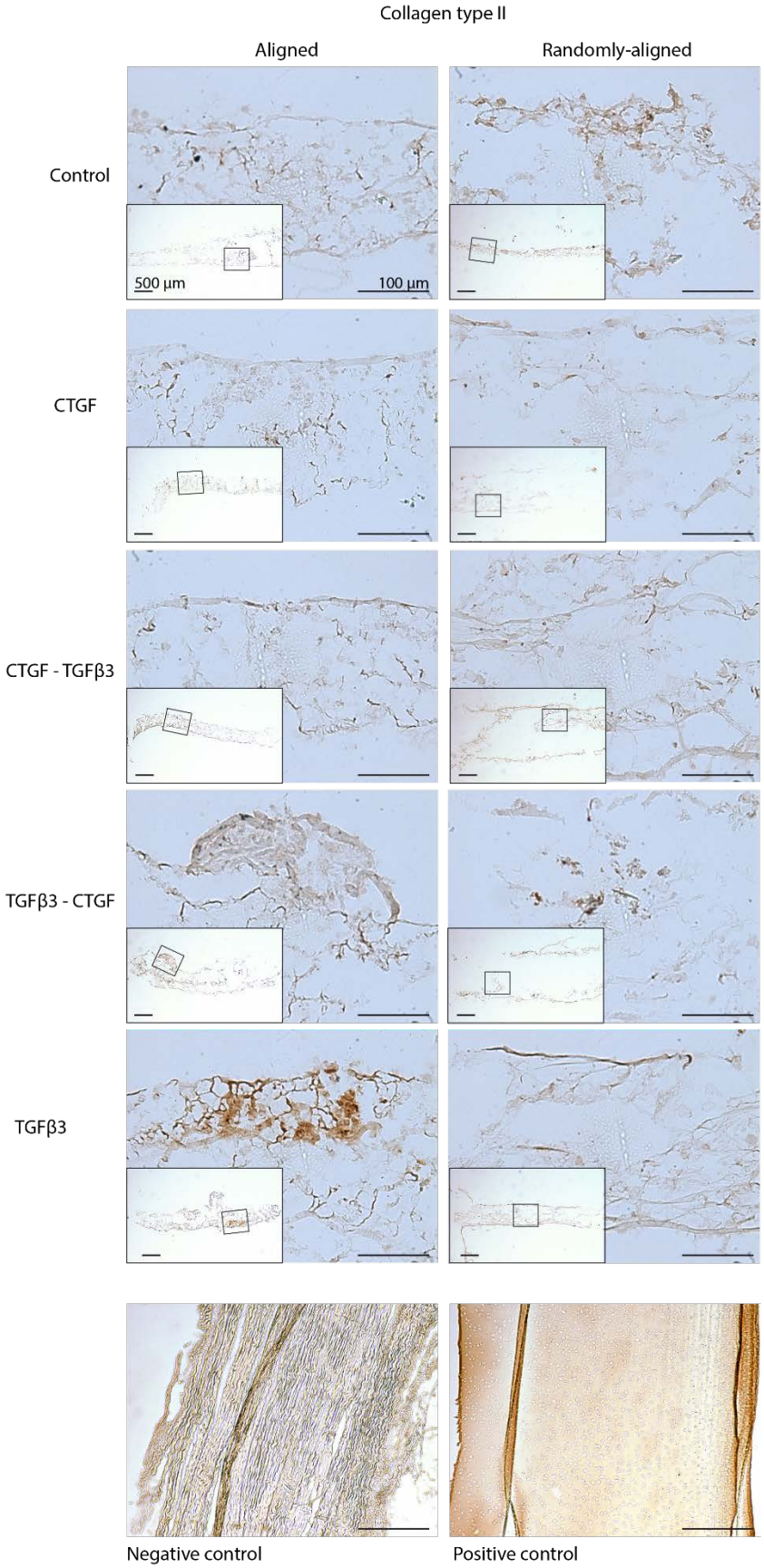

Figure 3.10 Immunohistochemistry of collagen type III. Scale bar, 100 µm. Scale bar in the insert 500 µm. Negative control: ligament tissue; positive control: cartilage tissue.

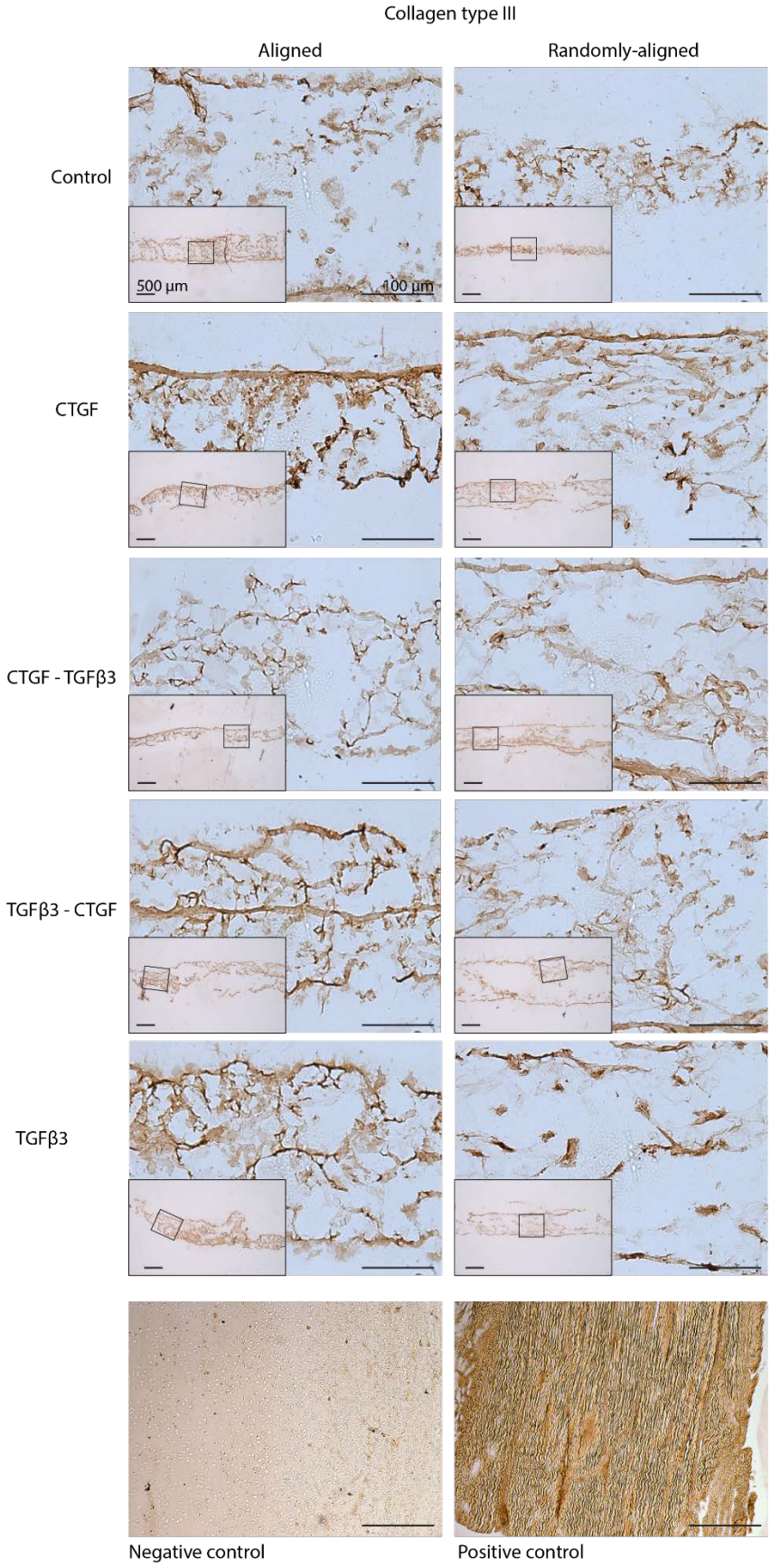

Figure 3.11 Immunohistochemistry of collagen type II. Scale bar, 100 µm. Scale bar in the insert 500 µm. Negative control: cartilage tissue; positive control: ligament tissue.

An increase in DNA content in randomly-aligned substrates indicated cell proliferation at day 21 in the control group. MSCs appeared to undergo higher levels of proliferation on random fibres, but this difference was not significant (Figure 3.8 c). MSCs subjected to TGFβ3 stimulation, transient or continuous, produced significantly higher levels of collagen and sGAG compared to other groups (Figure 3.8 d, e). Many of the aligned fibre scaffolds – particularly hosting TGFβ3-stimulated cells – folded due to cellular overgrowth and cell-mediated contraction, a phenomenon observed by others (Garrigues, 2011).

3.3.6 Culturing a scaffold with spatially defined presentation of CTGF and TGFβ3

Rectangular aligned-fibre scaffolds were cultured in a dual-chamber to expose half of the scaffold to CTGF for the ligamentous region and half exposed to TGFβ3 for the chondrogenic region. The dual-chamber consisted of two adjoined chambers one with CTGF and the other with TGFβ3. MSCs exposed to the CTGF side showed an elongated shape like the underlying substrate, while those exposed to the TGFβ3 supplementation showed a spread cell body, as previously seen in section 3.3.2. Underneath dual-chamber divisor, MSCs seemed to proliferate less and adopted an elongated morphology (Figure 3.12 c).

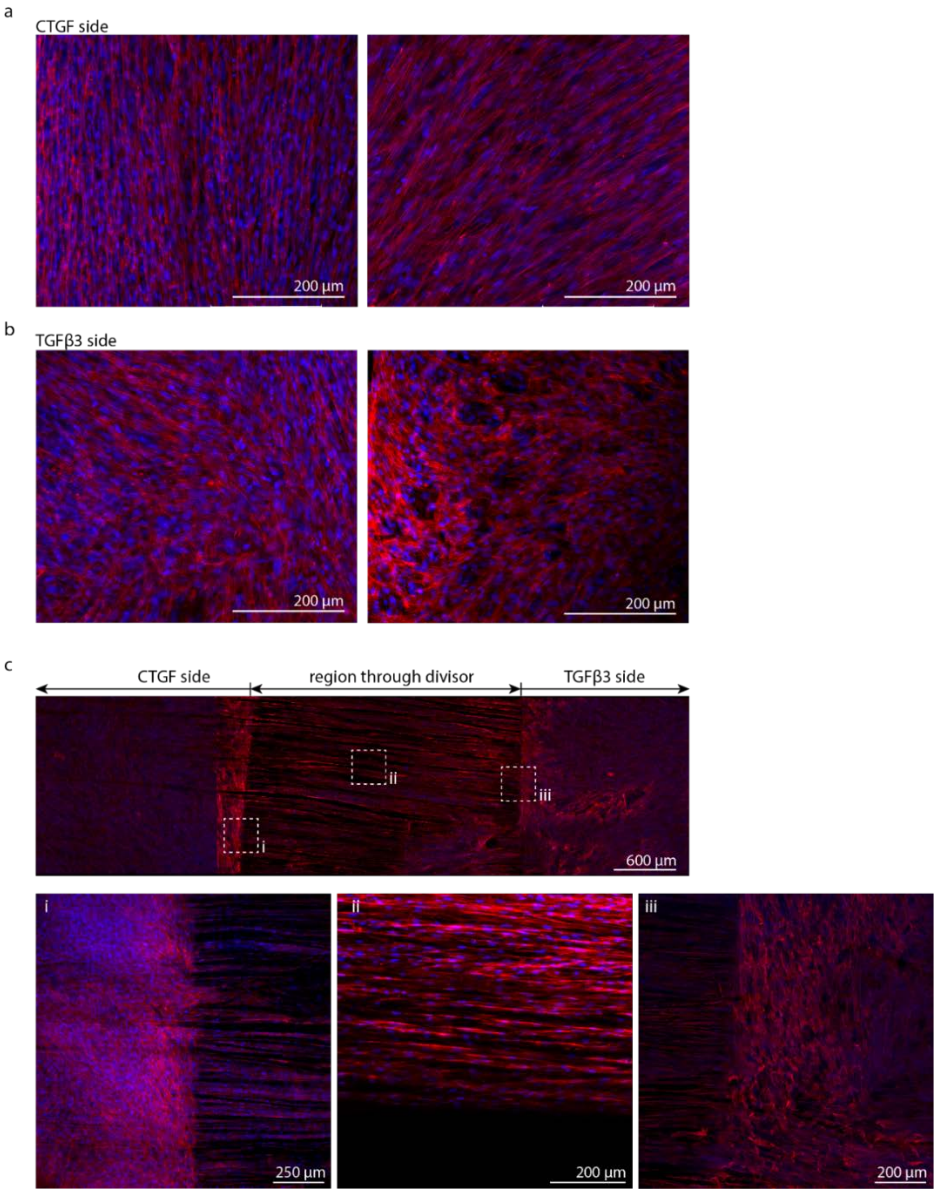

Figure 3.12 Aligned scaffolds seeded with MSCs and cultured in both CTGF and TGFβ3 using a dual-chamber. **a**, F-actin staining of MSCs cultured in the CTGF side of the dual chamber and (**b**) those culture in the TGFβ3 side of the chamber. MSCs were stained for F-actin (red) and cell nuclei (blue) after 20 days in culture.

3.4 Discussion

In this study, it was investigated how microfibrillar alignment and growth factor stimulation interact to regulate the chondrogenic, fibrochondrogenic and ligamentous differentiation of MSCs. The electrospun microfibrillar scaffold utilized here has advantageous properties for tissue engineering applications, including a high surface area for cell attachment

and matrix deposition and the possibility to functionalize the polymer chains with cell-adhesive peptides, growth factors or natural components of the extracellular matrix (ECM) to further increase cell adhesion and bioactivity (Ghasemi-Mobarakeh *et al.*, 2010). Further, PCL was used due to the polymer's biocompatibility and biodegradability and its tailorable degradation kinetics and mechanical properties (Woodruff and Hutmacher, 2010). PCL is used in certain FDA (U.S Food and Drug Administration) approved biomedical and drug-delivery devices (Woodruff and Hutmacher, 2010). Micro-scale as opposed to nano-scale fibres were used to encourage cell infiltration and ECM deposition through the thickness of the scaffold, to resemble the collagen fibre diameter range in ligaments (Silver, Freeman and Seehra, 2003) and to enhance ligament differentiation (Cardwell, Dahlgren and Goldstein, 2014). Consistent with the literature (Yin *et al.*, 2015), it was demonstrated that in the absence of biochemical cues, MSCs oriented parallel to fibres on aligned fibre scaffolds, while cells spread in all directions on randomly-aligned fibre scaffolds. This correlated with higher *TNMD* expression on aligned scaffolds, although no dramatic upregulation in key markers of differentiation were observed over time in the absence of growth factors. When coupled with appropriate growth factor stimulation, it was found that modulating the alignment of microfibrillar scaffolds could be used to promote either an endochondral, chondrogenic, fibro-chondrogenic or ligamentous phenotype. Such control over progenitor/stem cell differentiation is central to successful interface TE strategies.

The results demonstrate that aligned microfibers and co-stimulation with CTGF preferentially supported ligamentous differentiation of MSCs. In the presence of CTGF, MSCs on aligned microfibrillar scaffolds adopted an elongated fibroblastic phenotype, with cells aligning parallel to the fibre orientation. These environmental conditions promoted an upregulation of *COL1A1* and *COL3A1* gene expression and the highest expression of *TNMD*. *TNMD*, a transmembrane glycoprotein regulated by scleraxis, is a highly specific marker of ligamentocytes and tenocytes (Shukunami *et al.*, 2006). *TNMD* is implicated in collagen

organization, and localized to cells within thick bundles of aligned collagen fibres (Shukunami *et al.*, 2006). Up-regulation of ligamentous genes in MSCs has been reported on highly aligned collagen type I fibres *in vitro* in the absence of bioinductive molecules (Kishore *et al.*, 2012), suggesting that the alignment of the collagen effectively induces the expression *TNMD* and other ligamentous factors. In this study, scaffold anisotropy in the absence of CTGF was not sufficient to promote increased *TNMD* expression over day 0 values, suggesting that further growth factor stimulation is required on PCL scaffolds to induce robust differentiation. *ACTA2* was also more strongly expressed in the CTGF-stimulated cells. Previous studies have shown that fibroblasts expressing *ACTA2* are involved in the earliest stages of fibre bundle formation in the intact as well as the remodelled human ACL (Murray and Spector, 1999; Weiler, Unterhauser, *et al.*, 2002). MSCs stimulated with CTGF also showed higher levels of *RUNX2* expression compared to control groups and to those stimulated with TGFβ3; this might indicate that there was a heterogenous population of cells at day 10; although there was no *RUNX2* expression detected for any group at day 20 and no alizarin red positive staining was present after 20 days of culture.

Given the upregulation of fibrillar collagens I and III in CTGF-stimulated cells, it was examined whether these environmental conditions might also regulate collagen crosslinks, a result that has been demonstrated for cardiac fibroblast and CTGF activation during atrial fibrillation (Adam *et al.*, 2011). Thus, qRT-PCR analysis was extended to examine lysyl oxidase (*LOX*), a key regulator of collagen crosslinking (Makris *et al.*, 2014). CTGF-stimulated cells showed a ~6-fold increase in *LOX* gene expression compared to controls (MSCs on scaffolds cultured in expansion media). Associated upregulation of *LOX* mRNA expression likely indicates the crosslinking of fibrillary pro-collagens I and III in CTGF-stimulated cells which will form the final collagen types I and III fibres that are highly resistant against proteolytic enzymes and possess improved tensile strength, critical for ligament TE. Together, these results demonstrate that a combination of CTGF stimulation and an aligned electrospun

substrate promotes MSC elongation and coordinated alignment in a single direction (Figure 3.3 b), which correlates with robust ligamentous differentiation (Figure 3.5 and Figure 3.6).

TGFβ3-stimulated cells on both aligned and randomly-aligned microfiber-scaffolds expressed higher levels of cartilage specific markers and increased the deposition of collagen and sGAGs. On aligned fibres, MSCs formed large condensations which correlated with higher levels of collagen type II expression compared to MSCs seeded onto random fibres. Stem cell condensation is a key initiating step in chondrogenesis [29,38,49], with biomaterials that mimic aspects of condensation enhancing chondrogenesis (Bian *et al.*, 2013). Condensation did not appear to be a result of increased proliferation, as evidenced by similar DNA values in both random and aligned scaffolds at day 21 under TGFβ3 stimulation, but likely due to increased migration on aligned scaffolds. It is hypothesized that aligned fibres provide a substrate more conductive to MSC migration and hence aggregation. In agreement with this concept, aligned fibres have previously been shown to facilitate cell migration (Shang *et al.*, 2010; Kolambkar *et al.*, 2014). The fact that this clustering is exclusively observed in the presence of TGFβ3 is likely due to the known proliferative and chemotactic properties of this growth factor (Watabe and Miyazono, 2009; Baek, Kang and Ra, 2011). An alternative possibility is that cell-cell interaction is preferred over cell-substrate interaction (Lauffenburger and Griffith, 2001) in the presence of TGFβ3 on the aligned fibres.

As expected, TGFβ3-stimulated cells expressed *SOX9*, a transcription factor essential for chondrocyte differentiation and cartilage formation (Bi *et al.*, 1999), and activation of chondrocyte-specific extracellular matrix genes: collagen II (*COL2A1*) and *ACAN*, all suggestive of robust chondrogenic differentiation. Notably, *BMP2* and collagen I expression was upregulated in cells on randomly-aligned fibres, suggesting progression along the endochondral pathway. This finding is in agreement with other studies that have reported osteogenesis on randomly-aligned fibres in the absence of osteogenic media (Yin *et al.*, 2015).

It should be noted, however, that alkaline phosphatase (*ALPL*) gene expression was undetectable for all groups and no alizarin red positive staining was present after 20 days of culture (data not shown), suggesting only early progression along the endochondral pathway. These observations, combined with studies showing chondrogenesis and subsequent ossification on randomly-aligned fibres (Yin *et al.*, 2015), provide further evidence that differentiation of MSCs stimulated with TGFβ3 is dependent on substrate alignment.

Temporal co-stimulation of CTGF and TGFβ3 induced MSC differentiation into cells expressing high levels of both types I and II collagen and aggrecan. Sequential supplementation of CTGF and TGFβ3 has been shown to induce fibrochondrocytic differentiation of human MSCs (C. H. Lee *et al.*, 2014). Consistently in the electrospun microfibrillar scaffolds presented here, MSCs treated with sequential growth factor supplementation deposited fibrocartilaginous-like tissues that stained positive for picrosirius red (collagen) and Alcian blue (sGAGs). On aligned scaffolds, this temporal co-stimulation was found to promote at least comparable levels of sGAG synthesis and higher levels of collagen synthesis compared to stimulation with either growth factor alone. Both CTGF and TGFβ3 have been shown to induce proliferation and ECM synthesis (Frazier *et al.*, 1996; Murray *et al.*, 2003). In the ACL to bone junction, the fibrocartilage interfacial region subdivides into mineralized and non-mineralized fibrocartilage. The mineralized tissue shows expression of collagen X, as well as type II and aggrecan, while the un-mineralized tissue shows expression types I and II collagen and aggrecan (Visconti *et al.*, 1996; Galatz *et al.*, 2007). Collagen X is expressed at sites of endochondral ossification and in areas of transition from mineralized to soft tissue (Fujioka *et al.*, 1997). Cells stimulated with CTGF followed by TGFβ3 on the aligned scaffold showed upregulation of *COL1A1*, *COL2A1*, *ACAN* compared to day 0, and an increased level of *COL10A1* gene expression compared to the reverse (TGFβ3 → CTGF) and the rest of the groups. Cells stimulated with TGFβ3 followed by CTGF showed a downregulation of *COL10A1* while upregulating *COL1A1*, *COL2A1* and *ACAN*. These observations suggest that

CTGF and TGFβ3 sequential stimuli to cells on microfibrillar topography can further modulate MSC differentiation. The findings are summarized graphically in Figure 3.13.

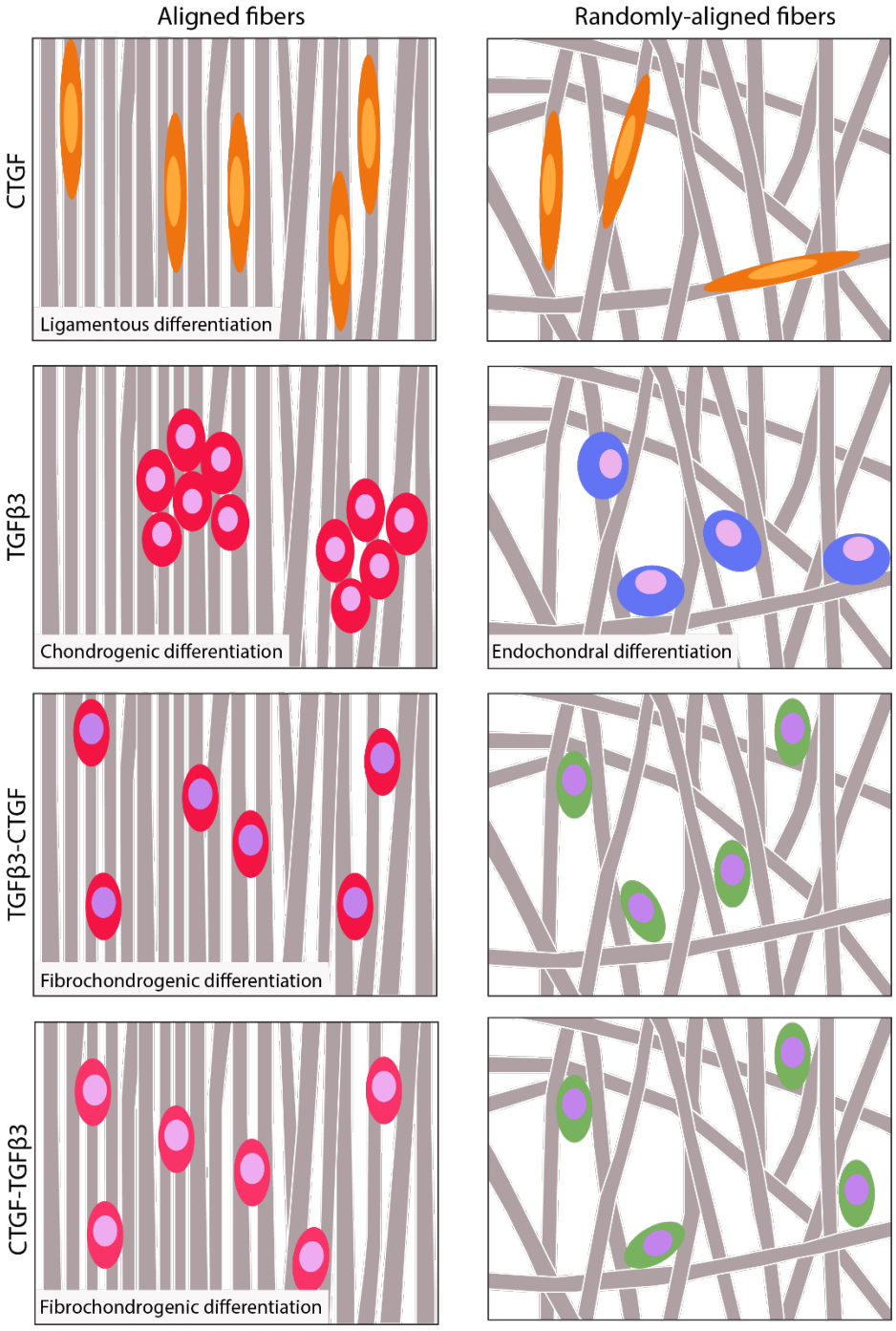

Figure 3.13 Graphical summary of the findings. Scaffold alignment and growth factor supplementation.

It has been a common practice to use mRNA concentrations as proxies for the concentrations of the corresponding proteins, thereby assuming that transcript abundances are the main determinant of protein abundances (Vogel and Marcotte, 2012). However, cellular concentrations of proteins do not strongly correlate with the abundance of their corresponding mRNAs (de Godoy *et al.*, 2008). Often their squared Pearson correlation coefficient is ~0.40; which suggests that ~40% of the variation in protein concentration can be explained by knowing mRNA abundances (Vogel and Marcotte, 2012). The remaining ~60% of the variation in protein concentration that cannot be explained by measuring mRNAs alone, could be explained by regulatory processes occurring after mRNA is made, such as post-transcriptional, translational and degradative regulation, acting through miRNAs or other mechanisms (Vogel and Marcotte, 2012). In the case where genes for which no mRNA but protein is observed could be due to that mRNA may exist at only very low levels or is rapidly degraded. In the opposite case, where mRNA is observed but protein is not could be due to protein production or degradation rates. Yet, even if the expression level of an mRNA only explains a fraction of variation in protein abundance, it has been shown that the abundance of an mRNA is often an excellent proxy for the presence of a protein (Ramakrishnan *et al.*, 2009). In the context of this chapter, twelve genes were analysed; from which protein was confirmed for the collagen types I, II and III using immunohistochemistry. Collagen type X gene expression was shown in some culture conditions, but it was not localized using immunohistochemistry. The remaining proteins could also be identifiable using immunohistochemistry and Western Blot.

Aligned scaffolds were then cultured using a dual-chamber to create a ligament primed region adjacent to a chondrogenic primed region. The dual-chamber allowed to separate the culture media to compartmentalize MSC differentiation; however, an undesirable middle section was formed caused by the divisor. Hence another method to scale this approach is needed.

The long-term goal is to use these engineered soft tissue templates to regenerate the bone-ligament interface, whereby an electrospun scaffold spatially patterned with growth factors will be used to support either cartilage and ligament tissue formation along the length of the implant. Following implantation into a bony tunnel to support ligament regeneration, it is envisioned that the cartilaginous region of the implant will in part undergo endochondral ossification (Scotti *et al.*, 2010, 2013; Harris *et al.*, 2017). To provide support for this concept, further studies are required to demonstrate that chondrogenically primed MSCs on these electrospun scaffolds will support endochondral bone formation *in vivo*. MSCs stimulated with TGFβ have been shown to support endochondral bone formation (Farrell *et al.*, 2011; Scotti *et al.*, 2013), and it is possible that this strategy can be further improved using co-stimulation with osteogenic factors such as *BMP2* (Yu *et al.*, 2010; Thompson *et al.*, 2015). Furthermore, additional investigation using more geometrically relevant scaffolds is warranted as this study was limited to the use of relatively thin electrospun sheets.

3.5 Conclusions

The coupled effects of microfibrillar-scaffold alignment and growth factor stimulation on MSC differentiation were investigated. Aligned microfibrillar scaffolds supported either ligamentogenesis, chondrogenesis or fibrochondrogenesis of MSCs acting when appropriately stimulated with CTGF and/or TGFβ3. Thus, these results have broad implications for regenerating other musculoskeletal interfaces such as articular cartilage-bone, tendon-bone, and meniscus-bone. This study opens the possibility of using aligned microfibrillar scaffolds that are spatially functionalized with specific growth factors to direct MSC differentiation for engineering the bone-ligament interface. Future work will investigate the spatial incorporation of the growth factors along the length of the scaffold to compartmentalize MSC differentiation.

Chapter 4 Electrospinning of human scale microfibrillar scaffolds for ligament tissue engineering

4.1 Introduction

Scaffolds produced by electrospinning of biodegradable fibres are particularly attractive for tissue engineering (TE) strategies as they provide high surface area and tailorable fibre diameter and alignment (Yang *et al.*, 2005; Pham, Sharma and Mikos, 2006a; Li *et al.*, 2007). However, developing porous electrospun scaffolds mimicking the size, stiffness and strength of human tissues remains a challenge, limiting their use for the TE of high load bearing tissues such as ligament and tendon. A well-documented limitation of electrospun fibre-scaffolds is limited cell infiltration to the body of the implant (Baker *et al.*, 2008; Simonet *et al.*, 2014). Large in-plane pores that facilitate cell migration through the body of the scaffold are reduced by the layer-by-layer deposition of densely packed fibres during electrospinning. The overall porosity of implants produced using sheets of electrospun fibres can be further reduced when they are tightly rolled (Pauly *et al.*, 2017), stacked (multi-layered scaffolds) (Nerurkar *et al.*, 2009; Chainani *et al.*, 2013; Fisher *et al.*, 2015), or braided (Rothrauff *et al.*, 2017) to form 3D scaffolds. Thus, cellular infiltration into these dense structures is slow, often taking between 6 and 10 weeks, with extracellular matrix (ECM) deposition restricted to the outer periphery *in vitro* (Baker and Mauck, 2007) and *in vivo* (Telemeco *et al.*, 2005).

Strategies to enhance cell infiltration and the diffusion of nutrients and waste products include the use of bioreactors (Lowery, Datta and Rutledge, 2010) or electrospraying cells during scaffold fabrication (Stankus *et al.*, 2006). Other strategies have aimed to enhance cell infiltration by increasing the scaffold pore size. Pore size (or interfibrillar space) is determined and constrained by the selected fibre diameter and the packing density (Eichhorn and Sampson, 2005; Simonet *et al.*, 2014). Larger pore sizes are obtained with larger fibre diameters and low packing density (Soliman *et al.*, 2011). Strategies include the use of micron-

size fibres in favour of nanofibers (Pham, Sharma and Mikos, 2006b), cutting holes into the implant (Sundararaghavan, Metter and Burdick, 2010; Lee *et al.*, 2012), or introducing a sacrificial component, such as soluble fibres (Baker *et al.*, 2008, 2012) and porogens (Kim, Chung and Park, 2008). Methods such as the use of sacrificial components or cutting holes alter the fibre morphology, lead to heterogenous fibre distributions in the scaffold, macroscopic delamination and deformation of the scaffold, while the pore size is still linked to the fibre diameter.

Realizing these limitations, others have decoupled the pore size from fibre diameter. Low-temperature electrospinning (LTE; below -30 °C) increases the interfibre distance by embedding ice particles as void spacers during fibre deposition (Simonet *et al.*, 2007; Kim *et al.*, 2014). The electrospinning conditions used in LTE also enhance the evaporation of the solvent (Kim *et al.*, 2014). When interfibre fusions fail to form during electro-spinning, larger voids/pores are formed in the scaffold (Kim *et al.*, 2014). Although this approach was found to enhance cell infiltration, cells compact LTE scaffolds to almost half its size after only 7 days in culture (Simonet *et al.*, 2014). Others report concavities on the surface of the fibres formed due to contact with water droplets at the time of electrospinning (Kim *et al.*, 2014). Another way to increase pore size independently of fibre diameter is the focused, low density, uncompressed nanofiber (FLUF) method. A disadvantage of FLUF is that its specific target limits the method to produce cotton ball shaped scaffolds. Other researchers have substituted the metal collector for a liquid medium to deposit electrospun fibres and then draw them to a rotating mandrel. In this way, controlled woven scaffolds composed of aligned fibres can be obtained and the thickness of these scaffolds can be controlled by varying the electrospinning time (Shang *et al.*, 2010).

The objective of this chapter was to develop a porous microfibrillar scaffold for ligament tissue engineering with comparable size to the human anterior cruciate ligament (ACL). Poly(ε-

caprolactone) (PCL), a degradable polymer with FDA approval for certain biomedical and drug-delivery devices (Woodruff and Hutmacher, 2010), was used to produce electrospun scaffolds. PCL-based scaffolds have several favourable features, such as a hydrophobic surface for protein adsorption, functional groups upon simple chemical modifications, etc. During electrospinning of polymers such as PCL, there is a fraction of fibres that fuse with juxtaposed fibres (Garg and Bowlin, 2011). These welds along the length of the fibres attach fibres to one another and restrain their movement, thereby forming a membrane-like fibre-sheet. In this study, it was demonstrated that increasing the fraction of unfused fibres (i.e. less welds in juxtaposed fibres) during electrospinning reduced the flexural rigidity of the resultant electrospun sheets, which in turn allowed the bundling of fibres into 3D scaffolds without the need for stacking or rolling. Furthermore, these unfused fibres allowed for higher interfibrillar spacing, which facilitated the rapid migration of mesenchymal stem cells (MSCs) into the body of the scaffolds. This strategy was achieved without compromising fibre diameter, alignment or mechanical integrity of the scaffolds.

4.2 Materials and Methods

4.2.1 Electrospinning

PCL (M_W 80 kDa, Sigma – Aldrich) was dissolved at 25% w/v in chloroform. The polymer solution was loaded in a 20-ml syringe and extruded using a syringe pump through a 20G blunt-end needle charged to 10 kV. Continuous polymeric fibres were collected at a flow rate of 5 ml/h on a grounded mandrel positioned 15 cm apart from its centre to the tip of the needle. Fibres were collected at 100 RPM (linear velocity: 0.525 m/s), 500 RPM (2.625 m/s), 1000 RPM (5.250 m/s), 1500 RPM (7.875 m/s), 2000 RPM (10.500 m/s), 2500 RPM (13.125 m/s), 3000 RPM (15.750 m/s), and 3500 RPM (18.375 m/s). At each of these velocities fibres were collected for 5 min, 10 min, 20 min, 1 h and 2 h. Fibres collected at 100 to 1500 RPMs

were rolled to form 'bundles' along the long axis of the fibres (for all electrospinning durations) (Figure 4.1 a). fibres collected at 2000 to 3500 RPM were wrapped/baled to form 'bundles' along the long axis of the fibres (for all electrospinning durations) (Figure 4.1 b). Bundles collected for 5 min were used for mechanical testing. Bundles collected for 10 mins were used to visualize cell morphology and for differentiation of MSC studies. Bundles collected for 20 mins were used to calculate porosity. Bundles collected for 1 h were used for cell infiltration. Bundles collected for 2 h were used to obtain ACL dimensions. Discs (8 mm Ø) were punched from 1 h electrospun sheets and used for scanning electron microscopy (SEM). Bundles used for cell culture were tied at each end using suture thread (VICRYL 3-0).

We measured the air flow at the collector using an anemometer (Proster TL017, range 0-30 m/s, accuracy ± 5%) at each of these collector velocities. We placed the anemometer 1.3 cm apart from the rotating collector in the side facing the spinneret. Three independent measurements were taken at each velocity ~30 s after the target velocity was reached.

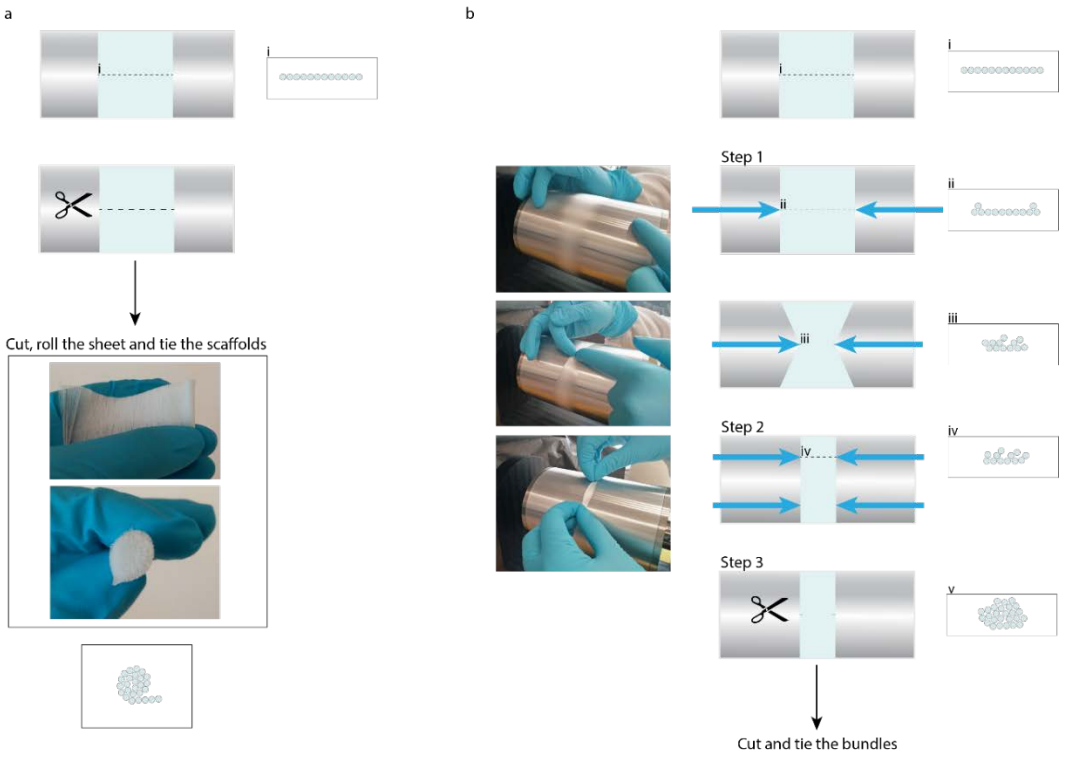

Figure 4.1 Bundling of fibres sheets collected at low and high speeds. **a,** Fibres collected at 100 – 1500 RPMs were cut transversely and dismounted from the collector in the shape of a rectangular sheet. Scaffolds were made by cutting the sheet transversely (4 cm long X width of the sheet), rolled and tied at edges using suture thread. **b,** Fibres collected at 2000 – 3500 RPMs were baled by pushing the edges towards each other at one point and around the perimeter of the collector. The resulting fibre bundle was cut transversely and dismounted from the collector with a cylindrical CSA shape. Scaffolds were made by cutting the bundle transversely (4 cm long).

4.2.2 Alignment and diameter of microfibers

Discs (8 mm in diameter, ~300 µm thick, collected for 1 h) were imaged using SEM (Zeiss Ultra FE-SEM) to measure fibre diameter and alignment. Samples were sputter coated with a mixture of gold/palladium (60:40) to a thickness of ~10 nm (Cressington 108) and imaged at an accelerating voltage of 5 kV. The average fibre diameters were determined from SEM micrographs, measuring a minimum of 50 fibres (n=3 scaffolds, n=2 images per scaffold) using ImageJ (National Institutes of Health). The principal axis of fibre orientation was computed using OrientationJ plugin of ImageJ using Fourier components and fitted to a Gaussian distribution (n=3 scaffolds, n=2 images per scaffold) as previously reported (Olvera *et al.*, 2017). Data are presented as the distribution of fibre orientations ranging from -90° to 90°.

4.2.3 Indirect measurements of fibre welding in electrospun-sheets

At lower rotational speeds, fibres within electrospun sheets were found to weld to each other. To indirectly characterize this, fibre-sheets (initially ~5 cm wide) were stretched laterally manually (perpendicular to the fibre direction) to bridge 10 cm. Stereo images were acquired at the two stages: before and after the stretch. Additionally, uniaxial tensile tests were performed to quantify the force (perpendicular to the fibre direction) required to pull fibres apart. Fibre-sheets for all RPMs collected for 1 h (n = 3) were stretched at a rate of 2 mm/min until failure using a Zwick Z2.5 single column testing instrument equipped with a 5 N load cell. A 2.5 kN load-cell was used to test the electrospun-sheets collected at 100 RPMs.

4.2.4 Isolation and expansion of bone marrow derived MSCs

Bone marrow derived MSCs were isolated from the femoral shafts of a 3 month-old pig and expanded as previously described (Thorpe *et al.*, 2012). Tripotentiality was confirmed prior to use. MSCs were expanded in high-glucose Dulbecco's modified Eagle's medium (DMEM) GlutaMAX supplemented with 10 % fetal bovine serum (FBS), penicillin (100 U/ml)-streptomycin (100 µg/ml) (all Gibco, Biosciences) and 0.25 µg/ml amphotericin B (Sigma-Aldrich) in a humidified atmosphere at 37 °C, 5% CO_2. At the end of passage 2, cells were trypsinized and seeded onto the electrospun scaffolds. All cell studies were performed with cells at passage 2.

4.2.5 Cell viability and visualization of cell morphology

Scaffolds were sterilized using ethylene oxide (EtO; Anprolene, Anderson products). Sterile scaffolds were hydrated and conditioned by incubating them in expansion media overnight at 37 °C before cell seeding. Expansion media consisted of DMEM high glucose (DMEM

glutaMAX), 10% FBS, penicillin (100 U/ml)-streptomycin (100 µg/ml) (all from Gibco), and 0.25 µg/ml amphotericin B (Sigma). Scaffolds (collected for 10 min) were seeded at a cell density of 500,000 cells per scaffold (in 30 µl aliquot) and were cultured individually in Teflon rectangular wells (2 ml/well). Scaffolds were maintained in expansion media at 20 % O_2 with medium exchanged twice weekly. At days 0 and 10, cell viability was assessed by staining cells using the LIVE/DEAD assay kit (Invitrogen, Bioscience). Briefly, scaffolds were rinsed with PBS and incubated in 2 µM calcein AM and 4 µM ethidium homodimer-1 (EthD) in phenol red-free DMEM for 1 h at 37 °C. Scaffolds were rinsed in PBS and visualized under a scanning confocal microscope (Leica SP8) at an excitation/emission wavelengths of 495/515 nm for calcein and 495/635 nm for EthD.

Cell morphology was assessed by staining cell nuclei with DAPI and filamentous actin with rhodamine phalloidin (Invitrogen). Scaffolds were fixed in 4% paraformaldehyde (PFA) overnight at 4 °C, rinsed with phosphate buffered saline (PBS) and permeabilized in 0.5% Triton-X 100, incubated in 1.5% bovine serum albumin (BSA) to block non-specific labelling and stained with a 1.5% BSA solution containing rhodamine phalloidin (1:40) for 1 h at room temperature (RT). Cell nuclei were stained with DAPI (1:100) for 10 min at RT (all from Sigma). Scaffolds were rinsed with PBS and visualized under a scanning confocal microscope (Leica SP8) at an excitation/emission of 540/565 nm for rhodamine phalloidin and 358/461 nm for DAPI. Analysis was performed in Leica Application Suite X (LAS X) software.

4.2.6 Mechanical testing

Fibre bundles (40 mm in length, collected for 5 min) were formed from the electrospun bundle with the long axis parallel to the fibre alignment. The ends of the bundles (10 mm) were protected with lab-tape to prevent slippage without damaging the fibres. Specimens were mounted in between custom-made serrated grips with a gauge length of ~20 mm. The test

was carried in a Zwick twin column testing instrument equipped with a 100 N load cell. Samples were subjected to uniaxial tensile testing parallel to the direction of fibre alignment at a constant rate of 5 mm/min (n=4). Cross-sectional area (CSA) of the testing specimens was calculated using 3 methods: (1) measurement of the width of the apparent CSA of the scaffolds from brightfield images (including the pore contribution to the sample thickness) of the specimens before testing; (2) measurement of the width of the squeezed CSA of the scaffolds from brightfield images (minimizing the pore contribution to the sample thickness to obtain true material CSA) of specimens prepared at the same time but that were not tested (squeezing the CSA might compromise the specimen for tensile testing); (3) theoretical CSA (=0.576 mm^2) defined by the mass of PCL proportional to the electrospinning time, flow rate and perimeter of the mandrel. Calculations of the CSA were performed assuming a circular cross-sectional area. When measuring the scaffold thickness from brightfield images, n=3 independent scaffolds were measured; n=3 sections of the scaffolds were imaged; and n=3 measurements were taken in each image for a total of 27 measurements per RPM. Stress was calculated as the ratio of the load measured (N) to the CSA. Young's modulus was calculated from the stress-strain curve in the elastic region. Yield stress and strain values were determined from the intersection of a 0.2% offset line (Pauly *et al.*, 2016).

4.2.7 Differential scanning calorimetry (DSC) analysis

Polymer crystallinity was determined by measuring the enthalpy of bulk PCL and electrospun PCL using DSC performed on a DSC 4000 apparatus (Perkin Elmer). Samples weighing ~1 mg were used. Samples were heated from -90 °C to 100 °C at a rate of 10 °C/min under nitrogen atmosphere (20 ml/min) and held for 2 min before cooling at 10 °C/min. A second heating scan was performed at 10 °C/min to characterize all the groups with the exact same thermal history. The melting enthalpies were obtained in the first and second heating scans. The

degree of crystallinity (X*c*) of each sample was calculated by dividing the endothermic area under the melting peaks of the first scan by the melting enthalpy of theoretical 100% crystalline PCL:

$$X_c = \frac{\Delta H_f}{\Delta H_f^0}$$

Where ΔH_f is the experimental melting enthalpy from DSC thermographs and ΔH_f^0 is the melting enthalpy value for 100% crystalline PCL (=139.5 J/g) (Wang *et al.*, 2013).

4.2.8 Microcomputed tomography (µCT) scans for 3D geometry

The 3D geometry of the electrospun-fibre scaffolds was analysed using µCT. Scans were performed using a Scanco Medical 40 µCT system (Scanco Medical) at a voltage of 70 kVp, and a current of 114 µA. A Gaussian filter (sigma = 1.2, support = 2) was used to suppress noise and a voxel resolution of 8 µm was used throughout. Resultant DICOM files were imported into ScanIP (Simpleware Ltd.). 2D slices were segmented by an operator-selected threshold with values of -800 for the Lower value and 240 for the Upper value. Scaffold volume and porosity were determined from cylindrical sections isolated from the middle region of the reconstructed 3D structures. The isolated sections had a thickness of 0.258 mm for both the 100 and 3500 RPM groups. Porosity was calculated as follows:

$$\varphi = 1 - \left(\frac{V_{sample}}{V_{solid}}\right) x100$$

where V_{sample} is the effective volume of the sample section analysed whereas V_{solid} is the volume of the same cylinder assuming a solid material.

4.2.9 Density of the fibre bundles, porosity and pore size

Density. To find how densely packed the fibres are within a scaffold, the density of the scaffolds was calculated as the mass of the scaffold divided by its volume. We determined the mass by weighing the scaffolds. The volume of the scaffolds was calculated by measuring the width of the squeezed CSA of the scaffolds from brightfield images (minimizing the pore contribution to the sample thickness) assuming the bundle was a solid straight rod.

Porosity. Porosity of dry scaffolds was calculated by gravimetry (Pham, Sharma and Mikos, 2006b) according to the equation:

$$\varphi = 1 - \frac{\rho_{scaffold}}{\rho_{PCL}}$$

The density of the scaffold ($\rho_{scaffold}$) was determined by measuring its mass and volume. The volume of the scaffold was calculated using the CSA from brightfield images assuming a solid rod (n=3 scaffolds, ≥25 measurements of the CSA). ρ_{PCL} is the density of PCL (1.145 g/cm^3).

Porosity of wet scaffolds was calculated by using the liquid intrusion method (Soliman *et al.*, 2011) according to the equation:

$$\varphi = \frac{V_{ethanol}}{V_{ethanol} + V_{PCL}}$$

Dry scaffolds were weighed and immersed in ethanol overnight on a shaker. Scaffolds were removed from the ethanol, blot dried and weighed to determine the mass of intruded ethanol. $V_{ethanol}$ is the volume of ethanol calculated as the difference of wet and dry mass of the scaffolds divided by the ethanol density (0.789 g/ml). V_{PCL} was calculated as the dry scaffold mass divided by the density of PCL (1.145 g/cm^3). Measurements were made on n=3 samples of each scaffold type.

Pore size. The pore sizes of the 100 RPM randomly-aligned meshes were estimated from SEM images (Rnjak-Kovacina *et al.*, 2011) using Particle Analysis plugin for ImageJ (n=3 scaffolds, n=3 images, 473 regions of interest (ROI)).

4.2.10 Validating cell infiltration potential

Bundles (1 h, 20 mm in length) were sterilized and conditioned for cell culture as described in section 4.2.5. Bundles were cultured individually in Teflon wells (2 ml/well). Each scaffold was seeded with 1 X 10^6 cells re-suspended in 500 µl of medium and cultured in expansion medium for 3 days. Scaffolds were maintained at 20% O_2. To assess cell infiltration, cell distribution was investigated after 10 days of culture. Scaffolds were fixed in 4% PFA overnight at 4 °C. Fixed scaffolds were rinsed with PBS and embedded in optimal cutting temperature (O.C.T.) compound (VWR Chemicals). Scaffolds were flash frozen with liquid nitrogen and sectioned to 5 µm thick slices using a cryotome. Sections were stained with Hematoxylin and Eosin (Sigma), dehydrated in grades of ethanol and mounted.

4.2.11 Culture conditions for MSC differentiation

For MSC differentiation, bundles (collected for 10 min at 3500 RPMs) were seeded at a cell density of 500,000 cells per scaffold (in 30 µl) and cultured in ligament induction medium, chondrogenic medium, or expansion medium at 20% O_2 for 10 days. Ligament induction medium consisted of high-glucose DMEM GlutaMAX supplemented with 2% FBS, penicillin (100 U/ml)-streptomycin (100 µg/ml), 0.25 µg/ml amphotericin B, 50 µg/ml L-ascorbic acid 2-phosphate and 100 ng/ml recombinant human connective tissue growth factor (CTGF; ProSpec-Tany, TechnoGene Ltd.). Chondrogenic medium consisted of high-glucose DMEM GlutaMAX, penicillin (100 U/ml)-streptomycin (100 µg/ml), 100 µg/ml sodium pyruvate, 40 µg/ml L-proline, 4.7 µg/ml linoleic acid, 50 µg/ml L-ascorbic acid 2-phosphate, 1.5 mg/ml bovine serum albumin (BSA), 1X insulin-transferrin-selenium, 100 nM dexamethasone, 0.25

µg/ml amphotericin B, and 10 ng/ml recombinant human transforming growth factor-β3 (TGF-β3; ProSpec-Tany, TechnoGene Ltd.). Bundles were cultured individually in Teflon rectangular wells (2 ml/well). Medium was changed twice weekly and cultures were maintained at 20% O_2.

4.2.12 Gene expression

Gene expression was assed at day 10 using quantitative real-time PCR (n=5/group/time point). Cells were lysed using RLT lysis buffer (Qiagen) supplemented with 10 µl/ml β-mercaptoethanol (Sigma-Aldrich) and stored at –80°C. For RNA isolation, cell lysates were thawed and homogenized using QIAshredder columns (Qiagen). Total RNA was isolated and further purified using RNeasy Mini kits (Qiagen) following manufacturer's instructions. Total RNA concentration and purity was determined using a Nanodrop spectrophotometer. 500 ng of each RNA sample were reverse transcribed into cDNA using High-Capacity cDNA Reverse Transcription Kit (Applied Biosystems) following manufacturer's instructions. 25 ng of cDNA per well were amplified using an ABI 7500 sequence detection system (Applied Biosystems) and SyberGreen select master mix (Applied Biosystems). Expression of collagen type I (*COL1A1*), II (*COL2A1*), X (*COL10A1*), tenomodulin (*TNMD*), SRY-Box 9 (*SOX9*), and glyceraldehyde-3-phosphate dehydrogenase (*GAPDH*) was evaluated. The porcine specific primer sequences (KiCqStart SYBR Green Primers, Sigma) used for amplification are listed in Table 4.1. CT values were analysed using the comparative 2^(- ΔΔCT) method with *GAPDH* as the internal control. Relative expression of the genes is presented as fold change relative to the same population of cells harvested at day 0 that were not seeded on scaffolds (except for *COL2A1*). *COL2A1* gene expression was undetected in the cells harvested at day 0, hence *COL2A1* was normalized to the expression of MSCs on scaffolds cultured in growth media.

Gene		Primer sequences
GAPDH	Forward:	TTTAACTCTGGCAAAGTGG
	Reverse:	GAACATGTAGACCATGTAGTG
COL1A1	Forward:	TAGACATGTTCAGCTTTGTG
	Reverse:	GTGGGATGTCTTCTTCTTG
COL2A1	Forward:	CGACGACATAATCTGTGAAG
	Reverse:	TCCTTTGGGTCCTACAATATC
COL10A1	Forward:	GTAGGTGTTTGGTATTGCTC
	Reverse:	GAGCAATACCAAACACCTAC
TNMD	Forward:	GCTAATTGTCCTATTTTGGGG
	Reverse:	GAAAGTGTGTTCCATGTCG
SOX9	Forward:	CAGACCTTGAGGAGACTTAG
	Reverse:	GTTCGAGTTGCCTTTAGTG

Table 4.1 Primer sequences used for qPCR

4.2.13 Statistical analysis

Results are presented as mean ± standard deviation or mean ± standard error of the mean (SEM) for qRT-PCR. Statistical analysis was performed with Prism 6 Graphpad Software. Experimental groups were analysed for significant differences using a general lineal model for analysis of variance (ANOVA) or t-tests where appropriate. Tukey's test for multiple comparisons was used to compare conditions. Significance was accepted at a level of $P < 0.05$. Sample size is indicated within corresponding method section and figure legends. Correlation coefficient between fibre diameter and load was calculated using a Pearson correlation.

4.3 Results

4.3.1 Fabricating bundles of aligned PCL fibres using high speed electrospinning

Sheets of electrospun PCL fibres with altered diameter and alignment were produced by increasing the rotational velocity of the collecting mandrel from 100 RPM (0.525 m/s) to 3500 RPM (18.375 m/s). 3500 RPM (18.375 m/s) was the limit of the system. Sheets of randomly-oriented fibres were produced at 100 RPM (Figure 4.2 a, c), while fibres became aligned at rotational velocities exceeding 500 RPM (2.625 m/s) (Figure 4.2 b, c). Fibre diameter decreased with increasing rotational speed (Figure 4.2 f). Fibres collected at 3500 RPM (∅ 4.48 ± 0.23 µm) were ~4 times smaller than fibres collected at 100 RPM (∅ 15.89 ± 1.45 µm) ($p < 0.0001$). Increasing the mandrel rotational velocity generated an increased airflow from the collector towards the spinneret (Table 4.2).

A lower fraction of welded/fused fibres was also obtained by increasing the rotational velocity of the collecting mandrel. At 100 RPM, there was clear evidence of fibre welding/fusing (Figure 4.2 d). This was also observed at 500, 1000 and 1500 RPMs. Sheets of electrospun fibres produced at these lower rotational velocities were relatively rigid upon removal from the collecting mandrel (Figure 4.2 i), maintaining a sheet-like shape upon hydration. In contrast, limited evidence of fibre welding was observed for rotational speeds exceeding 2000 RPM (10.472 m/s) (Figure 4.2 e). Sheets produced at these higher speeds were soft upon removal from the collecting mandrel, and could be easily manipulated to form cylindrical bundles of fibres upon hydration, while the rigid fibre-sheets (100, 500, 1000 and 1500 RPM) had to be rolled to form cylindrical scaffolds (Figure 4.2 j).

As an indirect measure of fibre fusion, the fibre-sheets were stretched perpendicular to the fibre axis. Fibres collected at low RPMs (100 – 1500 RPM) kept together upon stretch displaying fused bands of multiple fibres (Figure 4.2 g). When stretched perpendicular to the fibre axis, single fibres separated from one another. A uniaxial tensile test perpendicular to

the fibre axis was conducted to characterize this phenomenon. Fibre sheets collected at low RPMs showed a higher stiffness at low strains (Figure 4.4). With higher collection velocities, the stiffness of the fibre-sheets progressively decreased. The 3500 RPM bundle tested in this direction elongated by 4000 before total separation of the fibres.

MSCs seeded onto the fibre bundles/rolls remained viable (Figure 4.3 a) and conformed to the alignment of the underlying fibres (Figure 4.3 b).

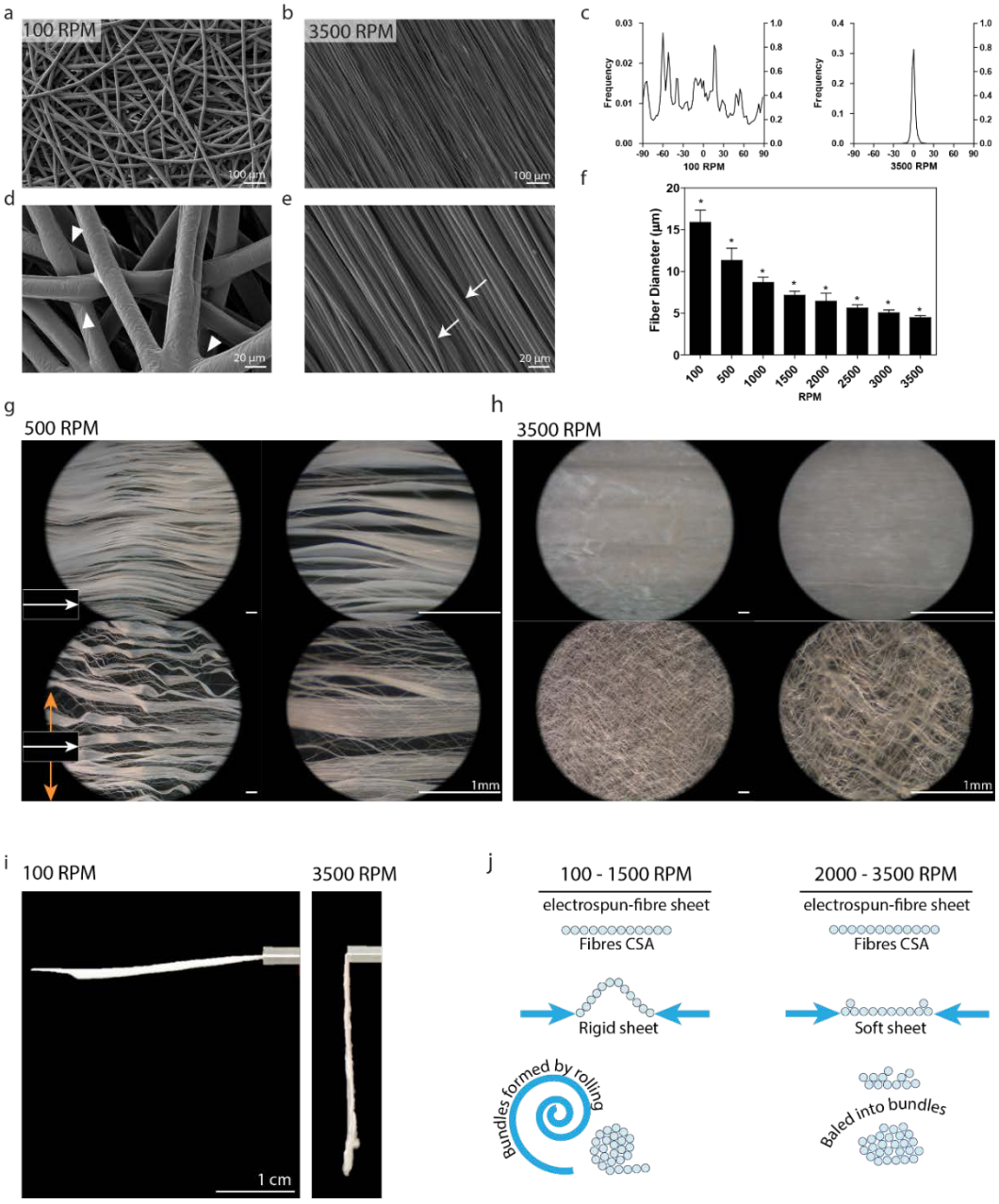

Figure 4.2 Characterization of the microfibers and MSC-microfibers interaction. **a, b**, SEM micrographs of electrospun fibres collected at 100 and 3500 RPM (100 RPM, randomly-oriented fibres; 500 – 3500 RPM, aligned fibres). Scale bars, 100 µm. **c**, Alignment of fibres collected at 100 and 3500 RPM; plots show alignment angle (x-axis) and frequency (y-axis; arbitrary units). **d**, Arrow heads point to welding/junctions of juxtaposed fused fibres in 100 RPM fibre sheet. Scale bar, 20 µm. **e**, Arrows point to single, unfused fibres from 3500 RPM group. Scale bar, 20 µm. **f**, Fibre diameter obtained at each RPM. Plot shows mean ± s.d., *: $P < 0.01$, significantly different to any other RPM; one-way ANOVA with Tukey's multiple comparisons test. **g, h**, Stereo images of aligned fibres at the lowest and highest collection velocities (500 RPM and 3500 RPM). Top row shows as-spun fibres, bottom row shows the same fibres stretched transversely. Scale bars, 1 mm. **i**, Flexural rigidity of electrospun sheets. As-spun electrospun sheets were cut into 1 X 2 cm width X length. Sheets were held between two glass slides and clamped parallel to the fibre axis. The sheet collected at 100 RPM shows its rigidity by maintaining a horizontal line while the 3500 RPM group show to be more flexible. **j**, Fibre-sheets collected at 100 –

1500 RPM were rolled to form bundles; those collected at 2000 – 3500 RPM were disrupted and baled into bundles.

RPM	Linear velocity (m/s)	Airflow at the collector (m/s)*
100	0.525	Not measurable
500	2.625	Not measurable
1000	5.250	Not measurable
1500	7.875	0.9
2000	10.500	1.3
2500	13.125	1.6
3000	15.750	1.9
3500	18.375	2.1

Table 4.2 Airflow generated at each RPM. *Measurement device has an accuracy of ± 5%. *n* = 3 independent measurements at each RPM.

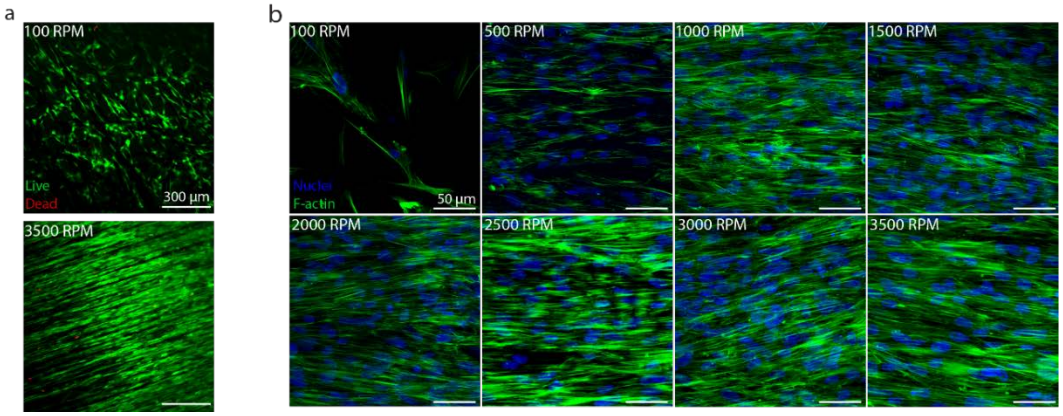

Figure 4.3 MSC viability and cell morphology. **a,** Live/dead staining (green: 'live', red: 'dead') at day 10. Scale bars, 300 µm. **b**, F-actin stained at day 10 (blue: nuclei, green: F-actin cytoskeleton). Scale bars, 50 µm.

a

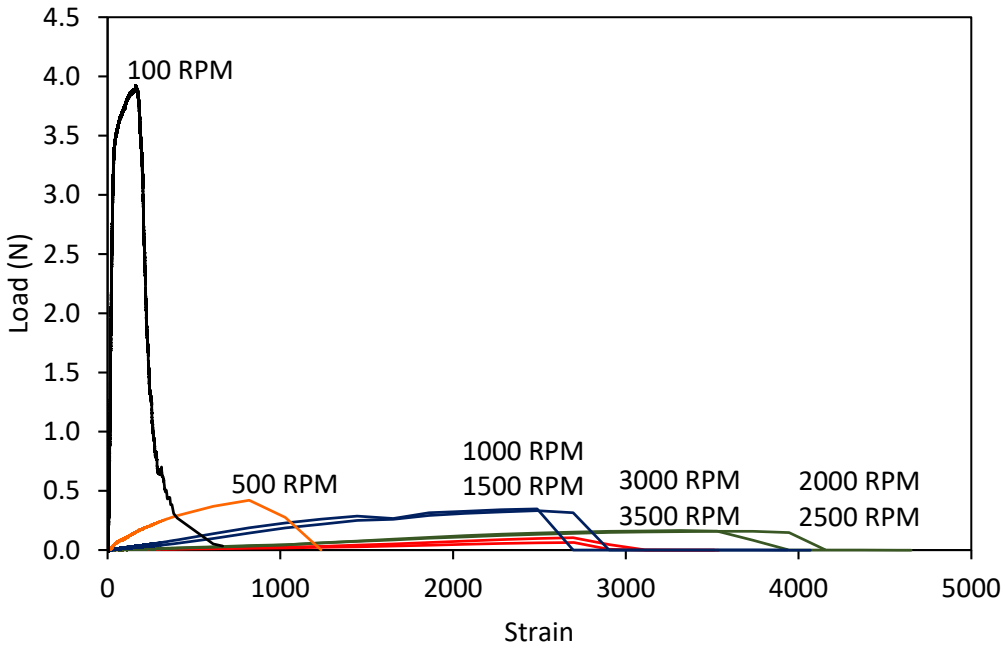

b

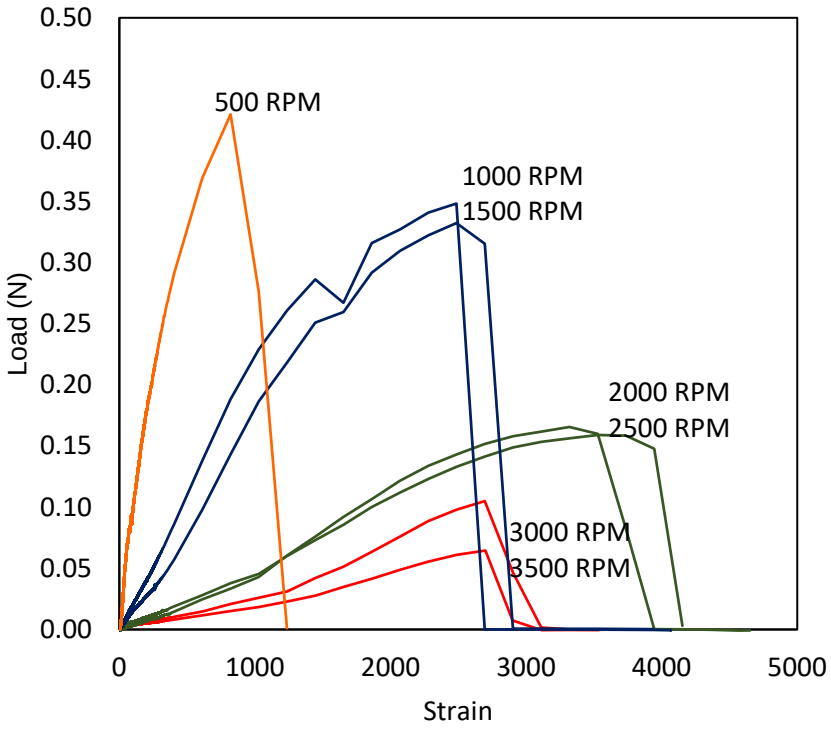

Figure 4.4 Load - strain curves of fibre-sheets when loaded perpendicular to the fibre axis. **a**, Comparison of the load- strain curves of 100 – 3500 RPM groups. **b**, Shows with detail the load-strain curves of the aligned fibre groups from 500 – 3500 RPM.

4.3.2 The mechanical properties of electrospun fibre bundles are strongly dependent on the rotational velocity of the collector

The mechanical properties of electrospun fibre bundles (parallel to the fibre direction) were strongly dependent on the rotational velocity of the collector. The increased collection velocity and the concomitant decrease in fibre diameter conferred different mechanical properties to the scaffolds (Figure 4.5 A). The mechanical properties of the scaffolds were calculated based on the apparent cross-sectional area (CSA) of the specimens before the tensile tests (Figure 4.5 B). Scaffolds produced at higher RPMs failed at higher loads (Figure 4.6). Figure 4.6 shows the stress-strain behaviour of the PCL bundles. The region after the yield point characterizes the permanent deformation of the PCL fibres where the stress continued to increase on the account of strain-hardening. The Young's modulus, yield stress and yield strain were all found to increase with increases in the rotational velocity of the collecting mandrel (Figure 4.5 D-F). At 3500 RPM, the Young's modulus of the fibre bundles reached 121.5 ± 3.8 MPa, with a yield stress of 6.3 ± 0.09 MPa and yield strain of ~10%. At 500 RPM, the Young's modulus of the fibre bundles were 14.4 ± 0.8 MPa, with a yield stress of 0.6 ± 0.03 MPa and yield strain of ~6% (Table 4.3). The same trend, although with less dramatic differences is reported when using the theoretical and compressed CSA (Figure 4.7, Table 4.4 and Table 4.5).

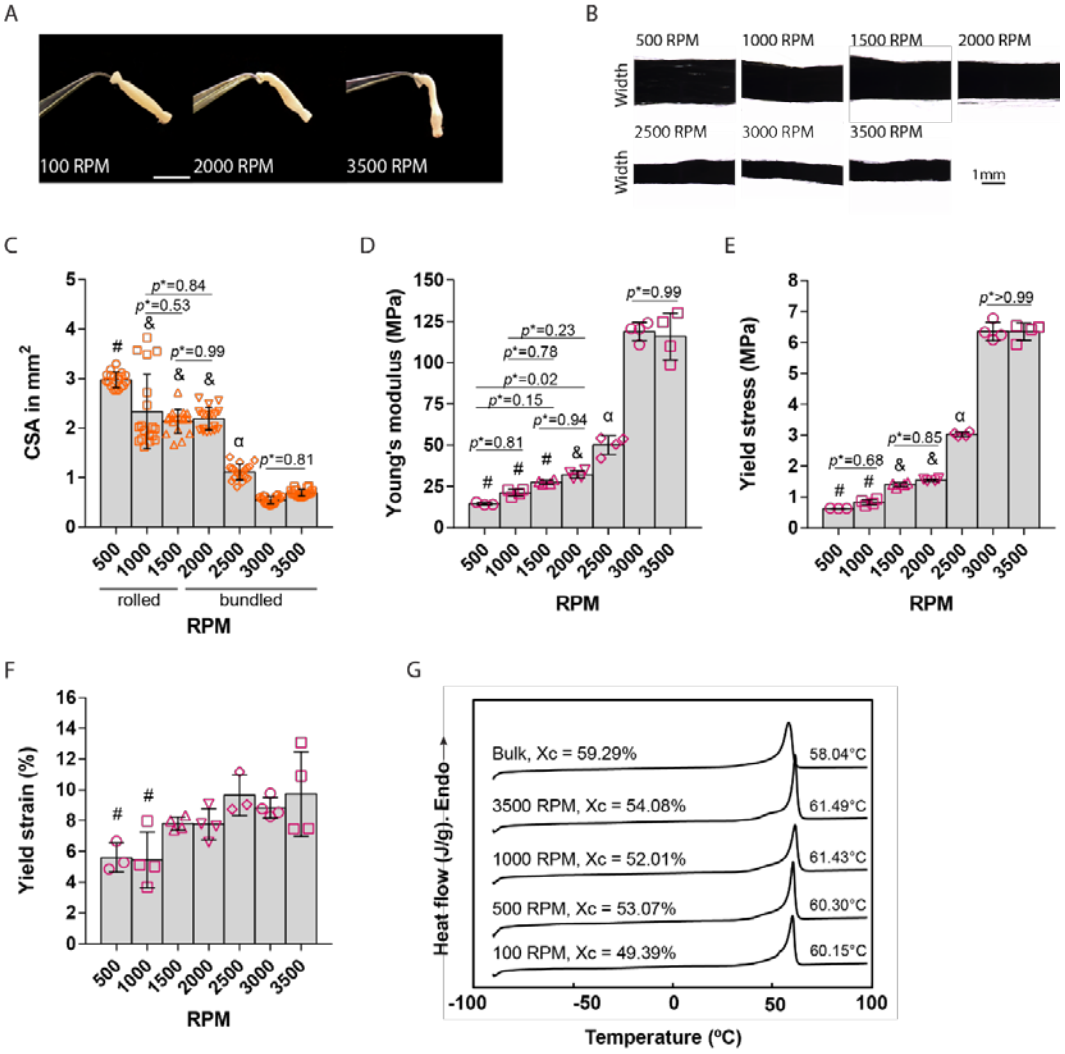

Figure 4.5 Mechanical properties increase as collection velocity increases. **A**, Macroscopic images of scaffolds after 10 days of cell culture (scaffolds collected for 1 h; scaffolds are hanging from a forceps). Scale bar, 2 cm. **B**, Longitudinal sections of the specimens prepared for tensile testing; images acquired with a brightfield microscope. Scale bar, 1 mm. **C**, Apparent cross-sectional area (CSA) calculated using the width measured from the brightfield images (B). #, $p < 0.0001$ versus 1000 – 3500 RPM; &, $p < 0.0001$ versus 2500 – 3500 RPM; α, $p < 0.0001$ versus 3000 – 3500 RPM. p^*, Tukey's adjusted p value. $n = 3$ scaffolds with a total of 18 regions of interest (ROI) per RPM group. Error bars, mean ± s.d., one-way ANOVA ($p < 0.05$) with Tukey's multiple comparisons test. **D**, Young's modulus. #, denotes significance versus 2500 – 3500 RPM, $p < 0.0001$; &, denotes significance versus 2500 – 3500 RPM, $p < 0.05$; α, denotes significance versus 3000 – 3500 RPM, $p < 0.0001$. **E**, Yield stress. #, denotes significance versus 1500 – 3500 RPM, $p < 0.0001$; &, denotes significance versus 2500 – 3500 RPM, $p < 0.0001$; α, denotes significance versus 3000 – 3500 RPM, $p < 0.0001$. **F**, Yield strain. #, $p < 0.05$ versus 2500 and 3500. **D** – **F**, Error bars, mean ± s.d., one-way ANOVA ($p < 0.05$) with Tukey's multiple comparisons tests ($n = 4$ scaffolds); p^*, Tukey's adjusted p value. **G**, DSC thermographs of the first heating scan of the samples, % of crystallinity (X_c) and temperature of the endothermic peak (°C). There is a slight shift in the endothermal peak observed with respect to the bulk PCL as electrospinning collection velocity increases. A second crystalline phase is formed prior to the main crystallization due to stress-induced crystallization. The glass transition temperature of PCL occurs at ~-60 °C with a less apparent peak in agreement with literature (Rusu, Ursu and Rusu, 2006).

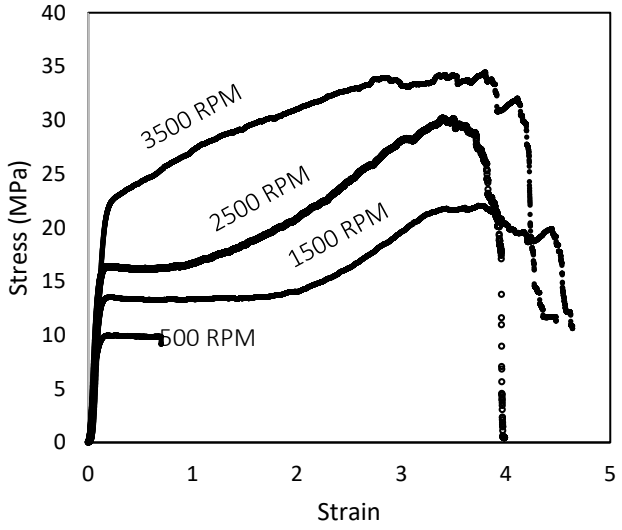

Figure 4.6 Stress-strain curves of 500, 1500, 2500 and 3500 RPMs. Scaffolds produced at higher RPMs failed at higher loads.

RPMs	Young's modulus (MPa)	Yield stress (MPa)	Yield strain
500	14.49 ± 0.83	0.62 ± 0.03	0.056 ± 0.009
1000	21.18 ± 2.09	0.83 ± 0.07	0.054 ± 0.007
1500	27.67 ± 1.20	1.40 ± 0.02	0.078 ± 0.003
2000	32.22 ± 2.33	1.55 ± 0.07	0.077 ± 0.007
2500	50.16 ± 5.66	3.03 ± 0.03	0.096 ± 0.013
3000	118.84 ± 0.13	6.36 ± 0.07	0.088 ± 0.008
3500	121.53 ± 3.89	6.35 ± 0.09	0.097 ± 0.028

Table 4.3 Material properties of the bundles calculated using the apparent cross-sectional area.

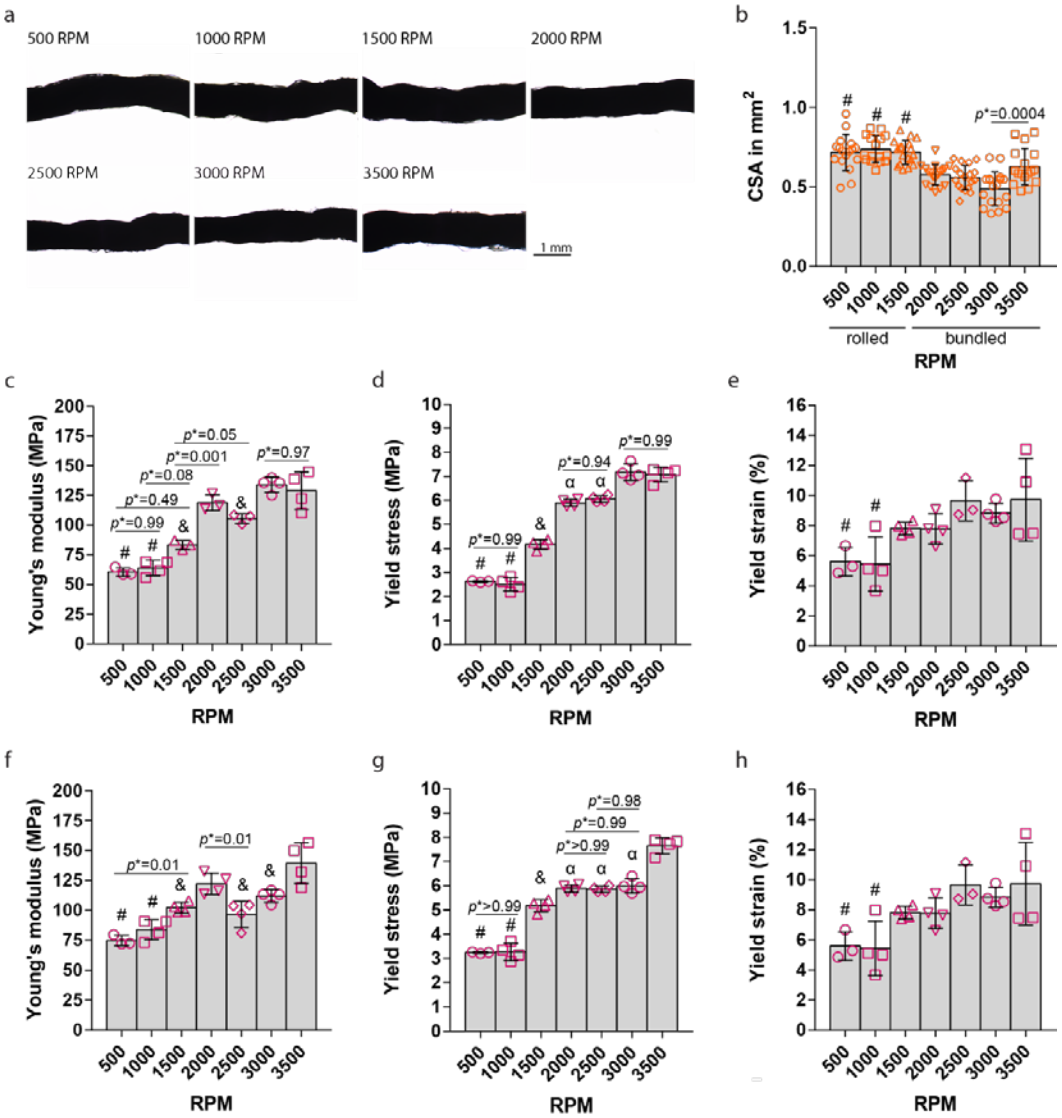

Figure 4.7 Material properties using the cross-sectional area (CSA) of compressed bundles and the theoretical CSA. **a**, Bright-field images of the aligned electrospun bundles show similar widths after twisting them to compress the void space. Scale bar, 1 mm. **b**, Cross-sectional areas (CSA) calculated using the width measurements from (**a**) and assuming a circular CSA. #, $p < 0.0001$ versus 2000 – 3000 RPM. p^*, Tukey's adjusted p value. $n = 3$ scaffolds with a total of 17 regions of interest (ROI) per RPM group. Error bars, mean ± s.d., one-way ANOVA ($p < 0.05$) with Tukey's multiple comparisons test. **c – e**, Young's modulus, yield stress and yield strain calculated using the CSA of compressed bundles (**b**). **c**, Young's modulus. #, denotes significance versus 2000 – 3500 RPM, $p < 0.0001$; &, denotes significance versus 3000 – 3500 RPM, $p < 0.0001$. **d**, Yield stress. #, denotes significance versus 1500 – 3500 RPM, $p < 0.0001$; &, denotes significance versus 2000 – 3500 RPM, $p < 0.0001$; α, significant versus 3000 – 3500 RPM, $p < 0.0001$. **e**, Yield strain, #, $p < 0.05$ versus 2500 and 3500. **f – h**, Young's modulus, yield stress and yield strain calculated using the calculated theoretical CSA of 0.576 mm^2. **f**, Young's modulus. #, denotes significance versus 2000, 3000 and 3500 RPM, $p < 0.001$; &, denotes significance versus 3500 RPM, $p < 0.001$. **g**, Yield stress. #, denotes significance versus 1500 – 3500 RPM, $p < 0.0001$; &, denotes significance versus 2000 – 3500 RPM, $p < 0.05$; α, significant versus 3500 RPM, $p < 0.0001$. **h**, Yield strain. #, $p < 0.05$ versus 2500 and 3500.

RPMs	Young's modulus (MPa)	Yield stress (MPa)	Yield strain
500	60.62 ± 3.48	2.62 ± 0.02	0.056 ± 0.009
1000	63.89 ± 6.33	2.50 ± 0.27	0.054 ± 0.007
1500	83.20 ± 3.85	4.16 ± 0.20	0.078 ± 0.003
2000	122.42 ± 6.67	5.89 ± 0.15	0.077 ± 0.007
2500	100.18 ± 4.23	6.06 ± 0.14	0.096 ± 0.013
3000	133.97 ± 6.36	7.17 ± 0.33	0.088 ± 0.008
3500	128.99 ± 11.63	7.07 ± 0.30	0.097 ± 0.028

Table 4.4 Material properties calculated using the compressed CSA (true material CSA)

RPMs	Young's modulus (MPa)	Yield stress (MPa)	Yield strain
500	74.84 ± 4.29	3.24 ± 0.03	0.056 ± 0.009
1000	83.93 ± 5.40	3.26 ± 0.35	0.054 ± 0.007
1500	102.22 ± 4.48	5.17 ± 0.25	0.078 ± 0.003
2000	122.25 ± 6.66	5.89 ± 0.15	0.077 ± 0.007
2500	101.18 ± 4.08	5.85 ± 0.12	0.096 ± 0.013
3000	112.04 ± 5.27	5.99 ± 0.29	0.088 ± 0.008
3500	139.41± 12.51	7.64 ± 0.33	0.097 ± 0.028

Table 4.5 Material properties calculated using the theoretical CSA

A strong correlation was observed between the fibre diameter and the maximum load reached before yield (correlation coefficient of -0.85). The improved mechanical strength and stiffness of small diameter fibres has previously been associated with higher crystallinity in the polymer after electrospinning due to jet stretching (Wong, Baji and Leng, 2008). To examine if this was contributing to the enhanced mechanical properties in the small diameter fibres, their degree of crystallinity was analysed using DSC. The melting temperature (T_m, °C) and melting enthalpy (ΔH_m, J/g) of the bulk PCL (as-received pellets) and electrospun fibres are presented in Table 4.6. The degrees of crystallinity were calculated to be 59.28% for the bulk PCL, 49.39% for fibres collected at 100 RPM, and 54.08% for those collected at 3500 RPM, suggesting that electrospinning alters the dynamics of crystallization. Crystallinity increased

when the fibres were collected at progressively higher speeds on the rotating mandrel. Fibres collected at the lowest velocity show the lowest degree of crystallinity. The crystallinity increases with the reduction of fibre diameter and straining level from the rotating mandrel. From the DSC thermographs, it was observed that the melting temperature (T_m) of the electrospun fibres shifted slightly to a higher temperature with the increase in collection velocity compared to the as-received bulk PCL (Figure 4.5 G). This shift is interpreted as a higher perfection in the crystal formation and thus can explain the increased mechanical properties in the 3500 RPM group. Since the scaffold mass is similar across the groups (see Figure 4.9 b), the increase in load bearing in the higher RPM groups (aligned fibres) can be attributed in part to the higher degree of crystallinity and molecular orientation in the thinner fibres.

	First heating		Second heating		Crystallinity
	ΔH_m (J/g)	ΔT_m (°C)	ΔH_m (J/g)	ΔT_m (°C)	(%)
Bulk	82.7006	58.04	60.2386	56.67	59.28
3500 RPM	75.4407	61.49	51.7114	55.71	54.08
1000 RPM	72.5535	61.43	60.1819	56.24	52.01
500 RPM	74.0392	60.30	56.2015	55.11	53.07
100 RPM	68.8973	60.15	58.7372	55.14	49.39

Table 4.6 Thermal properties of bulk and electrospun PCL fibres

To demonstrate the impact of fibre fusion on the mechanical properties in the scaffolds in the fibre direction, electrospun sheets were produced using different electrospinning parameters to produce scaffolds with similar fibre diameter but altered levels of inter-fibre fusion (Figure 4.8). Fused fibre scaffolds with fibres ~5 µm in diameter showed a lower Young's modulus compared to unfused fibre scaffolds of equal fibre diameter (Figure 4.8). Fused fibres displayed a Young's modulus of 42 ± 7MPa, yield stress 1.2 ± 0.1 MPa, and yield strain 3.6 ± 0.9% (Figure 4.8) compared to ~121 MPa of the same diameter, but with higher fraction of unfused fibres.

a

Processing conditions	Electrospun sheet of fused fibres	Electrospun sheet of unfused fibres
Voltage	15 kV	10 kV
Flow rate	4 ml/h	5 ml/h
Throw distance	15 cm	15 cm
Collection velocity	1000 RPM	3500 RPM
Collection time	1 h	5 min
Test specimen	rectangular sheet	bundle

b

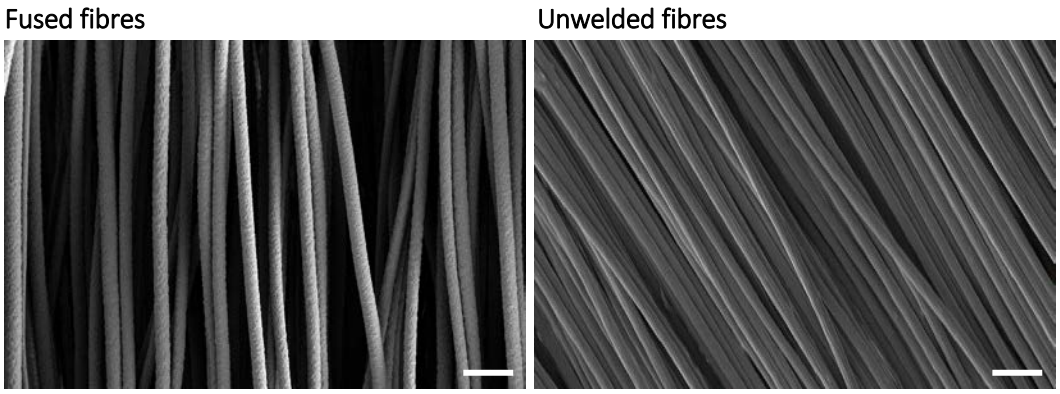

c

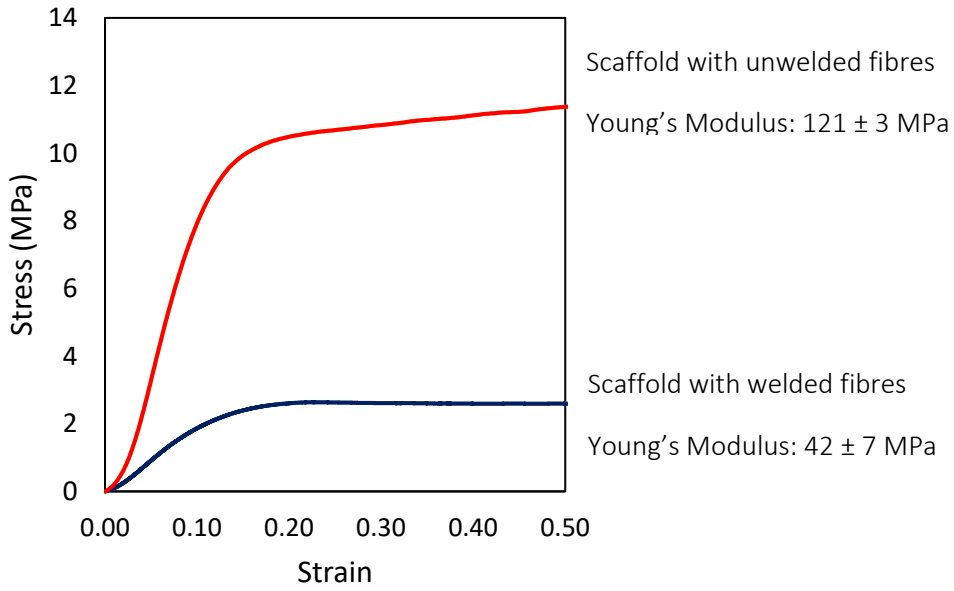

Figure 4.8 Unwelded fibres confer higher Young's modulus compared to welded fibres. **a**, Processing conditions for welded and unwelded ~5 µm fibres. **b**, SEM micrographs of similar diameter fibres. Scale bars, 20 µm. **c**, Stress-strain curve of welded and unwelded fibres.

4.3.3 MSCs rapidly migrate into the highly porous bundles generated by high speed electrospinning

µCT scans of the 100 and 3500 RPM scaffolds were taken to visualise their internal structure and to measure the void spaces within (Figure 4.9 a). Additionally, porosity was calculated as a function of the scaffold density. In dry samples, the 3000 and 3500 RPM groups appeared denser (g/cm^3) (Figure 4.9 c). Unfused finer fibres compact better than thicker fibres (welded or un-welded) and thus scaffolds composed of thin fibres had a smaller CSA. Evidence of this is the similar values of the apparent CSA and squeezed CSA values of the 3500 RPM group (see Figure 4.5 and Figure 4.7). Dry fibres collapse on one another, consequently, the volume of these scaffolds was lower, and while the mass was constant across all RPMs (Figure 4.9 b), its density was therefore higher. In contrast, rolling sheets of fused fibres generated void space between the outer layers of the spiral, increasing scaffold diameter; and while the mass was constant across all RPMS, its density appeared lower. Consequently, in dry scaffolds, higher RPM groups showed lower porosity and slower RPM groups showed higher porosity (Figure 4.9 d).

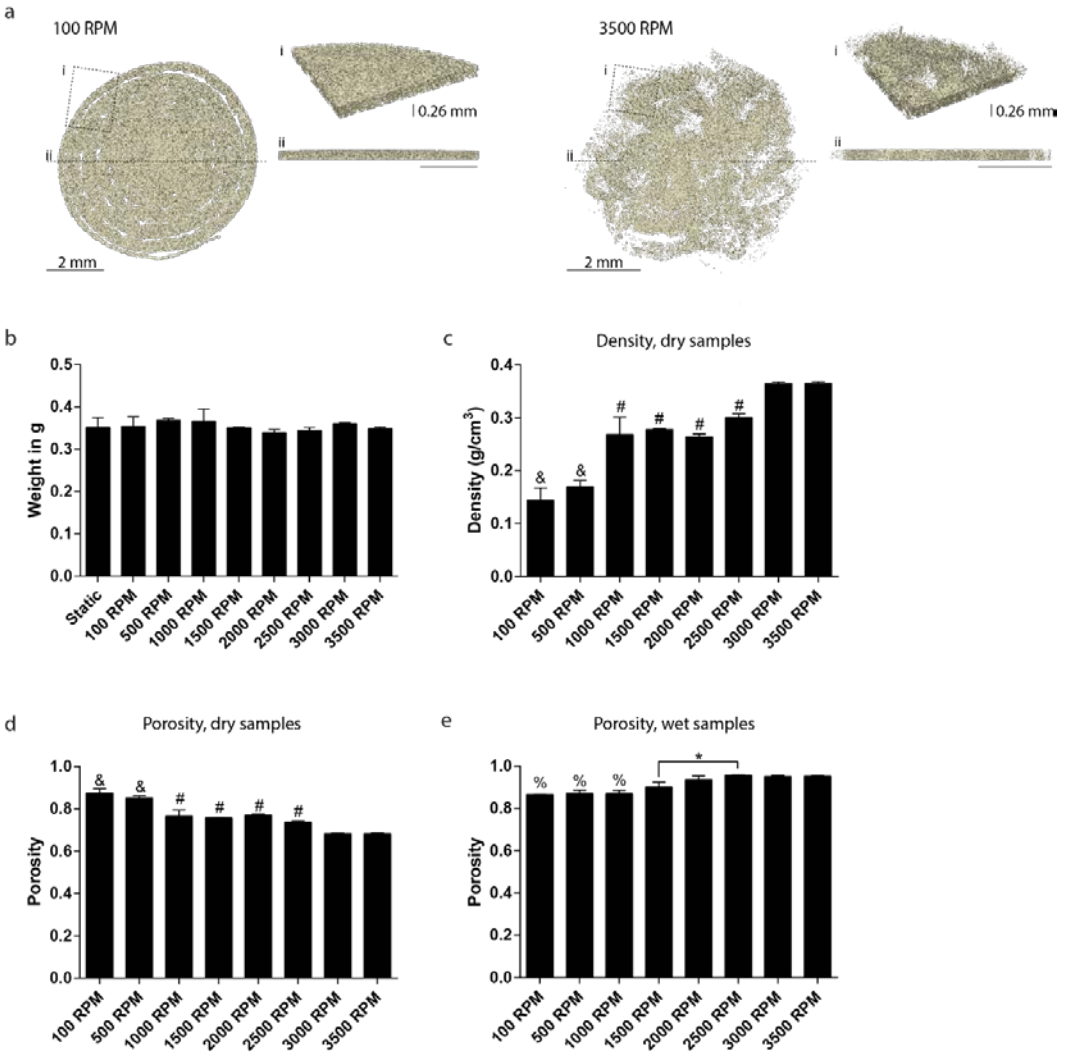

Figure 4.9 Porosity and density of fibre bundles. **a**, µCT scans of 100 RPM and 3500 RPM scaffolds collected for 1 h. Scale bars, 2 mm. **b**, Weight of bundles collected for 20 min (n = 3 scaffolds). The weight of fibres collected with the mandrel static is shown as a reference. **c**, Density of dry scaffolds. &, $p < 0.01$ versus 1000 – 3500 RPM; #, $p < 0.05$ versus 3000 and 3500 RPM. **d**, Porosity of dry scaffolds. &, $p < 0.01$ versus 1000 – 3500 RPM; #, $p < 0.05$ versus 3000 and 3500 RPM. **e**, Porosity of wet scaffolds. %, $p < 0.05$ versus 2000 – 3500 RPM; *, $p = 0.034$. One-way ANOVA with Tukey's multiple comparisons test.

In wet conditions (as they are during cell culture) porosity was calculated using the liquid intrusion method (as a function of mass) to best reflect the behaviour of the scaffolds in contact with liquid during culture. After incubation in ethanol, we found that groups collected at higher RPMS were heavier than those at lower RPMS. Wet scaffolds composed of a higher fraction of unwelded fibres facilitated a larger mass of ethanol to intrude into the

scaffold compared to the lower RPM scaffolds. Consequently, wet scaffolds collected at increased RPMs showed higher porosity compared to the lower RPMs. The calculated porosity of wet scaffolds, collected at higher RPMS, was ~94% (ranging from 93.49 ± 1.88% for 2000 RPM to 95.29 ± 0.30% for the 3500 RPM) (Figure 4.9 e). While the porosity of lower RPM groups was ~88% (ranging from 86.59 ± 0.20% for 100 RPM to 90.03 ± 2.33% for the 1500 RPM). The difference in dry and wet conditions is related to differences in interfibrillar space opening in wet conditions.

To determine whether fibres collected at higher speeds would allow cell infiltration, scaffolds were seeded with MSCs and cultured for 3 days. Homogenous cellular infiltration throughout the CSA of the scaffolds was observed for all RPMs. Representative images of the fibre-scaffolds collected at the lowest (100 RPM), highest (3500 RPM) and intermediate (1500 RPM) RPMs are shown (Figure 4.10). In the 100 RPM group, 60% of the pores were >500 μm^2 (the minimum pore size was 100 μm^2 and the maximum 18,015 μm^2) (data not shown). These results show that cells could migrate comparably through both the lower porosity high RPM scaffolds as more porous low RPM scaffolds. In conventional electrospinning strategies (with higher fraction of welded fibres) a higher packing density would reduce pore size limiting cellular infiltration. However, here it was observed that when wet, the un-welded fibre-bundles increased their interfibre space allowing for cell infiltration.

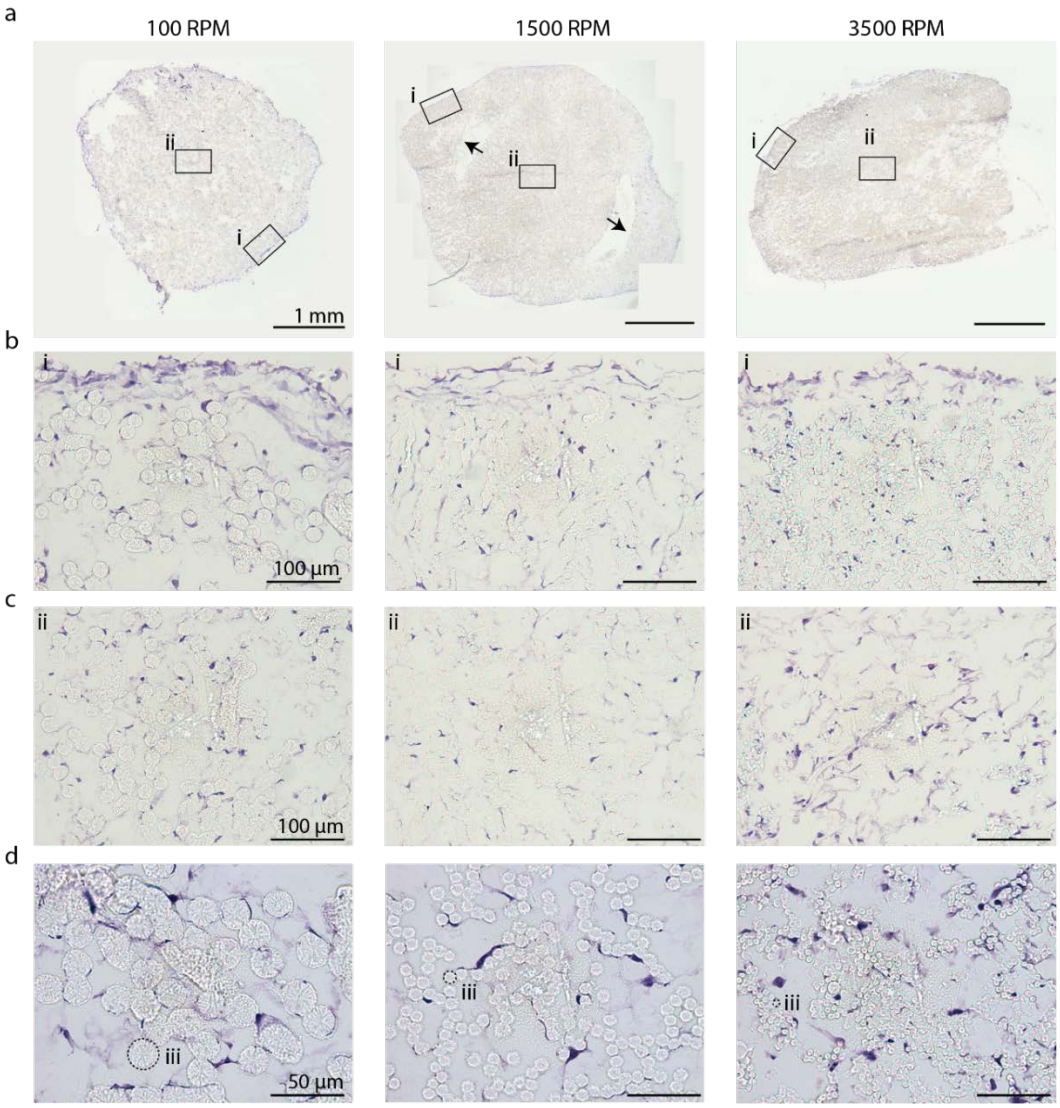

Figure 4.10 MSCs infiltrate through the thickness of the scaffolds. **a – d**, Histology of 100, 1500 and 3500 RPM specimens. H&E staining indicates cells. **a**, 4X magnification image of the whole scaffold. Arrows in 1500 RPM sample indicate separation of the electrospun fibre-sheet from the spiral core. Scale bars, 1 mm. **b**, 20X magnification of the periphery of the scaffolds (area indicated as 'i'). Scale bars, 100 µm. **c**, 20X magnification of the centre of the scaffolds (area indicated as 'ii'). Scale bars, 100 µm. **d**, 40X magnification of the centre of the scaffolds. Dotted line, outline of the electrospun fibres ('iii'). Scale bars, 50 µm.

4.3.4 Evaluating the instructive potential of 3D fibre-bundles towards chondrogenesis and ligamentogenesis

The 3500 RPM microfibrilliar architecture with a mean fibre diameter of ~5 µm (∅ 4.48 ± 0.23 µm) was selected to evaluate the instructive potential of the scaffolds for chondrogenesis and ligamentogenesis. This architecture possessed the highest Young's modulus and it could be collected to achieve human ACL dimensions, while still allowing MSC infiltration (Figure 4.11 a, b). MSCs were seeded onto the fibre-bundles and were cultured in growth, ligamentous or chondrogenic media for 10 days. MSCs showed an elongated shape following the topography of the underlying substrate (Figure 4.11 c). MSCs seeded on the scaffolds and stimulated with CTGF expressed higher levels of ligamentogenic genes collagen type I (*COL1A1*) and tenomodulin (*TNMD*). MSCs seeded on scaffolds and stimulated with TGFβ3 expressed higher levels of the chondrogenic marker collagen type II (*COL2A1*), although no significant difference in the expression of SYR-box 9 (*SOX9*) was observed between CTGF and TGFβ3 stimulated MSCs.

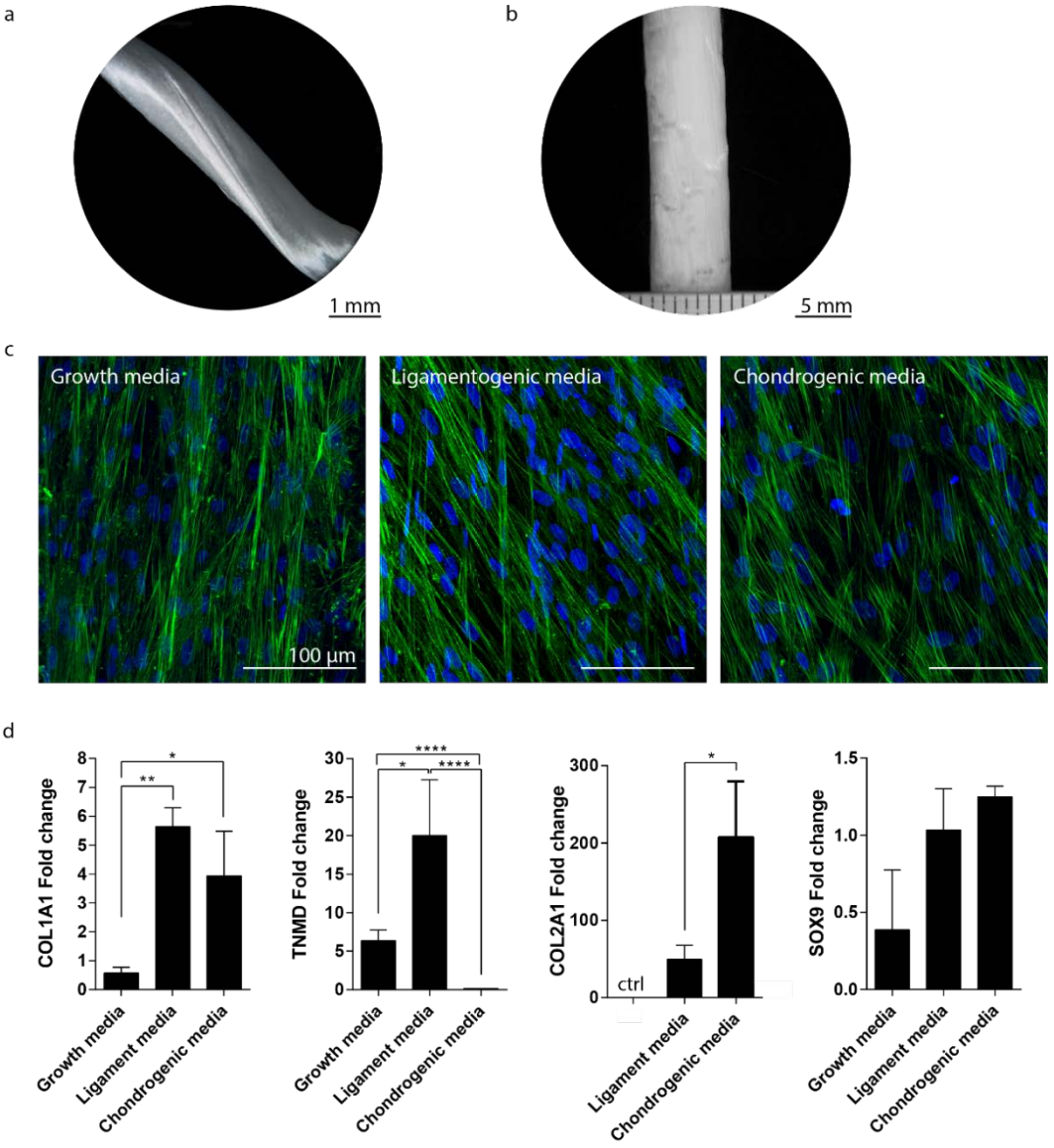

Figure 4.11 Cell morphology and gene expression of MCS on fibre-bundles. **a**, Electrospun fibre-bundle used to assess the instructive potential on MSCs. Scale bar, 1 mm. **b**, Fibre-bundle collected for 2 h with the dimensions of the human ACL. Scale bar, 5 mm. **c**, F-actin and nuclei staining of MSCs cultured in growth, ligamentous or chondrogenic media after 10 days in culture. **d**, Gene expression of ligamentous and chondrogenic genes at day 10. Collagen types I (*COL1A1*), II (*COL2A1*), tenomodulin (*TNMD*) and SRY-Box 9 (*SOX9*). *, $p < 0.05$; **, $p < 0.01$; ***, $p < 0.0001$. One-way ANOVA with Tukey's multiple comparisons tests ($n = 5$ scaffolds). Error bars, mean ± SEM. ctrl, indicates that the growth media group was used to normalize the expression of *COL2A1* since this gene was not expressed in cells at day 0.

4.4 Discussion

Aligned microfibrous electrospun scaffolds offer tremendous potential for tendon and ligament tissue engineering (TE). Such scaffolds can promote tendon/ligament gene

expression, cellular alignment in the fibre direction and ordered ECM deposition. Yet developing a porous scaffold mimicking the size, stiffness and strength of human tissues, whilst also providing an environment conductive to ligamentogenesis, remains a significant challenge in the field of TE. This chapter presents a method to produce porous, three-dimensional (3D) microfibrillar scaffolds with physical and mechanical properties appropriate for ligament TE.

By increasing the linear velocity of the collecting mandrel, it was possible to increase the fraction of unwelded microfibers within the electrospun sheets. Increasing the fraction of unwelded fibres reduced the flexural rigidity of the electrospun sheets, which in turn allowed the bundling of fibres into 3D scaffolds with similar dimensions to the human anterior cruciate ligament (ACL). Further, this increase in collection velocity enhanced the degree of molecular orientation and provided high resistance to uniaxial tensile forces. Increasing the rotational velocity of the collector also increased the airflow generated from the rotating collector, which potentially accelerated the solvent evaporation in the depositing fibre thread. This likely resulted in less welding throughout the fibre thread at juxtaposed fibres. Solvents with medium volatility, like chloroform, can provide conditions to stretch and dry the fibre before collection. Chloroform has higher volatility (boiling point 62.2 °C) compared to tetrahydrofuran (THF, 66 °C) and dimethylformamide (DMF, 153 °C) commonly used solvents in electrospinning. Thus, at higher RPMS with higher airflow that enhances solvent evaporation, fibres are deposited solid with little to no excess solvent to weld to other fibres, thereby reducing fibre-fibre interconnections. This phenomenon is reported for needleless electrospinning, where by using air flow the solvent evaporation is accelerated and reduced fibre-fibre interconnections are achieved (Lin and Wang, 2013). Fibres collected at lower RPMs likely weld with each other due to ineffective solvent evaporation. It would be interesting to explore the effect of solvents with higher volatility such as dichloromethane (boiling point 39.6 °C) (this would occur at the expense of fibre diameter; if evaporation rates are too high the

elongation of the fibre jet is disturbed producing fibres with large diameter (Padron *et al.*, 2013)).

The fibre sheets produced at higher RPMs could be disrupted and bailed to form bundles, enabling the formation of 3D scaffolds. In electrospinning, the thickness of the collected fibre-sheet is limited by the accumulation of residual charge on the deposited fibres, which eventually interferes with the alignment or deposition of incoming fibres. Therefore, in many cases a physiologically relevant 3D electrospun scaffold can only be achieved by stacking several sheets or rolling a sheet. The system presented here is also limited by the same phenomenon, however after electrospinning for 2 h, scaffolds with dimensions within the range of human ACL were achieved. The length of the human ACL is 27 – 32 mm (Vunjak-Novakovic *et al.*, 2004), and it is ~5 mm - 8mm wide (axial view - sagittal view) (Anderson *et al.*, 2001; Triantafyllidi *et al.*, 2013). The mid-substance cross-sectional area (CSA) is reported to range between 36 – 48 mm^2 (Anderson *et al.*, 2001; Triantafyllidi *et al.*, 2013; Iriuchishima *et al.*, 2014). When fibres were collected for 2 h and bailed, the resulting bundle was 7 mm wide, with a CSA of ~39 mm^2 for the 3500 RPM group (Figure 4.11 b). As a comparison, the average CSA of commonly used tissue grafts include ~40 mm^2 of bone – patella tendon – bone, and ~52 mm^2 of semitendinosus tendon grafts (Iriuchishima *et al.*, 2014). Electrospinning for 2 h is not the limit of the system and hence the electrospinning could be continued until the desired CSA is reached. Alternatively, several independent bundles of predominantly single-fibres can be integrated almost seamlessly into one larger bundle, facilitating further scale-up (data not shown).

It has previously been demonstrated that fibre diameter is a key determinant of the resulting scaffold pore size (or inter-fibre spacing), with the highest pore size associated with large microfibers (12 µm) (Pham, Sharma and Mikos, 2006b; Balguid *et al.*, 2009). In the method presented here, it was possible to decouple these two parameters. It was

demonstrated that in the scaffolds produced with a higher fraction of unwelded fibres the interfibrillar space when wet is independent of fibre diameter. Hence the porosity of the electrospun fibre scaffold was increased without increasing the fibre diameter. Ultimately, this allows appropriate selection of a desired fibre diameter, for example one that can appropriately modulate stem cell fate and cellular morphology, migration and proliferation (Wang *et al.*, 2010; Cardwell, Dahlgren and Goldstein, 2014; Bean and Tuan, 2015) without compromising porosity.

The collection velocity impacted crystallinity and hence the scaffold mechanical properties. When the diameter of the electrospun fibres is reduced the degree of crystallinity and molecular orientation of the polymer are enhanced, resulting in improved mechanical strength and stiffness (Wong, Baji and Leng, 2008). Mechanical strength and stiffness typically vary inversely with fibre diameter (Wong, Baji and Leng, 2008; Monteiro *et al.*, 2010). Finer fibres were obtained as a result of a dramatic material elongation during polymer jet stretching and with the additional elongation at the last stage of fibre formation when reaching the high-spinning collector (Richard-Lacroix and Pellerin, 2013). These elongations confine the polymer coils, and the electric field during electrospinning align the molecular chains in the direction of fibre axis, resulting in a higher molecular chain orientation (Greiner and Wendorff, 2007; Wong, Baji and Leng, 2008). Consequently, aligned finer fibres showed higher crystallinity, in agreement with previous reports (Wang *et al.*, 2013). The degree of crystallinity varied within the aligned fibres due to the increasingly stronger tensile forces from the high-speed rotating mandrel increasing velocities. As the collection velocities increased, the melting point shifted to a slightly higher temperature in the first heating, which indicates that the crystallites had a higher crystalline perfection. In agreement, others have suggested that polymer crystals might have higher perfection under higher stress (Yee *et al.*, 2008). However, the electrospun fibres showed lower crystallinity than the bulk PCL. This can be explained by the different processing of PCL pellets for commercialization; the production of

PCL pellets does not involve dissolution in solvents; crystallization is controlled by cooling processes where the molecular chains have time to arrange, nucleate and crystalize. The crystallization process in the electrospun fibres was incomplete relative to the bulk material (Obregon *et al.*, 2016). On the other hand, the lower crystallinity of fibres collected at low RPMs was partially attributed to residual chloroform on the fibres. Additionally, larger fibres inherently contain more defects, which, for example, can arise from fluctuations in the rotating mandrel.

The electrospun fibre scaffolds mimicked some, but not all, of the mechanical properties of the human ACL. The Young's modulus of ACL is 111 ± 26 MPa for younger humans (16–26 years) and 65 ± 24 MPa for older humans (48–86 years)(Noyes and Grood, 1976). The bundles collected at 3500 RPM were within the range of human ACL (~121 MPa). The yield stress and yield strain of human ACL are ~38 MPa and 45% for younger humans, and ~13 MPa and ~30% for older humans (Noyes and Grood, 1976). The bundles collected at 3500 RPM displayed inferior yield stress and strain.

Fibres in conventional electrospun sheets are densely packed, have many entanglements and are partially welded along their length. The scaffolds collected at higher collection velocities presented here, have less welded fibres, but preserve entanglements arising from handling fine fibres. Entanglements create pore interconnections, desirable for cell-cell interaction. Here, the small diameter fibres achieved the same level of cellular infiltration than the large fibre diameter scaffolds. Furthermore, electrospun fibres are flexible due to their high aspect ratio (length/diameter) enabling attached cells to push against the fibres to assemble or migrate into the scaffold (Chu and Liu, 2008). Thinner fibres with less welding could facilitate this phenomenon.

Biomimetic scaffolds, such as aligned electrospun fibres, present structural cues similar to that found in native ligament and can potentially direct the differentiation of MSCs

towards specific musculoskeletal lineages (Lyu *et al.*, 2013). Micro-scale fibres resemble the collagen fibre diameter range in ligaments (1-20 µm) (Silver, Freeman and Seehra, 2003) and have been shown to enhance ligament differentiation (Cardwell, Dahlgren and Goldstein, 2014). The structural effect is further enhanced by exposure to soluble biomolecules known to orchestrate ligament and cartilage development. Particularly, the transforming growth factor beta (TGFβ) superfamily plays an essential role in chondrogenesis (Johnstone *et al.*, 1998; Tuli *et al.*, 2003), while MSCs exposed to connective tissue growth factor (CTGF) have demonstrated a fibroblastic lineage commitment (Lee *et al.*, 2010; Pauly *et al.*, 2017). As seen previously, MSCs aligned in a direction parallel to the underlying fibre direction when maintained in expansion media. MSCs in the presence of CTGF also generally aligned and showed upregulation of tenomodulin (*TNMD*), a transmembrane glycoprotein regulated by scleraxis, and a highly specific marker of ligamentocytes and tenocytes (Shukunami *et al.*, 2006). *TNMD* is implicated in collagen organization, and localized to cells within thick bundles of aligned collagen fibres (Shukunami *et al.*, 2006). In the previous chapter it was observed that MSCs condense when cultured on sheets of aligned electrospun fibres in the presence of TGFβ3, which correlated with higher expression of the chondrogenic markers *SOX9*, a transcription factor essential for chondrocyte differentiation and cartilage formation (Bi *et al.*, 1999), and activator of chondrocyte-specific extracellular matrix gene collagen type II (*COL2A1*). In this study, cellular condensation was not observed on these 3D fibre bundles, which may be due to the larger void spaces created in these bundles when hydrated. These larger spaces likely reduce the incidence of cell-cell interaction within the scaffold. In spite of this and the elongated morphology of the MSCs when stimulated with TGFβ3 on these scaffolds, they still showed higher levels of *COL2A1* expression compared to the other conditions.

4.5 Conclusions

Engineering soft tissues using 3D electrospun scaffolds is dependent on the capacity of cells to populate the construct. This is especially challenging with aligned-fibre scaffolds where the inherent higher packing density reduces pore size and hence limits cellular infiltration. Here, a method to produce biomimetic, aligned fibre scaffolds analogous to the parallel collagen fibres of ligamentous tissue is described. This method could be used to produce scaffolds with dimensions comparable to the human ACL, and furthermore, a Young's modulus within the range of human ACL. Critically, the porous nature of these scaffolds facilitated the migration of MSCs homogenously throughout the body of the construct. When stimulated with relevant growth factors, MSCs seeded onto these scaffolds expressed higher levels of ligament and cartilage-specific genes. This electrospinning technique could form the basis of tissue engineering strategies targeting the regeneration of ligament, tendon and other load-bearing fibre-reinforced tissues.

Chapter 5 Assessing the bioactivity of ligament and cartilage derived extracellular matrices (ECM) for interface tissue engineering

5.1 Introduction

Ligament-bone insertions, termed entheses, are highly specialized load-bearing connections between ligaments and bones. They facilitate the transfer of mechanical loads across synovial joints by minimizing stress concentrations at the interface of tissues with vastly different mechanical properties, biochemical compositions and microstructure (Benjamin, Evans and Copp, 1986) (Zantop, Petersen and Fu, 2005). Conventional soft tissue autografts or allografts commonly fail at the bone insertion site due to inadequate tissue integration (Rodeo *et al.*, 1993; D. Lee *et al.*, 2014), highlighting the critical importance of these entheses. Tissue engineering strategies aim to engineer graded biomaterials to mimic tissue interfaces and restore native tissue architecture and function. Current approaches often rely on multiple cell types within such multiphasic scaffolds, but the complexity of such strategies can limit translation to the clinic. Furthermore, strategies based on bi/tri-layered scaffolds that aim to replicate the structural heterogeneity across the distinct tissues at the enthesis (Spalazzi *et al.*, 2006; Samavedi *et al.*, 2012; Caliari *et al.*, 2015; Criscenti *et al.*, 2016) can display discontinuities across the dissimilar materials used, restricting their potential for regenerating continuous, graded interfaces.

An alternative approach to interface tissue engineering would be to direct the development of a soft tissue template that can remodel to form the bone – calcified fibrocartilage – uncalcified fibrocartilage – ligament interface (Harris *et al.*, 2017). Developmentally this bone-ligament interface is derived from a soft tissue precursor (Lu and Thomopoulos, 2013), suggesting that functionalising the interface region of a scaffold targeting bone-ligament region to promote chondrogenesis might be a promising route for

interface tissue engineering. Realising this goal requires spatially engineering environments that can either support chondrogenesis (for the enthesis) or fibrogenesis (for the main ligament region) within mechanically functional scaffolds.

Recently, scaffolds incorporating tissue-derived ECM have been shown to promote tissue-specific stem cell differentiation through the preservation of biophysical and biochemical motifs characteristic of the native tissues (Keane *et al.*, 2015; Hussey, Keane and Badylak, 2017; Nyberg *et al.*, 2017). Furthermore, recent studies have pointed to the potential of solubilized ECM derived biomaterials for orthopaedic tissue engineering applications (Rothrauff, Yang and Tuan, 2017). Specifically, solubilized ECMs derived from tendon and cartilage have been proposed as tissue-specific biomaterials (Rothrauff, Yang, and Tuan 2017). When seeded with MSC, tendon derived biomaterials were found to enhance scleraxis expression, while cartilage derived biomaterials were found to upregulate SOX9 expression.

In this chapter, polymeric microfibre-scaffolds adorned with tissue-specific ECM were engineered with the goal of enhancing either ligamentous or chondrogenic differentiation of MSCs. To achieve this, ligament and cartilage ECM were immobilized via covalent conjugation or hydrophobic adsorption on to the surface of electrospun polycaprolactone fibres. Polymeric microfibrillar scaffolds were used as they are mechanically robust (Chapter 4), present structural cues found in native ligament (Silver, Freeman and Seehra, 2003) and cartilage (Minns and Steven, 1977; Broom and Marra, 1986) and can facilitate the differentiation of MSCs towards these musculoskeletal lineages (Lee *et al.*, 2005; Bashur, Dahlgren and Goldstein, 2006; de Mulder *et al.*, 2013). Cellular activities including cell spreading, migration, proliferation and differentiation are known to be sensitive to the topography of scaffolds (Cardwell, Dahlgren and Goldstein, 2014; Yin *et al.*, 2015). The ECM functionalized scaffolds were seeded with MSCs and then either exposed to basal media, to assess the contribution of the physical and biochemical cues of the ECM alone, or to CTGF or

TGFβ3, to assess the synergistic effect of ECM and growth factors on stem cell differentiation. CTGF has shown to play a role in ligament-fibroblast differentiation (Lee *et al.*, 2010), and the transforming growth factor beta family (TGFβ) plays an essential role in chondrogenesis (Johnstone *et al.*, 1998; Tuli *et al.*, 2003). Ultimately such ECM functionalisation could be used to engineer graded biomaterials with different tissue-specific microenvironments for bone-ligament interface tissue engineering.

5.2 Materials and Methods

5.2.1 Electrospinning

Polycaprolactone (PCL, M_W 80 kDa, Sigma – Aldrich) was dissolved at 25% w/v in chloroform. The polymer solution was loaded in a 20-ml syringe and extruded using a syringe pump through a 20G blunt-end needle charged to 10 kV. Continuous polymeric fibres were collected at a flow rate of 5 ml/h on a grounded mandrel positioned 15 cm apart from its centre to the tip of the needle. Fibres were collected at 3500 RPM for 10 min and 1 h. Fibres collected for 10 min were wrapped/baled to form 'bundles' along the long axis of the fibres as previously shown (Chapter 4) and used for bone marrow-derived mesenchymal stem cell (MSC) culture. Discs (8 mm Ø) were punched from 1 h electrospun sheets and used for scanning electron microscopy (SEM).

5.2.2 Solubilization of cartilage and ligament ECM

Cartilage was harvested under sterile conditions from the articular surfaces of femoral condyles and trochlear groove hind limbs of three-month-old pigs (3 donors). Articular ligaments were harvested from the same donors. Tissues were minced to 1 – 2 mm^3 pieces and then solubilized using 1 ml of 0.2 M sodium hydroxide (NaOH) per 50 mg of wet tissue at 4°C with agitation (24 h). The resulting solutions were pelleted and washed with ultra-pure

water to remove residual NaOH. The resulting pellets were digested with pepsin solution (1500 units of pepsin dissolved in 0.5 M acetic acid per 50 mg of tissue) at RT with rotation (24 h). The resulting mixtures were centrifuged to eliminate insoluble material. The supernatants were then salt precipitated using a 0.9 M final concentration sodium chloride (NaCl) solution for the cartilage solubilized ECM, and 0.8 M final concentration NaCl solution for the ligament solubilized ECM. These mixtures were allowed to equilibrate at 4°C (6 h). The mixtures were centrifuged and the supernatants (unprecipitated material) discarded. The pellets were dissolved in 0.5 M acetic acid overnight and salt precipitated again. The acid solubilized ECM was dialyzed against sodium phosphate (Na_2HPO_4) for 24 h with a change of dialysate. The dialyzed ECM digest was freeze dried and stored at – 80°C. Tissue harvesting and solubilisation steps were performed under sterile conditions.

5.2.3 SDS-PAGE

Lyophilised ligament and cartilage ECM were resuspended in phosphate-buffered saline (PBS) at 1 mg/ml and protein concentration was determined by Bradford reaction and verified by means of spectrophotometry using NanoDrop 2000c UV-Vis Spectophotometer (Thermo Scientific). Samples were prepared by the addition of 5X Laemmli buffer (containing 25% β-mercaptoethanol) in a ratio of 1:4 prior to boiling at 100 °C for 5 min. 50 µg of sample and a pre-stained protein standard were loaded and resolved through a 7.5% SDS-PAGE gel under fully reducing and denaturing conditions, at 120 V for 90 min. Gels were then soaked in Coomassie Brilliant Blue R-250 solution (0.1% Coomassie Brilliant Blue R-250, 50% methanol, 10% glacial acetic acid, 40% water) for 1 h with gentle agitation. The staining solution was poured off and gels were soaked in De-stain (20% methanol, 10% glacial acetic acid, 70% water) for several hours with gentle agitation. The de-stain solution was replenished several

times until the background of the gel was fully de-stained. Collagen type I (from rat tail tendon) and collagen type II (from bovine tissue, Corning) were used as controls.

5.2.4 Protein immobilization and characterization of functionalized scaffolds

Cartilage and ligament solubilized ECM, and collagen type I (from rat tail tendon, Corning) were immobilized onto the surface of the microfibers by physical adsorption or covalent conjugation (also referred to as chemical immobilization). For the characterization of the functionalized scaffolds, collagen type I was used as a model protein representative of all the proteins. Characterization was performed with X-ray photoelectron spectroscopy (XPS) (section 5.2.5), SEM (section 5.2.6) and by quantifying amount of immobilized protein (section 5.2.7). For the characterization, scaffolds underwent physical and covalent conjugation of collagen type I as follows.

Physical adsorption: scaffolds were washed in 70% ethanol and rinsed in deionized water. Scaffolds were then incubated in collagen solutions at different concentrations (0.1, 0.5, 1, 5, 10 mg/ml) for specific time periods (6, 12, 24, 48 h) at 4 °C in MES buffer, pH 5. Scaffolds were rinsed gently and air-dried (see diagram below).

Covalent conjugation: scaffolds were washed in 70% ethanol and rinsed in deionized water. The PCL surface was hydrolysed with 1 N sodium hydroxide (NaOH) solution for 15 min, 30 min, 1 h, 3 h, 5 h and 8 h at room temperature. Scaffolds were rinsed and air-dried for X-ray photoelectron spectroscopy (XPS) characterization. Otherwise, after 3 h of hydrolysis, scaffolds were incubated in an aqueous treatment of excess 1-ethyl-3-(3-dimethylaminopropyl carbodiimide hydrochloride (EDC, 5mg/ml) and N-hydroxysulfosuccinimide (NHS, 5mg/ml) prepared in MES buffer, pH 5 (all from Sigma-Aldrich) for 2 h at 4°C. Scaffolds were rinsed in MES buffer and incubated in collagen type I at different concentrations (0.1, 0.5, 1, 5, 10 mg/ml) for 24 h at 4°C in MES buffer, pH 5. Scaffolds were

rinsed and incubated in deionized water for 24 h under gentle constant agitation to remove physically adsorbed collagen. Scaffolds were air-dried.

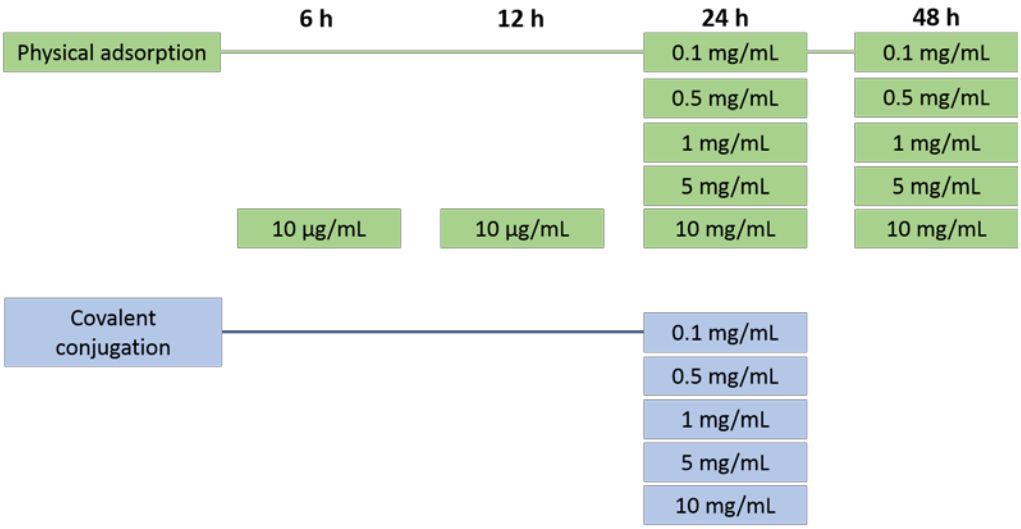

Control scaffolds with no immobilized protein ('bare') were incubated in ultra-pure water while the rest underwent collagen immobilization. XPS was conducted to confirm presence of collagen onto PCL fibres. SEM images were acquired to confirm topography was maintained after collagen immobilization.

5.2.5 Changes in surface composition and ECM distribution

Changes in surface composition after immobilizing collagen type I (used as model protein representative of all ECMs) were analysed by X-ray photoelectron spectroscopy (XPS). XPS was performed under ultra-high vacuum conditions (< $5x10^{-10}$ mbar) on a VG Scientific ECSAlab Mk II system using Al Kα X-rays (1486.6 eV). The analyser pass energy was set to 200 eV for survey spectra and 20 eV for high resolution scans recorded. An electron flood gun was used for charge compensation and the binding energy scale was referenced to the adventitious carbon 1s core-level at 284.8 eV.

Picrosirius red staining was used to evaluate the distribution of collagen type I and ECMs on the scaffolds. After incubation in collagen type I and ECMs the scaffolds were rinsed in de-ionized water and incubated in Picrosirius red stain for 5 mins, then submerged 3 times in 2% acetic acid and rinsed with de-ionized water. Bare scaffolds were used as controls. Images of the scaffolds were acquired using a stereo microscope (Leica).

5.2.6 SEM

Samples for scanning electron microscopy (SEM) were sputter coated with a mixture of gold/palladium (60:40) to a thickness of ~10 nm (Cressington 108) and imaged with a Zeiss Ultra FE-SEM at an accelerating voltage of 5 kV.

5.2.7 Quantification of immobilized solubilized ECM

To quantify the amount of immobilized ECM per g of scaffold, collagen type 1 was used as model protein representative of all ECMs. Collagen type 1 was immobilized onto the surface of the fibres (4 cm in length, 0.25 ± 0.02 g) either physically (at 1 mg/ml) or chemically (at 0.5 mg/ml) as described in section 5.2.4. Collagen on the scaffolds was extracted using 100 mM sodium phosphate buffer with 5 mM ethylenediaminetetra-acetic acid (EDTA), 5 mM L-cysteine hydrochloride (HCl) and 3.88 U/ml papain, pH 6.5 (all Sigma-Aldrich) for 18 h at 50 °C under constant rotation. Collagen content was determined by quantifying the hydroxyproline content using the dimethylaminobenzaldehyde and chloramine-T assay (n=4 scaffolds) (Kafienah and Sims, 2004). A hydroxyproline-to-collagen ratio of 1:7.69 was used (Ignat'eva *et al.*, 2007). Digested samples were weighed to normalize the collagen values to wet/dry weight of scaffolds.

5.2.8 Immobilization of solubilized ECM and collagen type I onto the PCL fibres by physical adsorption for cell culture studies (sections 5.3.2 – 5.3.4)

For physical adsorption, scaffolds were washed in 70% ethanol and rinsed in deionized water. Scaffolds were then incubated in ECM and collagen type I solutions at 1 mg/ml for 48 h at 4 °C in MES buffer, pH 5. Scaffolds were rinsed gently. Immobilization of ECM was done under sterile conditions for all experiments.

5.2.9 Immobilization of solubilized ECM and collagen type I onto the PCL fibres by covalent conjugation for cell culture studies (sections 5.3.2 – 5.3.4)

For covalent conjugation (also referred to as chemical immobilization) scaffolds were washed in 70% ethanol and rinsed in deionized water. The PCL surface was hydrolysed with 1 N sodium hydroxide (NaOH) solution for 3 h. Scaffolds were then incubated in an aqueous treatment of excess 1-ethyl-3-(3-dimethylaminopropyl carbodiimide hydrochloride (EDC, 5mg/ml) and N-hydroxysulfosuccinimide (NHS, 5mg/ml) prepared in MES buffer, pH 5 (all from Sigma-Aldrich) for 2 h at 4°C. Scaffolds were rinsed in MES buffer and incubated in ECM and collagen type I at 0.5 mg/ml for 24 h at 4°C in MES buffer, pH 5. Scaffolds were rinsed and incubated in deionized water for 24 h under gentle constant agitation to remove physically adsorbed collagen. Control scaffolds with no immobilized protein (‘bare’) were incubated in ultra-pure water while the rest underwent collagen immobilization.

5.2.10 Isolation and expansion of mesenchymal stem cells (MSCs)

Bone marrow derived porcine MSCs were isolated as previously described (Thorpe *et al.*, 2012). Tripotential differentiation capacity was assessed. We used one isolate of porcine MSCs for all the experiments. MSCs were expanded in high-glucose Dulbecco’s modified Eagle’s

medium (DMEM) GlutaMAX supplemented with 10 % fetal bovine serum (FBS), penicillin (100 U/ml)-streptomycin (100 µg/ml) (all Gibco, Biosciences) and 0.25 µg/ml amphotericin B (Sigma-Aldrich) in a humidified atmosphere at 37 °C, 5% CO2. At the end of passage 2, cells were trypsinized and seeded onto the electrospun scaffolds. All cell studies were performed with cells in P2.

5.2.11 Seeding of MSCs on scaffolds and culture conditions

Scaffolds (collected for 10 min, 35 mm in length) were sterilized using ethylene oxide (EtO; Anprolene, Anderson products) and treated under sterile conditions thereafter. Sterile scaffolds were hydrated and divided into covalent conjugation, physical adsorption or bare scaffolds. Bare scaffolds were stored in ultra-pure water until the other groups underwent protein immobilization. Scaffolds underwent either covalent or physical immobilization of ligament solubilized ECM, cartilage solubilized ECM or collagen type 1 as described in sections 5.2.8 and 5.2.9. Ligament and cartilage ECM were dissolved in 0.02M acetic acid and diluted in MES buffer to 1 mg/ml for physical adsorption and 0.5 mg/ml for chemical conjugation. Collagen type 1 was diluted in MES buffer to the same concentrations. For physical adsorption scaffolds were incubated in 1 mg/ml cartilage or ligament ECM, or type 1 collagen for 48 h at 4 °C (as described in section 5.2.8). For covalent immobilization scaffolds underwent alkaline hydrolysis and then incubated in 0.5 mg/ml of cartilage or ligament ECM, or type 1 collagen for 24 h at 4 °C (as described in section 5.2.9). After ECM immobilization, all scaffolds (including bare scaffolds) were incubated in expansion media overnight at 37 °C before cell seeding. Expansion media consisted of high-glucose Dulbecco's Modified Eagle's Medium (DMEM, glutaMAX), 10% FBS, penicillin (100 U/ml)-streptomycin (100 µg/ml) (all from Gibco), and 0.25 µg/ml amphotericin B (Sigma).

Scaffolds were seeded at a cell density of 500,000 cells per scaffold (in 30 µl aliquot) and were cultured individually in Teflon rectangular wells. After 4 h, 2 ml of expansion media were added to each well. Scaffolds were maintained in expansion media at 20 % O_2 for 24 h. After this period, expansion media was replaced by basal media, basal media +CTGF, or basal media +TGFβ3. Basal media consisted of high-glucose DMEM (DMEM glutaMAX), penicillin (100 U/ml)-streptomycin (100 µg/ml), 100 µg/ml sodium pyruvate, 40 µg/ml L-proline, 4.7 µg/ml linoleic acid, 50 µg/ml L-ascorbic acid 2-phosphate, 1.5 mg/ml bovine serum albumin (BSA), 1X insulin-transferrin-selenium, 100 nM dexamethasone, (all from Gibco) and 0.25 µg/ml amphotericin B (Sigma). Basal media +CTGF was basal media supplemented with 100 ng/ml recombinant human connective tissue growth factor (CTGF; ProSpec-Tany, TechnoGene Ltd.). Basal media +TGFβ3 was basal media supplemented with 10 ng/ml recombinant human transforming growth factor-β3 (TGF-β3; ProSpec-Tany, TechnoGene Ltd.). Medium was changed twice weekly and cultures were maintained at 20% O_2. Acellular scaffolds were maintained under the same conditions as cellular scaffolds. A short study was conducted to confirm the confirm viability of MSCs with basal media plus the addition of CTGF. MSCs seeded scaffolds were cultured for 10 days after which a live/dead assay was performed (Figure 5.1).

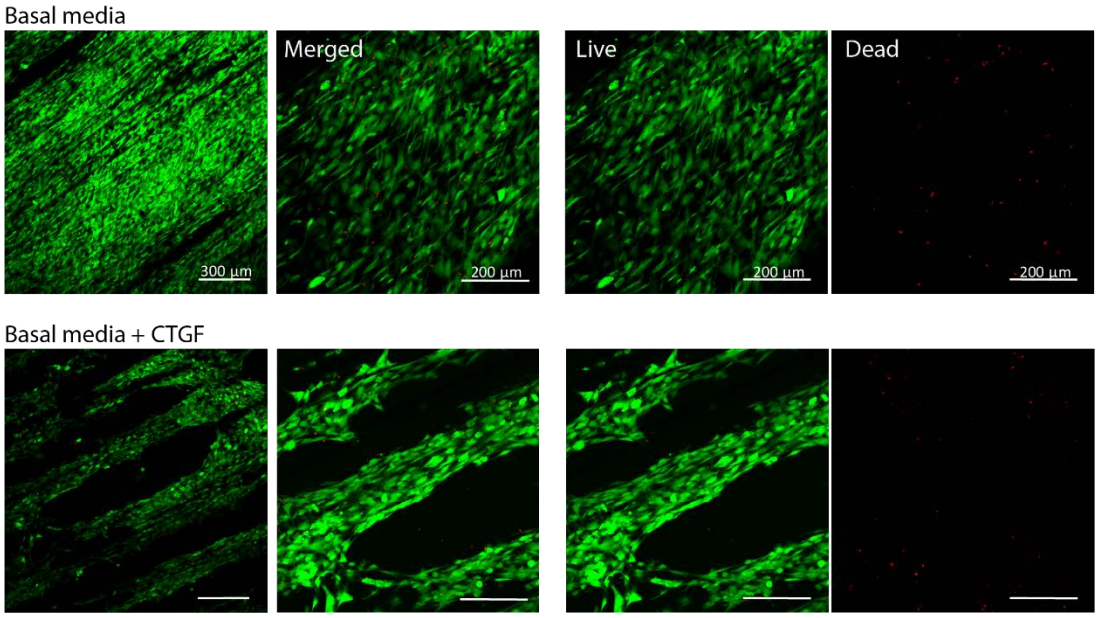

Figure 5.1 Basal media composition was favorable for MSCs with the addition of CTGF. Live/dead (live: green, dead: red) 10 days after cell seeding.

5.2.12 Cell viability, visualization of cell morphology, and counting of pre-adipocytes

Cell viability was assessed after 24 h by staining cells using the Live/dead assay kit (Invitrogen, Bioscience). Briefly, scaffolds were rinsed in PBS and incubated in 4 mM calcein-AM and 2 mM ethidium homodimer-1 in PBS for 1 h at 37 °C. Scaffolds were rinsed in PBS and visualized under a scanning confocal microscope (Leica SP8) at an excitation and emission wavelengths of 515 and 615 nm. Analysis was performed in Leica Microsystems software (Leica Application Suite X).

Cell morphology was assessed by staining cell nuclei with DAPI and filamentous actin with rhodamine phalloidin (Invitrogen). Scaffolds were fixed in 4% paraformaldehyde (PFA) overnight at 4 °C, rinsed with PBS and permeabilized in 0.5% Triton-X 100, incubated in 1.5% bovine serum albumin (BSA) to block non-specific labelling and stained with a 1.5% BSA solution containing rhodamine phalloidin (1:40) for 1 h at room temperature (RT). Cell nuclei were stained with DAPI (1:100) for 10 min at RT (all from Sigma). Samples were imaged using a scanning confocal microscope (Leica SP8). Analysis was performed in Leica Microsystems

software (Leica Application Suite X). Cell area, circularity and aspect ratio were calculated using ImageJ. In circularity, a value of 1 indicates a perfect circle; as the value approaches 0, it indicates an increasingly elongated shape.

To count pre-adipocityes per cm, brightfield images were acquired for each condition (n= 4). Pre-adipocytes were counted manually using ImageJ. Data is presented as mean ± standard deviation of the number of pre-adipocytes per cm^2.

5.2.13 Gene expression

Gene expression was assessed after 10 days using quantitative real-time PCR (n=5/group). Cells were lysed using RLT lysis buffer (Qiagen) supplemented with 10 µl/ml β-mercaptoethanol (Sigma-Aldrich) and stored at –80°C. For RNA isolation, cell lysates were thawed and homogenized using QIAshredder columns (Qiagen). Total RNA was isolated and further purified using RNeasy Mini kits (Qiagen) following manufacturer's instructions. Total RNA concentration and purity was determined using a Nanodrop spectrophotometer. 500 ng of RNA per sample was reverse transcribed into cDNA using High-Capacity cDNA Reverse Transcription Kit (Applied Biosystems) following manufacturer's instructions. 25 ng of cDNA were amplified using an ABI 7500 sequence detection system (Applied Biosystems) and Syber select master mix (Applied Biosystems). Expression of collagen type I (*COL1A1*) and III (*COL3A1*), tenomodulin (*TNMD*), cartilage oligomeric matrix protein (COMP), aggrecan (*ACAN*), SRY-Box 9 (*SOX9*) and beta-2 microglobulin (*B2M*) was evaluated. The porcine specific primer sequences (KiCqStart SYBR Green Primers, Sigma) used for amplification are listed in Table 1. The primer concentrations were optimized for efficiency (95 – 105% efficiency) and specificity (analysis of melting curve). Quantification of the target gene expression relative to 'day 0' was performed using the $2^{-\Delta\Delta C_T}$ method (Schmittgen and Livak, 2008) with *B2M* as an endogenous control. 'day 0' expression is the gene expression of the same population of cells harvested at day 0 that were not seeded on scaffolds.

Gene	Primer sequences	
B2M	Forward:	ACTGAGTTCACTCCTAACG
	Reverse:	TGCAGCATCTTCATAATCTC
COL1A1	Forward:	TAGACATGTTCAGCTTTGTG
	Reverse:	GTGGGATGTCTTCTTCTTG
COL3A1	Forward:	TCATCCCACTGTTATTTTGG
	Reverse:	CTCTATCCGCATAGGACTG
ACAN	Forward:	GACCACTTTACTCTTGGTG
	Reverse:	TCAGGCTCAGAAACTTCTAC
TNMD	Forward:	GCTAATTGTCCTATTTTGGGG
	Reverse:	GAAAGTGTGTTCCATGTCG
SOX9	Forward:	CAGACCTTGAGGAGACTTAG
	Reverse:	GTTCGAGTTGCCTTTAGTG
COMP	Forward:	AAGGACAGTGATGGTGATG
	Reverse:	ATCCCTCTGATCTGCATTG

Table 5.1 Primer sequences used for qPCR

5.2.14 Histology

Matrix synthesis was evaluated from histological appearance of cryosections of the scaffolds after 21 days of culture. Samples were fixed overnight in 4% PFA at 4 °C and rinsed in PBS. Samples were embedded in optimal cutting temperature (O.C.T.) medium and flash frozen in liquid nitrogen. Embedded samples were cryosectioned longitudinally to 5 µm thickness perpendicular to the fiber plane. Sections were stained with Alcian blue, and Picrosirius red to assess glycosaminoglycan (GAG) and collagen content.

5.2.15 Statistical analysis

Statistical analysis was performed with Prism 6 Graphpad software. Comparisons were made using one-way or two-way analysis of variance (ANOVA) with Tukey post-hoc testing for multiple comparisons. Data are presented as mean ± standard deviation (s.d.) and as mean ± standard error of the mean (SEM) for qRT-PCR. Sample sizes are indicated in the methods

section and within the corresponding figure legends. Significance was accepted at a level of $p < 0.05$.

5.3 Results

5.3.1 Characterization of the ECM-functionalized scaffolds

Aligned fibres with a diameter of ~5 µm were electrospun for 10 min and baled to form scaffolds as described in Chapter 4 (Figure 5.2 a). Solubilized ligament and cartilage ECMs were immobilized onto the surface of the microfibres. The solubilized ECMs were characterized using SDS-PAGE gels (Figure 5.2 b). Defined protein bands were observed between 98 and 198 kDa, corresponding to collagen type 1 (130 kDa) and collagen type 2 (142 kDa). This confirms the presence of collagen type 1, the major structural protein in ligament tissue (Sugimoto, Takimoto, Akiyama, *et al.*, 2013), in the solubilized ligament-ECM; and collagen type 2, the major structural protein in cartilage tissue (Sugimoto, Takimoto, Akiyama, *et al.*, 2013), in the solubilized cartilage-ECM. The commercially available collagen types 1 and 2 were included as positive controls.

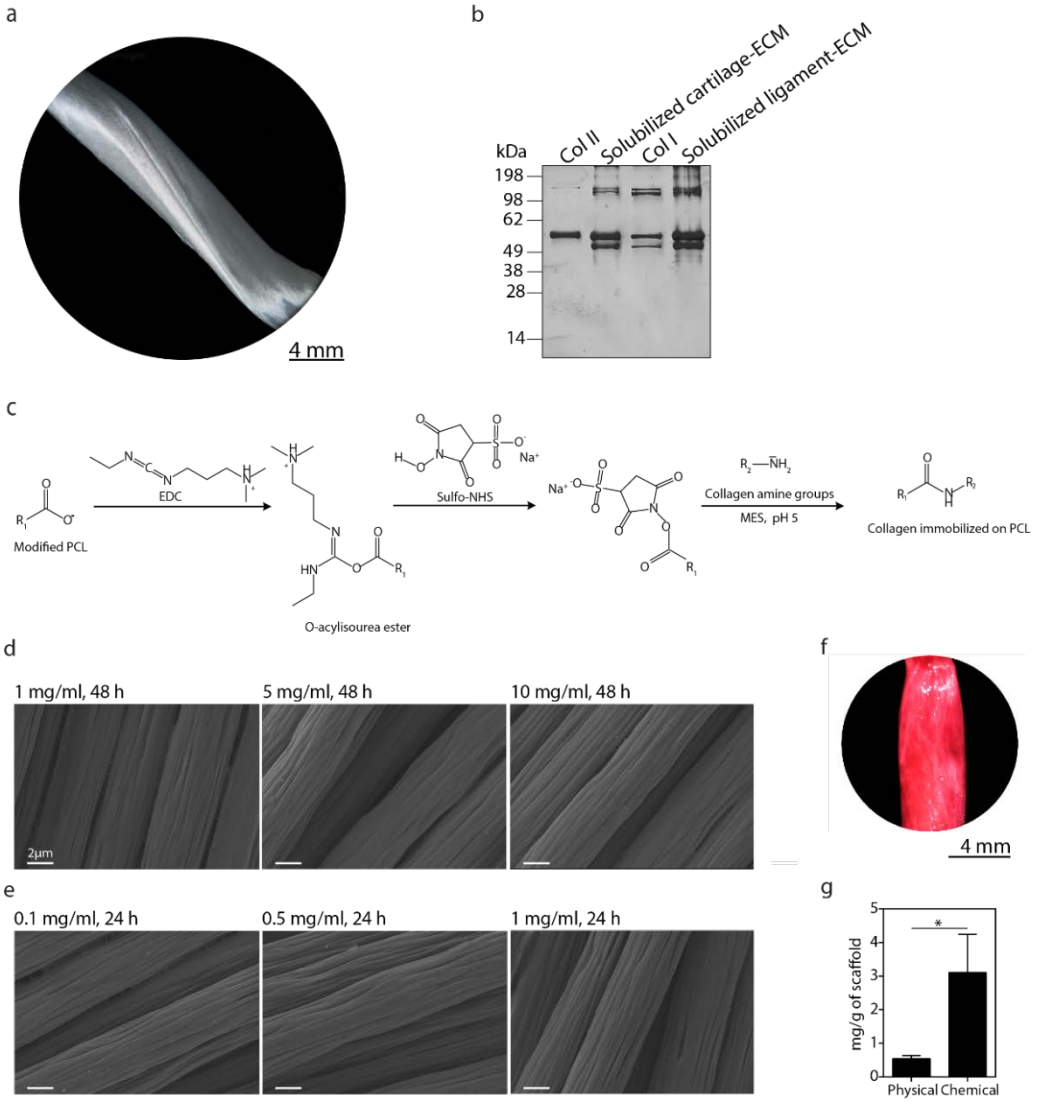

Figure 5.2 Characterization of the ECM and of the ECM-functionalized scaffolds. **a** Stereo-image of an electrospun-fibre bundle collected for 10 min and baled to form the scaffolds used for cell culture studies. Scale bar, 4mm. **b** SDS-PAGE showing the Coomassie stained protein bands of solubilized ligament and cartilage ECM and commercially available collagen types I and II. **c** PCL and collagen coupling reaction by carbodiimide chemistry. **d** SEM images of scaffolds with collagen type I immobilized at 1, 5 and 10 mg/ml via physical adsorption for 48 h. Scale bars, 2 µm. **e** SEM images of scaffolds with collagen type I immobilized at 0.1, 0.5 and 1 mg/ml of via covalent conjugation for 24 h. Scale bars, 2 µm. **f** Stereo-image of a bundle undergone physical adsorption of collagen (1 mg/ml for 48 h) and stained with Picrosirius red. Scale bar, 4 mm. **g** mg of ECM attached to the fibre-bundles by both methods per gram of microfibers. Student's t-test, *: $P<0.0001$ ($n = 6$).

Commercially available collagen type 1 from rat tail (Col-1) was used as a model protein with which to characterize the different protein and solubilized ECM immobilization treatments. Protein immobilization onto the PCL fibres was performed by covalent

conjugation as well as physical adsorption. For the covalent conjugation, fibres underwent an alkaline hydrolysis pre-treatment to introduce carboxylic acid groups on the PCL surface (Figure 5.3). The chemical composition of the PCL scaffolds after alkaline hydrolysis was analysed using X-ray photoelectron spectroscopy (XPS) to confirm the introduction of carboxylic acid (-COOH) groups on the surface (Figure 5.4). An analysis of the atomic percentage of oxygen (O), carbon (1s) (C) and the ratio of O to C (O/C) was performed as a measure of the extent of degradation of PCL ester groups into –COOH and –OH groups after alkaline hydrolysis. Incubation for 15 min, 3 h, 5 h and 8 h in 1 N NaOH was investigated. Incubation in sodium hydroxide for 8 h resulted in the highest O/C ratio indicating the highest oxidation of the PCL chain. The hydrolysis treatment of 3 h was selected since prolonged surface alkaline hydrolysis resulted in fibre breakage (data not shown). Reports have shown that 1 - 4 h of 1N NaOH treatment is ideal for protein immobilization (Park *et al.*, 2007; Ghasemi-Mobarakeh *et al.*, 2010; Hartman *et al.*, 2010). EDC/NHS chemistry was then used to activate the carboxyl groups which further reacted with the collagen amines to form amide linkages (Figure 5.2 c and Figure 5.5). For the physical adsorption, PCL fibres were incubated directly with the ECM and Col-1 solutions. Physical immobilization occurs by the strong hydrogen bonding between the carbonyl functional groups (C=O) of PCL and the carboxylic acid (R-COOH) of the collagen and ECM solutions.

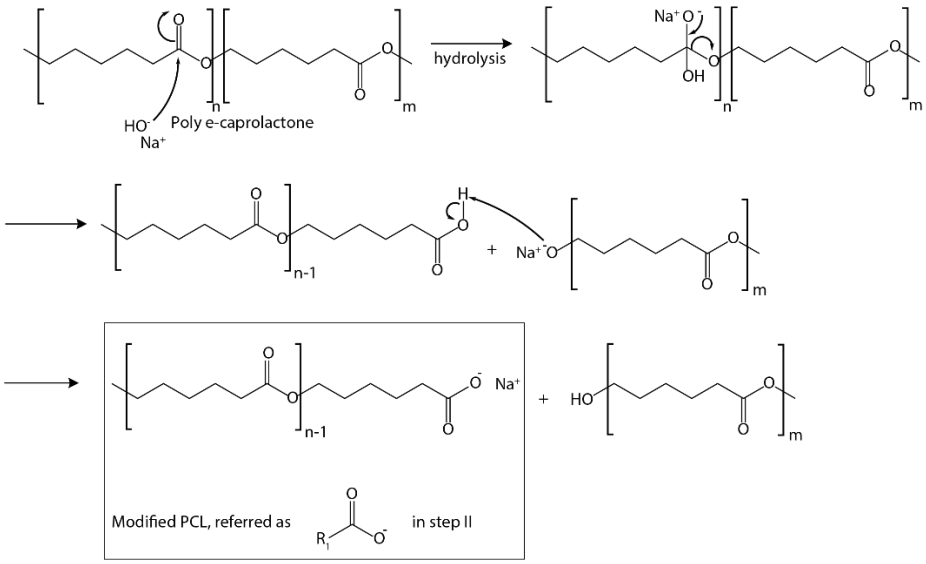

Figure 5.3 Hydrolysis of polycaprolactone with NaOH to expose carboxylic groups. By products were washed with water.

a

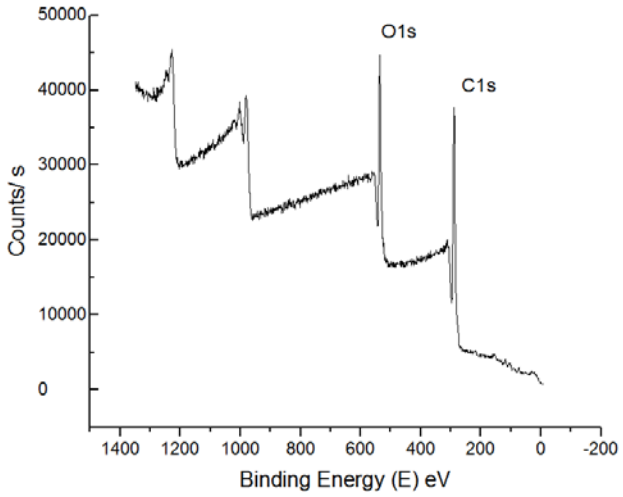

b

Atomic %	Carbon	Oxygen	O/C ratio
Bare PCL	77.95	22.05	0.2828
15 min	77.18	22.82	0.2956
3 h	77.09	22.91	0.2971
8 h	76.61	23.39	0.3053

Figure 5.4 Atomic composition of the PCL scaffolds before and after alkaline hydrolysis. **a** XPS survey spectrum for 3 h of NaOH incubation. **b** Peak analysis and oxygen/carbon ratio. Upon alkaline hydrolysis, some ester groups in PCL chains degraded into oxygen-containing groups (i.e. -COOH and -OH groups) therefore the increase in the O/C atomic ratio.

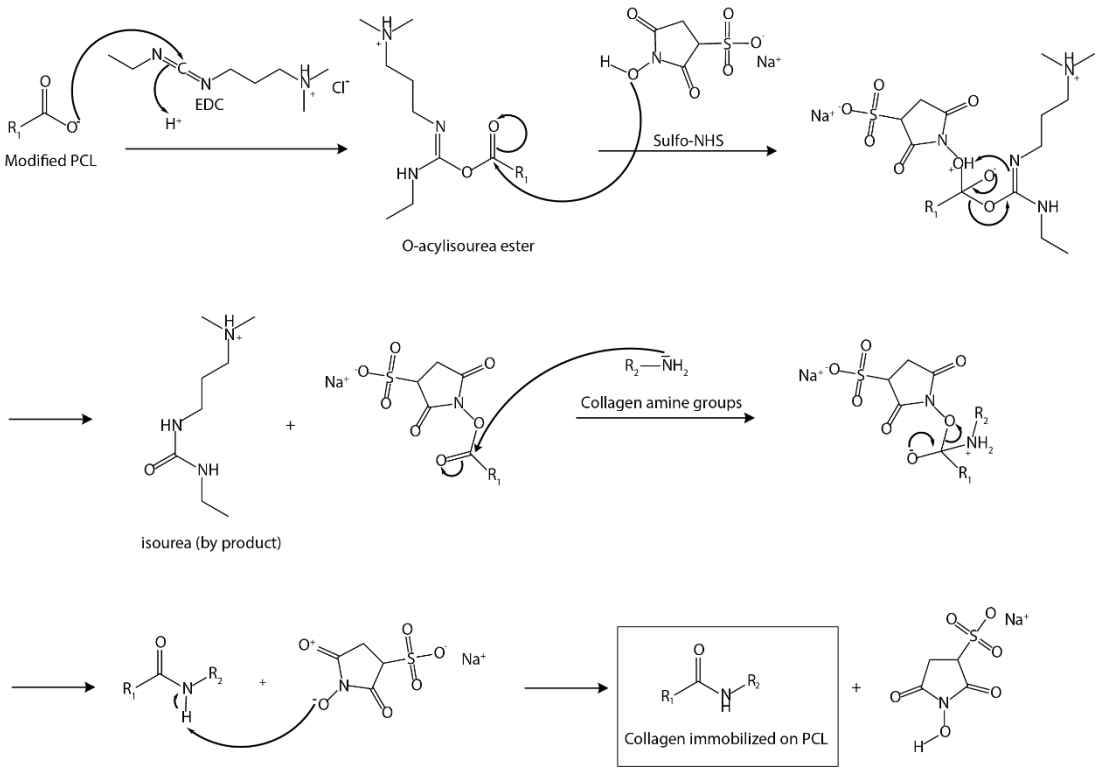

Figure 5.5 ECM components were covalently conjugated onto the hydrolysed PCL surface by a condensation reaction between the carboxylic acid groups on the hydrolysed PCL surface and the primary amines (-NH2) of ECM components using carbodiimide chemistry. NHS was used to prepare amine-reactive esters of carboxylate groups (-COOH) for chemical immobilization. Carboxylates (- COOH) were reacted to NHS in the presence of EDC, resulting in a semi-stable NHS ester, which may then be reacted with the primary groups to form amide crosslinks. Reaction by-products were removed with washes in between the reaction steps.

XPS analysis shows the successful immobilization of collagen type 1 onto the scaffold by the appearance of the Nitrogen (N1s) peak in the spectrum (Figure 5.6). The N% was quantified by integrating the area of the element peaks (Table 5.2), which demonstrated that even the lowest concentrations of collagen (0.1 mg/ml) could be successfully immobilized and detected on the scaffold surface. Similar N% (or N/C ratio) on the scaffolds was obtained by using 1 mg/ml for the physical adsorption and 0.5 mg/ml for the chemical conjugation. The N/C ratio is used to assess the relative amount of immobilized collagen. Therefore, 1 mg/ml for 48 h for the physical and 0.5 mg/ml for 24 h for the chemical conjugation were selected for further analysis.

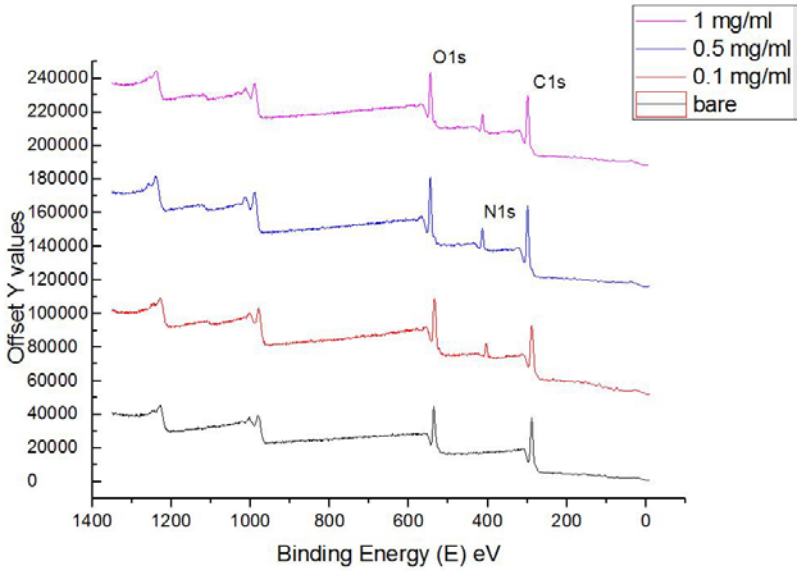

Figure 5.6 XPS spectrum of bare PCL and scaffolds that underwent collagen immobilization. The analysis confirmed the presence of collagen on the scaffolds by the appearance of the Nitrogen peak (N1s). Oxygen (O1s), nitrogen (N1s) and carbon (C1s) with binding energies at 530 eV, 400.14 eV and 285.0 eV are indicated.

Collagen concentration	N (%)	C (%)	O (%)	N/C
Physical adsorption				
Bare	-	77.95	22.05	-
0.1 mg/mL	5.62	77.89	16.49	0.072
0.5 mg/mL	8.9	74.16	16.94	0.120
1 mg/mL	9.87	73.92	16.21	0.133
Chemical conjugation				
Bare	-	77.09	22.91	-
0.1 mg/mL	8.05	69.32	22.63	0.116
0.5 mg/mL	9.83	70.31	19.86	0.139
1 mg/mL	10.14	70.57	19.29	0.143

Table 5.2 Chemical composition of PCL scaffolds after physical or chemical immobilization

SEM micrographs were acquired to confirm topography was maintained after ECM immobilization. Images show that physically immobilized collagen maintained the fibrillary topography (Figure 5.2 d). Similarly, the covalently conjugated collagen maintained the fibrillary topography (Figure 5.2 e). The distribution of the collagen type 1 after physical and chemical immobilization onto the scaffolds was visually evaluated by Picrosirius red staining, which confirmed that collagen was uniformly distributed through the scaffold (even at the

lowest collagen concentration) (Figure 5.2 f). When solubilized ECM was immobilized onto the scaffold using the same concentrations as used for type I collagen, the amount of total collagen on the scaffold after covalent immobilization was higher than that achieved for physical adsorption (as measured using a hydroxyproline assay).

5.3.2 The bioactivity of solubilized ligament and cartilage ECM

To assess the bioactivity of the solubilized ECMs, MSCs were cultured on microfibrillar scaffolds functionalized covalently (0.5 mg/ml for 24 h) or physically (1 mg/ml for 48 h) with ligament (L-ECM) or cartilage-ECM (C-ECM) in the absence of growth factors. MSCs were also cultured on scaffolds functionalized with type I collagen (Col-1) as a control. After 24 hours and 10 days in culture, MSC shape was analysed (Figure 5.8) as cell shape has been linked to lineage commitment (McBeath *et al.*, 2004; Engler *et al.*, 2006). As early as 24 h after cell seeding, cells adopted distinct morphologies in response to the underlying immobilized protein (Figure 5.7). MSCs seeded onto bare and L-ECM functionalized scaffolds show elongated cell bodies (Figure 5.7 a, b). MSCs seeded onto C-ECM functionalized scaffolds show smaller and more rounded cell bodies (Figure 5.7 c). MSCs seeded onto Col-1 functionalized scaffolds adopted a mixture of elongated and smaller, rounded cell bodies (Figure 5.7 d).

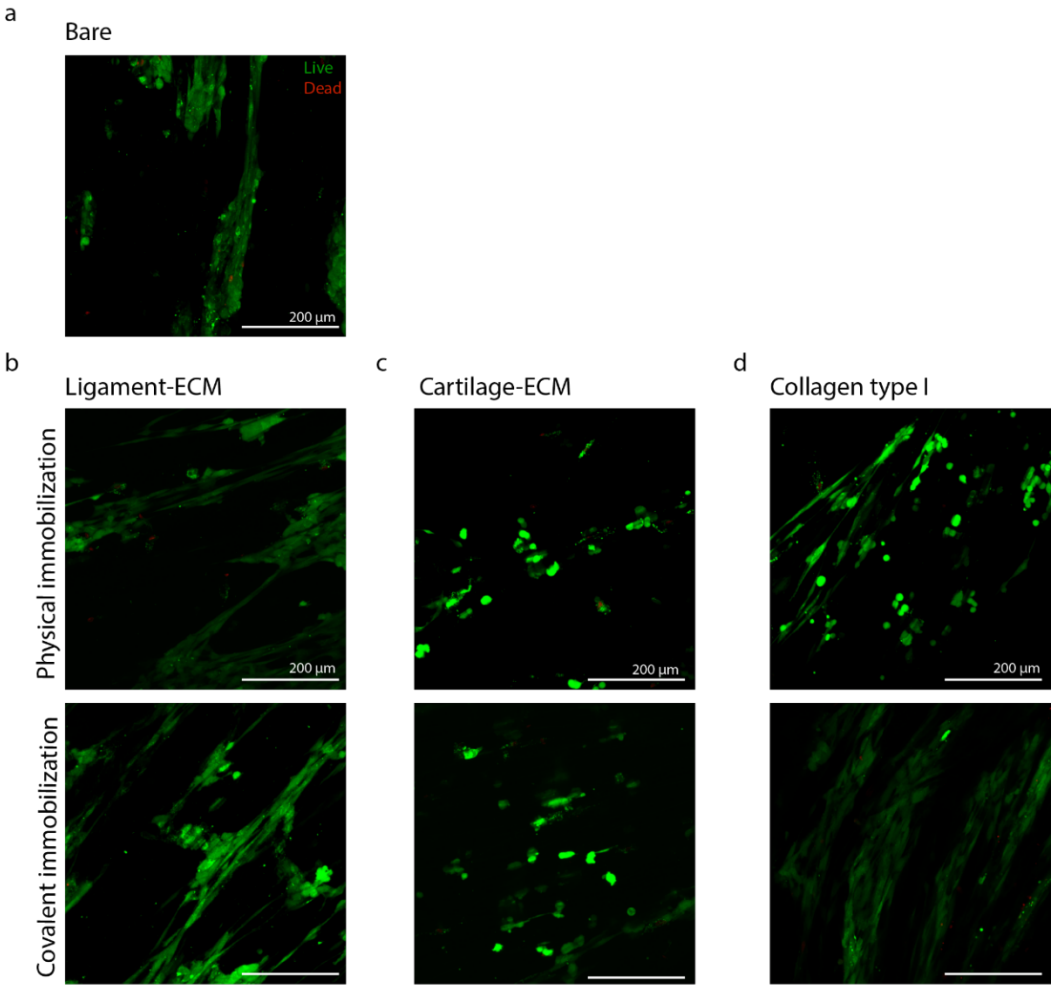

Figure 5.7 Live/dead staining (green: 'live', red: 'dead') of MSCs 24 h after seeding. Scale bars, 200 µm.

After 10 days in culture, MSCs predominantly adopted elongated cell bodies, aligned in the direction of the underlying substrate. This was particularly evident on covalently bound ligament-ECM, where MSCs appeared highly elongated and organized parallel to the orientation of the fibres (Figure 5.8 b). MSCs on bare scaffolds, covalently immobilized C-ECM, and on physically immobilized Col-1 extended laterally to bridge across multiple fibres. Despite the general elongated cell shape, differences in the shape of cell nuclei were observed. The nuclei of MSCs on C-ECM and Col-1 could be better described as rounded, displaying the highest degree of circularity (C-ECM physical, circularity: 0.65 ± 0.09; C-ECM chemical, circularity: 0.62 ± 0.11; Col-1 physical, circularity: 0.65 ± 0.05 and Col-1 chemical, circularity:

0.65 ± 0.12) (Figure 5.9 a). Conversely, MSCs on L-ECM displayed cell nuclei with high aspect ratio indicating an elongated shape (physical, aspect ratio: 1.84 ± 0.34 and chemical, aspect ratio: 2.88 ± 0.76) (Figure 5.9 b). MSC nuclei area was similar across conditions (Figure 5.9 c).

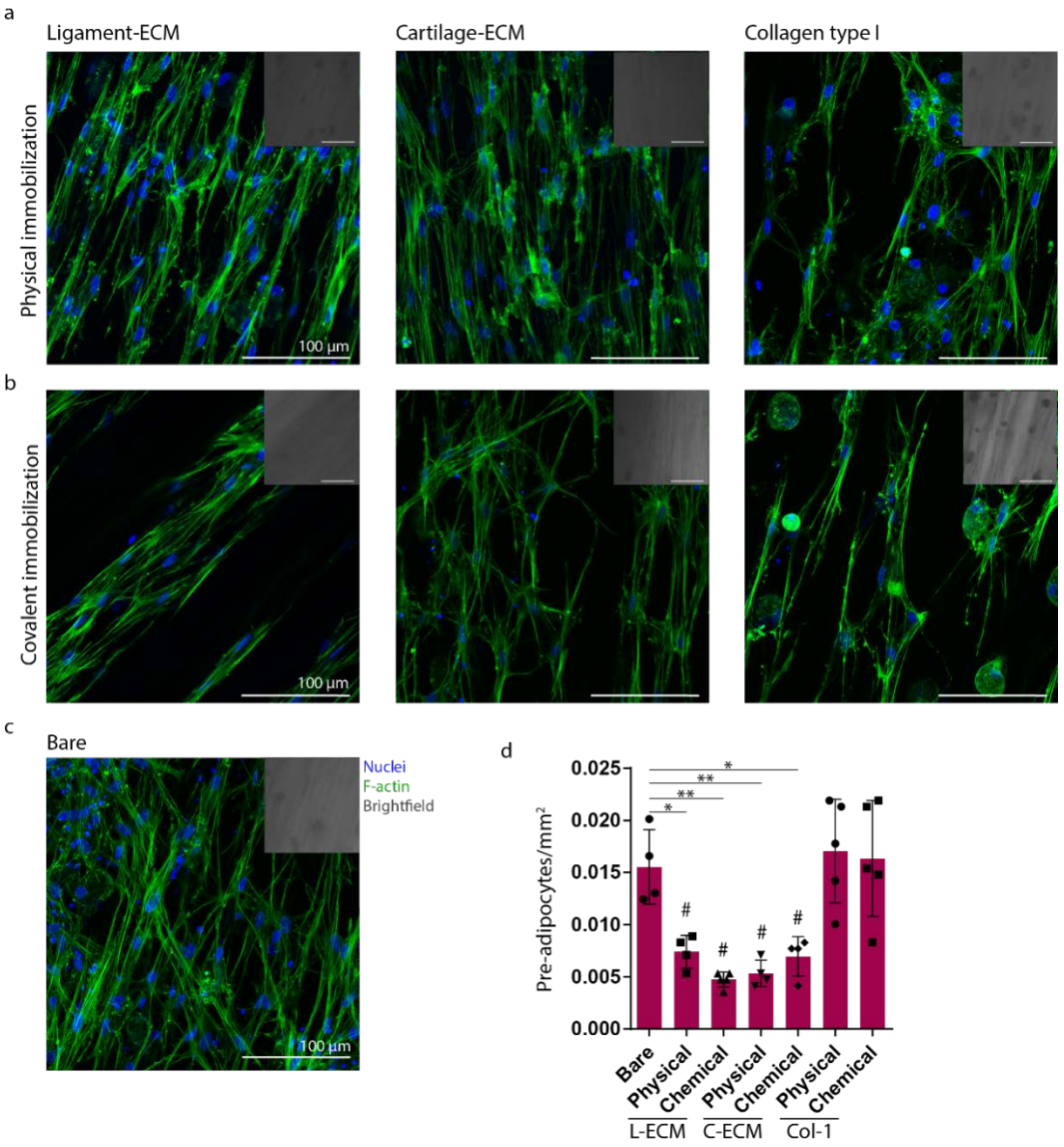

Figure 5.8 Cell nuclei (blue) and F-actin (green) staining of MSCs on bare and functionalized scaffolds in the absence of growth factors. **a** MSCs on ligament ECM, cartilage ECM or collagen type I immobilized by physical adsorption and covalent conjugation (**b**). **c** MSCs on bare scaffolds. Brightfield images appear in the top right corner (grey). Scale bars, 100 µm. **d** Pre-adipocytes per mm^2 of scaffold. #, $p < 0.05$ versus Col-1 physical and chemical. Error bars, mean ± s.d., one-way ANOVA ($p < 0.05$) with Tukey's multiple comparisons test (n =4).

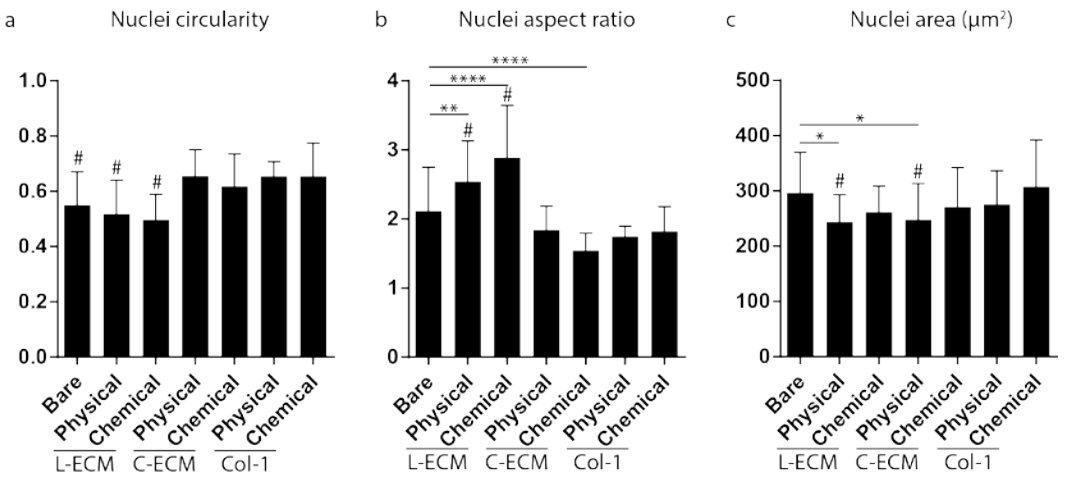

Figure 5.9 Circularity, aspect ratio and area of MSCs in the absence of growth factors. L-ECM: ligament-ECM; C-ECM: cartilage-ECM; and Col-1: type I collagen. **a** Nuclear circularity. A value of 1 indicates a perfect circle. #, $p < 0.05$ versus C-ECM physical and chemical, and Col-1 physical and chemical. **b** Nuclei aspect ratio. #, $p < 0.0001$ versus C-ECM physical and chemical, and Col-1 physical and chemical. **c** Nuclei area. #, $p < 0.001$ versus Col-1 chemical. Error bars, mean ± s.d., one-way ANOVA ($p < 0.05$) with Tukey's multiple comparisons test ($n \geq 50$ regions of interest (ROI)).

Somewhat unexpectedly, in the absence of growth factors, lipid droplets were observed on the surface of the MSC laden scaffolds (see brightfield images of Figure 5.8). Pre-adipocytes were distinguishable by their multiple locus with small lipid inclusions. Bare scaffolds and scaffolds with Col-1 showed the highest number of lipid droplets per mm^2 of scaffold, while the scaffolds functionalized with solubilized ECM showed the lowest number of pre-adipocytes per mm^2 (Figure 5.8 d).

The physical incorporation of any of the proteins (namely, L-ECM, C-ECM or Col-1) enhanced the expression of *COL1A1* and *COL3A1* in the absence of growth factors (Figure 5.10). Physical immobilization of L-ECM further promoted the expression of the highly specific ligament-hallmark gene *TNMD* (Shukunami *et al.*, 2006).

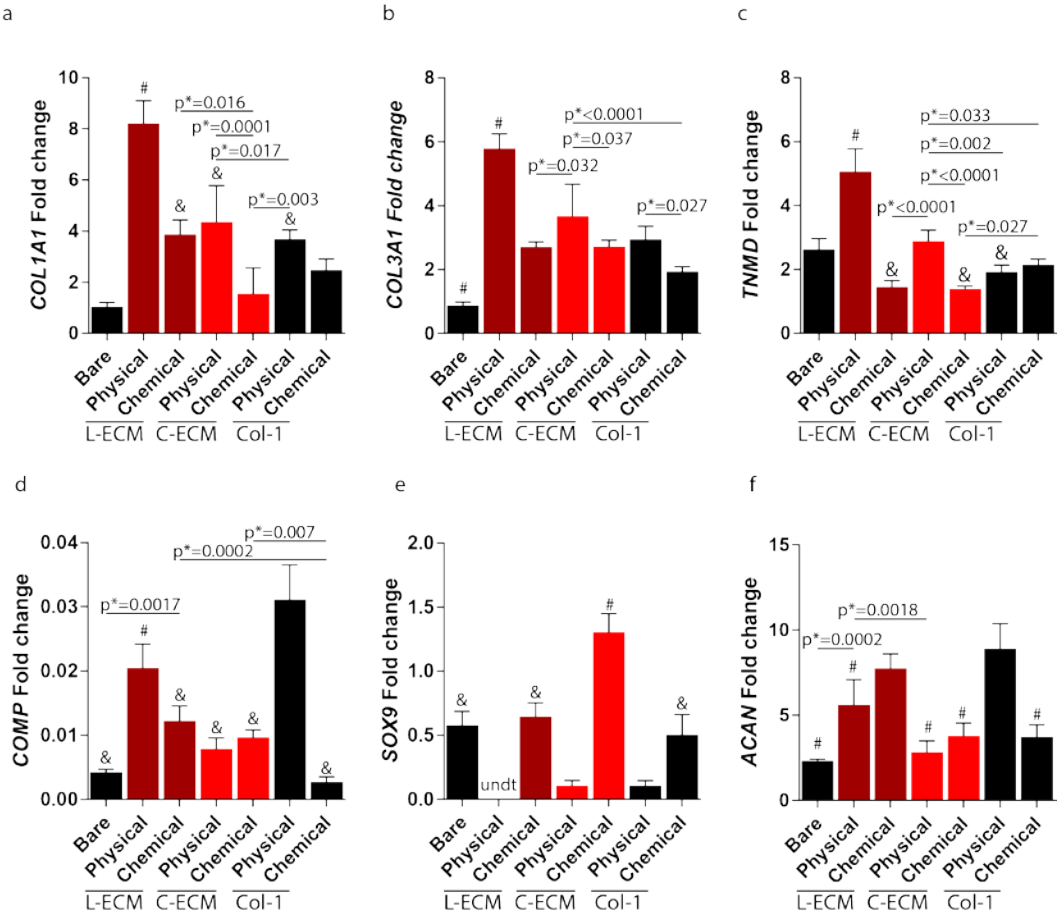

Figure 5.10 Gene expression of cartilage and ligament genes of MSCs in the absence of growth factors. L-ECM: ligament-ECM; C-ECM: cartilage-ECM; and Col-1: type I collagen. **a** Collagen type I (*COL1A1*). #, $p < 0.0001$ versus the rest of the conditions; &, $p < 0.001$ versus bare. **b** Collagen type 3 (*COL3A1*). #, $p < 0.0001$ versus the rest of the conditions. **c** Tenomodulin (*TNMD*). #, $p < 0.0001$ versus the rest of the conditions; &, $p < 0.05$ versus bare. **d** Cartilage Oligomeric Matrix Protein (*COMP*). #, $p < 0.0001$ versus the rest of the conditions; &, $p < 0.0001$ versus chemical Col-1. **e** SYR box-9 (*SOX9*). #, p< 0.0001 versus the rest of the condition; &, $p \leq 0.001$ versus C-ECM physical and Col-1 physical. Undt, indicates undetermined. **f** Aggrecan (*ACAN*). #, $p < 0.0001$ versus chemical immobilization of L-ECM and chemically/physically immobilized Col-1. Data was normalized to MSCs harvested at day 0. Error bars, mean ± SEM., one-way ANOVA ($p < 0.05$) with Tukey's multiple comparisons test (n= 5).

Expression of SYR-box 9 (SOX9), a transcription factor essential for cartilage formation (Bi *et al.*, 1999), was highest on scaffolds with chemically immobilized C-ECM. Surprisingly, the expression of *COMP* (a non-collagenous matrix protein that precedes *COL2A1* during chondrogenesis (Li *et al.*, 2011)) and *ACAN* in C-ECM scaffolds was lower than on scaffolds functionalized with L-ECM and Col-1.

In summary, the initial elongated cell shape adopted as early as 24 h, was maintained in the MSCs on L-ECM, and their nuclei is elongated. Physical immobilization of L-ECM promoted the highest expression of ligament-hallmark genes *COL1A1*, *COL3A1* and *TNMD*. On the other hand, the initial rounded and small cell shapes that MSCs adopted on C-ECM was not maintained over time, however their nuclei were rounded and chemical immobilization of C-ECM showed modest upregulation of *SOX9*.

5.3.3 Effect of solubilized ligament and cartilage ECM on MSC differentiation in the presence of CTGF

To enhance ligament differentiation, MSCs were further stimulated with CTGF. After 10 days of culture in the presence of CTGF, MSCs predominantly elongated in the direction of the underlying fibres (Figure 5.11), especially on L-ECM, Col-1 and bare scaffolds. MSCs on C-ECM functionalised scaffolds, especially the physically immobilized group, spread and showed cell bodies bridging perpendicular to the fibre axis, similar to that observed in the absence of growth factors (Figure 5.8). In the presence of CTGF, MSCs on bare and L-ECM displayed cell nuclei with higher aspect ratios (bare: 3.11 ± 0.69; L-ECM physical: 2.67 ± 0.57; L-ECM chemical: 2.93 ± 0.77) compared to nuclei of MSCs on C-ECM or Col-1 functionalised scaffolds (Figure 5.12 a). The latter groups also showed the highest circularity (C-ECM physical: 0.65 ± 0.09; C-ECM chemical: 0.57 ± 0.09; Col-1 physical: 0.69 ± 0.09; Col-1 chemical: 0.68 ± 0.11) (Figure 5.12 b). Cell nuclei area was similar across conditions, with cell nuclei area of ~250 μm^2 (Figure 5.12 c).

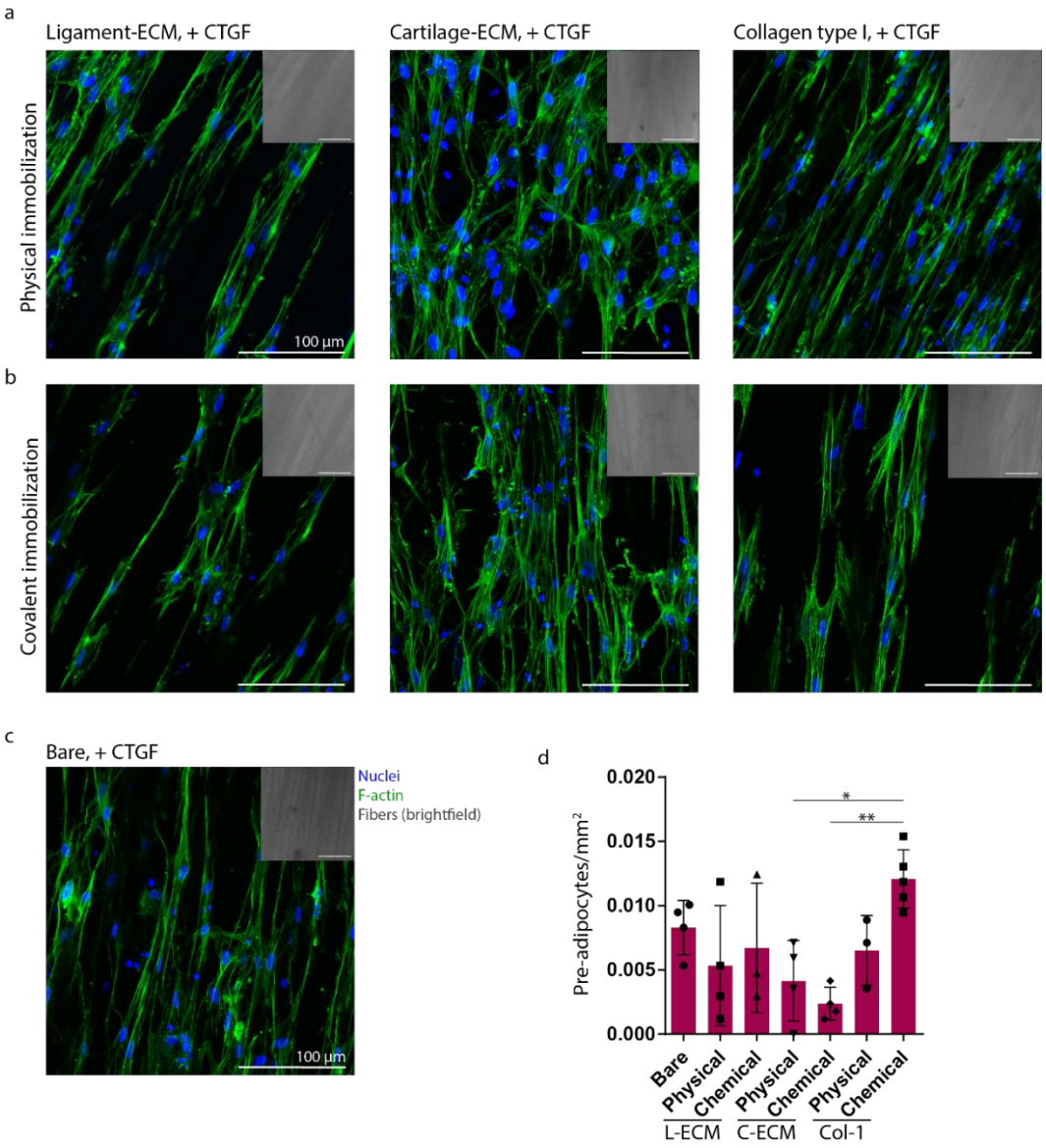

Figure 5.11 Cell nuclei (blue) and F-actin (green) staining of MSCs on bare and functionalized scaffolds in the presence of CTGF. **a** MSCs on ligament ECM, cartilage ECM or collagen type I immobilized by physical adsorption and covalent conjugation (**b**). **c** MSCs on bare scaffolds. Brightfield images appear in the top right corner (grey). Scale bars, 100 µm. **d** Pre-adipocytes per mm^2 of scaffold. Error bars, mean ± s.d., one-way ANOVA ($p < 0.05$) with Tukey's multiple comparisons test (n =4).

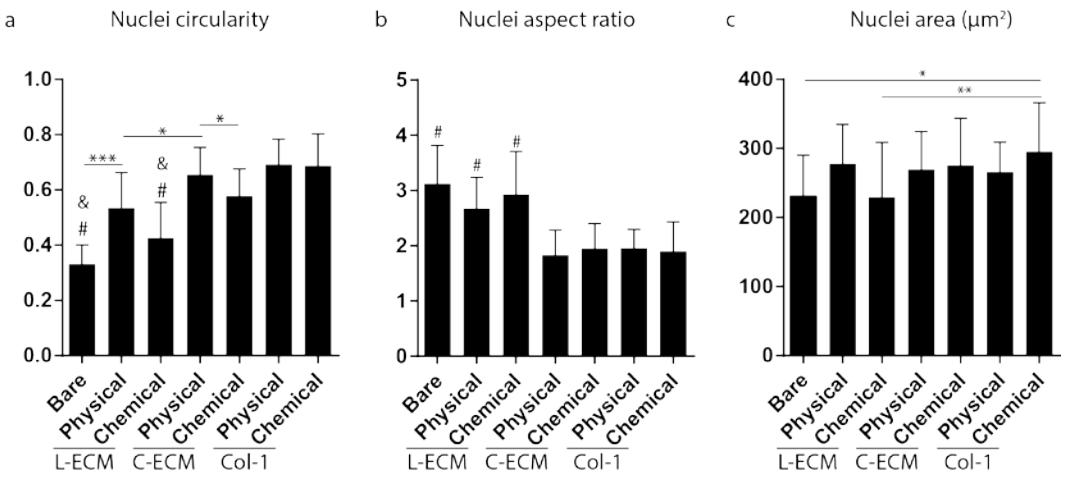

Figure 5.12 Circularity, aspect ratio and area of MSCs stimulated with CTGF. L-ECM: ligament-ECM; C-ECM: cartilage-ECM; and Col-1: type I collagen. **a** Nuclear circularity. A value of 1 indicates a perfect circle. #, $p < 0.0001$ versus Col-1 physical and chemical; &, $p < 0.0001$ versus C-ECM physical and chemical. **b** Nuclei aspect ratio. #, $p < 0.01$ versus C-ECM physical and chemical, and Col-1 physical and chemical. **c** Nuclei area. #, $p < 0.001$ versus Col-1 chemical. Error bars, mean ± s.d., one-way ANOVA ($p < 0.05$) with Tukey's multiple comparisons test ($n \geq 50$ regions of interest (ROI)).

In the presence of CTGF, lipid droplets were also observed (see brightfield images of Figure 5.11), but in lower numbers compared to those in the absence of growth factors (section 5.3.2) (Figure 5.8 d). MSC on C-ECM showed the lowest number of lipid droplets per mm^2 of scaffold in the presence of CTGF.

The physical immobilization of L-ECM and Col-1 in the presence of CTGF stimulated the MSCs to express the higher levels of *COL1A1, COL3A1* and *TNMD* compared to all other conditions (Figure 5.13). Levels of *COL1A1* expression for L-ECM + CTGF were ~2-fold lower than in the absence of CTGF, but ~2 fold higher for *TNMD* expression with the addition of CTGF. CTGF stimulation of MSCs seeded onto Col-1 scaffolds lead to higher expression of *COL1A1, COL3A1* and *TNMD* compared to that observed in the absence of this growth factor (Figure 5.13). In general *COMP* expression was lower in the presence of CTGF compared to no growth factor conditions, especially for physically immobilised Col-1 scaffolds. Despite stimulation with CTGF, the expression of *SOX9* in the chemically immobilized (C-ECM) scaffolds was higher than that observed in L-ECM or Col-1 scaffolds.

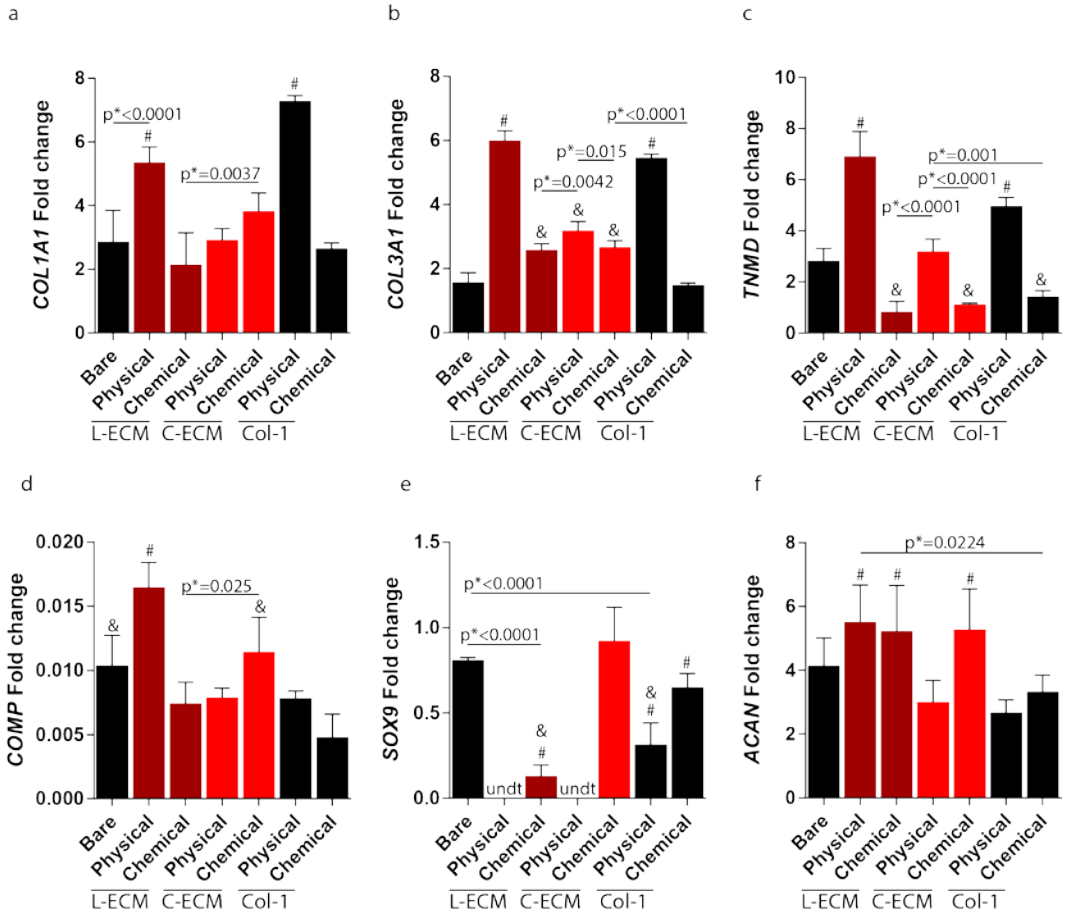

Figure 5.13 Gene expression of cartilage and ligament genes in MSCs stimulated with CTGF. L-ECM: ligament-ECM; C-ECM: cartilage-ECM; and Col-1: type I collagen. **a** Collagen type I (COL1A1). #, $p < 0.01$ versus the rest of the conditions. **b** Collagen type 3 (COL3A1). #, $p < 0.05$ versus the rest of the conditions; &, p<0.0001 versus bare. **c** Tenomodulin (TNMD). #, $p < 0.0001$ versus the rest of the conditions; &, $p < 0.01$ versus bare. **d** Cartilage Oligomeric Matrix Protein (*COMP*). #, $p < 0.01$ versus the rest of the conditions. **e** SYR box-9 (SOX9). #, p< 0.0001 versus C-ECM chemical; &, p < 0.01 versus Col-1 chemical. Undt, indicates undetermined. **f** Aggrecan (ACAN). #, $p < 0.05$ versus C-ECM physical and Col-1 chemical. Data was normalized to MSCs harvested at day 0. Error bars, mean ± SEM., one-way ANOVA ($p < 0.05$) with Tukey's multiple comparisons test (n= 5).

In summary, the addition of CTGF did not dramatically enhance ligament-specific differentiation on scaffolds functionalised with ECM components. Physical immobilization with L-ECM still provided an environment most conducive to ligamentogenesis, although in these conditions differentiation was similar to that observed on physically immobilized Col-1 scaffolds.

5.3.4 Effect of solubilized ligament and cartilage ECM on MSC differentiation in the presence of TGF-β3

MSCs on ECM functionalised scaffolds were also stimulated with TGF-β3 to enhance chondrogenic differentiation. After 10 days in culture in the presence of TGF-β3, the shape of MSCs was different to that observed in the absence of growth media and in the presence of CTGF (sections 5.3.2 and 5.3.3) (Figure 5.14). Cellular aggregations were visible, especially in scaffolds with covalently immobilized L-ECM and C-ECM. In the presence of TGFβ-3, MSCs on bare scaffolds displayed the lowest values of circularity compared to the functionalized scaffolds (Figure 5.15 a). MSCs in the presence of TGF-β3 showed the largest nuclei across all conditions, including MSCs in the absence of growth factors or in the presence of CTGF. In the presence of TGF-β3, no pre-adipocytes were observed (see brightfield images of Figure 5.14).

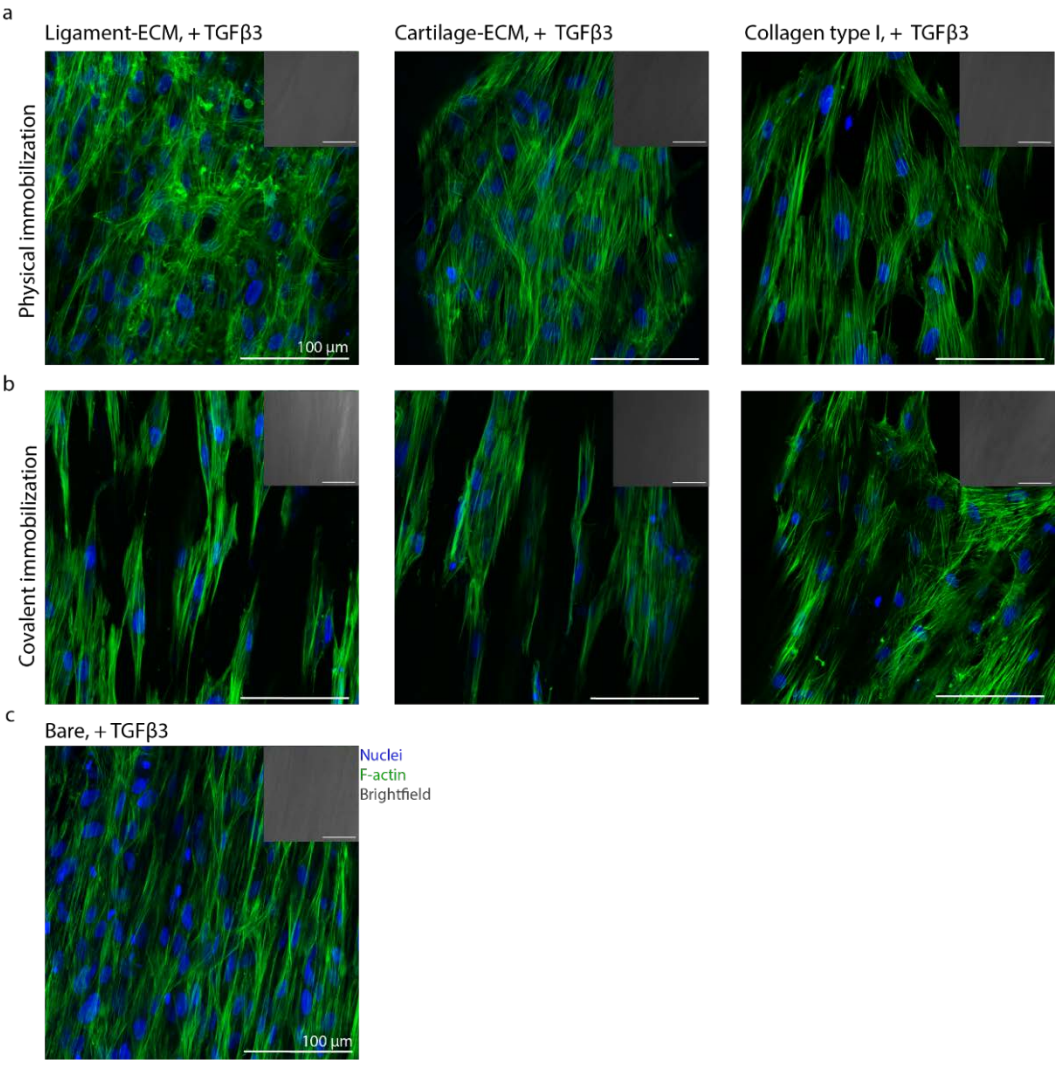

Figure 5.14 Cell nuclei (blue) and F-actin (green) staining of MSCs on bare and functionalized scaffolds in the presence of TGFβ3. **a** MSCs on ligament ECM, cartilage ECM or collagen type I immobilized by physical adsorption and covalent conjugation (**b**). **c** MSCs on bare scaffolds. Brightfield images appear in the top right corner (grey). Scale bars, 100 µm.

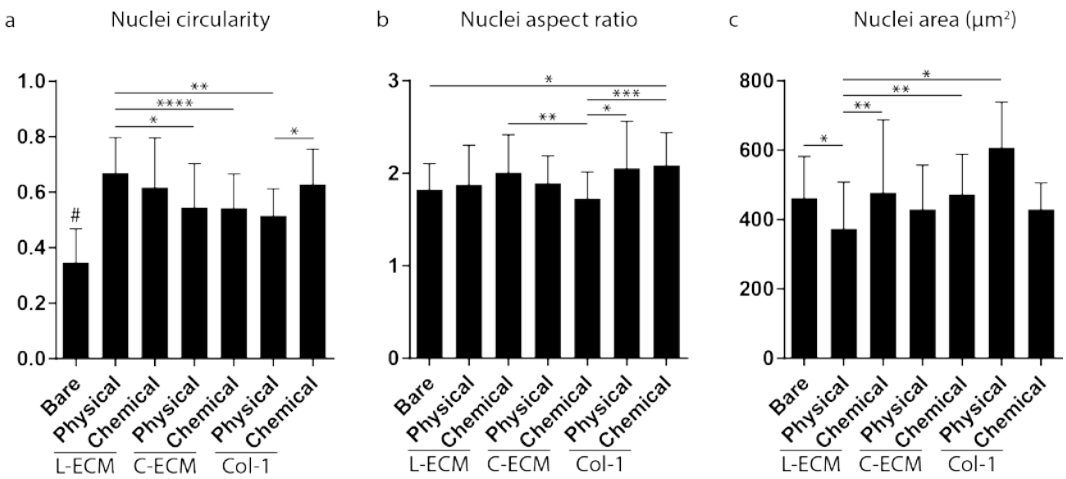

Figure 5.15 Circularity, aspect ratio and area of MSCs in the presence of TGFβ3. L-ECM: ligament-ECM; C-ECM: cartilage-ECM; and Col-1: type I collagen. **a** Nuclear circularity. A value of 1 indicates a perfect circle. #, $p < 0.001$ versus the rest of the groups. **b** Nuclei aspect ratio. **c** Nuclei area. Error bars, mean ± s.d., one-way ANOVA ($p < 0.05$) with Tukey's multiple comparisons test ($n \geq 50$ regions of interest (ROI)).

In the presence of TGF-β3, the expression of *COL1A1* and *COL3A1* was highest in scaffolds with physically immobilized L-ECM (Figure 5.16). In fact, the highest expression of *COL1A1* across the entire study was observed on physical L-ECM scaffolds stimulated with TGF-β3. *TNMD* expression was generally supressed on all scaffolds by TGF-β3 stimulation.

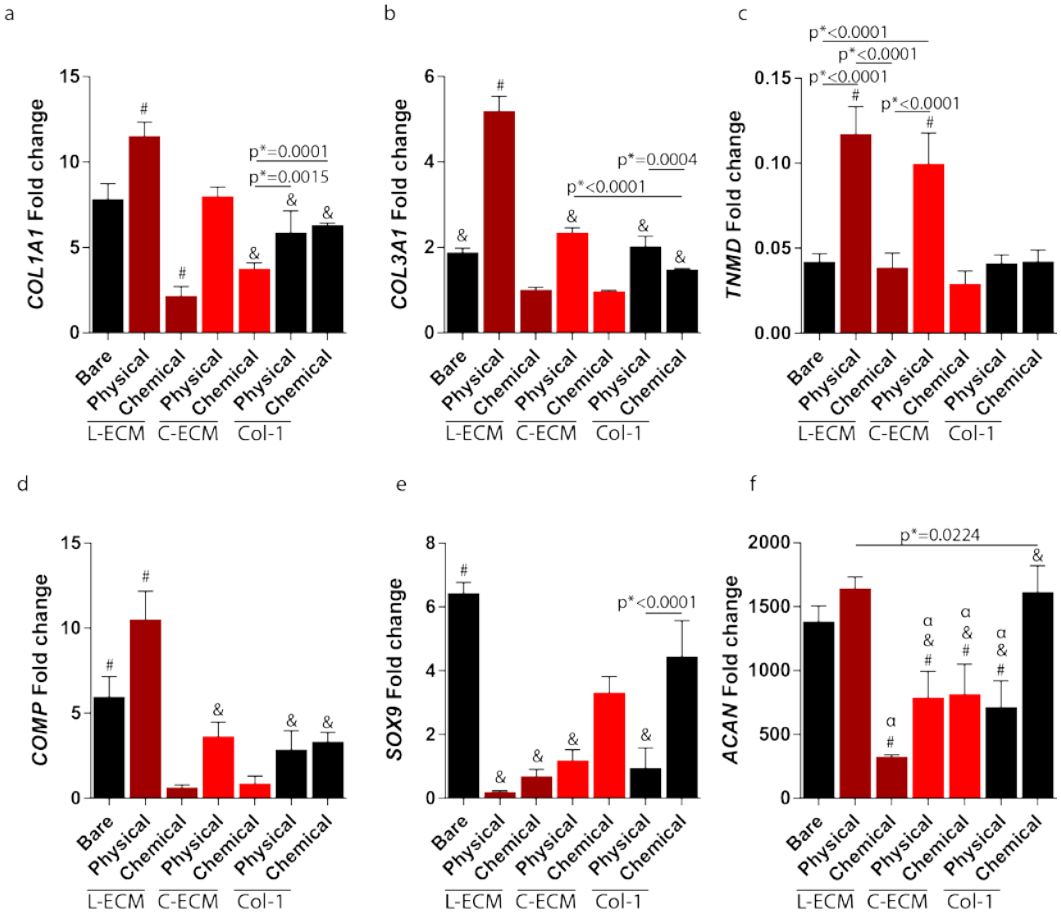

Figure 5.16 Gene expression of cartilage and ligament genes in MSCs stimulated with TGF-β3. L-ECM: ligament-ECM; C-ECM: cartilage-ECM; Col-1: type I collagen. **a** Collagen type I (COL1A1). #, p<0.05 versus the rest of the conditions; &, p < 0.05 versus bare and C-ECM physical. **b** Collagen type 3 (COL3A1). #, p < 0.0001 versus the rest of the conditions; &, p<0.001 versus L-ECM chemical and C-ECM chemical. **c** Tenomodulin (TNMD). #, p < 0.0001 versus C-ECM chemical and Col-1 (physical and chemical); &, p < 0.01 versus bare. **d** Cartilage Oligomeric Matrix Protein (*COMP*). #, p < 0.01 versus the rest of the conditions; &, p < 0.05 versus L-ECM chemical and C-ECM chemical. **e** SYR box-9 (SOX9). #, p< 0.0001 versus the rest of the conditions; &, p < 0.01 versus Col-1 chemical. **f** Aggrecan (ACAN). #, p < 0.001 versus bare and physical L-ECM; &, p < 0.05 versus L-ECM chemical; α, p < 0.0001. Data was normalized to MSCs harvested at day 0. Error bars, mean ± SEM., one-way ANOVA (p < 0.05) with Tukey's multiple comparisons test (n= 5).

As expected, the expression of cartilage-specific genes was higher following TGF-β3 stimulation. Surprisingly, the highest expression of *COMP* was observed in the physical L-ECM scaffolds stimulated with TGFβ3, however Sox-9 expression was supressed in these conditions. The addition of TGFβ3 promoted greater matrix synthesis compared to no growth factors or with CTGF supplementation (only TGF-β3 data is shown in Figure 5.17).

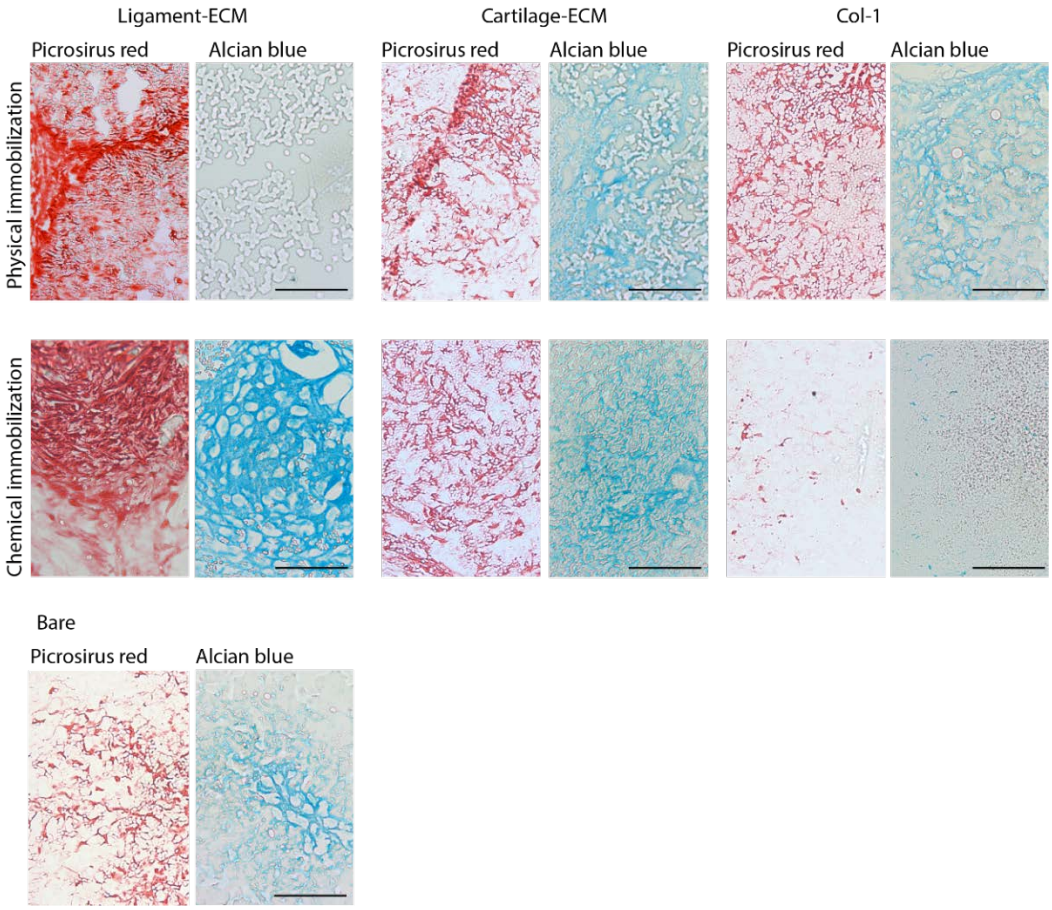

Figure 5.17 Histology images of Picrosirius red and Alcian blue for the TGF-β3. Scale bars, 100 µm.

In summary, with the addition of TGF-β3 bare scaffolds seem to better support a chondrogenic phenotype.

5.4 Discussion

The tissue-specific bioactivity of solubilized ligament and cartilage extracellular matrices (ECM) was assessed for regulating the ligamentous and chondrogenic differentiation of MSCs within microfibrillar scaffolds. It was demonstrated that the solubilization method yielded tissue-specific matrices, preserving the major structural ECM proteins that make up each tissue. These compositional differences might underlie the observed differences in

bioactivity (Rothrauff, Yang and Tuan, 2017). Physically immobilized L-ECM consistently up-regulated ligament genes to a greater extent than bare scaffolds or scaffolds functionalised with Col-1 or with C-ECM. This suggests that the solubilization method preserve non-collagenous proteins that are likely ligament-specific regulatory factors. Chemical immobilization of C-ECM was found to enhance chondrogenesis on microfibrillar scaffolds in the absence of soluble differentiation factors, although this was not observed when MSCs were additionally stimulated with TGF-β3.

Control over scaffold protein coverage was achieved by varying the concentration of the collagen/solubilized-ECMs and incubation time with both methods of immobilization. The method of protein immobilization was found to play a significant role on the expression of ligament and cartilage specific genes. Both methods are widely used in literature. Physically adsorbed proteins such as collagen can be desorbed from the surface, which is advantageous for cell clustering; but cell migration, for example, is enhanced on covalently attached collagen (Hou *et al.*, 2014). The effect of physically adsorbed L-ECM was different to that of Col-1 (physical or chemical), and surprisingly, different to its covalently immobilized counterpart. Why the physical immobilization of L-ECM was more beneficial to ligamentogenesis than chemical immobilization is unclear. It could be attributed to the differences in the amount of collagen immobilized or to the presentation of the collagen molecule to the MSCs. Previous reports show that carbodiimide treatments chemically modify integrin-binding sites on collagen-based materials (Davidenko *et al.*, 2015). It has been reported that the consumption of free amine groups during carbodiimide crosslinking results in a proportional reduction of free carboxylate anions. This in turn might lead to a reduction of available cell binding sites on the coated scaffolds and hence reduction of its bioactivity (Davidenko *et al.*, 2015). It could also be possible that chemical immobilization modifies the presentation of collagen in a way that the cell-binding sites are sterically hindered, which in turn reduces its bioactivity.

No dramatic increases in ligamentogenesis was observed on scaffolds with physically immobilized L-ECM following additional CTGF stimulation. In contrast, the addition of CTGF worked in synergy with bare scaffolds and Col-1-functinalized scaffolds to up-regulate ligament-hallmark genes. Previous reports show that commercially available collagen type 1 increases cell attachment and proliferation onto otherwise bioinert scaffolds (Zhang *et al.*, 2005), but MSC on Col-1 substrates need an external cue, such as alignment, mechanical stimulation or growth factors for MSC differentiation (Nöth *et al.*, 2005). Furthermore, the different effects caused by Col-1 and tissue-specific ECM described in this chapter contrast with studies that report that tissue-specific ECM provides no additional benefit over Col-1 (Lin *et al.*, 2012).

The highest expression of *COL1A1* and *COL3A1* was observed on scaffolds with physically immobilized L-ECM in the presence of TGFβ3. This somewhat agrees with previous studies demonstrating that aligned polycaprolactone fibres in combination with TGFβ3 stimulation support tenogenic differentiation of bone marrow stem cells (Leung *et al.*, 2013), although only a modest up-regulation of *TNDM* was observed under these conditions in this study.

When chemically conjugated to microfibrillar scaffolds, solubilized cartilage-ECM promoted the expression of Sox-9 , a transcription factor required for cartilage formation (Bi *et al.*, 1999), in the absence of soluble differentiation factors. A number of previous studies have demonstrated that type II collagen or cartilage ECM can be chondro-inductive (Almeida *et al.*, 2016; Emily C Beck *et al.*, 2016). In contrast, in the presence of TGF-β3, a potent stimulus for chondrogenesis of MSCs (Tuli *et al.*, 2003), C-ECM functionalised scaffolds were less conducive to chondrogenesis than bare scaffolds. It remains unclear at this stage why cartilage-ECM might have differential effects on chondrogenesis in the presence or absence of TGF-β3. It should be noted that all previous work points to a positive benefit of cartilage-

ECM for MSC chondrogenesis, and previous studies have suggested pepsin digestion might remove important ECM biomolecules essential for cartilage development (Rothrauff, Yang and Tuan, 2017). Other reports using solubilized cartilage ECM found that it did not affect the chondrogenic differentiation of MSCs compared to a heterologous matrix (Visser, Levett, *et al.*, 2015; Emily C. Beck *et al.*, 2016). These discrepancies in findings within the literature could also be attributed to the fact that the bioactivity of ECM is sometimes assessed as a medium supplement to MSCs cultured on tissue culture plastic (Rothrauff, Yang and Tuan, 2017) or as a crosslinked hydrogel (Visser et al. 2015) rather than as a scaffold coating as it was used here.

5.5 Conclusions

ECM components represents a strong signalling milieu to differentiate progenitor cells (Embree *et al.*, 2016) and ECM-based biomaterials have successfully promoted tissue-specific phenotypes. The results presented in this study motivate the concept of using tissue-specific ECMs to engineer the distinct tissue regions at the bone-ligament interface. This chapter assessed the bioactivity of solubilized cartilage and ligament extracellular matrix (ECM). Microfibrillar scaffolds developed in Chapter 4 were functionalized with ligament (L-ECM) or cartilage ECM (C-ECM) via physical adsorption or covalent conjugation. Pepsin-solubilized L-ECM was validated as a tissue-specific biomaterial when immobilized by physical adsorption onto polymeric microfibres. Pepsin-solubilized C-ECM, on the other hand, showed only modest bioactivity towards the chondrogenic lineage. Chapter 6 will spatially control the immobilization of ECM components to create distinct regions along the length of a scaffold, including a mineralized region that could potentially support osteogenesis in the bone tunnel following implantation of such an implant.

Chapter 6 : Spatial presentation of growth factors and extracellular matrix components for bone-ligament tissue engineering

6.1 Introduction

Ligaments and tendons undergo a transition in fibre structure and molecular composition before inserting to bone (Fujioka *et al.*, 1997; Moffat *et al.*, 2008). This transition, termed the enthesis, facilitates uniform load transfer across a region characterized by a large mismatch in material properties between ligament and the bone, and this in turn reduces injury (Moffat *et al.*, 2008). In ligaments such as the anterior cruciate ligament (ACL), greater than 85% of ruptures require surgical reconstruction (Prodromos *et al.*, 2007). Surgical reconstruction does not restore the anatomic features of the enthesis (Rodeo *et al.*, 1993), instead the interface heals as a fibrovascular tissue with inferior mechanical properties. Consequently, the tissue at the bone insertion is subjected to high stress concentrations which compromises the graft stability and long-term clinical outcome (Deneweth *et al.*, 2010; Engelman *et al.*, 2014). In young active patients revision surgeries are common, making regeneration of the soft tissue – bone interface a key challenge in the field of tissue engineering.

A paradigm for tissue engineering the enthesis is developing biomaterials containing graded biophysical and/or biochemical cues that instruct cells to undergo spatially defined differentiation. Different graded scaffolds have been developed in an attempt to sustain the fibroblastic, chondrogenic and osteogenic phenotypes, or to drive differentiation of MSCs into the different cell types that make up the enthesis (Li *et al.*, 2009; Paxton, Grover and Baar, 2010). However, none of the current strategies have generated long-lasting cartilage tissue adjacent to a mineralized bone tissue.

One defining feature of fibrocartilaginous entheses is that they form via endochondral ossification. Type I collagen bundles from the ligament insert first to primordial cartilage, which is progressively replaced by bone (Fujioka *et al.*, 1997). At neonatal and immature developmental time points, the biochemical composition of the ACL-to-bone interface resembles that of hyaline cartilage (Wang *et al.*, 2006). As the interface matures, non-mineralized and mineralized collagen fibers penetrate the hyaline cartilage matrix in response to site-specific compressive loads during postnatal maturation (Benjamin and Ralphs, 1998).

Recapitulating aspects of enthesis development may represent a superior approach for engineering a functional enthesis. Engineering a cartilage tissue adjacent to a ligament tissue may provide a template that can mature into towards the more complex entheseal tissue *in vivo*. Mesenchymal stem cells (MSCs) have been successfully used by several groups, including ours, to generate cartilage-like tissue (Almeida *et al.*, 2016; Rothrauff, Yang and Tuan, 2017). Such engineered cartilage tissues can calcify and progress along an endochondral pathway (Sheehy *et al.*, 2013). Some of these reports involve the use of tissue-specific extracellular matrix (ECM). For example, biomaterials derived from decellularized cartilage ECM have been shown to support endochondral bone formation when seeded with MSCs (Gawlitta *et al.*, 2015). Therefore, spatially functionalizing the appropriate region of a bone-ligament scaffold with cartilage ECM may provide a substrate that can support the development of a cartilage template that can ultimately give rise to the different tissue types found in the enthesis (fibrocartilage, calcified cartilage and bone).

The objective of this chapter was to develop a biomaterial for bone-ligament tissue engineering that recapitulates early stages of enthesis development, where a ligamentenous tissue is adjacent to a cartilage template. It was envisioned that this could be accomplished by controlling the spatial incorporation of growth factors and ECM components (both organic

and inorganic) onto specific regions in a mechanically functional microfibrillar scaffold to direct the fibroblastic and chondrogenic differentiation of MSCs (see Figure 6.1).

6.2 Materials and Methods

6.2.1 Electrospinning

Unwelded microfibers were electrospun using the electrospinning parameters described in Chapter 4. Polycaprolactone (PCL, M_W 80 kDa, Sigma – Aldrich) was dissolved at 25% w/v in chloroform; the polymer solution was loaded in a 20-ml syringe and extruded using a syringe pump through a 20G blunt-end needle charged to 10 kV. Continuous polymeric fibres were collected at a flow rate of 5 ml/h on a grounded mandrel positioned 15 cm apart from its centre to the tip of the needle. Fibres were collected at 3500 RPM for 10 min. Fibre sheets were wrapped/baled to form bundles along the long axis of the fibres as previously shown (Chapter 4).

6.2.2 Isolation and expansion of mesenchymal stem cells (MSCs)

Bone marrow derived porcine MSCs were isolated as previously described (Thorpe *et al.*, 2012). Tripotential differentiation capacity was assessed. We used one isolate of porcine MSCs for all the experiments. MSCs were expanded in high-glucose Dulbecco's modified Eagle's medium (DMEM) GlutaMAX supplemented with 10% fetal bovine serum (FBS), penicillin (100 U/ml)-streptomycin (100 µg/ml) (all Gibco, Biosciences) and 0.25 µg/ml amphotericin B (Sigma-Aldrich) in a humidified atmosphere at 37 °C, 5% CO2. At the end of passage 2, cells were trypsinized and seeded onto the electrospun scaffolds. All cell studies were performed with cells in P2.

6.2.3 Solubilization of cartilage and ligament ECM

Cartilage was harvested under sterile conditions from the articular surfaces of femoral condyles and trochlear groove hind limbs of three-month-old pigs (3 donors). Articular ligaments were harvested from the same donors. Tissues were minced to 1 – 2 mm^3 pieces and then solubilized using 1 ml of 0.2 M sodium hydroxide (NaOH) per 50 mg of wet tissue at 4°C with agitation (24 h). The resulting solutions were pelleted and washed with ultra-pure water to remove residual NaOH. The resulting pellets were digested with pepsin solution (1500 units of pepsin dissolved in 0.5 M acetic acid per 50 mg of tissue) at RT with rotation (24 h). The resulting mixtures were centrifuged to eliminate insoluble material. The supernatants were then salt precipitated using a 0.9 M final concentration sodium chloride (NaCl) solution for the cartilage solubilized ECM, and 0.8 M final concentration NaCl solution for the ligament solubilized ECM. These mixtures were allowed to equilibrate at 4°C (6 h). The mixtures were centrifuged and the supernatants (unprecipitated material) discarded. The pellets were dissolved in 0.5 M acetic acid overnight and salt precipitated again. The acid solubilized ECM was dialyzed against sodium phosphate (Na_2HPO_4) for 24 h with a change of dialysate. The dialyzed ECM digest was freeze dried and stored at – 80°C. Tissue harvesting and solubilisation steps were performed under sterile conditions.

6.2.4 SEM

Samples for scanning electron microscopy (SEM) were sputter coated with a mixture of gold/palladium (60:40) to a thickness of ~10 nm (Cressington 108) and imaged with a Zeiss Ultra FE-SEM at an accelerating voltage of 5 kV.

6.2.5 Cell viability

Cell viability was assessed after 24 h by staining cells using the Live/dead assay kit (Invitrogen, Bioscience). Briefly, scaffolds were rinsed in PBS and incubated in 4 mM calcein-AM and 2 mM ethidium homodimer-1 in PBS for 1 h at 37 °C. Scaffolds were rinsed in PBS and visualized under a scanning confocal microscope (Leica SP8) at an excitation and emission wavelengths of 515 and 615 nm. Analysis was performed in Leica Microsystems software (Leica Application Suite X).

6.2.6 Gene expression

Gene expression was assessed after 10 days using quantitative real-time PCR (n=5/group). Cells were lysed using RLT lysis buffer (Qiagen) supplemented with 10 µl/ml β-mercaptoethanol (Sigma-Aldrich) and stored at –80°C. For RNA isolation, cell lysates were thawed and homogenized using QIAshredder columns (Qiagen). Total RNA was isolated and further purified using RNeasy Mini kits (Qiagen) following manufacturer's instructions. Total RNA concentration and purity were determined using a Nanodrop spectrophotometer. 500 ng of RNA per sample was reverse transcribed into cDNA using High-Capacity cDNA Reverse Transcription Kit (Applied Biosystems) following manufacturer's instructions. 25 ng of cDNA were amplified using an ABI 7500 sequence detection system (Applied Biosystems) and Syber select master mix (Applied Biosystems). Expression of collagen type I (*COL1A1*), tenomodulin (*TNMD*), cartilage oligomeric matrix protein (*COMP*), runt-related transcription factor 2 (*RUNX2*), aggrecan (*ACAN*), SRY-Box 9 (*SOX9*) and beta-2 microglobulin (*B2M*) was evaluated. The porcine specific primer sequences (KiCqStart SYBR Green Primers, Sigma) used for amplification are listed in Table 6.1. The primer concentrations were optimized for efficiency (95 – 105% efficiency) and specificity (analysis of melting curve). Quantification of the target gene expression was performed using the $2^{-\Delta\Delta C_T}$ method with *B2M* as an endogenous control

(Schmittgen and Livak, 2008). Gene expression was normalized relative to day 0 for Study 1. Gene expression was normalized relative to MSCs on bare scaffolds for Study 2 and Study 3.

Gene	Primer sequences	
B2M	Forward:	ACTGAGTTCACTCCTAACG
	Reverse:	TGCAGCATCTTCATAATCTC
COL1A1	Forward:	TAGACATGTTCAGCTTTGTG
	Reverse:	GTGGGATGTCTTCTTCTTG
OPN	Forward:	CTGCAGACCAAGGAAAATC
	Reverse:	AGCATCTGTGTATTTGTTGG
ACAN	Forward:	GACCACTTTACTCTTGGTG
	Reverse:	TCAGGCTCAGAAACTTCTAC
TNMD	Forward:	GCTAATTGTCCTATTTTGGGG
	Reverse:	GAAAGTGTGTTCCATGTCG
COMP	Forward:	AAGGACAGTGATGGTGATG
	Reverse:	ATCCCTCTGATCTGCATTG
RUNX2	Forward:	CCAACAGAGGCATTTAAGG
	Reverse:	CCAAAAGAAGTTTTGCTGAC
ALPL	Forward:	TTTCACTCTTCTTAGTGCTG
	Reverse:	CGTTACGGAATGAGGAAAC

Table 6.1 Primer sequences used for qPCR

6.2.7 DNA quantification

DNA content was analysed from samples at day 0 (24 h after cell seeding) and day 21 (n= 4). Samples were digested with 3.88 U/ml papain enzyme in 100 mM sodium phosphate buffer containing 5 mM ethylenediaminetetra-acetic acid (EDTA) and 10 mM L-cysteine hydrochloride (HCl), pH 6.5 (all Sigma-Aldrich) for 18 h at 55 °C under constant rotation. Following digestion of the samples, DNA content was quantified using the Hoescht Bisbenzimide 33258 dye assay (Quant-iT ssDNA assay kit, Biosciences).

6.2.8 Study 1. Finding the appropriate composition of culture media

This chapter will attempt to spatially direct MSC differentiation towards either a ligamentogenic, chondrogenic or an osteogenic phenotype along the length of an electrospun

scaffold. To this end, the first study of this chapter sought to identify a culture media that would support these different tissue phenotypes. Scaffolds (collected for 10 min, 35 mm in length) were sterilized using ethylene oxide (EtO; Anprolene, Anderson products) and treated under sterile conditions thereafter. Scaffolds were hydrated and incubated in expansion media overnight at 37 °C before cell seeding. Expansion media consisted of high-glucose Dulbecco's Modified Eagle's Medium (DMEM, glutaMAX), 10% FBS, penicillin (100 U/ml)-streptomycin (100 µg/ml) (all from Gibco), and 0.25 µg/ml amphotericin B (Sigma). Scaffolds were seeded at a cell density of 500,000 cells per scaffold (in 30 µl aliquot) and were cultured individually in Teflon rectangular wells. After 4 h, 1.5 ml of expansion media were added to each well. Scaffolds were maintained in expansion media at 20 % O_2 for 24 h. After this period, expansion media was replaced by one of the 9 media formulations. Formulation supplements are listed in Table 6.2 and Table 6.3. High glucose Dulbecco's Modified Eagle's Medium (DMEM, glutaMAX) was the base for all compositions, all contained penicillin (100 U/ml)-streptomycin (100 µg/ml) and 0.25 µg/ml amphotericin B. TGF-β3 was supplemented in a concentration of 10 ng/ml (recombinant human transforming growth factor-β3; ProSpec-Tany, TechnoGene Ltd.), and CTGF at 100 ng/ml (recombinant human connective tissue growth factor; ProSpec-Tany, TechnoGene Ltd.). Live/dead staining and qRT-PCR were performed after 10 days in culture to confirm viability of MSCs. Live/dead staining and imaging were performed as described in section 6.2.5, gene expression as described in section 6.2.6.

Media composition	FBS	BSA	AA	SP	L-PRO	ITS	DEX	LA	CTGF
CDM, CTGF		■	■	■	■				■
CDM+, CTGF		■	■	■	■	■	■	■	■
Basal, CTGF		■	■						■
Expan, CTGF	■		■						■
Expan	■								

Table 6.2 Supplements for each media composition for CTGF-mediated fibrogenesis. Abbreviations: fetal bovine serum (FBS), bovine serum albumin (BSA), ascorbic acid (AA), sodium pyruvate (SP), L-proline (L-Pro), insulin-transferrin-selenium (ITS), dexamethasone (DEX), linoleic acid (LA) and connective tissue growth factor (CTGF).

Media composition	FBS	BSA	AA	SP	L-PRO	ITS	DEX	LA	TGF-β3
CDM, TGF-β3		■	■	■	■				■
CDM+, TGF-β3		■	■	■	■	■	■	■	■
Basal, TGF-β3		■	■						■
Expan, TGF-β3	■		■						■
Expan	■								

Table 6.3 Supplements for each media composition for TGFβ3-mediated chondrogenesis. Abbreviations: fetal bovine serum (FBS), bovine serum albumin (BSA), ascorbic acid (AA), sodium pyruvate (SP), L-proline (L-Pro), insulin-transferrin-selenium (ITS), dexamethasone (DEX), linoleic acid (LA) and transforming growth factor-β3 (TGF-β3).

6.2.9 Study 2. Coating of electrospun PCL scaffolds with hydroxyapatite

Scaffolds (collected for 10 min, 35 mm in length) were sterilized using ethylene oxide (EtO; Anprolene, Anderson products) and treated under sterile conditions thereafter. Scaffolds were hydrated and hydrolysed with an alkaline treatment to expose polar groups. Hydrolysed scaffolds were incubated in 1X or 10X simulated body fluid (SBF). SBF is a solution with ion concentrations nearly equal to those in human blood plasma. The apatite nuclei spontaneously grow by consuming the supersaturated calcium and phosphate ions in the SBF solution. After SBF incubation, MSCs were culture in growth media for 10 days. Mineral coating was visually assessed using SEM as described in section 6.2.4. Cell viability and qRT-PCR were evaluated after 10 days in culture. Live/dead staining was performed as described in section 6.2.5, and gene expression of *RUNX2* and osteopontin (*OPN*) was performed on day 10 as described in section 6.2.6.

Preparation of simulated body fluid (SBF). 1X SBF was prepared using the conventional SBF recipe (Oyane *et al.*, 2003). All equipment used for the preparation was washed in 1 M hydrochloric acid solution (HCl) for 8 hours and rinsed with tap water, washed with neutral detergent and immersed in neutral detergent overnight, and rinsed with ultra-pure water (UPW). Solution was prepared with the chemicals listed in Table 6.4, in that order. pH was

adjusted to 7.4 at 36 – 37°C using 1 M HCl. The solution was sterile filtered (polyether sulfone filter, pore size 0.22µm) and stored at 4°C.

Order	Reagent	Amount
1	NaCl	7.996 g
2	NaHCO3	0.350 g
3	KCl	0.224 g
4	K2HPO4·3H2O	0.228 g
5	MgCl2·6H2O	0.305 g
6	1M-HCl	40 mL
7	CaCl2	0.278 g
8	Na2SO4	0.071 g
9	(CH2OH)3CNH2	6.057 g

Table 6.4 Reagents for preparing 1X SBF (pH 7.4, 1L)

10X SFB was prepared according to Bhaduri (Tas and Bhaduri, 2004). The chemicals given in Table 6.5 were added in the order written to deionized water at RT. Sodium bicarbonate was added to rise the pH to 6.50 just before using the solution.

Order	Reagent	Amount
1	NaCl	58.443 g
2	KCl	0.3728 g
3	CaCl2 2H2O	3.6754 g
4	MgCl2·6H2O	1.0165 g
5	NaH2PO4	1.1998 g
6	NaHCO3	~ 0.96 g

Table 6.5 Reagents for preparing 10X SBF (pH 4.3, 1L)

Hydroxyapatite coating with 1X simulated body fluid (SBF). Scaffolds were incubated in 1X SBF at 37°C for 4 h, rinsed gently with distilled water and left them to air-dry at RT. During 1X SBF coating process, the temperature and pH are adjusted to almost equal those of human plasma.

Hydroxyapatite coating with 10X simulated body fluid (SBF). Fibre scaffolds were hydrolysed in 1N NaOH at 45°C for 6 h, with constant rotation. Scaffolds were incubated for 2h at RT. Scaffolds were gently rinsed with deionized water.

6.2.10 Study 3. Controlling the spatial presentation of ECM components and growth factors

Scaffolds with spatial presentation of growth factors, or ECM, or both are detailed in Table 6.6 and in Figure 6.1.

Group A	Bare scaffold		
	Ligament region	***Cartilage region***	***Endochondral region***
Group B (growth factors)	+ CTGF	+ TGFβ3	+ BMP2
Group C (ECM)	Ligament-ECM	Cartilage-ECM	Cartilage-ECM + HA
Group D (ECM + growth factors)	Ligament-ECM + CTGF	Cartilage-ECM + TGFβ3	Cartilage-ECM + HA + BMP2

Table 6.6 Groups with spatial immobilization of growth factors, ECM or both.

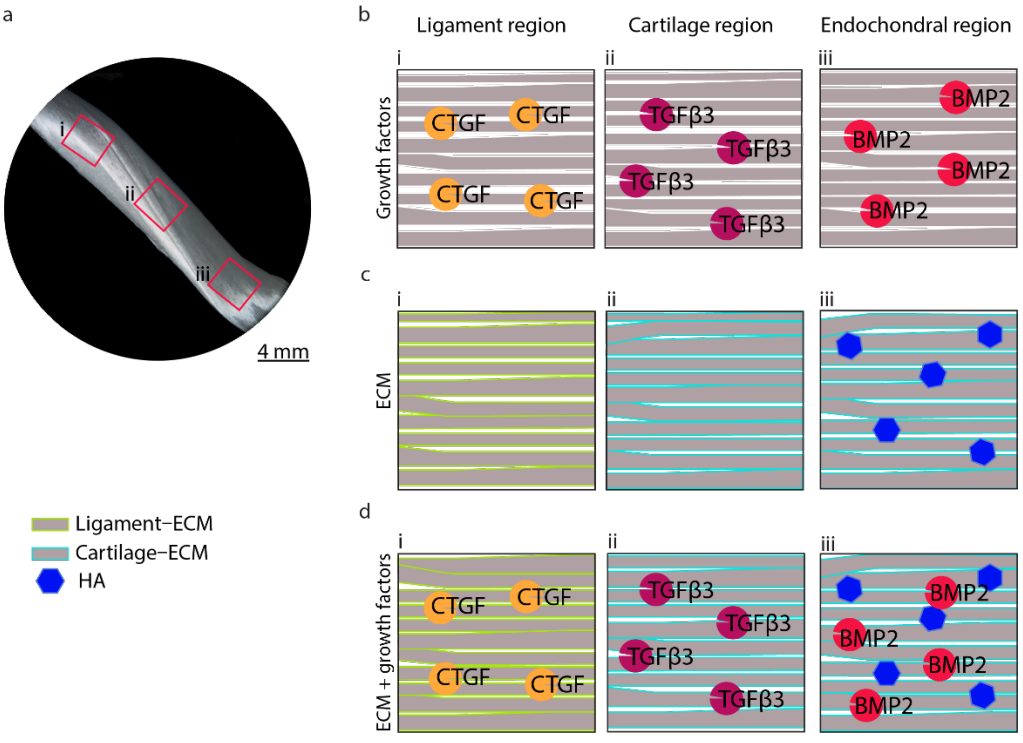

Figure 6.1 Schematic representation of the regions in the scaffolds. **a**, Stereo image of a fibre-bundle used in this study. Scale bar, 4 mm. Red rectangles represent the (i) ligament region, (ii) cartilage region, and (iii) endochondral region. **b**, Scaffolds with (CTGF) connective tissue growth factor in the ligament region; (TGF-β3) transforming growth factor β3 in the cartilage region; (BMP2) bone morphogenetic protein 2 in the endochondral region. **c**, Scaffolds with covalently attached decellularized extracellular matrices, (green) ligament ECM (L-ECM) in the ligament region; (blue) cartilage ECM (C-ECM) for the cartilage and endochondral region. Blue hexagons represent hydroxyapatite (HA). **d**, Scaffolds incorporating both, ECM and growth factors. (i) L-ECM with CTGF, (ii) C-ECM and TGF-β3.

Group A (bare). Scaffolds were stored in ultra-pure water while the rest underwent immobilization treatments. When scaffolds were ready, bare scaffolds were incubated for 4 h in growth media prior seeding of MSCs.

Group B (growth factors). Scaffolds underwent alkaline hydrolysis with 1N NaOH for 3h at RT. Scaffolds were rinsed with deionized water. Scaffolds were incubated for 2h at RT in 5 mg/ml EDC (1-ethyl-3-(3-dimethylaminopropyl carbodiimide hydrochloride) and 5 mg/ml NHS (N-hydroxysulfosuccinimide) dissolved in MES buffer, pH 5 (all from Sigma-Aldrich). Growth factors were reconstituted upon manufacturer´s instructions and diluted with MES buffer to the specific concentration. Connective tissue growth factor (CTGF, ProSpec-Tany, TechnoGene Ltd.) was prepared at 50 ng per 80 µl aliquot; transforming growth factor-β3 (TGFβ3, ProSpec-Tany, TechnoGene Ltd.) at 5 ng per 80 µl aliquot; and bone morphogenetic protein 2 (BMP2, ProSpec-Tany, TechnoGene Ltd.) at 100 ng per 80 µl aliquot. Concentrations were chosen based on literature (Bhattacharjee *et al.*, 2016). The ligament region of the scaffolds (1.5 cm) were incubated in aliquots of CTGF for 2 h at RT. Simultaneously, the endochondral region of the scaffolds (1 cm) were incubated in aliquots of BMP2 for 2 h at RT. Next, the cartilage region of the scaffolds (0.5 cm) were incubated in aliquots of TGF-β3 for 2 h at RT. Scaffolds were rinsed with ultra-pure water. Scaffolds were incubated in growth media for 4 h before MSCs seeding.

Group C (ECM). The bone region of the scaffold (1 cm) underwent alkaline hydrolysis with 1N NaOH at 45°C for 6 h. Next, the rest of the scaffold (cartilage and ligament regions, 2 cm) underwent alkaline hydrolysis with 1N NaOH for 3h at RT. Scaffolds were rinsed with deionized water. After surface modifications, cartilage-ECM was covalently conjugated onto half of the scaffolds (endochondral and cartilage regions, 1.5 cm) using carbodiimide coupling as described in Chapter 5, section 5.2.4. Briefly, scaffolds were incubated for 2h at RT in 5 mg/ml EDC and 5 mg/ml NHS dissolved in MES buffer, pH 5. Scaffolds were rinsed and incubated in

the cartilage-ECM solution (0.5 mg/ml, in MES buffer, pH 5) for 24h at 4°C. The endochondral region of the scaffolds were incubated in 10X SBF for 2 h at RT. Next, the adjacent halves of the scaffolds (ligament region, 1.5 cm) were incubated for 2h at RT in 5 mg/ml EDC and 5 mg/ml NHS dissolved in MES buffer, pH 5. And subsequently incubated in ligament-ECM (0.5 mg/ml, in MES buffer, pH 5) 24h at 4°C. Scaffolds were rinsed with deionized water, the second wash was performed with 0.05% Tween to remove unbound ECM. Scaffolds were incubated for 4 h before cell seeding.

Group D (ECM and growth factors). Scaffolds underwent ECM immobilization as described above for Group C. Next, scaffolds underwent growth factor immobilization as described above for Group B (Figure 6.2).

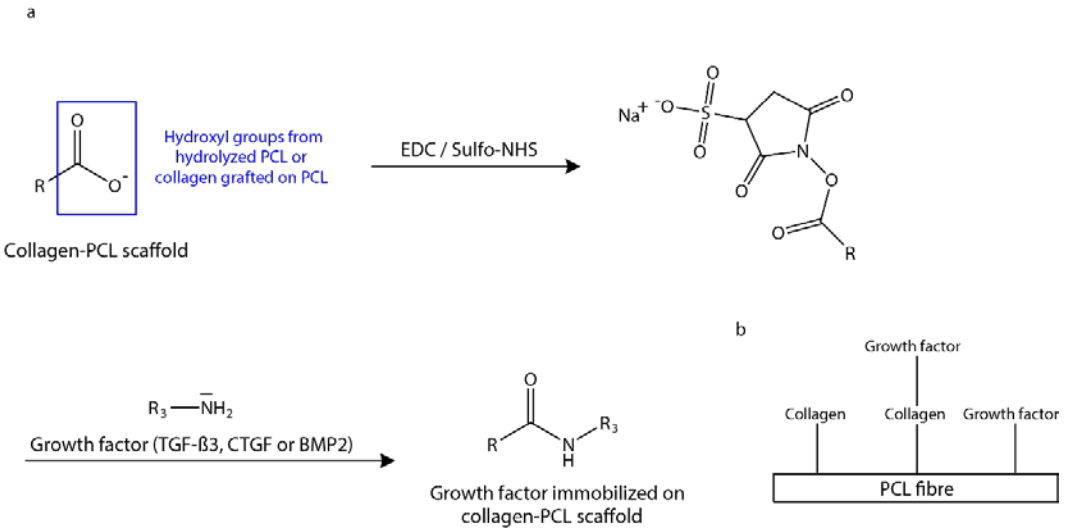

Figure 6.2 Immobilization of growth factors on ECM-PCL scaffolds. a, Carbodiimide bonding of growth factors to the functional groups of PCL and the collagen in the ECM. b, Diagram of a PCL fibre with molecules of collagen (from the ECM) and growth factors.

6.2.11 Statistical analysis

Statistical analysis was performed with Prism 6 Graphpad software. Comparisons were made using one-way or two-way analysis of variance (ANOVA) with Tukey post-hoc testing for multiple comparisons. Data are presented as mean ± standard deviation (s.d.) and as mean ±

standard error of the mean (SEM) for qRT-PCR. Sample sizes are indicated in the methods section and within the corresponding figure legends. Significance was accepted at a level of $p < 0.05$.

6.3 Results

6.3.1 Finding the appropriate culture media composition

The goal of this study was to find a culture media composition permissive of both CTGF-mediated fibrogenesis and TGF-β3-mediated chondrogenesis. Four media compositions were screened using high glucose Dulbecco's Modified Eagle's Medium (DMEM, glutaMAX) as the base for all compositions. These media compositions were CDM, CDM+, basal and expansion media. MSCs cultured in expansion medium (Expan) and in CDM+ based medias (CDM+, TGFβ3 and CDM+, CTGF) were used as controls. First, the four media compositions were assessed for CTGF-mediated fibrogenesis (see Table 6.2).

The four media compositions were also assessed for TGF-β3 mediated chondrogenesis (see Table 6.3). The selection criteria for the culture media composition were MSC viability and upregulation of the ligament markers (*COL1A1* and *TNMD*) with the supplementation of CTGF, and upregulation of chondrogenic markers (*COL2A1* and *SOX9*) with the addition of TGF-β3.

Expansion media (Expan)-based formulations promoted increased MSC proliferation (Figure 6.3 G and H, and Figure 6.4 a), but MSCs showed the lowest expression of cartilage and ligament markers compared to MSCs in basal, CDM and CDM+-based formulations (Figure 6.4 b, c).

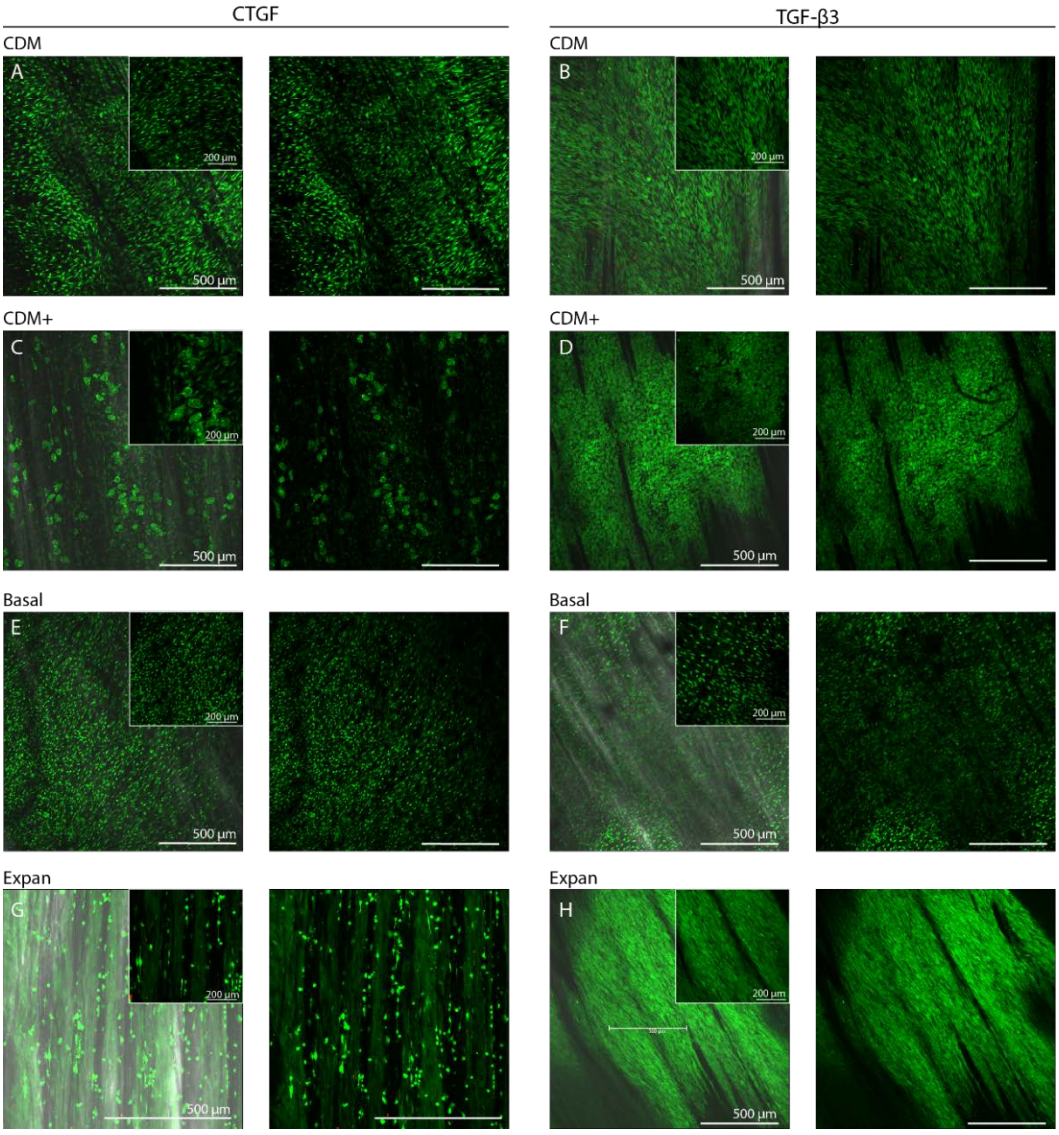

Figure 6.3 Viability of MSCs seeded on to the scaffolds after 10 days in culture. Live (green)/dead (red) staining was performed.

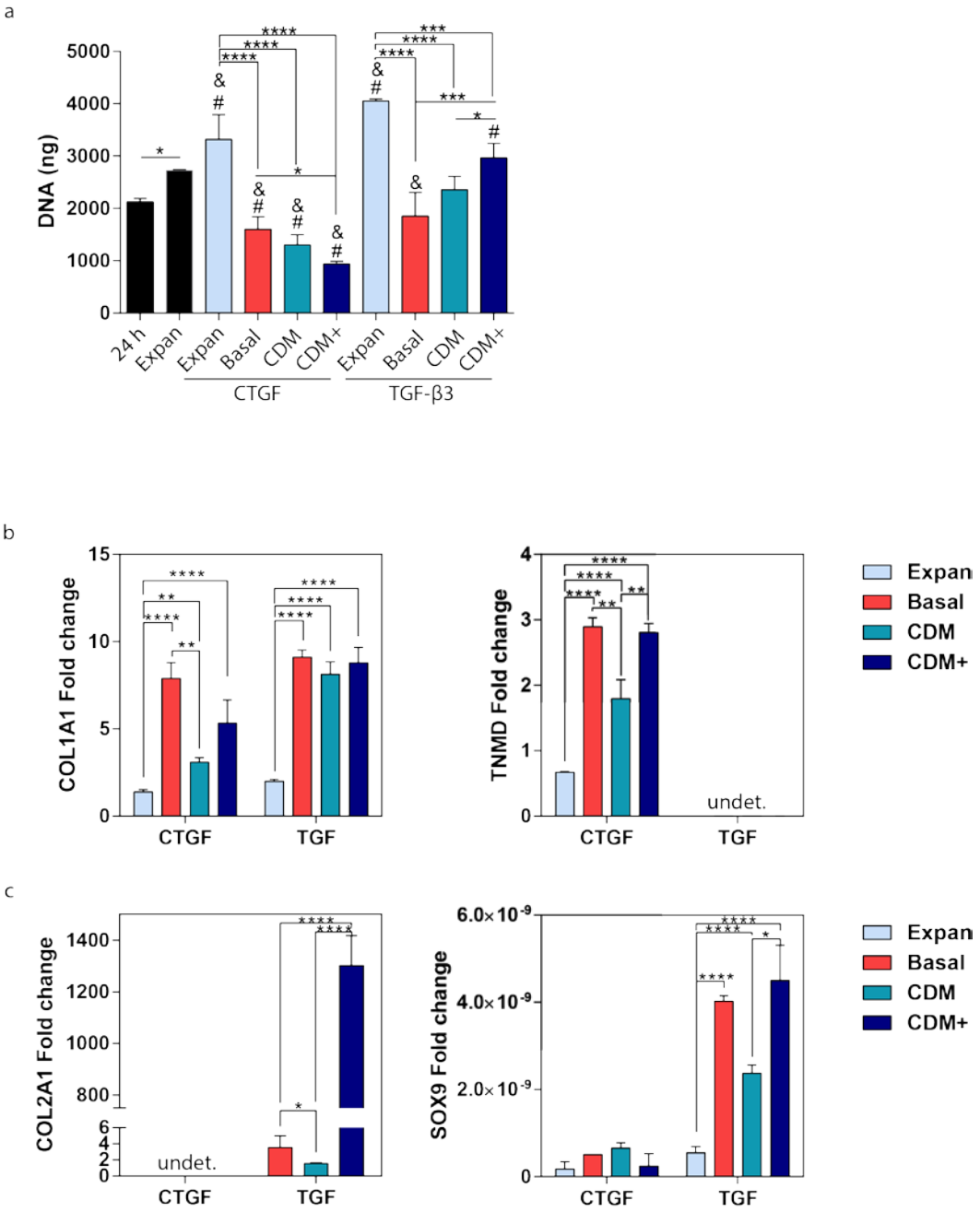

Figure 6.4 DNA quantification and gene expression of MSCs at day 10. **a,** DNA quantification after 10 days in culture. #, significantly different from 24 h, $p < 0.05$. &, significantly different from Expan (control), $p < 0.05$. *, $p < 0.05$; ***, $p < 0.001$; ****, $p < 0.0001$. **b,** Ligament genes collagen type I (*COL1A1*) and tenomodulin (*TNMD*). **, $p < 0.01$; ****, $p < 0.0001$. **c,** Chondrogenic genes collagen type II (*COL2A1*) and SYR-box 9 (*SOX9*). *, $p < 0.05$; ****, $p < 0.0001$. Error bars, mean ± SEM, one-way ANOVA ($p < 0.05$) with Tukey's multiple comparisons test ($n = 5$).

MSCs cultured in basal medias showed less proliferation than expansion media-based groups ($p<0.001$). Basal media and CDM+ formulations supplemented with CTGF supported

the highest expression of *COL1A1* among the different medias supplemented with CTGF (Figure 6.4). These formulations also showed the highest level of *TNMD* expression. CDM+ supplemented with CTGF was used as control to confirm previous observations from Chapter 5, where pre-adipocytes were observed. When supplemented with TGF-β3, the basal media supported high levels of *COL1A1* expression, upregulation of *COL2A1* and high expression of *SOX9,* not significantly different from CDM+ supplemented with TGF-β3 (Figure 6.4 c).

As expected, MSCs exposed to CTGF expressed high levels of *TNDM*, and MSCs exposed to TGF-β3 expressed higher levels of chondrogenic genes. CDM and CDM+ based medias supplemented with CTGF supported the lowest proliferation of MSCs. In contrast, when these formulations were supplemented with TGF-β3 instead they supported comparable proliferation to that observed in expansion media with TGF-β3. In the presence of CTGF, MSCs in CDM and CDM+ based medias supported upregulation of *COL1A1* and *TNMD*. CDM supplemented with TGF-β3 supported high levels of *COL1A1* and *SOX9* expression, with a modest upregulation of *COL2A1*. MSCs cultured with CDM+ supplemented with TGF-β3, on the other hand, supported the highest expression of *COL2A1*, along with robust expression of *SOX9* and *COL1A1*. Together these observations suggest that the basal media is the most effective formulation for supporting CTGF-mediated fibrogenesis, while at the same time supporting TGF-β3-mediated upregulation of Sox-9, suggesting this culture media is also supportive of chondrogenesis.

6.3.2 Hydroxyapatite coating

An apatite coating on the polymeric fibres was formed by a biomimetic process (i.e. incubation in simulated body fluid, SBF). SBF has been shown to efficiently nucleate the osteoconductive hydroxyapatite (HA) in synthetic scaffolding materials (Kokubo and Takadama, 2006). The apatite layer obtained by this process is considered bone-like apatite

and has shown to bond to bone (Hench and Wilson, 1984; Abe, Kokubo and Yamamuro, 1990). HA is the major inorganic component of bone mineral; *in vitro*, it is osteoconductive and *in vivo* can induce new bone formation. The polar groups of the hydrolysed PCL as well as those in the immobilized decellularized ECM acted as nucleating agents of apatite on the surfaces of the fibres. Nucleation of HA using 1X SBF was not observed (data not shown), thus 10X SBF was used instead. Figure 6.5 a-d shows nucleation of apatite on bare scaffolds after surface modification, and on type I collagen (Col-1) covalently conjugated onto the PCL fibres.

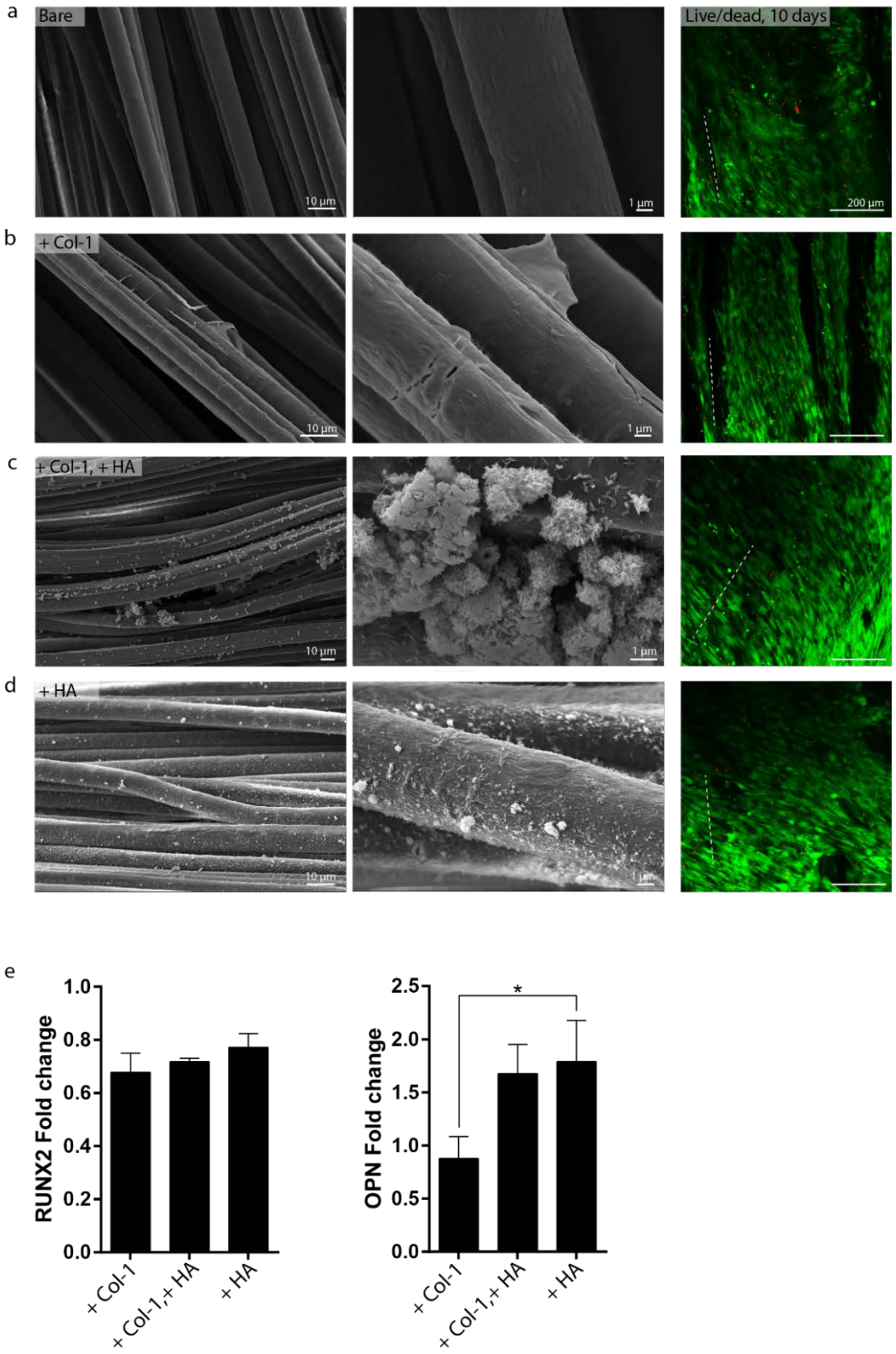

Figure 6.5 The effect of hydroxyapatite (HA) coating on cell viability and gene expression of MSCs after 10 days in culture. **a,** SEM micrographs of bare scaffolds and live/dead staining (right) of MSCs seeded on to the bare fibres. **b**, PCL fibres functionalized with type I collagen (Col-1) and live/dead staining of MSCs on these fibres. **c**, PCL-fibres with Col-1 and HA. **d**, PCL fibres with HA. For SEMs, Scale bars, 10 µm and 1 µm. In live/dead images, green: live; red: dead. Scale bars, 200 µm. **e**, Gene expression of

runt-related transcription factor 2 (RUNX2) and osteopontin (OPN), *p < 0.05. Data is reported as fold-change relative to MSCs on bare scaffolds. The values plotted are means ± SEMs of n=5 scaffolds for each condition; one-way ANOVA with Tukey's multiple comparisons test.

To assess the bioactivity of the HA coating, the gene expression of *RUNX2* and *OPN* were analysed (Figure 6.5 e). There was no significant difference among the groups in *RUNX2* expression, a major driver for the later stages of endochondral ossification (Chen *et al.*, 2014). *OPN*, a noncollagenous protein related to calcified cartilage (McKee, Glimcher and Nanci, 1992) was significantly higher in fibres directly coated with HA.

6.3.3 Spatial functionalization of scaffolds with ECM and growth factors

Three scaffolds were developed to assess whether ECM and growth factors immobilized onto a microfibrillar scaffold could drive fibrogenic and chondrogenic differentiation of MSCs. Overall, the three scaffolds, namely growth factors only, extracellular matrices (ECM) only, and ECM and growth factors, showed MSCs elongating in the direction of the underlying substrate in the ligament region (Figure 6.6). MSCs in the cartilage region (Figure 6.6 middle) were smaller with more rounded cell bodies in the three scaffolds with TGF-β3, or C-ECM or both. The bone region also provided a substrate that supported rounded MSCs.

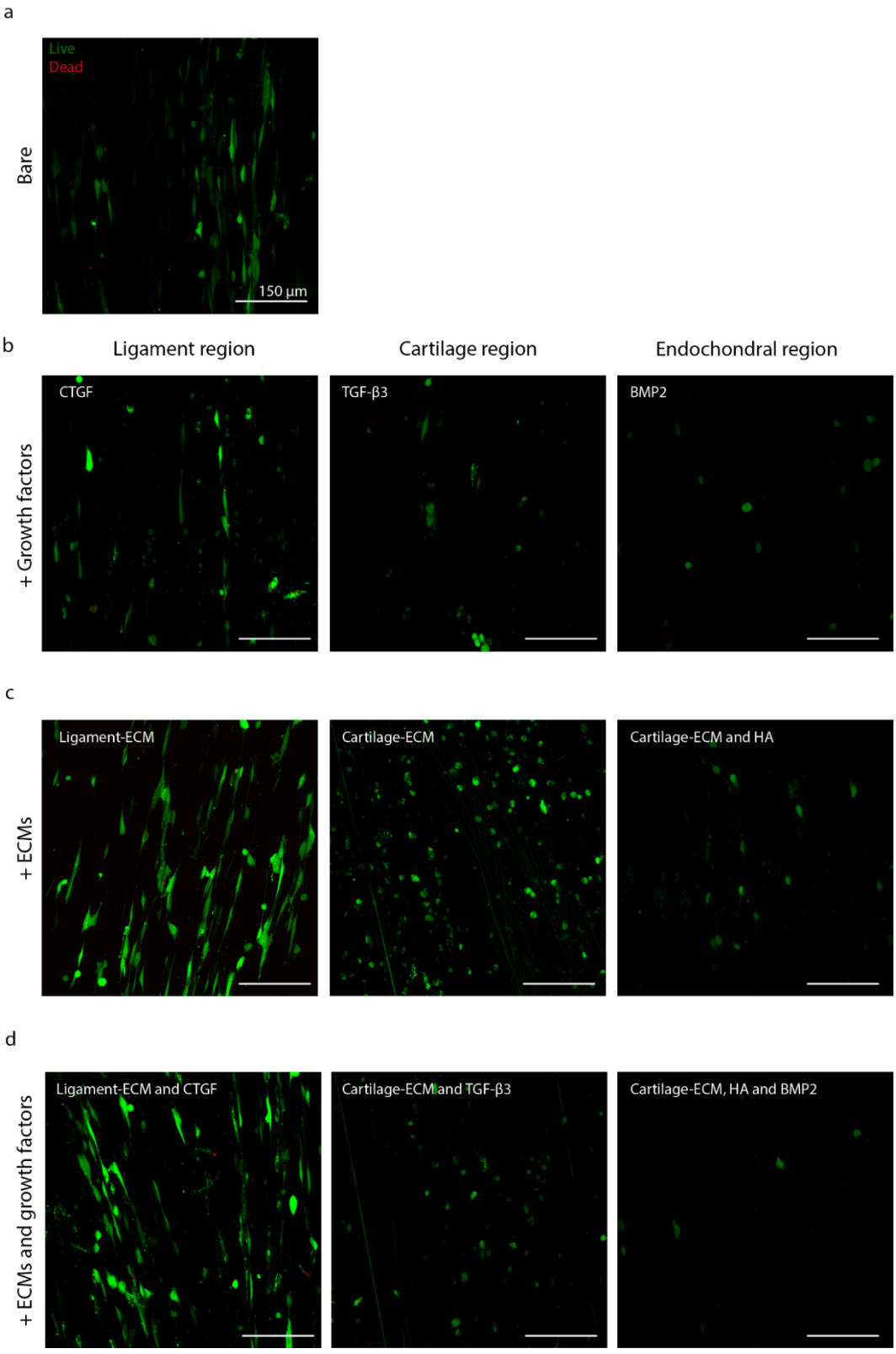

Figure 6.6 Viability and morphological differences of MSCs within each one of the regions. Ligament region (left), cartilage region (centre) and bone region (right). **a**, Live (green)/Dead (red) staining of MSCs on bare scaffolds. **b**, Group with growth factors only. **c**, Group with extracellular matrices (ECM) only, and d, Group of scaffolds with ECM and growth factors. Scale bars, 150 µm.

After 10 days in culture, gene expression was assessed. Comparable levels of *COL1A1* expression were observed on all scaffolds (Figure 6.7 a), with no significant difference in the expression of this gene in the different regions of each scaffold (Note: the first bar on each graph within Figure 6.7 represents the ligament region, the second bar the cartilage region and the third bar the bone region). Scaffolds with growth factor immobilization only supported the lowest levels of *TNMD* expression (Figure 6.7 b). The cartilage region (functionalised with TGF-β3) of these growth factor only scaffolds promoted the highest expression of *COMP* and the highest expression of *ACAN* compared to the other two scaffold regions (Figure 6.7 c, d). *BMP2* immobilized onto the bone region of these scaffolds did not stimulate MSCs to express higher levels of *OPN* and *COL10A1* compared to other regions of the scaffold (Figure 6.7 e, f).

Functionalization with ligament-ECM (L-ECM) and cartilage-ECM (C-ECM) only promoted the highest levels of *TNMD* expression of MSCs. Attaching L-ECM only to the ligament region was more effective than CTGF only or L-ECM with CTGF in stimulating the expression of *TNMD*. Functionalizing the bone region with C-ECM and HA coating supported the highest expression of *COMP* among the three regions in the ECM only scaffolds. Similarly, this group supports the highest expression of *ACAN, OPN* and *COL10A1*, suggesting progression along the endochondral pathway.

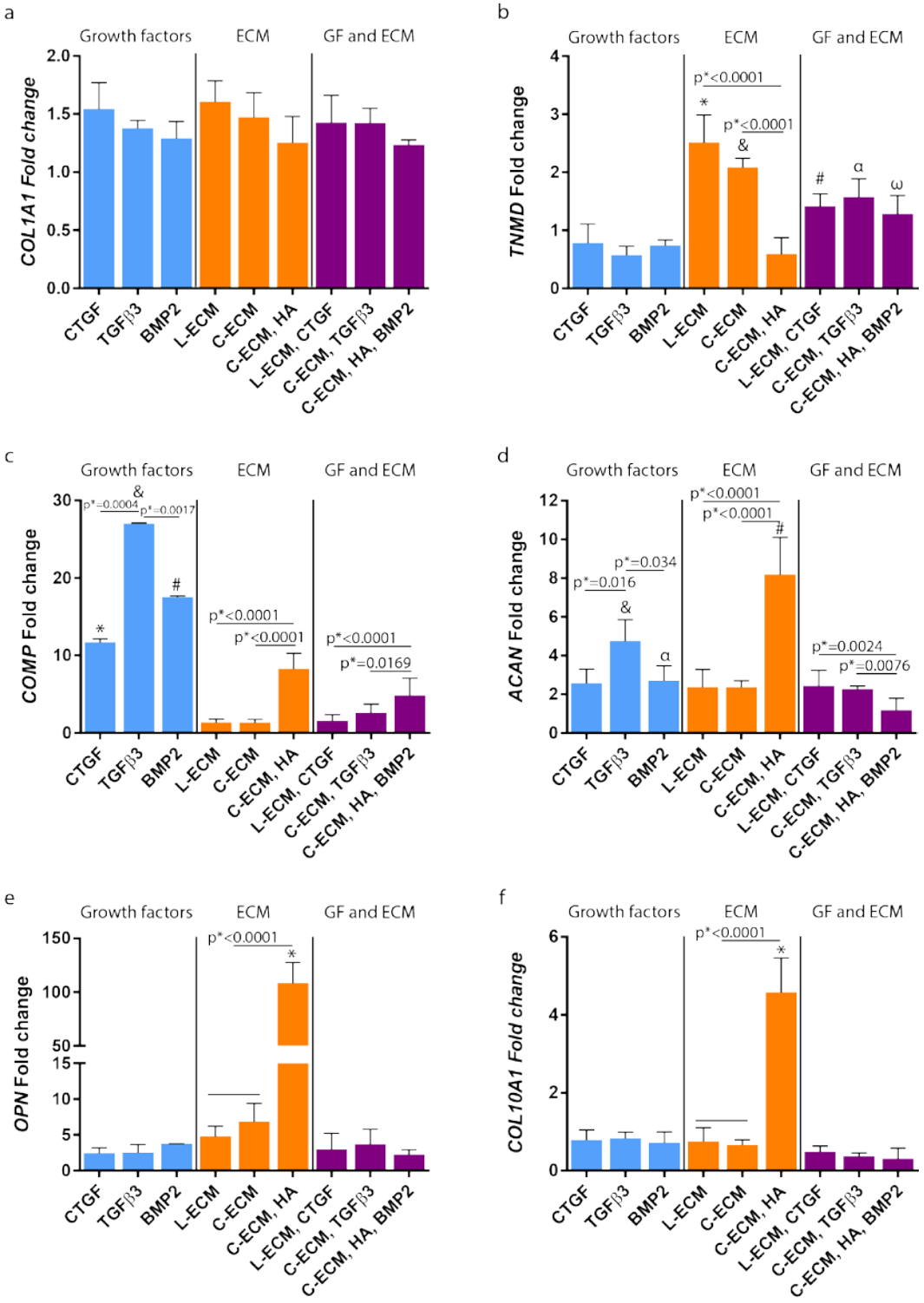

Figure 6.7 Gene expression at day 10. Collagen type I (*COL1A1*), tenomodulin (*TNMD*), cartilage oligomeric matrix protein (*COMP*), aggrecan (*ACAN*), osteopontin (*OPN*), and collagen type X (*COL10A1*). Blue bars correspond to scaffolds with growth factors only, orange bars to scaffolds with ECM only, and purple bars to scaffolds with both ECM and growth factors. Within each group, the first bar corresponds to the ligament region, the second to the cartilage region, and the third to the bone regions. For statistical analysis groups were compared within and among those of the same region. L-ECM: ligament-ECM; C-ECM: cartilage-ECM; HA: hydroxyapatite. **a**, Collagen type I (*COL1A1*). **b**, Tenomodulin (*TNMD*). *, $p<0.01$ versus CTGF and L-ECM, CTGF; #, $p < 0.01$ versus CTGF. &, $p<0.0001$ versus TGF-β3 and C-ECM, TGF-β3; α, $p<0.0001$ versus TGF-β3. ω, $p<0.01$ versus BMP2. **c**, Cartilage

Oligomeric Matrix Protein (*COMP*). *, p<0.0001 versus CTGF and L-ECM, CTGF; &, p<0.0001 versus TGF-β3 and C-ECM, TGF-β3; #, p < 0.01 versus C-ECM, HA and C-ECM, HA, BMP2. **d**, Aggrecan (*ACAN*). &, p<0.01 versus C-ECM and C-ECM, TGF-β3; #, p < 0.0001 versus BMP2 and C-ECM, HA, BMP2; α, p<0.0001 versus C-ECM, HA, BMP2. **e**, Aggrecan (ACAN). &, p<0.01 versus C-ECM and C-ECM, TGF-β3; #, p < 0.0001 versus BMP2 and C-ECM, HA, BMP2; α, p<0.0001 versus C-ECM, HA, BMP2. **f**, Osteopontin (*OPN*). *, p<0.0001 versus BMP2 and C-ECM, HA, BMP2. **g**, Collagen type X (*COL10A1*). *, p<0.0001 versus BMP2 and C-ECM, HA, BMP2. Gene expression was relative to the expression of MSCs on bare scaffolds. Error bars, mean ± SEM., one-way ANOVA (p < 0.05) with Tukey's multiple comparisons test (n= 5).

6.4 Discussion

The goal of this chapter was to create a zonal organization of endochondral, chondrogenic and ligamentogenic cellular phenotypes along the length of an electrospun PCL scaffold. It was envisioned that this could be achieved by a one-step seeding of MSCs onto scaffolds containing a spatial presentation of tissue-specific extracellular matrices (ECM) and growth factors. Polycaprolactone microfibre-scaffolds were used as carrier for the immobilization of regulatory cues and to provide mechanical stiffness and strength (Chapter 5).

Finding an appropriate culture media is key to the successful differentiation of MSCs for *in vitro* tissue engineering strategies. The introduction of insulin-transferrin-selenium (ITS), dexamethasone (DEX) and linoleic acid to CDM media supplemented with CTGF was permissive to differentiation towards pre-adipocytes. As observed in chapter 5, this can result in two distinct populations rather than the targeted homogenous population of fibroblasts. ITS, DEX and IBMX (3-isobutyl-1-methylxanthine) are standard components in adipogenic induction media for MSCs (Scott *et al.*, 2011). Although IBMX (a regulator of PPARγ (peroxisome proliferator-activated receptor-gamma), required for the conversion of pre-adypocytes (Kim *et al.*, 2010)) was not used, dexamethasone can stimulate either osteogenesis or adipogenesis depending in its concentration and time; and insulin can induce proliferation and differentiation of pre-adipocytes (Scott *et al.*, 2011). Further, gene expression showed

that there are more favourable culture medias for CTGF-mediated ligamentogenesis and TGF-β3-mediated chondrogenesis. Basal media was selected based on high expression levels of target genes, however, such a basic formulation might have caused limited matrix synthesis. Histology showed little to no deposition of collagen or glycosaminoglycans at day 21 (data not shown).

In an attempt to provide a substrate more supportive of endochondral ossification, the ends of the scaffolds were additionally coated with hydroxyapatite (HA). The HA chemical structure is similar to the inorganic composition of human bone, and previous studies have shown that HA bonds with bone (Müller-Mai *et al.*, 1995; Edwards, Brunski and Higuchi, 1997). The HA layer obtained in this study was formed in a process analogous to mineral formation in teeth and bones and the process of shell development on molluscs (Murphy, Kohn and Mooney, 2000). By this process, ceramics, metals and polymers have been successfully coated with a HA layer (Kokubo *et al.*, 1999; Oyane *et al.*, 1999). In the context of tissue engineering, the adhesive strength of the apatite layer formed via SBF incubation is enhanced in biomaterials with increased surface roughness and/or with increased amount of polar groups (Tanahashi *et al.*, 1994, 1995; Liu *et al.*, 1998). PCL has functional groups (i.e. ester groups) that can be hydrolysed to polar groups (i.e. carboxyl, COO–, COOH, and OH) formed by the alkaline hydrolysis (NaOH treatment) of the ester groups. In this case, the polar groups on the PCL fibres are needed for apatite to be nucleated on the surface. The negatively charged PCL surface (with COO–, COOH, and OH) then chelates, accumulates calcium and phosphate ions available in the solution by electrostatic force and hydrogen bonding. The local increase of supersaturation of these ionic precursors to mineral formation stimulates surface nucleation and mineral growth follows (Zhang and Ma, 1999; Murphy, Kohn and Mooney, 2000). MSCs on scaffolds coated with HA showed higher levels of *OPN* expression compared to scaffolds coated with Col-1.

The addition of ligament-ECM (L-ECM) onto the fibres was sufficient to enhance *TNMD* and *COL1A1* gene expression. Previous studies have demonstrated the tissue-specific differentiation using tendon-ECM (Rothrauff, Yang and Tuan, 2017). The use of ECM only showed to be more suitable for fibroblastic MSC differentiation that the incorporation of CTGF. CTGF has been used for promoting fibroblastic MSC differentiation (Lee *et al.*, 2010).

As early as 24 h after cell seeding onto the region of the scaffold functionalised with cartilage ECM (C-ECM), MSCs adopted a round shape characteristic of chondrocytes. While the expression of *ACAN* was higher on C-ECM compared to bare scaffolds, the expression of *COMP* and *ACAN* (chondrogenic markers in this study) was inferior to that of MSCs exposed to TGF-β3 directly on the scaffolds. Interestingly, C-ECM coupled with HA showed increased endochondral gene expression, as evident by the upregulation of *OPN* and *COL10A1*. Type II collagen (Col-2) is the main structural protein in articular cartilage, and it was the major component of the decellularized cartilage-ECM used in this study (Chapter 6). Col-2 provides the mechanical strength in articular cartilage, supports cell proliferation and maintains the chondrogenic phenotype (Huber, Trattnig and Lintner, 2000). Previous studies have demonstrated that incorporating Col-2 into a hydrogel enhanced cellular condensation and deposition of cartilaginous ECM by chondrocytes or MSCs (Choi *et al.*, 2014). Furthermore, it is known that cartilage ECM can act as a substrate to support endochondral bone formation (Gawlitta *et al.*, 2015).

Surprisingly, the group with ECM and growth factors showed only marginal upregulation of key markers for either ligamentogenic, chondrogenic or endochondral pathways. In summary, microfibres coated with L-ECM for the ligament region, TGF-β3 enriched region for the cartilage segment, and C-ECM with HA coating for an endochondral region could be the most suitable combination of biochemical cues to instruct the differentiation of MSCs into a template for the bone-ligament enthesis.

6.5 Conclusions

Having developed a super porous 3D fibre-bundle that was mechanically approaching the native human ligament, it was adorned with components of the native articular cartilage and ligament, a mineral phase, and growth factors. Scaffolds spatially patterned with ECM components and growth factors offer the benefit of enabling a single progenitor cell population, either seeded onto the scaffold prior to implantation or recruited into the scaffold post-implantation, to promote multiple lineage commitment on a single material and hence regeneration the complex bone-ligament unit.

Chapter 7 Discussion and conclusions

The objective of this thesis was to develop a mechanically functional and spatially defined scaffold for ligament tissue engineering with the potential to regenerate the stratified interface between ligament and bone. This thesis began by investigating how fibre alignment and growth factor stimulation interact to regulate the chondrogenic and ligamentous differentiation of mesenchymal stem cells (MSCs) (Chapter 3). Electrospinning was selected as the manufacturing technique to produce the fibrillar scaffolds. It is a versatile technique to produce fibres of a wide range of materials and the processing parameters can be controlled to produce fibres of diverse diameters and alignment. Micro was favoured over nano-sized fibres as microfibres generate scaffolds containing larger pores and with higher overall porosity for cell infiltration and nutrient diffusion. Previous studies have shown that microfibres induce higher expression of marker genes of mature ligamentocytes (Cardwell, Dahlgren and Goldstein, 2014), as well as chondrogenic gene expression compared to nanofibers (Bean and Tuan, 2015). Chapter 3 shows that without growth factor stimulation, mesenchymal stem cells (MSCs) on aligned-microfibers showed higher levels of tenomodulin (*TNMD*) and aggrecan (*ACAN*) gene expression compared to MSCs on randomly-oriented fibres. Aligned microfibers and co-stimulation with connective tissue growth factor (CTGF) preferentially supported ligamentous differentiation of MSCs. MSCs on aligned-microfibers stimulated with TGF-β3 formed cellular aggregates and underwent robust chondrogenesis, evidenced by increased type II collagen expression and sulphated glycosaminoglycans (sGAG) synthesis compared to MSCs on randomly-oriented scaffolds. Bone morphogenetic protein 2 (*BMP2*) and type I collagen gene expression were higher on randomly-oriented scaffolds stimulated with TGF-β3 stimulation, suggesting this substrate was more supportive of an endochondral phenotype. Upon sequential growth factor stimulation, MSCs expressed types I and II collagen and deposited higher overall levels of collagen compared to scaffolds stimulated with either growth factor in isolation. These findings demonstrate that modulating

the alignment of microfibrillar scaffolds can be used to promote either an endochondral, chondrogenic, fibrochondrogenic or ligamentous MSC phenotype upon presentation of appropriate biochemical cues. Chapter 3 of this thesis highlights the relevance of using aligned polymeric electrospun fibres not only for the ligament proper but also to recapitulate the cellular phenotypes observed across the bone-ligament interface.

The next step of this thesis was to scale-up the electrospun fibre sheet used in Chapter 3 into three-dimensional (3D) scaffolds with the size of a human ligament. In Chapter 4, the anterior cruciate ligament was used as a model system to set target dimensions. The two challenges described in the literature in scaling-up electrospun fibres are (1) the design (e.g. rolling, braiding, stacking, etc.) to achieve mechanical properties close to native ACL and (2) improving the limited cell infiltration into the body of the dense electrospun fibre scaffolds which limits their regenerative potential. Chapter 4 of this thesis describes a method to produce porous, 3D microfibrillar scaffolds with promising mechanical properties for ligament TE. By varying the rotational speed of the collecting mandrel during the electrospinning of PCL, but keeping all other parameters constant, fibre sheets with different fractions of unwelded fibres (i.e. less welds in juxtaposed fibres) were produced. Increasing the fraction of unwelded fibres reduced the flexural rigidity of the electrospun sheets, which in turn enabled the bundling of the fibres into 3D scaffolds with similar dimensions to the ACL. Furthermore, these unwelded fibres allowed for higher interfibrillar spacing, which facilitated the rapid migration of MSCs into the body of the scaffolds. The scaffolds were also capable of supporting the differentiation of MSCs towards either the fibrocartilage or ligament lineage. Mechanical testing of the 3D fibre-bundles demonstrated that they possessed a Young's modulus similar to native human ACL. Future work could be conducted to test the mechanical properties of the bundle with ACL dimensions (electrospun for 2 h) to better characterize the mechanical properties of the bundles that could be used in an *in vivo* scenario. These scaffolds mimicked some, but not all, of the mechanical properties of the human ACL. The yield stress and yield

strain were less than 50% of the yield stress and strain of ACL. Future work must focus on a way to increase yield stress and strain, for example by altering the bundle arrangement as the geometry of the fibre bundle plays a key role in the mechanical properties (Pauly *et al.*, 2016). The general biofabrication strategy described in this study could be used to produce implants for a wide range of biomedical applications.

The next two chapters of the thesis used the scaffolds from Chapter 4 to develop a tissue engineered template with a ligament region, a cartilaginous region and a mineralized cartilaginous region, which could potentially remodel into a more complex interface tissue upon implantation into the joint environment. Developmentally, the bone-ligament interface is derived from a soft tissue precursor (Lu and Thomopoulos, 2013). In Chapter 5, the polymeric microfibre-scaffolds were adorned with decellularized ligament (L-ECM) or cartilage ECM (C-ECM) via covalent conjugation of hydrophobic adsorption. Two methods of protein immobilization were used to elucidate whether MSCs were sensitive to the different immobilization conditions. Physically immobilized L-ECM consistently up-regulated ligament genes to a greater extent than bare scaffolds or scaffolds functionalised with Col-1 or with C-ECM. Chemical immobilization of ECM was found to enhance chondrogenesis on microfibrillar scaffolds in the absence of growth factors, although this was not observed with TGFβ3 co-stimulation. This contrast with reports in literature that have shown that when cartilage ECM was incorporated within a hydrogel it enhanced chondrogenesis of encapsulated MSCs upon TGFβ supplementation in the medium (Rothrauff, Yang and Tuan, 2017). No dramatic increases in ligamentogenesis was observed on scaffolds with physically immobilized L-ECM following additional CTGF stimulation. Chapter 5 highlights the importance of considering the method of protein immobilization onto scaffolds. Future work could provide evidence in support of this observation by conducting X-ray crystallography analysis on the immobilized proteins. This chapter also validates that the engineered ligament graft using L-ECM supported fibrogenesis when immobilized by physical adsorption, and the engineered cartilage

environment using chemically immobilized C-ECM supported chondrogenesis. A limitation of this chapter was that ECM stability on the fibre scaffolds in culture conditions was not investigated, this could have been partially addressed by using a hydroxyproline assay before and after the culture period.

Though no major positive effect of chemical immobilization of ligament ECM on ligamentogenesis was demonstrated in chapter 5, chemical immobilization offers molecular stability and better control over coating density (Schuler *et al.*, 2006); physical adsorption of biomolecules has shown instability and is often reversible owing to the phase equilibrium between adsorbed molecules and culture conditions (Luginbuehl *et al.*, 2004). This is because the adsorption mechanism is through electrostatic interactions. In literature, there are a mix of results when using passively adsorbed proteins on surfaces (Schuler *et al.*, 2006). To avoid these problems, for Chapter 6, ECM was linked covalently to the surface of the fibres. Control of protein immobilization was achieved by soaking the scaffolds in the different solutions to create the different regions, although some overlapping might have occurred. Future work should focus in developing a less time intensive process to achieve higher precision. To create a mineralized matrix contiguous to a cartilage region, a strategy was required to deposit mineral. The most common mineralization techniques in TE are immersion the scaffolds in solutions rich in calcium and phosphate (Yamauchi *et al.*, 2004; Al-Munajjed *et al.*, 2009; Li *et al.*, 2009), or by incorporating hydroxyapatite particles (Huang *et al.*, 2009). Immersion in SBF was selected due to its simplicity; ions at high supersaturation simply precipitate on the surface of the fibres; hydroxyapatite particles are commonly embedded in hydrogels. Future work could be undertaken to measure the amount of apatite deposited on the fibres so that the results can be translatable to others using HA but not necessarily nucleated with SBF. For example, this could be done with Raman spectroscopy and calcium assays. The scaffolds functionalised with cartilage ECM and a HA coating were found to spatially support an osseous/endochondral phenotype. This response may be due in part to local stiffening of the

ECM environment with the addition of HA (Engler *et al.*, 2006; Pek, Wan and Ying, 2010; Zander *et al.*, 2010; Mao, Shin and Mooney, 2016). No beneficial effect of introducing growth factors was observed when coupled with ECM. An unexpected result was that covalently conjugated CTGF onto bare fibres did not elicit a positive effect in *TNMD* gene expression that soluble CTGF did in Chapters 3, 4 and 5; it was only when immobilized onto Col-1 and C-ECM that an effect of immobolized CTGF was observed. It is tempting to conclude that an appropriate scaffold for ligament-bone TE would be physically coated with L-ECM in the engineered ligament region, next to an engineered cartilage region of covalently immobilized TGFβ3, next to an endochondral region of C-ECM and HA.

Together, this thesis describes a novel methodology to develop a scaffold for ligament tissue engineering that is close in size and stiffness to the human ACL and presents spatially defined regions with the potential to regenerate the stratified interface between ligament and bone. This work provides insights into the appropriate combinations of biophysical and biochemical factors that can be used to promote the bone-ligament interface, using a novel framework that is inspired by aspects of the developmental skeletal process. The emergence of endochondral ossification as a paradigm for bone tissue engineering could be also applied for ligament tissue engineering to engineer the complexity of the bone-ligament unit.

7.1 Limitations

Porcine bone marrow derived MSCs were used for all studies in this thesis. The pig is the most commonly used preclinical large animal model in many fields of medicine (Bharti *et al.*, 2016). Porcine MSCs show comparable multi-lineage differentiation potential and immune-modulatory capacity to human MSCs (Noort *et al.*, 2012). Further studies are required to replicate the findings of this work using human MSCs.

In vivo studies of this work would have demonstrated whether the endochondral region underwent endochondral ossification. In addition, such studies would confirm whether the cartilaginous and ligamentous regions underwent continued chondrogenesis and fibrogenesis, respectively. This work would have benefitted from an ectopic *in vivo* model, but ideally an orthotopic model would have elucidated the stability and efficacy of the scaffold (e.g. in a small animal model such as a rat). An ectopic *in vivo* model would have elucidated if host cells migrate into the body of the scaffold.

The bundles collected at 3500 RPM displayed inferior yield stress and strain. The yield stress and yield strain of human ACL are ~38 MPa and 45% for younger humans, and ~13 MPa and ~30% for older humans (Noyes and Grood, 1976). A limitation of this thesis may be that additional strategies were not utilised to increase the yield stress and yield strain of the scaffolds, either by exploring another scaffold geometry, or another polymer, or by performing the characterization of the 2 h bundles (similar in size with the ACL). Potentially, higher yield stress and strain could be addressed by electrospinning thinner fibres; a report conducted with the goal of characterizing the mechanical properties of single electrospun PCL fibres found that yield stress and yield strain increase with decreasing fibre diameter. Fibres of 1.03 μm (compared to the range they studied: 1.35 - 1.7 μm fibres) displayed mechanical properties similar to the ones reported in Chapter 4 with some benefit: tensile modulus of 120 ± 30 MPa, yield stress of 13 ± 7 MPa and yield strain of 20 ± 10% (Tang and Lim, 2006). However, the experiments in this thesis would have to be repeated to confirm differentiation of MSC is the same with ~4 times thinner fibres. Electrospinning a different material might be another route to increase the yield stress and yield strain. Another way could be to introduce structure hierarchy to the fibres bundles. For example, wrapping some fibres with a highly porous thin sleeve, and then wrapping many of these together in another wrap, to try to mimic the hierarchy in native ligaments and tendons (see Figure 2.4). studies recapitulating some

aspects of the native tissue hierarchy have shown mechanical properties similar to native human ACL (Pauly *et al.*, 2016, 2017).

In chapters 5 and 6, the bioactivity of the scaffolds was assessed using gene expression through qRT-PCR. Exploring approaches to confirm long-term transcription stability might have been taken, such as histology and biochemical assays. Histology was performed, however in Chapter 5, only scaffolds co-stimulated with TGFβ3 synthesized significant levels of extracellular matrix proteins. Examining several different slices at different depths of the same and different constructs might have shown some collagen and GAGs in the rest of the conditions. In Chapter 6, negligible ECM synthesis was seen in the sections stained for any of the experimental conditions.

The method of protein immobilization was found to play a significant role on the expression of ligament and cartilage specific genes. Although it was elucidated that MSCs are sensitive to the method of protein immobilization, the exact feature to what they were sensitive to was not investigated.

Alkaline hydrolysis is used as a treatment for surface modification of polymers such as PCL, but it is also used to degrade these polymers. Scaffolds that underwent surface modification through incubation with NaOH (Chapter 5 and 6) were not mechanically tested, this represents a lack of consideration of the effects that surface degradation might have on the tissue engineered grafts.

A limitation of this thesis was that immobilization of growth factors was not confirmed by any experiment. The evidence that growth factor was immobilized was the difference in the gene expression with the addition of growth factors. For example, fibres + TGFβ3 showed increased gene expression of *COMP* and *ACAN* compared to bare fibres, another example is that Col-1 gene expression enhanced with the addition of CTGF. Future work will require to

characterize the immobilization of the growth factors. For example, others have shown that using BSA as a model protein representative of the growth factor, can be used to quantify the amount and visualize the distribution of the growth factor under investigation (Bhattacharjee *et al.*, 2016).

7.2 Conclusions

- Fibre alignment regulates the ligamentous, chondrogenic, fibrochondrogenic and endochondral phenotype of bone marrow derived MSC upon the appropriate growth factor supplementation. For the engineering of ligament grafts, aligned microfibres coupled with CTGF stimulation can be used to enhance ligament matrix production, and aligned microfibres coupled with TGFβ3 can be used to promote chondrogenesis.

- Collecting the electrospun fibre thread at high speeds during electrospinning can be used to encourage the deposition of unwelded microfibres. Unwelded microfibres display a decreased flexural rigidity that enables the bundling of fibre-sheets into 3D scaffolds.

- Scaffolds formed by unwelded fibres allow for higher interfibre space that facilitates infiltration of bone marrow derived MSCs.

- The bioactivity of pepsin-solubilised decellularized ligament ECM is validated to promote homologous MSC differentiation when physically immobilized onto the biomimetic aligned fibre-bundles.

- An engineered graft with a distal region functionalised with cartilage ECM and HA is conductive of an endochondral phenotype.

7.3 Future work

Future studies are required to evaluate the capacity of these functionalized-scaffolds to generate endochondral ossification, chondrogenesis and fibrogenesis *in vivo*. An ectopic *in vivo* model could elucidate if host cells migrate into the body of the scaffold; an orthotopic model could elucidate the stability and efficacy of the scaffold in a small animal model such as a rat, additionally.

Future work should focus on designing the ends of the scaffolds (i.e. how to wrap the ends for surgery fixation), as in this thesis scaffolds were bundled by using sutures to tie each end, or by melting the ends to form a solid PCL small flat plug. Alternatively, these bundle designs should be tested to withstand pull-out from a pin or from surgery sutures to comply with the rigour of the surgical fixation and to demonstrate clinical translatability.

The fibres produced in this study could have broader implications for strategies for fibre-reinforcement. Hydrogels could be reinforced with a phase of (unwelded) fibres (Huang *et al.*, 2017). Hydrogels have been reinforced with nanofibers (Shin *et al.*, 2012), microfibres (Yodmuang *et al.*, 2015) and woven (Moutos, Freed and Guilak, 2007; Visser, Melchels, *et al.*, 2015) scaffolds. For example, when hydrogel scaffolds were reinforced with a fibre network, its compressive stiffness was increased ~54-fold compared to either component in isolation. This fibre-reinforced hydrogel approached the stiffness of articular cartilage (Visser, Melchels, *et al.*, 2015).

Bibliography

Abe, Y., Kokubo, T. and Yamamuro, T. (1990) 'Apatite coating on ceramics, metals and polymers utilizing a biological process', *Journal of Materials Science: Materials in Medicine*. Kluwer Academic Publishers, 1(4), pp. 233–238. doi: 10.1007/BF00701082.

Adam, O. *et al.* (2011) 'Increased lysyl oxidase expression and collagen cross-linking during atrial fibrillation', *Journal of Molecular and Cellular Cardiology*, 50(4), pp. 678–685. doi: 10.1016/j.yjmcc.2010.12.019.

Adesida, A. B. *et al.* (2006) 'The matrix-forming phenotype of cultured human meniscus cells is enhanced after culture with fibroblast growth factor 2 and is further stimulated by hypoxia.', *Arthritis research & therapy*, 8(3), p. R61. doi: 10.1186/ar1929.

Adesida, A. B. *et al.* (2012) 'Oxygen tension is a determinant of the matrix-forming phenotype of cultured human meniscal fibrochondrocytes.', *PLoS ONE*, 7(6), p. e39339. doi: 10.1371/journal.pone.0039339.

Akiyama, H. *et al.* (2002) 'The transcription factor Sox9 has essential roles in successive steps of the chondrocyte differentiation pathway and is required for expression of Sox5 and Sox6.', *Genes & development*, 16(21), pp. 2813–28. doi: 10.1101/gad.1017802.

Akiyama, H. *et al.* (2005) 'Osteo-chondroprogenitor cells are derived from Sox9 expressing precursors.', *Proceedings of the National Academy of Sciences of the United States of America*, 102(41), pp. 14665–70. doi: 10.1073/pnas.0504750102.

Al-Munajjed, A. A. *et al.* (2009) 'Development of a biomimetic collagen-hydroxyapatite scaffold for bone tissue engineering using a SBF immersion technique', *Journal of Biomedical Materials Research Part B: Applied Biomaterials*, 90B(2), pp. 584–591. doi: 10.1002/jbm.b.31320.

Almeida, H. V. *et al.* (2016) 'Fibrin hydrogels functionalized with cartilage extracellular matrix and incorporating freshly isolated stromal cells as an injectable for cartilage regeneration', *Acta Biomaterialia*. Acta Materialia Inc., 36, pp. 55–62. doi: 10.1016/j.actbio.2016.03.008.

Altman, G. H. *et al.* (2002) 'Silk matrix for tissue engineered anterior cruciate ligaments', *Biomaterials*, 23(20), pp. 4131–4141. doi: 10.1016/S0142-9612(02)00156-4.

Amiel, D. *et al.* (1983) 'Tendons and ligaments: A morphological and biochemical comparison',

Journal of Orthopaedic Research, 1(3), pp. 257–265. doi: 10.1002/jor.1100010305.

Amis, A. A. and Dawkins, G. P. (1991) 'Functional anatomy of the anterior cruciate ligament. Fibre bundle actions related to ligament replacements and injuries.', *The Journal of bone and joint surgery. British volume*, 73(2), pp. 260–7.

Anderson, A. F. *et al.* (2001) 'Correlation of Anthropometric Measurements, Strength, Anterior Cruciate Ligament Size, and Intercondylar Notch Characteristics to Sex Differences in Anterior Cruciate Ligament Tear Rates', *The American Journal of Sports Medicine*. SAGE PublicationsSage CA: Los Angeles, CA, 29(1), pp. 58–66. doi: 10.1177/03635465010290011501.

Athanasiou, K. A. and Sanchez-Adams, J. (2009) *Engineering the Knee Meniscus*. Morgan & Claypool Publishers.

Aune, A. K. *et al.* (2001) 'Four-strand hamstring tendon autograft compared with patellar tendon-bone autograft for anterior cruciate ligament reconstruction. A randomized study with two-year follow-up.', *The American journal of sports medicine*, 29(6), pp. 722–8.

Baek, S. J., Kang, S. K. and Ra, J. C. (2011) 'In vitro migration capacity of human adipose tissue-derived mesenchymal stem cells reflects their expression of receptors for chemokines and growth factors', *Experimental & molecular medicine*. Korean Society for Biochemistry and Molecular Biology, 43(10), pp. 596–603. doi: 10.3858/emm.2011.43.10.069.

Baker, B. M. *et al.* (2008) 'The potential to improve cell infiltration in composite fiber-aligned electrospun scaffolds by the selective removal of sacrificial fibers.', *Biomaterials*, 29(15), pp. 2348–58. doi: 10.1016/j.biomaterials.2008.01.032.

Baker, B. M. *et al.* (2012) 'Sacrificial nanofibrous composites provide instruction without impediment and enable functional tissue formation.', *Proceedings of the National Academy of Sciences of the United States of America*, 109(35), pp. 14176–81. doi: 10.1073/pnas.1206962109.

Baker, B. M. and Mauck, R. L. (2007) 'The effect of nanofiber alignment on the maturation of engineered meniscus constructs', *Biomaterials*, 28(11), pp. 1967–77. doi: 10.1016/j.biomaterials.2007.01.004.

Balguid, A. *et al.* (2009) 'Tailoring Fiber Diameter in Electrospun Poly(ε-Caprolactone) Scaffolds

for Optimal Cellular Infiltration in Cardiovascular Tissue Engineering', *Tissue Engineering Part A*. Mary Ann Liebert, Inc., 15(2), pp. 437–444. doi: 10.1089/ten.tea.2007.0294.

Barry, F. *et al.* (2001) 'Chondrogenic differentiation of mesenchymal stem cells from bone marrow: differentiation-dependent gene expression of matrix components.', *Experimental cell research*, 268(2), pp. 189–200. doi: 10.1006/excr.2001.5278.

Bashur, C. A., Dahlgren, L. A. and Goldstein, A. S. (2006) 'Effect of fiber diameter and orientation on fibroblast morphology and proliferation on electrospun poly(D,L-lactic-co-glycolic acid) meshes', *Biomaterials*, 27(33), pp. 5681–8. doi: 10.1016/j.biomaterials.2006.07.005.

Bean, A. C. and Tuan, R. S. (2015) 'Fiber diameter and seeding density influence chondrogenic differentiation of mesenchymal stem cells seeded on electrospun poly(ε-caprolactone) scaffolds.', *Biomedical materials (Bristol, England)*. NIH Public Access, 10(1), p. 015018. doi: 10.1088/1748-6041/10/1/015018.

Beaulieu, M. L. *et al.* (2015) 'Quantitative comparison of the microscopic anatomy of the human ACL femoral and tibial entheses.', *Journal of orthopaedic research : official publication of the Orthopaedic Research Society*. NIH Public Access, 33(12), pp. 1811–7. doi: 10.1002/jor.22966.

Beck, E. C. *et al.* (2016) 'Chondroinduction from Naturally Derived Cartilage Matrix: A Comparison Between Devitalized and Decellularized Cartilage Encapsulated in Hydrogel Pastes.', *Tissue engineering. Part A*. Mary Ann Liebert, Inc., 22(7–8), pp. 665–79. doi: 10.1089/ten.TEA.2015.0546.

Beck, E. C. *et al.* (2016) 'Chondroinductive Hydrogel Pastes Composed of Naturally Derived Devitalized Cartilage', *Annals of Biomedical Engineering*, 44(6), pp. 1863–1880. doi: 10.1007/s10439-015-1547-5.

Benders, K. E. M. *et al.* (2013) 'Extracellular matrix scaffolds for cartilage and bone regeneration', *Trends in Biotechnology*, 31(3), pp. 169–176. doi: 10.1016/j.tibtech.2012.12.004.

Benjamin, M. *et al.* (2006) 'Where tendons and ligaments meet bone: attachment sites ('entheses') in relation to exercise and/or mechanical load.', *Journal of anatomy*, 208(4), pp. 471–90. doi: 10.1111/j.1469-7580.2006.00540.x.

Benjamin, M., Evans, E. J. and Copp, L. (1986) 'The histology of tendon attachments to bone in man', *Journal of Anatomy*. Wiley-Blackwell, 149, pp. 89–100.

Benjamin, M. and Ralphs, J. R. (1998) 'Fibrocartilage in tendons and ligaments--an adaptation to compressive load.', *Journal of anatomy*, 193(4), pp. 481–94. doi: 10.1046/j.1469-7580.1998.19340481.x.

Benjamin, M. and Ralphs, J. R. (2000) 'A Survey of Cell Biology', in Jeon, K. (ed.) *International Review of Cytotology*. 1st edn. Academic Press, p. 324.

Bharti, D. *et al.* (2016) 'Research Advancements in Porcine Derived Mesenchymal Stem Cells.', *Current stem cell research & therapy*, 11(1), pp. 78–93.

Bhattacharjee, P. *et al.* (2016) 'Non-mulberry silk fibroin grafted poly (Ie-caprolactone)/nano hydroxyapatite nanofibrous scaffold for dual growth factor delivery to promote bone regeneration', *Journal of Colloid and Interface Science*. Elsevier Inc., 472(March), pp. 16–33. doi: 10.1016/j.jcis.2016.03.020.

Bi, F. *et al.* (2015) 'Anterior Cruciate Ligament Reconstruction in a Rabbit Model Using Silk-Collagen Scaffold and Comparison with Autograft', *PLOS ONE*. Edited by X. Liu. Public Library of Science, 10(5), p. e0125900. doi: 10.1371/journal.pone.0125900.

Bi, W. *et al.* (1999) 'Sox9 is required for cartilage formation.', *Nature genetics*, 22(1), pp. 85–9. doi: 10.1038/8792.

Bian, L. *et al.* (2011) 'Enhanced MSC chondrogenesis following delivery of TGF-β3 from alginate microspheres within hyaluronic acid hydrogels in vitro and in vivo', *Biomaterials*, 32(27), pp. 6425–6434. doi: 10.1016/j.biomaterials.2011.05.033.

Bian, L. *et al.* (2013) 'Hydrogels that mimic developmentally relevant matrix and N-cadherin interactions enhance MSC chondrogenesis', *Proceedings of the National Academy of Sciences of the United States of America*. National Academy of Sciences, 110(25), pp. 10117–22. doi: 10.1073/pnas.1214100110.

Blitz, E. *et al.* (2009) 'Bone ridge patterning during musculoskeletal assembly is mediated through SCX regulation of Bmp4 at the tendon-skeleton junction.', *Developmental cell*, 17(6), pp. 861–73. doi: 10.1016/j.devcel.2009.10.010.

Bonnin, M. *et al.* (2012) *The Knee Joint*. 2011th edn. Paris: Springer Paris. doi: 10.1007/978-2-

287-99353-4.

Brand, J. *et al.* (2000) 'Biomechanical comparison of quadriceps tendon fixation with patellar tendon bone plug interference fixation in cruciate ligament reconstruction.', *Arthroscopy : the journal of arthroscopic & related surgery : official publication of the Arthroscopy Association of North America and the International Arthroscopy Association*, 16(8), pp. 805–12. doi: 10.1053/jars.2000.18240.

Brent, A. E., Braun, T. and Tabin, C. J. (2005) 'Genetic analysis of interactions between the somitic muscle, cartilage and tendon cell lineages during mouse development.', *Development (Cambridge, England)*, 132(3), pp. 515–28. doi: 10.1242/dev.01605.

Di Brezzo, R. and Oliver, G. (2000) 'ACL Injuries in Active Girls and Women', *Journal of Physical Education, Recreation & Dance*, 71(6), pp. 24–27. doi: 10.1080/07303084.2000.10605157.

Broom, N. D. and Marra, D. L. (1986) 'Ultrastructural evidence for fibril-to-fibril associations in articular cartilage and their functional implication.', *Journal of anatomy*, 146, pp. 185–200.

Brown, J. P. *et al.* (2015) 'Comparative analysis of mesenchymal stem cell and embryonic tendon progenitor cell response to embryonic tendon biochemical and mechanical factors', *Stem Cell Research & Therapy*, 6(1), p. 89. doi: 10.1186/s13287-015-0043-z.

Caliari, S. R. *et al.* (2015) 'Collagen Scaffolds Incorporating Coincident Gradations of Instructive Structural and Biochemical Cues for Osteotendinous Junction Engineering', *Advanced Healthcare Materials*, 4(6), pp. 831–837. doi: 10.1002/adhm.201400809.

Caliari, S. R. and Harley, B. A. C. (2014a) 'Collagen-GAG scaffold biophysical properties bias MSC lineage choice in the presence of mixed soluble signals.', *Tissue engineering. Part A*, 20(17–18), pp. 2463–72. doi: 10.1089/ten.TEA.2013.0400.

Caliari, S. R. and Harley, B. A. C. (2014b) 'Structural and biochemical modification of a collagen scaffold to selectively enhance MSC tenogenic, chondrogenic, and osteogenic differentiation.', *Advanced healthcare materials*, 3(7), pp. 1086–96. doi: 10.1002/adhm.201300646.

Caliari, S. R., Ramirez, M. A. and Harley, B. A. C. (2011) 'The development of collagen-GAG scaffold-membrane composites for tendon tissue engineering', *Biomaterials*, 32(34), pp. 8990–8998. doi: 10.1016/j.biomaterials.2011.08.035.

Calve, S. *et al.* (2004) 'Engineering of functional tendon.', *Tissue engineering*. Mary Ann Liebert, Inc., 10(5–6), pp. 755–61. doi: 10.1089/1076327041348464.

Canale, S. T. and Beaty, J. H. (2012) *Campbell's Operative Orthopaedics: Expert Consult Premium Edition - Enhanced Online Features*. Elsevier Health Sciences.

Caplan, A. I. (2007) 'Adult mesenchymal stem cells for tissue engineering versus regenerative medicine.', *Journal of cellular physiology*, 213(2), pp. 341–7. doi: 10.1002/jcp.21200.

Cardwell, R. D., Dahlgren, L. a and Goldstein, A. S. (2014) 'Electrospun fibre diameter, not alignment, affects mesenchymal stem cell differentiation into the tendon/ligament lineage.', *Journal of tissue engineering and regenerative medicine*. doi: 10.1002/term.1589.

Chainani, A. *et al.* (2013) 'Multilayered electrospun scaffolds for tendon tissue engineering.', *Tissue engineering. Part A*, 19(23–24), pp. 2594–604. doi: 10.1089/ten.TEA.2013.0165.

Chamberlain, G. *et al.* (2007) 'Concise review: mesenchymal stem cells: their phenotype, differentiation capacity, immunological features, and potential for homing.', *Stem cells (Dayton, Ohio)*, 25(11), pp. 2739–49. doi: 10.1634/stemcells.2007-0197.

Chen, B. *et al.* (2016) 'Enhancement of tendon-to-bone healing after anterior cruciate ligament reconstruction using bone marrow-derived mesenchymal stem cells genetically modified with bFGF/BMP2.', *Scientific reports*. Nature Publishing Group, 6, p. 25940. doi: 10.1038/srep25940.

Chen, C.-H. (2009) 'Graft healing in anterior cruciate ligament reconstruction', *Sports medicine, arthroscopy, rehabilitation, therapy & technology : SMARTT*. BioMed Central, 1(1), p. 21. doi: 10.1186/1758-2555-1-21.

Chen, E. H. and Black, J. (1980) 'Materials design analysis of the prosthetic anterior cruciate ligament', *Journal of Biomedical Materials Research*. Wiley-Blackwell, 14(5), pp. 567–586. doi: 10.1002/jbm.820140504.

Chen, H. *et al.* (2014) 'Runx2 Regulates Endochondral Ossification Through Control of Chondrocyte Proliferation and Differentiation', *Journal of Bone and Mineral Research*, 29(12), pp. 2653–2665. doi: 10.1002/jbmr.2287.

Choi, B. *et al.* (2014) 'Cartilaginous extracellular matrix-modified chitosan hydrogels for cartilage tissue engineering', *ACS Applied Materials and Interfaces*, 6(22), pp. 20110–20121.

doi: 10.1021/am505723k.

Choi, J. S. *et al.* (2008) 'The influence of electrospun aligned poly(ε-caprolactone)/collagen nanofiber meshes on the formation of self-aligned skeletal muscle myotubes', *Biomaterials*, 29(19), pp. 2899–2906. doi: 10.1016/j.biomaterials.2008.03.031.

Chowdhury, F. *et al.* (2010) 'Material properties of the cell dictate stress-induced spreading and differentiation in embryonic stem cells.', *Nature materials*, 9(1), pp. 82–8. doi: 10.1038/nmat2563.

Christ, B., Huang, R. and Scaal, M. (2004) 'Formation and differentiation of the avian sclerotome.', *Anatomy and embryology*, 208(5), pp. 333–50. doi: 10.1007/s00429-004-0408-z.

Chu, P. K. and Liu, X. (2008) *Biomaterials fabrication and processing handbook*. 1st edn. Taylor & Francis.

Chung, E. J. *et al.* (2014) 'A biodegradable tri-component graft for anterior cruciate ligament reconstruction', *Journal of Tissue Engineering and Regenerative Medicine*, p. n/a-n/a. doi: 10.1002/term.1966.

Cooper, J. A. *et al.* (2007) 'Biomimetic tissue-engineered anterior cruciate ligament replacement', *Proceedings of the National Academy of Sciences*. National Academy of Sciences, 104(9), pp. 3049–3054. doi: 10.1073/pnas.0608837104.

Cooper, J. a *et al.* (2005) 'Fiber-based tissue-engineered scaffold for ligament replacement: design considerations and in vitro evaluation.', *Biomaterials*, 26(13), pp. 1523–32. doi: 10.1016/j.biomaterials.2004.05.014.

Crisan, M. *et al.* (2008) 'A perivascular origin for mesenchymal stem cells in multiple human organs.', *Cell stem cell*, 3(3), pp. 301–13. doi: 10.1016/j.stem.2008.07.003.

Criscenti, G. *et al.* (2016) 'Triphasic scaffolds for the regeneration of the bone–ligament interface', *Biofabrication*. IOP Publishing, 8(1), p. 015009. doi: 10.1088/1758-5090/8/1/015009.

Dalby, M. J. *et al.* (2007) 'The control of human mesenchymal cell differentiation using nanoscale symmetry and disorder.', *Nature materials*. Nature Publishing Group, 6(12), pp. 997–1003. doi: 10.1038/nmat2013.

Davidenko, N. *et al.* (2015) 'Control of crosslinking for tailoring collagen-based scaffolds stability and mechanics', *Acta Biomaterialia*. Acta Materialia Inc., 25, pp. 131–142. doi: 10.1016/j.actbio.2015.07.034.

Deneweth, J. M. *et al.* (2010) 'Tibiofemoral Joint Kinematics of the Anterior Cruciate Ligament-Reconstructed Knee During a Single-Legged Hop Landing', *The American Journal of Sports Medicine*. SAGE PublicationsSage CA: Los Angeles, CA, 38(9), pp. 1820–1828. doi: 10.1177/0363546510365531.

Dienst, M., Burks, R. T. and Greis, P. E. (2002) 'Anatomy and biomechanics of the anterior cruciate ligament', *Orthopedic Clinics of North America*. Elsevier, 33(4), pp. 605–620. doi: 10.1016/S0030-5898(02)00010-X.

Doroski, D. M., Brink, K. S. and Temenoff, J. S. (2007) 'Techniques for biological characterization of tissue-engineered tendon and ligament.', *Biomaterials*, 28(2), pp. 187–202. doi: 10.1016/j.biomaterials.2006.08.040.

Edwards, J. T., Brunski, J. B. and Higuchi, H. W. (1997) 'Mechanical and morphologic investigation of the tensile strength of a bone-hydroxyapatite interface.', *Journal of biomedical materials research*, 36(4), pp. 454–68.

Eichhorn, S. J. and Sampson, W. W. (2005) 'Statistical geometry of pores and statistics of porous nanofibrous assemblies.', *Journal of the Royal Society, Interface*. The Royal Society, 2(4), pp. 309–18. doi: 10.1098/rsif.2005.0039.

Van Eijk, F. *et al.* (2004) 'Tissue engineering of ligaments: a comparison of bone marrow stromal cells, anterior cruciate ligament, and skin fibroblasts as cell source.', *Tissue engineering*, 10(5–6), pp. 893–903. doi: 10.1089/1076327041348428.

Ellis, H. B. *et al.* (2012) 'Outcomes and Revision Rate After Bone–Patellar Tendon–Bone Allograft Versus Autograft Anterior Cruciate Ligament Reconstruction in Patients Aged 18 Years or Younger With Closed Physes', *Arthroscopy: The Journal of Arthroscopic & Related Surgery*, 28(12), pp. 1819–1825. doi: 10.1016/j.arthro.2012.06.016.

Embree, M. C. *et al.* (2016) 'Exploiting endogenous fibrocartilage stem cells to regenerate cartilage and repair joint injury', *Nature Communications*. Nature Publishing Group, 7, p. 13073. doi: 10.1038/ncomms13073.

Engelman, G. H. *et al.* (2014) 'Comparison of Allograft Versus Autograft Anterior Cruciate Ligament Reconstruction Graft Survival in an Active Adolescent Cohort', *The American Journal of Sports Medicine*. SAGE PublicationsSage CA: Los Angeles, CA, 42(10), pp. 2311–2318. doi: 10.1177/0363546514541935.

Engler, A. J. *et al.* (2006) 'Matrix elasticity directs stem cell lineage specification.', *Cell*, 126(4), pp. 677–89. doi: 10.1016/j.cell.2006.06.044.

Fan, H. *et al.* (2009) 'Anterior cruciate ligament regeneration using mesenchymal stem cells and silk scaffold in large animal model', *Biomaterials*, 30(28), pp. 4967–4977. doi: 10.1016/j.biomaterials.2009.05.048.

Farrell, E. *et al.* (2011) 'In-vivo generation of bone via endochondral ossification by in-vitro chondrogenic priming of adult human and rat mesenchymal stem cells.', *BMC musculoskeletal disorders*. BioMed Central, 12, p. 31. doi: 10.1186/1471-2474-12-31.

Faunø, P., Rahr-Wagner, L. and Lind, M. (2014a) 'Risk for Revision After Anterior Cruciate Ligament Reconstruction Is Higher Among Adolescents: Results From the Danish Registry of Knee Ligament Reconstruction.', *Orthopaedic journal of sports medicine*. SAGE Publications, 2(10), p. 2325967114552405. doi: 10.1177/2325967114552405.

Faunø, P., Rahr-Wagner, L. and Lind, M. (2014b) 'Risk for Revision After Anterior Cruciate Ligament Reconstruction Is Higher Among Adolescents', *Orthopaedic Journal of Sports Medicine*. SAGE PublicationsSage CA: Los Angeles, CA, 2(10). doi: 10.1177/2325967114552405.

Fisher, M. B. *et al.* (2015) 'Engineering meniscus structure and function via multi-layered mesenchymal stem cell-seeded nanofibrous Scaffolds', *Journal of Biomechanics*, 48(8), pp. 1412–1419. doi: 10.1016/j.jbiomech.2015.02.036.

Frazier, K. *et al.* (1996) 'Stimulation of fibroblast cell growth, matrix production, and granulation tissue formation by connective tissue growth factor', *The Journal of investigative dermatology*, 107(3), pp. 404–11.

Freeman, J. W., Woods, M. D. and Laurencin, C. T. (2007) 'Tissue engineering of the anterior cruciate ligament using a braid–twist scaffold design', *Journal of Biomechanics*, 40(9), pp. 2029–2036. doi: 10.1016/j.jbiomech.2006.09.025.

Fujioka, H. *et al.* (1997) 'Changes in the expression of type-X collagen in the fibrocartilage of rat Achilles tendon attachment during development', *Journal of orthopaedic research : official publication of the Orthopaedic Research Society*, 15(5), pp. 675–81. doi: 10.1002/jor.1100150508.

Galatz, L. *et al.* (2007) 'Development of the supraspinatus tendon-to-bone insertion: localized expression of extracellular matrix and growth factor genes.', *Journal of orthopaedic research : official publication of the Orthopaedic Research Society*, 25(12), pp. 1621–8. doi: 10.1002/jor.20441.

Garg, K. and Bowlin, G. L. (2011) 'Electrospinning jets and nanofibrous structures', *Biomicrofluidics*, 5(1), pp. 1–19. doi: 10.1063/1.3567097.

Garrigues, N. W. (2011) *Electrospun Scaffolds for Cartilage Tissue Engineering: Methods to Affect Anisotropy, Material and Cellular Infiltration*. Duke University.

Gawlitta, D. *et al.* (2015) 'Decellularized cartilage-derived matrix as substrate for endochondral bone regeneration.', *Tissue engineering. Part A*, 21(3–4), pp. 694–703. doi: 10.1089/ten.TEA.2014.0117.

Ge, Z., Goh, J. C. H. and Lee, E. H. (2005) 'Selection of Cell Source for Ligament Tissue Engineering', *Cell Transplantation*. Cognizant Communication Corporation, 14(8), pp. 573–583. doi: 10.3727/000000005783982819.

Gentleman, E. *et al.* (2009) 'Comparative materials differences revealed in engineered bone as a function of cell-specific differentiation.', *Nature materials*. Nature Publishing Group, 8(9), pp. 763–70. doi: 10.1038/nmat2505.

Ghasemi-Mobarakeh, L. *et al.* (2010) 'Bio-functionalized PCL nanofibrous scaffolds for nerve tissue engineering', *Materials Science and Engineering: C*, 30(8), pp. 1129–1136. doi: 10.1016/j.msec.2010.06.004.

de Godoy, L. M. F. *et al.* (2008) 'Comprehensive mass-spectrometry-based proteome quantification of haploid versus diploid yeast', *Nature*. Nature Publishing Group, 455(7217), pp. 1251–1254. doi: 10.1038/nature07341.

Greiner, A. and Wendorff, J. H. (2007) 'Electrospinning: A Fascinating Method for the Preparation of Ultrathin Fibers', *Angewandte Chemie International Edition*. WILEY-VCH Verlag,

46(30), pp. 5670–5703. doi: 10.1002/anie.200604646.

Hairfield-stein, M. *et al.* (2007) 'Development of Self-Assembled, Tissue-Engineered Ligament from Bone Marrow Stromal Cells', *Tissue engineering*, 13(4), pp. 703–10. doi: 10.1089/ten.2006.0203.

Harner, C. D. *et al.* (1995) 'Comparative study of the size and shape of human anterior and posterior cruciate ligaments', *Journal of Orthopaedic Research*. Wiley-Blackwell, 13(3), pp. 429–434. doi: 10.1002/jor.1100130317.

Harris, E. *et al.* (2017) 'Biofabrication of soft tissue templates for engineering the bone-ligament interface', *Biotechnology and Bioengineering*. doi: 10.1002/bit.26362.

Hartman, O. *et al.* (2010) 'Biofunctionalization of electrospun PCL-based scaffolds with perlecan domain IV peptide to create a 3-D pharmacokinetic cancer model.', *Biomaterials*. NIH Public Access, 31(21), pp. 5700–18. doi: 10.1016/j.biomaterials.2010.03.017.

Heinrich, D., van den Bogert, A. J. and Nachbauer, W. (2014) 'Relationship between jump landing kinematics and peak ACL force during a jump in downhill skiing: a simulation study.', *Scandinavian journal of medicine & science in sports*, 24(3), pp. e180-7. doi: 10.1111/sms.12120.

Hench, L. and Wilson, J. (1984) 'Surface-active biomaterials', *Science*, 226(4675). Available at: http://science.sciencemag.org/content/226/4675/630.long.

Hildebrand, K. A., Frank, C. B. and Hart, D. A. (2004) 'Gene intervention in ligament and tendon: current status, challenges, future directions.', *Gene therapy*, 11(4), pp. 368–78. doi: 10.1038/sj.gt.3302198.

Hoben, G. M. *et al.* (2007) 'Self-assembly of fibrochondrocytes and chondrocytes for tissue engineering of the knee meniscus.', *Tissue engineering*. Mary Ann Liebert, Inc. 140 Huguenot Street, 3rd Floor New Rochelle, NY 10801 USA, 13(5), pp. 939–46. doi: 10.1089/ten.2006.0116.

Hou, Y. *et al.* (2014) 'Collagen attachment to the substrate controls cell clustering through migration', *Physical Biology*, 11(5). doi: 10.1088/1478-3975/11/5/056007.

Huang, Y.-C. *et al.* (2005) 'Rapid formation of functional muscle in vitro using fibrin gels.', *Journal of applied physiology (Bethesda, Md. : 1985)*, 98(2), pp. 706–13. doi:

10.1152/japplphysiol.00273.2004.

Huang, Y. *et al.* (2017) 'Energy-Dissipative Matrices Enable Synergistic Toughening in Fiber Reinforced Soft Composites', *Advanced Functional Materials*, 27(9), p. 1605350. doi: 10.1002/adfm.201605350.

Huang, Z. *et al.* (2009) 'A bone-like nano-hydroxyapatite/collagen loaded injectable scaffold', *Biomedical Materials*, 4(5), p. 055005. doi: 10.1088/1748-6041/4/5/055005.

Huber, M., Trattnig, S. and Lintner, F. (2000) 'Anatomy, biochemistry, and physiology of articular cartilage.', *Investigative radiology*, 35(10), pp. 573–80.

Hussey, G. S., Keane, T. J. and Badylak, S. F. (2017) 'The extracellular matrix of the gastrointestinal tract: A regenerative medicine platform', *Nature Reviews Gastroenterology and Hepatology*. Nature Publishing Group, 14(9), pp. 540–552. doi: 10.1038/nrgastro.2017.76.

Ifkovits, J. L. *et al.* (2010) 'The influence of fibrous elastomer structure and porosity on matrix organization.', *PloS one*. Public Library of Science, 5(12), p. e15717. doi: 10.1371/journal.pone.0015717.

Ignat'eva, N. Y. *et al.* (2007) 'Determination of hydroxyproline in tissues and the evaluation of the collagen content of the tissues', *Journal of Analytical Chemistry*, 62(1), pp. 51–57. doi: 10.1134/S106193480701011X.

Iriuchishima, T. *et al.* (2014) 'Evaluation of ACL mid-substance cross-sectional area for reconstructed autograft selection', *Knee Surgery, Sports Traumatology, Arthroscopy*. Springer Berlin Heidelberg, 22(1), pp. 207–213. doi: 10.1007/s00167-012-2356-0.

Johnstone, B. *et al.* (1998) 'In vitro chondrogenesis of bone marrow-derived mesenchymal progenitor cells', *Experimental cell research*, 238(1), pp. 265–72. doi: 10.1006/excr.1997.3858.

Kafienah, W. and Sims, T. J. (2004) 'Biochemical Methods for the Analysis of Tissue-Engineered Cartilage', in *Biopolymer Methods in Tissue Engineering*. New Jersey: Humana Press, pp. 217–230. doi: 10.1385/1-59259-428-X:217.

Kartus, J., Movin, T. and Karlsson, J. (2001) 'Donor-site morbidity and anterior knee problems after anterior cruciate ligament reconstruction using autografts.', *Arthroscopy : the journal of arthroscopic & related surgery : official publication of the Arthroscopy Association of North*

America and the International Arthroscopy Association, 17(9), pp. 971–80. doi: 10.1053/jars.2001.28979.

Keane, T. J. *et al.* (2015) 'Tissue-Specific Effects of Esophageal Extracellular Matrix.', *Tissue engineering. Part A*, 21(17–18), pp. 2293–300. doi: 10.1089/ten.TEA.2015.0322.

Kilian, K. A. *et al.* (2010) 'Geometric cues for directing the differentiation of mesenchymal stem cells.', *Proceedings of the National Academy of Sciences of the United States of America*, 107(11), pp. 4872–7. doi: 10.1073/pnas.0903269107.

Kim, H.-L. *et al.* (2014) 'Fabrication of three-dimensional poly(lactic-co-glycolic acid) mesh by electrospinning using different solvents with dry ice', *Macromolecular Research*. The Polymer Society of Korea, 22(4), pp. 377–381. doi: 10.1007/s13233-014-2060-7.

Kim, S. *et al.* (2010) 'Transcriptional activation of peroxisome proliferator-activated receptor-γ requires activation of both protein kinase A and Akt during adipocyte differentiation', *Biochemical and Biophysical Research Communications*, 399(1), pp. 55–59. doi: 10.1016/j.bbrc.2010.07.038.

Kim, T. G., Chung, H. J. and Park, T. G. (2008) 'Macroporous and nanofibrous hyaluronic acid/collagen hybrid scaffold fabricated by concurrent electrospinning and deposition/leaching of salt particles', *Acta Biomaterialia*, 4(6), pp. 1611–1619. doi: 10.1016/j.actbio.2008.06.008.

Kishore, V. *et al.* (2012) 'Tenogenic differentiation of human MSCs induced by the topography of electrochemically aligned collagen threads', *Biomaterials*, 33(7), pp. 2137–44. doi: 10.1016/j.biomaterials.2011.11.066.

Kokubo, T. *et al.* (1999) 'Ceramic–metal and ceramic–polymer composites prepared by a biomimetic process', *Composites Part A: Applied Science and Manufacturing*. Elsevier, 30(4), pp. 405–409. doi: 10.1016/S1359-835X(98)00127-4.

Kokubo, T. and Takadama, H. (2006) 'How useful is SBF in predicting in vivo bone bioactivity?', *Biomaterials*, 27(15), pp. 2907–2915. doi: 10.1016/j.biomaterials.2006.01.017.

Kolambkar, Y. M. *et al.* (2014) 'Nanofiber orientation and surface functionalization modulate human mesenchymal stem cell behavior in vitro', *Tissue engineering. Part A*, 20(1–2), pp. 398–409. doi: 10.1089/ten.TEA.2012.0426.

Kuo, C. K., Marturano, J. E. and Tuan, R. S. (2010) 'Novel strategies in tendon and ligament tissue engineering: Advanced biomaterials and regeneration motifs', *BMC Sports Science, Medicine and Rehabilitation*. BioMed Central, 2(1), p. 20. doi: 10.1186/1758-2555-2-20.

Lauffenburger, D. A. and Griffith, L. G. (2001) 'Who's got pull around here? Cell organization in development and tissue engineering', *Proceedings of the National Academy of Sciences*, 98(8), pp. 4282–4284. doi: 10.1073/pnas.081083698.

Lee, B. L.-P. *et al.* (2012) 'Femtosecond laser ablation enhances cell infiltration into three-dimensional electrospun scaffolds', *Acta Biomaterialia*, 8(7), pp. 2648–2658. doi: 10.1016/j.actbio.2012.04.023.

Lee, C. H. *et al.* (2005) 'Nanofiber alignment and direction of mechanical strain affect the ECM production of human ACL fibroblast', *Biomaterials*, 26(11), pp. 1261–70. doi: 10.1016/j.biomaterials.2004.04.037.

Lee, C. H. *et al.* (2010) 'CTGF directs fibroblast differentiation from human mesenchymal stem/stromal cells and defines connective tissue healing in a rodent injury model', *The Journal of clinical investigation*, 120(9), pp. 3340–9. doi: 10.1172/JCI43230.

Lee, C. H. *et al.* (2014) 'Protein-releasing polymeric scaffolds induce fibrochondrocytic differentiation of endogenous cells for knee meniscus regeneration in sheep', *Science translational medicine*, 6(266), p. 266ra171. doi: 10.1126/scitranslmed.3009696.

Lee, D. *et al.* (2014) 'Tendon to bone healing and its implications for surgery', *Muscles, Ligaments and Tendons Journal*, 4(3), pp. 343–350.

Legnani, C. *et al.* (2010) 'Anterior cruciate ligament reconstruction with synthetic grafts. A review of literature', *International Orthopaedics*. Springer, 34(4), p. 465.

Leong, N. L., Petrigliano, F. A. and McAllister, D. R. (2014) 'Current tissue engineering strategies in anterior cruciate ligament reconstruction', *Journal of Biomedical Materials Research Part A*, 102(5), pp. 1614–1624. doi: 10.1002/jbm.a.34820.

Leung, M. *et al.* (2013) 'Tenogenic differentiation of human bone marrow stem cells via a combinatory effect of aligned chitosan–poly-caprolactone nanofibers and TGF-β3', *Journal of Materials Chemistry B*, 1(47), p. 6516. doi: 10.1039/c3tb20825g.

Li, H. *et al.* (2011) 'Comparative analysis with collagen type II distinguishes cartilage oligomeric

matrix protein as a primary TGFβ- responsive gene', *Osteoarthritis Cartilage*, 27(3), pp. 320–331. doi: 10.1002/nbm.3066.Non-invasive.

Li, H. *et al.* (2016) 'Functional Regeneration of Ligament-Bone Interface Using a Triphasic Silk-based Graft', *Biomaterials*. doi: 10.1016/j.biomaterials.2016.08.012.

Li, W.-J. *et al.* (2007) 'Engineering controllable anisotropy in electrospun biodegradable nanofibrous scaffolds for musculoskeletal tissue engineering.', *Journal of biomechanics*, 40(8), pp. 1686–93. doi: 10.1016/j.jbiomech.2006.09.004.

Li, X. *et al.* (2009) 'Nanofiber scaffolds with gradations in mineral content for mimicking the tendon-to-bone insertion site.', *Nano letters*, 9(7), pp. 2763–8. doi: 10.1021/nl901582f.

Lin, H. *et al.* (2012) 'Influence of decellularized matrix derived from human mesenchymal stem cells on their proliferation, migration and multi-lineage differentiation potential', *Biomaterials*, 33(18), pp. 4480–4489. doi: 10.1016/j.biomaterials.2012.03.012.

Lin, T. and Wang, X. (2013) *Needleless electrospinning of nanofibers : technology and applications*. 1st edn. Pan Stanford.

Liu, G. J. *et al.* (1998) 'Apatite–organic polymer composites prepared by a biomimetic process: improvement in adhesion of the apatite layer to the substrate by ultraviolet irradiation', *JOURNAL OF MATERIALS SCIENCE: MATERIALS IN MEDICINE*, 9, pp. 285–290.

Lowery, J. L., Datta, N. and Rutledge, G. C. (2010) 'Effect of fiber diameter, pore size and seeding method on growth of human dermal fibroblasts in electrospun poly(ε-caprolactone) fibrous mats', *Biomaterials*, 31(3), pp. 491–504. doi: 10.1016/j.biomaterials.2009.09.072.

Lu, H. H. and Jiang, J. (2006) 'Interface tissue engineering and the formulation of multiple-tissue systems.', *Advances in biochemical engineering/biotechnology*, 102, pp. 91–111.

Lu, H. H. and Thomopoulos, S. (2013) 'Functional attachment of soft tissues to bone: development, healing, and tissue engineering.', *Annual review of biomedical engineering*, 15, pp. 201–26. doi: 10.1146/annurev-bioeng-071910-124656.

Luginbuehl, V. *et al.* (2004) 'Localized delivery of growth factors for bone repair', *European Journal of Pharmaceutics and Biopharmaceutics*, 58(2), pp. 197–208. doi: 10.1016/j.ejpb.2004.03.004.

Lutolf, M. P., Gilbert, P. M. and Blau, H. M. (2009) 'Designing materials to direct stem-cell fate.', *Nature*. Nature Publishing Group, 462(7272), pp. 433–41. doi: 10.1038/nature08602.

Lyu, S. *et al.* (2013) 'Electrospun Fibers as a Scaffolding Platform for Bone Tissue Repair', *J Orthop Res*, 31(9), pp. 1382–1389. doi: 10.1002/jor.22367.

Makris, E. a *et al.* (2014) 'Developing functional musculoskeletal tissues through hypoxia and lysyl oxidase-induced collagen cross-linking', *Proceedings of the National Academy of Sciences of the United States of America*, 111(45), pp. E4832-41. doi: 10.1073/pnas.1414271111.

Mao, A. S., Shin, J.-W. and Mooney, D. J. (2016) 'Effects of substrate stiffness and cell-cell contact on mesenchymal stem cell differentiation.', *Biomaterials*. NIH Public Access, 98, pp. 184–91. doi: 10.1016/j.biomaterials.2016.05.004.

Matyas, J. R. *et al.* (1995) 'Stress governs tissue phenotype at the femoral insertion of the rabbit MCL.', *Journal of biomechanics*, 28(2), pp. 147–57.

McBeath, R. *et al.* (2004) 'Cell Shape, Cytoskeletal Tension, and RhoA Regulate Stem Cell Lineage Commitment', *Developmental Cell*, 6(4), pp. 483–495. doi: 10.1016/S1534-5807(04)00075-9.

McKee, M. D., Glimcher, M. J. and Nanci, A. (1992) 'High-resolution immunolocalization of osteopontin and osteocalcin in bone and cartilage during endochondral ossification in the chicken tibia', *The Anatomical Record*. Wiley Subscription Services, Inc., A Wiley Company, 234(4), pp. 479–492. doi: 10.1002/ar.1092340404.

Minns, R. J. and Steven, F. S. (1977) 'The collagen fibril organization in human articular cartilage.', *Journal of anatomy*, 123, pp. 437–457.

Moffat, K. L. *et al.* (2008) 'Characterization of the structure-function relationship at the ligament-to-bone interface.', *Proceedings of the National Academy of Sciences of the United States of America*, 105(23), pp. 7947–52. doi: 10.1073/pnas.0712150105.

Monteiro, S. N. *et al.* (2010) 'Selection of high strength natural fibers', *Matéria (Rio de Janeiro)*. Revista Matéria, 15(4), pp. 488–505. doi: 10.1590/S1517-70762010000400002.

Mori-Akiyama, Y. *et al.* (2003) 'Sox9 is required for determination of the chondrogenic cell lineage in the cranial neural crest', *Proceedings of the National Academy of Sciences of the United States of America*, 100(16), pp. 9360–5. doi: 10.1073/pnas.1631288100.

Moutos, F. T., Freed, L. E. and Guilak, F. (2007) 'A biomimetic three-dimensional woven composite scaffold for functional tissue engineering of cartilage.', *Nature materials*, 6(2), pp. 162–7. doi: 10.1038/nmat1822.

Mueller, S. (1999) 'Meniscus cells seeded in type I and type II collagen–GAG matrices in vitro', *Biomaterials*, 20(8), pp. 701–709. doi: 10.1016/S0142-9612(98)00189-6.

de Mulder, E. L. W. *et al.* (2013) 'Similar Hyaline-Like Cartilage Repair of Osteochondral Defects in Rabbits Using Isotropic and Anisotropic Collagen Scaffolds', *Tissue Engineering Part A*, 20, p. 131019071548003. doi: 10.1089/ten.tea.2013.0083.

Müller-Mai, C. M. *et al.* (1995) 'Nanoapatite and organoapatite implants in bone: Histology and ultrastructure of the interface', *Journal of Biomedical Materials Research*, 29(1), pp. 9–18. doi: 10.1002/jbm.820290103.

Murchison, N. D. *et al.* (2007) 'Regulation of tendon differentiation by scleraxis distinguishes force-transmitting tendons from muscle-anchoring tendons.', *Development (Cambridge, England)*, 134(14), pp. 2697–708. doi: 10.1242/dev.001933.

Murphy, W. L., Kohn, D. H. and Mooney, D. J. (2000) 'Growth of continuous bonelike mineral within porous poly(lactide-co-glycolide) scaffolds in vitro.', *Journal of biomedical materials research*, 50(1), pp. 50–8.

Murray, A. W. and Macnicol, M. F. (2004) '10–16 year results of Leeds-Keio anterior cruciate ligament reconstruction', *The Knee*, 11(1), pp. 9–14. doi: 10.1016/S0968-0160(03)00076-0.

Murray, M. M. *et al.* (2003) 'The effect of selected growth factors on human anterior cruciate ligament cell interactions with a three-dimensional collagen-GAG scaffold', *Journal of Orthopaedic Research*, 21(2), pp. 238–244. doi: 10.1016/S0736-0266(02)00142-0.

Murray, M. M. and Spector, M. (1999) 'Fibroblast distribution in the anteromedial bundle of the human anterior cruciate ligament: the presence of alpha-smooth muscle actin-positive cells', *Journal of orthopaedic research : official publication of the Orthopaedic Research Society*, 17(1), pp. 18–27. doi: 10.1002/jor.1100170105.

Nam, J. *et al.* (2007) 'Improved Cellular Infiltration in Electrospun Fiber via Engineered Porosity', *http://dx.doi.org/10.1089/ten.2006.0306*. Mary Ann Liebert, Inc. 140 Huguenot Street, 3rd Floor New Rochelle, NY 10801 USA .

Nau, T. and Teuschl, A. (2015) 'Regeneration of the anterior cruciate ligament: Current strategies in tissue engineering.', *World journal of orthopedics*. Baishideng Publishing Group Inc, 6(1), pp. 127–36. doi: 10.5312/wjo.v6.i1.127.

Nerurkar, N. L. *et al.* (2009) 'Nanofibrous biologic laminates replicate the form and function of the annulus fibrosus', *Nature materials*. Nature Publishing Group, 8(12), pp. 986–92. doi: 10.1038/nmat2558.

Nerurkar, N. L. *et al.* (2011) 'Homologous structure-function relationships between native fibrocartilage and tissue engineered from MSC-seeded nanofibrous scaffolds', *Biomaterials*. Elsevier Ltd, 32(2), pp. 461–468. doi: 10.1016/j.biomaterials.2010.09.015.

Niyibizi, C. *et al.* (1996) 'Identification and Immunolocalization of Type X Collagen at the Ligament–Bone Interface', *Biochemical and Biophysical Research Communications*. Academic Press, 222(2), pp. 584–589. doi: 10.1006/bbrc.1996.0787.

Noort, W. A. *et al.* (2012) 'Human versus porcine mesenchymal stromal cells: phenotype, differentiation potential, immunomodulation and cardiac improvement after transplantation', *Journal of Cellular and Molecular Medicine*, 16(8), pp. 1827–1839. doi: 10.1111/j.1582-4934.2011.01455.x.

Nöth, U. *et al.* (2005) 'Anterior cruciate ligament constructs fabricated from human mesenchymal stem cells in a collagen type I hydrogel.', *Cryotherapy*, 7(5), pp. 447–55. doi: 10.1080/14653240500319093.

Nourissat, G. *et al.* (2010) 'Mesenchymal stem cell therapy regenerates the native bone-tendon junction after surgical repair in a degenerative rat model.', *PloS one*, 5(8), p. e12248. doi: 10.1371/journal.pone.0012248.

Noyes, F. R. and Grood, E. S. (1976) 'The strength of the anterior cruciate ligament in humans and Rhesus monkeys.', *The Journal of bone and joint surgery. American volume*, 58(8), pp. 1074–82.

Nyberg, E. *et al.* (2017) 'Comparison of 3D-Printed Poly-ε-Caprolactone Scaffolds Functionalized with Tricalcium Phosphate, Hydroxyapatite, Bio-Oss, or Decellularized Bone Matrix <sup/>', *Tissue Engineering Part A*, 23(11–12), pp. 503–514. doi: 10.1089/ten.tea.2016.0418.

Obregon, N. *et al.* (2016) 'Effect of Polymer Concentration, Rotational Speed, and Solvent Mixture on Fiber Formation Using Forcespinning®', *Fibers*. Multidisciplinary Digital Publishing Institute, 4(2), p. 20. doi: 10.3390/fib4020020.

Oh, S. *et al.* (2009) 'Stem cell fate dictated solely by altered nanotube dimension.', *Proceedings of the National Academy of Sciences of the United States of America*, 106(7), pp. 2130–5. doi: 10.1073/pnas.0813200106.

Olvera, D. *et al.* (2017) 'Modulating microfibrillar alignment and growth factor stimulation to regulate mesenchymal stem cell differentiation', *Acta Biomaterialia*. doi: 10.1016/j.actbio.2017.10.010.

Oyane, A. *et al.* (1999) 'Sol-gel modification of silicone to induce apatite-forming ability.', *Biomaterials*, 20(1), pp. 79–84.

Oyane, A. *et al.* (2003) 'Preparation and assessment of revised simulated body fluids', *Journal of Biomedical Materials Research*, 65A(2), pp. 188–195. doi: 10.1002/jbm.a.10482.

Padron, S. *et al.* (2013) 'Experimental study of nanofiber production through forcespinning', *Journal of Applied Physics*, 113(2). doi: 10.1063/1.4769886.

Park, J. S. *et al.* (2007) 'Surface hydrolysis of fibrous poly(ε-caprolactone) scaffolds for enhanced osteoblast adhesion and proliferation', *Macromolecular Research*. Springer-Verlag, 15(5), pp. 424–429. doi: 10.1007/BF03218809.

Pauly, H. M. *et al.* (2016) 'Mechanical properties and cellular response of novel electrospun nanofibers for ligament tissue engineering: Effects of orientation and geometry', *Journal of the Mechanical Behavior of Biomedical Materials*, 61, pp. 258–270. doi: 10.1016/j.jmbbm.2016.03.022.

Pauly, H. M. *et al.* (2017) 'Hierarchically Structured Electrospun Scaffolds with Chemically Conjugated Growth Factor for Ligament Tissue Engineering', *Tissue Engineering Part A*. Mary Ann Liebert, Inc. 140 Huguenot Street, 3rd Floor New Rochelle, NY 10801 USA, 23(15–16), pp. 823–836. doi: 10.1089/ten.tea.2016.0480.

Paxton, J. Z. *et al.* (2010) 'Factors affecting the longevity and strength in an in vitro model of the bone-ligament interface.', *Annals of biomedical engineering*, 38(6), pp. 2155–66. doi: 10.1007/s10439-010-0044-0.

Paxton, J. Z., Barr, K. and Grover, L. M. (2012) 'Current Progress in Enthesis Repair: Strategies for Interfacial Tissue Engineering', *Orthopedic & Muscular System*, S1, pp. 1–13. doi: 10.4172/2161-0533.S1-003.

Paxton, J. Z., Grover, L. M. and Baar, K. (2010) 'Engineering an in vitro model of a functional ligament from bone to bone.', *Tissue engineering. Part A*. Mary Ann Liebert, Inc. 140 Huguenot Street, 3rd Floor New Rochelle, NY 10801 USA, 16(11), pp. 3515–25. doi: 10.1089/ten.TEA.2010.0039.

Pedowitz, R. A., O'Connor, J. J. and Akeson, W. H. (2003) *Daniel's knee injuries : ligament and cartilage structure, function, injury, and repair*. Second edi. Edited by R. A. Pedowitz, J. J. O'Connor, and W. H. Akeson. Lippincott Williams & Wilkins.

Pek, Y. S., Wan, A. C. A. and Ying, J. Y. (2010) 'The effect of matrix stiffness on mesenchymal stem cell differentiation in a 3D thixotropic gel.', *Biomaterials*, 31(3), pp. 385–91. doi: 10.1016/j.biomaterials.2009.09.057.

Petrigliano, F. A. *et al.* (2015) 'In vivo evaluation of electrospun polycaprolactone graft for anterior cruciate ligament engineering.', *Tissue engineering. Part A*, 21(7–8), pp. 1228–36. doi: 10.1089/ten.TEA.2013.0482.

Pham, Q. P., Sharma, U. and Mikos, A. G. (2006a) 'Electrospinning of Polymeric Nanofibers for Tissue Engineering Applications: A Review', *Tissue Engineering*, 12(5), pp. 1197–1211. doi: 10.1089/ten.2006.12.1197.

Pham, Q. P., Sharma, U. and Mikos, A. G. (2006b) 'Electrospun poly (e-caprolactone) microfiber and multilayer nanofiber/microfiber scaffolds: Characterization of scaffolds and measurement of cellular infiltration', *Biomacromolecules*, 7(10), pp. 2796–2805. doi: 10.1021/bm060680j.

Phillips, J. E. *et al.* (2008) 'Engineering graded tissue interfaces', *Proceedings of the National Academy of Sciences of the United States of America*, 105(34), pp. 12170–5. doi: 10.1073/pnas.0801988105.

Pittenger, M. F. *et al.* (1999) 'Multilineage potential of adult human mesenchymal stem cells.', *Science*, 284(5411), pp. 143–7.

Prodromos, C. C. *et al.* (2007) 'A meta-analysis of the incidence of anterior cruciate ligament

tears as a function of gender, sport, and a knee injury-reduction regimen.', *Arthroscopy : the journal of arthroscopic & related surgery : official publication of the Arthroscopy Association of North America and the International Arthroscopy Association*, 23(12), p. 1320–1325.e6. doi: 10.1016/j.arthro.2007.07.003.

Pryce, B. A. *et al.* (2007) 'Generation of transgenic tendon reporters, ScxGFP and ScxAP, using regulatory elements of the scleraxis gene.', *Developmental dynamics : an official publication of the American Association of Anatomists*, 236(6), pp. 1677–82. doi: 10.1002/dvdy.21179.

Ramakrishnan, S. R. *et al.* (2009) 'Integrating shotgun proteomics and mRNA expression data to improve protein identification', *Bioinformatics*, 25(11), pp. 1397–1403. doi: 10.1093/bioinformatics/btp168.

Ricchetti, E. T. *et al.* (2012) 'Scaffold devices for rotator cuff repair', *Journal of Shoulder and Elbow Surgery*, 21(2), pp. 251–265. doi: 10.1016/j.jse.2011.10.003.

Richard-Lacroix, M. and Pellerin, C. (2013) 'Molecular Orientation in Electrospun Fibers: From Mats to Single Fibers', *Macromolecules*. American Chemical Society, 46(24), pp. 9473–9493. doi: 10.1021/ma401681m.

Rnjak-Kovacina, J. *et al.* (2011) 'Tailoring the porosity and pore size of electrospun synthetic human elastin scaffolds for dermal tissue engineering', *Biomaterials*. Elsevier, 32(28), pp. 6729–6736. doi: 10.1016/J.BIOMATERIALS.2011.05.065.

Rodeo, S. A. *et al.* (1993) 'Tendon-healing in a bone tunnel. A biomechanical and histological study in the dog', *The Journal of bone and joint surgery. American volume*. The American Orthopedic Association, 75(12), pp. 1795–803.

Rodeo, S. A. *et al.* (1999) 'Use of recombinant human bone morphogenetic protein-2 to enhance tendon healing in a bone tunnel.', *The American journal of sports medicine*. American Orthopaedic Society for Sports Medicine, 27(4), pp. 476–88.

Rossetti, L. *et al.* (2017) 'The microstructure and micromechanics of the tendon–bone insertion', *Nature materials*, 16, pp. 664–670. doi: 10.1038/NMAT4863.

Rothrauff, B. B. *et al.* (2017) 'Braided and Stacked Electrospun Nanofibrous Scaffolds for Tendon and Ligament Tissue Engineering', *Tissue Engineering Part A*, 23, pp. 378–389. doi: 10.1089/ten.tea.2016.0319.

Rothrauff, B. B., Yang, G. and Tuan, R. S. (2017) 'Tissue-specific bioactivity of soluble tendon-derived and cartilage-derived extracellular matrices on adult mesenchymal stem cells.', *Stem cell research & therapy*. BioMed Central, 8(1), p. 133. doi: 10.1186/s13287-017-0580-8.

Rumian, A. P., Wallace, A. L. and Birch, H. L. (2007) 'Tendons and ligaments are anatomically distinct but overlap in molecular and morphological features—a comparative study in an ovine model', *Journal of Orthopaedic Research*, 25(4), pp. 458–464. doi: 10.1002/jor.20218.

Rusu, M., Ursu, M. and Rusu, D. (2006) 'Poly(vinyl chloride) and Poly(e-caprolactone) Blends for Medical Use', *Journal of Thermoplastic Composite Materials*. Sage PublicationsSage CA: Thousand Oaks, CA, 19(2), pp. 173–190. doi: 10.1177/0892705706056463.

Samavedi, S. *et al.* (2012) 'Response of bone marrow stromal cells to graded co-electrospun scaffolds and its implications for engineering the ligament-bone interface', *Biomaterials*, 33(31), pp. 7727–35. doi: 10.1016/j.biomaterials.2012.07.008.

Samavedi, S. *et al.* (2014) 'Electrospun meshes possessing region-wise differences in fiber orientation, diameter, chemistry and mechanical properties for engineering bone-ligament-bone tissues.', *Biotechnology and bioengineering*, 111(12), pp. 2549–59. doi: 10.1002/bit.25299.

Schmittgen, T. D. and Livak, K. J. (2008) 'Analyzing real-time PCR data by the comparative CT method', *Nature Protocols*. Nature Publishing Group, 3(6), pp. 1101–1108. doi: 10.1038/nprot.2008.73.

Schuler, M. *et al.* (2006) 'Biomedical interfaces: titanium surface technology for implants and cell carriers', *Nanomedicine*. Future Medicine Ltd London, UK , 1(4), pp. 449–463. doi: 10.2217/17435889.1.4.449.

Schünke, M. *et al.* (2006) *THIEME Atlas of Anatomy. General Anatomy and Musculoskeletal System*. Thieme.

Schwartz, A. G. *et al.* (2012) 'Mineral distributions at the developing tendon enthesis.', *PloS one*, 7(11), p. e48630. doi: 10.1371/journal.pone.0048630.

Schweitzer, R. *et al.* (2001) 'Analysis of the tendon cell fate using Scleraxis, a specific marker for tendons and ligaments.', *Development (Cambridge, England)*, 128(19), pp. 3855–66.

Scott-Burden, T. (1994) 'Extracellular Matrix: The Cellular Environment', *Physiology*. American

Physiological Society, 9(3), pp. 110–115.

Scott, M. A. *et al.* (2011) 'Current Methods of Adipogenic Differentiation of Mesenchymal Stem Cells', *Stem Cells and Development*, 20(10), pp. 1793–1804. doi: 10.1089/scd.2011.0040.

Scotti, C. *et al.* (2010) 'Recapitulation of endochondral bone formation using human adult mesenchymal stem cells as a paradigm for developmental engineering.', *Proceedings of the National Academy of Sciences of the United States of America*, 107(16), pp. 7251–6. doi: 10.1073/pnas.1000302107.

Scotti, C. *et al.* (2013) 'Engineering of a functional bone organ through endochondral ossification', *Proceedings of the National Academy of Sciences*, 110(10), pp. 3997–4002. doi: 10.1073/pnas.1220108110.

Shaerf, D. A. *et al.* (2014) 'Anterior cruciate ligament reconstruction best practice: A review of graft choice.', *World journal of orthopedics*. Baishideng Publishing Group Inc, 5(1), pp. 23–9. doi: 10.5312/wjo.v5.i1.23.

Shang, S. *et al.* (2010) 'The effect of electrospun fibre alignment on the behaviour of rat periodontal ligament cells', *European cells & materials*, 19(23), pp. 180–92. doi: 10.22203/eCM.v019a18.

Sharma, R. I. and Snedeker, J. G. (2010) 'Biochemical and biomechanical gradients for directed bone marrow stromal cell differentiation toward tendon and bone', *Biomaterials*, 31(30), pp. 7695–7704. doi: 10.1016/j.biomaterials.2010.06.046.

Sheehy, E. J. *et al.* (2013) 'Engineering osteochondral constructs through spatial regulation of endochondral ossification.', *Acta biomaterialia*, 9(3), pp. 5484–92. doi: 10.1016/j.actbio.2012.11.008.

Shimomura, K., Rothrauff, B. B. and Tuan, R. S. (2017) 'Region-Specific Effect of the Decellularized Meniscus Extracellular Matrix on Mesenchymal Stem Cell–Based Meniscus Tissue Engineering', *The American Journal of Sports Medicine*, 45(3), pp. 604–611. doi: 10.1177/0363546516674184.

Shin, S. R. *et al.* (2012) 'Carbon Nanotube Reinforced Hybrid Microgels as Scaffold Materials for Cell Encapsulation', *ACS Nano*. American Chemical Society, 6(1), pp. 362–372. doi: 10.1021/nn203711s.

Shukunami, C. *et al.* (2006) 'Scleraxis positively regulates the expression of tenomodulin, a differentiation marker of tenocytes', *Developmental Biology*, 298(1), pp. 234–247. doi: 10.1016/j.ydbio.2006.06.036.

Shukunami, C. *et al.* (2016) 'Molecular characterization and function of tenomodulin, a marker of tendons and ligaments that integrate musculoskeletal components', *Japanese Dental Science Review*, 52(4), pp. 84–92. doi: 10.1016/j.jdsr.2016.04.003.

Silver, F. H., Freeman, J. W. and Seehra, G. P. (2003) 'Collagen self-assembly and the development of tendon mechanical properties', *Journal of Biomechanics*, 36(10), pp. 1529–1553. doi: 10.1016/S0021-9290(03)00135-0.

Simonet, M. *et al.* (2007) 'Ultraporous 3D polymer meshes by low-temperature electrospinning: Use of ice crystals as a removable void template', *Polymer Engineering & Science*. Wiley Subscription Services, Inc., A Wiley Company, 47(12), pp. 2020–2026. doi: 10.1002/pen.20914.

Simonet, M. *et al.* (2014) 'Tailoring the void space and mechanical properties in electrospun scaffolds towards physiological ranges', *J. Mater. Chem. B*, 2(3), pp. 305–313. doi: 10.1039/C3TB20995D.

Smith, C. *et al.* (2014) 'The Use of the Ligament Augmentation and Reconstruction System (LARS) for Posterior Cruciate Reconstruction', *Arthroscopy: The Journal of Arthroscopic & Related Surgery*, 30(1), pp. 111–120. doi: 10.1016/j.arthro.2013.09.081.

Smith, K. D. *et al.* (2011) 'The organisation of elastin and fibrillins 1 and 2 in the cruciate ligament complex.', *Journal of anatomy*. Wiley-Blackwell, 218(6), pp. 600–7. doi: 10.1111/j.1469-7580.2011.01374.x.

Soliman, S. *et al.* (2011) 'Controlling the porosity of fibrous scaffolds by modulating the fiber diameter and packing density', *Journal of Biomedical Materials Research Part A*, 96A(3), pp. 566–574. doi: 10.1002/jbm.a.33010.

Spalazzi, J. P. *et al.* (2006) 'Development of controlled matrix heterogeneity on a triphasic scaffold for orthopedic interface tissue engineering', *Tissue engineering*, 12(12), pp. 3497–508. doi: 10.1089/ten.2006.12.3497.

Spalazzi, J. P. *et al.* (2008) 'In vivo evaluation of a multiphased scaffold designed for

orthopaedic interface tissue engineering and soft tissue-to-bone integration.', *Journal of biomedical materials research. Part A*, 86(1), pp. 1–12. doi: 10.1002/jbm.a.32073.

Spindler, K. P. *et al.* (2004) 'Anterior cruciate ligament reconstruction autograft choice: bone-tendon-bone versus hamstring: does it really matter? A systematic review.', *The American journal of sports medicine*, 32(8), pp. 1986–1995. doi: 10.1177/0363546504271211.

Spindler, K. P. and Wright, R. W. (2008) 'Clinical practice. Anterior cruciate ligament tear.', *The New England journal of medicine*. NIH Public Access, 359(20), pp. 2135–42. doi: 10.1056/NEJMcp0804745.

Stankus, J. J. *et al.* (2006) 'Microintegrating smooth muscle cells into a biodegradable, elastomeric fiber matrix', *Biomaterials*, 27(5), pp. 735–744. doi: 10.1016/j.biomaterials.2005.06.020.

Strohman, R. C. *et al.* (1990) 'Myogenesis and histogenesis of skeletal muscle on flexible membranes in vitro', *In Vitro Cellular & Developmental Biology*, 26(2), pp. 201–208. doi: 10.1007/BF02624113.

Subramony, S. D. *et al.* (2013) 'The guidance of stem cell differentiation by substrate alignment and mechanical stimulation', *Biomaterials*. Elsevier Ltd, 34(8), pp. 1942–53. doi: 10.1016/j.biomaterials.2012.11.012.

Sugimoto, Y., Takimoto, A., Hiraki, Y., *et al.* (2013) 'Generation and characterization of ScxCre transgenic mice.', *Genesis (New York, N.Y. : 2000)*, 51(4), pp. 275–83. doi: 10.1002/dvg.22372.

Sugimoto, Y., Takimoto, A., Akiyama, H., *et al.* (2013) 'Scx+/Sox9+ progenitors contribute to the establishment of the junction between cartilage and tendon/ligament.', *Development (Cambridge, England)*. Oxford University Press for The Company of Biologists Limited, 140(11), pp. 2280–8. doi: 10.1242/dev.096354.

Sun, W., Moffat, K. and Lu, H. (2007) 'Characterization of fibrochondrocytes derived from the ligament-bone insertion', *Trans Orthop Res Soc*.

Sundararaghavan, H. G., Metter, R. B. and Burdick, J. A. (2010) 'Electrospun Fibrous Scaffolds with Multiscale and Photopatterned Porosity', *Macromolecular Bioscience*, 10(3), pp. 265–270. doi: 10.1002/mabi.200900363.

Tanahashi, M. *et al.* (1994) 'Apatite coated on organic polymers by biomimetic process:

Improvement in its adhesion to substrate by NaOH treatment', *Journal of Applied Biomaterials*, 5(4), pp. 339–347. doi: 10.1002/jab.770050409.

Tanahashi, M. *et al.* (1995) 'Apatite coated on organic polymers by biomimetic process: improvement in adhesion to substrate by HCl treatment', *Journal of Materials Science: Materials in Medicine*. Kluwer Academic Publishers, 6(6), pp. 319–326. doi: 10.1007/BF00120299.

Tanaka, T., Fujii, K. and Kumagae, Y. (1999) 'Comparison of biochemical characteristics of cultured fibrochondrocytes isolated from the inner and outer regions of human meniscus.', *Knee surgery, sports traumatology, arthroscopy : official journal of the ESSKA*, 7(2), pp. 75–80. doi: 10.1007/s001670050125.

Tang, E. P. S. and Lim, C. T. (2006) *Nanomechanics of materials and structures*. Edited by S. H. Tze-jer Chuang, P. M. Anderson, M.-K. Wu. Springer.

Tas, A. C. and Bhaduri, S. B. (2004) 'Rapid coating of Ti6Al4V at room temperature with a calcium phosphate solution similar to 10× simulated body fluid', *Journal of Materials Research*, 19(09), pp. 2742–2749. doi: 10.1557/JMR.2004.0349.

Telemeco, T. A. *et al.* (2005) 'Regulation of cellular infiltration into tissue engineering scaffolds composed of submicron diameter fibrils produced by electrospinning', *Acta Biomaterialia*, 1(4), pp. 377–385. doi: 10.1016/j.actbio.2005.04.006.

Thompson, E. M. *et al.* (2015) 'Recapitulating endochondral ossification: a promising route to *in vivo* bone regeneration', *Journal of Tissue Engineering and Regenerative Medicine*, 9(8), pp. 889–902. doi: 10.1002/term.1918.

Thorpe, S. D. *et al.* (2012) 'European Society of Biomechanics S.M. Perren Award 2012: The external mechanical environment can override the influence of local substrate in determining stem cell fate', *Journal of Biomechanics*, 45(15), pp. 2483–2492. doi: 10.1016/j.jbiomech.2012.07.024.

Toy, B. J. *et al.* (1995) 'Arterial supply to the human anterior cruciate ligament.', *Journal of athletic training*. National Athletic Trainers Association, 30(2), pp. 149–52.

Triantafyllidi, E. *et al.* (2013) 'The Shape and the Thickness of the Anterior Cruciate Ligament Along Its Length in Relation to the Posterior Cruciate Ligament: A Cadaveric Study',

Arthroscopy: The Journal of Arthroscopic & Related Surgery, 29(12), pp. 1963–1973. doi: 10.1016/j.arthro.2013.09.007.

Tuli, R. *et al.* (2003) 'Transforming growth factor-beta-mediated chondrogenesis of human mesenchymal progenitor cells involves N-cadherin and mitogen-activated protein kinase and Wnt signaling cross-talk', *The Journal of biological chemistry*. American Society for Biochemistry and Molecular Biology, 278(42), pp. 41227–36. doi: 10.1074/jbc.M305312200.

Turner, N. J. *et al.* (2010) 'Xenogeneic extracellular matrix as an inductive scaffold for regeneration of a functioning musculotendinous junction.', *Tissue engineering. Part A*, 16(11), pp. 3309–17. doi: 10.1089/ten.TEA.2010.0169.

Tzezana, R., Zussman, E. and Levenberg, S. (2008) 'A layered ultra-porous scaffold for tissue engineering, created via a hydrospinning method.', *Tissue engineering. Part C, Methods*, 14(4), pp. 281–8. doi: 10.1089/ten.tec.2008.0201.

Visconti, C. S. *et al.* (1996) 'Biochemical Analysis of Collagens at the Ligament–Bone Interface Reveals Presence of Cartilage-Specific Collagens', *Archives of Biochemistry and Biophysics*. Academic Press, 328(1), pp. 135–142. doi: 10.1006/abbi.1996.0153.

Visser, J., Levett, P. A., *et al.* (2015) 'Crosslinkable Hydrogels Derived from Cartilage, Meniscus, and Tendon Tissue', *Tissue Engineering Part A*, 21(7–8), pp. 1195–1206. doi: 10.1089/ten.tea.2014.0362.

Visser, J., Melchels, F. P. W., *et al.* (2015) 'Reinforcement of hydrogels using three-dimensionally printed microfibres', *Nature Communications*. Nature Publishing Group, 6, p. 6933. doi: 10.1038/ncomms7933.

Vogel, C. and Marcotte, E. M. (2012) 'Insights into the regulation of protein abundance from proteomic and transcriptomic analyses.', *Nature reviews. Genetics*. NIH Public Access, 13(4), pp. 227–32. doi: 10.1038/nrg3185.

Vunjak-Novakovic, G. *et al.* (2004) 'Tissue engineering of ligaments.', *Annual review of biomedical engineering*, 6, pp. 131–56. doi: 10.1146/annurev.bioeng.6.040803.140037.

Wang, H. B. *et al.* (2010) 'Varying the diameter of aligned electrospun fibers alters neurite outgrowth and Schwann cell migration.', *Acta biomaterialia*, 6(8), pp. 2970–8. doi: 10.1016/j.actbio.2010.02.020.

Wang, I.-N. E. *et al.* (2006) 'Age-dependent changes in matrix composition and organization at the ligament-to-bone insertion.', *Journal of orthopaedic research : official publication of the Orthopaedic Research Society*, 24(8), pp. 1745–55. doi: 10.1002/jor.20149.

Wang, X. *et al.* (2013) 'Crystalline Morphology of Electrospun Poly(ε-caprolactone) (PCL) Nanofibers', *Industrial & Engineering Chemistry Research*, 52(13), pp. 4939–4949. doi: 10.1021/ie302185e.

Watabe, T. and Miyazono, K. (2009) 'Roles of TGF-β family signaling in stem cell renewal and differentiation', *Cell Research*. Nature Publishing Group, 19(1), pp. 103–115. doi: 10.1038/cr.2008.323.

Webb, W. R. *et al.* (2013) 'The application of poly(3-hydroxybutyrate-co-3-hydroxyhexanoate) scaffolds for tendon repair in the rat model', *Biomaterials*. Elsevier Ltd, 34(28), pp. 6683–6694. doi: 10.1016/j.biomaterials.2013.05.041.

Weiler, A., Hoffmann, R. F. G., *et al.* (2002) 'Tendon healing in a bone tunnel. Part II: Histologic analysis after biodegradable interference fit fixation in a model of anterior cruciate ligament reconstruction in sheep', *Arthroscopy: The Journal of Arthroscopic & Related Surgery*, 18(2), pp. 124–135. doi: 10.1053/jars.2002.30657.

Weiler, A., Unterhauser, F. N., *et al.* (2002) 'α-Smooth muscle actin is expressed by fibroblastic cells of the ovine anterior cruciate ligament and its free tendon graft during remodeling', *Journal of Orthopaedic Research*, 20(2), pp. 310–317. doi: 10.1016/S0736-0266(01)00109-7.

Wong, S.-C., Baji, A. and Leng, S. (2008) 'Effect of fiber diameter on tensile properties of electrospun poly(ε-caprolactone)', *Polymer*, 49(21), pp. 4713–4722. doi: 10.1016/j.polymer.2008.08.022.

Woo, S. L.-Y. *et al.* (2006) 'Biomechanics of knee ligaments: injury, healing, and repair.', *Journal of biomechanics*, 39(1), pp. 1–20. doi: 10.1016/j.jbiomech.2004.10.025.

Woo, S. L. *et al.* (1983) 'Measurement of mechanical properties of ligament substance from a bone-ligament-bone preparation.', *Journal of orthopaedic research : official publication of the Orthopaedic Research Society*, 1(1), pp. 22–9. doi: 10.1002/jor.1100010104.

Woo, S. L. *et al.* (1991) 'Tensile properties of the human femur-anterior cruciate ligament-tibia complex. The effects of specimen age and orientation.', *The American journal of sports*

medicine, 19(3), pp. 217–25.

Woodruff, M. A. and Hutmacher, D. W. (2010) 'The return of a forgotten polymer—Polycaprolactone in the 21st century', *Progress in Polymer Science*, 35(10), pp. 1217–1256. doi: 10.1016/j.progpolymsci.2010.04.002.

Wu, Y. *et al.* (2017) 'Evaluation of the Bone-ligament and tendon insertions based on Raman spectrum and its PCA and CLS analysis', *Scientific Reports*. Nature Publishing Group, 7, p. 38706. doi: 10.1038/srep38706.

Xie, J. *et al.* (2010) '"Aligned-to-random" nanofiber scaffolds for mimicking the structure of the tendon-to-bone insertion site.', *Nanoscale*. The Royal Society of Chemistry, 2(6), pp. 923–6. doi: 10.1039/c0nr00192a.

Xie, J. *et al.* (2012) 'Fabrication of nanofiber scaffolds with gradations in fiber organization and their potential applications.', *Macromolecular bioscience*, 12(10), pp. 1336–41. doi: 10.1002/mabi.201200115.

Yahia, L.-H. and Drouin, G. (1989) 'Microscopical investigation of canine anterior cruciate ligament and patellar tendon: Collagen fascicle morphology and architecture', *Journal of Orthopaedic Research*, 7(2), pp. 243–251. doi: 10.1002/jor.1100070212.

Yamauchi, K. *et al.* (2004) 'Preparation of collagen/calcium phosphate multilayer sheet using enzymatic mineralization', *Biomaterials*. Elsevier, 25(24), pp. 5481–5489. doi: 10.1016/J.BIOMATERIALS.2003.12.057.

Yang, F. *et al.* (2005) 'Electrospinning of nano/micro scale poly(L-lactic acid) aligned fibers and their potential in neural tissue engineering.', *Biomaterials*, 26(15), pp. 2603–10. doi: 10.1016/j.biomaterials.2004.06.051.

Yee, W. A. *et al.* (2008) 'Stress-induced structural changes in electrospun polyvinylidene difluoride nanofibers collected using a modified rotating disk', *Polymer*, 49(19), pp. 4196–4203. doi: 10.1016/j.polymer.2008.07.032.

Yin, Z. *et al.* (2015) 'Electrospun scaffolds for multiple tissues regeneration in vivo through topography dependent induction of lineage specific differentiation', *Biomaterials*, 44, pp. 173–85. doi: 10.1016/j.biomaterials.2014.12.027.

Yodmuang, S. *et al.* (2015) 'Silk microfiber-reinforced silk hydrogel composites for functional

cartilage tissue repair', *Acta Biomaterialia*, 11, pp. 27–36. doi: 10.1016/j.actbio.2014.09.032.

Yu, Y. Y. *et al.* (2010) 'Bone morphogenetic protein 2 stimulates endochondral ossification by regulating periosteal cell fate during bone repair', *Bone*, 47(1), pp. 65–73. doi: 10.1016/j.bone.2010.03.012.

Zander, N. E. *et al.* (2010) 'Surface-modified nanofibrous biomaterial bridge for the enhancement and control of neurite outgrowth.', *Biointerphases*, 5(4), pp. 149–58. doi: 10.1116/1.3526140.

Zantop, T., Petersen, W. and Fu, F. (2005) 'Anatomy of the anterior cruciate ligament', *Operative Techniques in Orthopaedics*, 15, pp. 20–28. doi: 10.1053/j.oto.2004.11.011.

Zhang, R. and Ma, P. X. (1999) 'Porous poly(L-lactic acid)/apatite composites created by biomimetic process.', *Journal of biomedical materials research*, 45(4), pp. 285–93.

Zhang, Y. Z. *et al.* (2005) 'Characterization of the surface biocompatibility of the electrospun PCL-Collagen nanofibers using fibroblasts', *Biomacromolecules*, 6(5), pp. 2583–2589. doi: 10.1021/bm050314k.

Zhu, X. *et al.* (2008) 'Electrospun Fibrous Mats with High Porosity as Potential Scaffolds for Skin Tissue Engineering'. American Chemical Society.